Dissertation

submitted to the

Combined Faculties for the Natural Sciences and for Mathematics

of the Ruperto–Carola University of Heidelberg, Germany

for the degree of

Doctor of Natural Sciences

presented by

Diplom-Physiker Thorsten Straßel

born in Pirmasens

Oral examination: 22.10.2008

Quantum Memory with Atomic Ensembles of Rubidium and Single Photons for Long Distance Quantum Communication

Referees: Prof. Dr. Jian-Wei Pan

Prof. Dr. Michael Fleischhauer

Zusammenfassung

Quantenspeicher mit atomaren Ensembles aus Rubidium und mit Einzelphotonen zur Langstrecken-Quantenkommunikation

Die Arbeit, die in dieser Dissertation vorgestellt wird, untersucht theoretisch und experimentell Quantenspeicher mit atomaren Ensembles, die zur Quantenkommunikation über lange Strecken (long-distance quantum communication) geeignet sind. Dabei werden laser-gekühlte, ultrakalte Atomwolken aus ^{87}Rubidium als Speicher für nichtklassische Einzelphotonenzustände verwendet. Basierend auf der Atom-Licht Schnittstelle des Protokolls von Duan, Lukin, Cirac, Zoller (DLCZ) zur Langstrecken-Quantenkommunikation werden die Einzelphotonenzustände abgespeichert und wieder ausgelesen. Mithilfe der nichtklassischen Korrelationen und des Quantenspeichers wird eine deterministische Einzelphotonenquelle demonstriert. Der Hong-Ou-Mandel Dip zwischen zwei so generierten einzelnen Photonen wurde gemessen. Es wird dargelegt, wie unter Benutzung von magnetfeld-insensitiven atomaren Zustände ein Quantenspeicher mit langer Lebenszeit in einer optischen Dipolfalle realisiert wurde und mit einer verlängerten Spinwellen-Wellenlänge die Dephasierung des Speichers durch thermische Bewegung unterdrückt werden konnte. Gemessene Speicherzeiten von über einer Millisekunde stellen einen erheblichen Fortschritt zur Umsetzung der Quantenkommunikation über lange Strecken dar.

Abstract

Quantum Memory with Atomic Ensembles of Rubidium and Single Photons for Long Distance Quantum Communication

The work presented in this thesis investigates theoretically and experimentally quantum memories with atomic ensembles, which are suited for long-distance quantum communication. For this purpose laser-cooled, ultracold atomic clouds of ^{87}Rubidium are used as memory for nonclassical single-photon states. Base on the atom-light interface of the protocol from Duan, Lukin, Cirac, Zoller (DLCZ) for long distance quantum communication the single photons states are stored and retrieved. By the help of non-classical correlations and the quantum memory a deterministic single photon source is demonstrated. The Hong-Ou-Mandel dip between two single photons created in this way has been measured. Moreover it is reported on the realization of a long-lived quantum memory by using magnetic-field insensitive atomic states in an optical trap and that by extending the spinwave's wavelength the dephasing of the memory due to thermal motion could be suppressed. Measured storage times of over a millisecond represent a significant progress towards the realization of long distance quantum communication.

Contents

Chapter 1

Introduction

"**Quantum Communication** *is the art of transferring a quantum state from one place to another*"[1].

This statement does not only define the subject of quantum communication, it presents its realization as an art. This may sound strange to a reader which becomes acquainted to this field. But indeed, since it is already difficult to prepare and protect a quantum state against the influence of its environment, its transfer to a different location is very challenging. In the age of information many technologies (for classical messages) unthinkable in the previous centuries are technically mature. Thus the transfer of quantum states for purposes of information exchange could superficially be seen as a pure extension of present concepts. As we will present in the first two chapters of the thesis at hand, it is justified to speak of quantum communication as an art due the creativity needed in solving the existing challenges.

Before immersing into details of these challenges, let us give a general survey of the field. In the first half of the twentieth century quantum mechanics has been developed in order to overcome the dead end of classical mechanics which became obvious in case of the black body radiation. After the successful application of the quantum mechanical principle to various questions of physics in the following decades, *quantum information* emerged in the beginning of the eighties in the last century, especially as **quantum cryptography**. Classical cryptography has shown that a secure transfer of a message is possible by using one-time pads [1]. The message is encoded by the sender with a randomly generated key which has the same length as the message. Then the encrypted message is transmitted by a communication channel. The receiver who posses the same key can decode the message. In order to provide the best security it is important to use the key only once. Thus the problem of the secure exchange of a message is "reduced" to the task of distributing the keys between the communication partners without leaking information of the key (**key distribution problem**). Obviously, it is impractical to exchange keys for every single message by trusted messengers carrying the keys. Thus most common in cryptography nowadays is the use of asymmetric key encryption like the RSA algo-

---

[1]N. Gisin and R. Thew in Quantum Communication, Nature Physics, **1**, 167,(2007)

rithm [2]. Both communication partners have two keys, a public and a private one. Party A, or Alice, encodes the messages with her private key and with the public key of party B, or Bob, which she receives by using an insecure transmission channel. The encrypted message is send through the (same) insecure channel. Then Bob can use his private key and Alice's public to decode the message. The security stems of the mathematical complexity of factoring large numbers and taking n-th roots modulo a composite, unknown number n [3]. With the so-called Shor algorithm a quantum computer can perform in principle the factorization in polynomial time [4]. Despite the technical challenges of constructing a quantum computer still ahead, the security of key distribution based on mathematical complexity may be overcome in the future.

Quantum key distribution (**QKD**) provides a physical secure mean to exchange keys between two parties. Its security originates from the fact that in general a quantum state [2] cannot be copied or cloned [5][6]. The first proposal for QKD, the so-called BB84 protocol, uses very faint laser pulses where the qubits are encoded in the polarization state of the photons [7] [8]. Alice prepares randomly specific non-orthogonal qubit states which are send through the communication channel. Bob applies projective measurements in randomly switched bases on received "single" qubit states and notes the measured results. From the quantum mechanically correlation between the measured and the prepared states Alice and Bob can distill a key by communicating the chosen measurement bases by the help of an classical and insecure channel. An eavesdropper, usually called Eve, cannot gain any information from spying on this channel since she has no access on the sufficient quantum mechanical correlations without blocking the connection between Alice and Bob. If there is only one photon send for every quantum state any attempt to measure or copy the quantum states during the transmission will disturb the state according to the no-cloning theorem. Unfortunately the transmission channel introduces noise which means that the qubit states can be disturbed. The BB84 protocol provides a procedure to check the quantum error bit rate (QBER) of the specific communication channel by comparison of a partial key. Only if the rate is below a certain threshold it can be guaranteed that the communication is secure. Otherwise an eavesdropper could gain information by using for example the photon splitting attack [9]. Since the noise increases with the channel length (absorption of the photons), the secure communication distance is limited by the condition that the channel noise must be smaller than the threshold of the QBER. Additional technical limitations like the dark count rate of the photon detectors introduce more noise and reduce the communication distance further. Despite the significant progress [10] [11] [12] [13] of this approach within the last years, the fact that the communication distance cannot be larger than in the order of a few hundred kilometers due to the photon absorption is a fundamental limitation [9].

By using entangled photon pairs (EPR pairs)[14] the communication distance can be enhanced. Spontaneous parametric down conversion (SPDC) with nonlinear crystals [15] has been the workhorse of the investigations on quantum computation and communication with photons [9]. The entangled photon pairs generated by these sources have enabled the fundamental experiments with linear optics (e.g. quantum

---

[2]non-orthogonal with respect to the measurement bases

teleporation [16], observation of three-photon Greenberger-Horne-Zeilinger entanglement [17], quantum nonlocality in three-photon Greenberger-Horne-Zeilinger entanglement [18], experimental demonstration of four-Photon entanglement and high-fidelity teleportation [19], entanglement purification for quantum communication[20], entanglement purification of arbitrary unknown states [21], entanglement swapping [22], realization of freely propagating teleported qubits [23], quantum cryptography with entangled photons [24], quantum teleportation of a two-qubit composite system [25], entanglement-based quantum communication over 144 km [26]). The application of entanglement sources for QKD has inspired much progress on various approaches to increase the distance of communication [27][28][29][26][30]). When Alice an Bob share an entangled pair they can measure quantum correlations which are used to distill a key. The restriction of the communication distance due to the noise of the transmission channels can be relaxed by entanglement distribution, but it can not be overcome nevertheless. During the distribution of the entangled photons pairs the channel noise reduces their quality or even destroys their joint state. The transfer of a quantum state with high fidelity for means of information processing is in the focus of quantum communication as well. Quantum teleportation provides a an elegant solution to this problem [31]. But it, too, suffers from the channel noise, since entanglement distribution over transmission lines is required. The fidelity, i.e. quality, of the quantum state after teleportation (see chapter 2) is affected by the quality of the EPR pair, if available at all.

Ideas for the construction of a quantum computer have triggered considerations to connect spatially separated of these machines by a network. The expression of a "*quantum internet*" which should describe quantum networks suitable for secure communication or the exchange of quantum "data" was formed [32][33]. An interface is necessary to convert the quantum states of matter used in the quantum computer to photonic quantum states for transmission and vice versa. The conceptional "simplest" approach which is the interaction of a single atom with a single photon in a high finesse cavity [34] (the so-called strong coupling regime) was proposed first. Despite the successes [35] [36] which have been achieved in implementing that interface type it has turned out that it needs considerable efforts before that technology is mature. The demonstration of a first building block with this interface for a future quantum network has not been realized yet.

In the mean time two new developments, the stopping of classical light pulses in atomic ensembles [37][38] [39] [40] and the theoretical concept of a quantum repeater [41], have paved way for a seminal proposal by Duan, Lukin, Cirac and Zoller (DLCZ) for long distance quantum communication with atomic ensembles and linear optics with single photons [42].

The protocol combines entanglement generation, connection, noise-reduction (purification of errors due to photon loss) and quantum memory such that it finally provides an entangled pair between the two distant communication partners with a sub-exponential scaling of temporal and spatial resources with distance. The quantum memory is crucial for the scaling. In the ground-braking proposal of DLCZ an atom-light interface is introduced which also determines the character of the quantum memory. In the thesis presented here, we use of this atom-light interface and atomic ensembles as quantum memory for DLCZ-type protocols [43][44][45] [46] [47].

Quantum memory can be a valuable resource for quantum computation as well. This application is out of scope of the present thesis and thus we refer the interested reader to [48] [49][50].

Since the publication of the DLCZ protocol in the year 2001 a tremendous experimental progress has been made in order to implement the protocol in thermal ensembles [51] [52][53] and in ultra-cold atomic ensembles [54] [55] [56] [57] [58] [59][60][61] [62] [63] [64] [65] [66][67] [68] [69] [70] [71] [72] [73] [74] [75] [76] [77] [78]. Nevertheless the key bottleneck for a practical realization of long distance quantum communication is the limited lifetime of the present memory (see chapter (4)).

In the following thesis, we present the successful implementation of single photon sources based on atomic ensembles as quantum memory. The work on a deterministic single-photon source is outlined. Using two sources of this new type we generated entangled photon pairs with a narrowband width. Moreover, the improvement of the quantum memory as a key element of long-distance quantum communication is reported. We investigate and isolate the various decoherence mechanisms limiting the storage time of such a memory. Further on we introduce methods to control and overcome these limiting factors and show important results on the way to make this quantum memory type suitable for long distance quantum communication.

- In the second chapter, basic concepts of long-distance quantum communication are reviewed.

- The DLCZ protocol is introduced with emphasis on the proposed atom-light interface in chapter 3.

- In chapter 4 the DLCZ-type quantum memory is analyzed in order to determine its requirements and the mechanisms for decoherence during the storage time.

- The implementation of such a quantum memory as an ensemble of cold atoms is described in chapter 5 by outlining the experimental set-ups. Important experimental methods used in the subsequent chapters are presented as well.

- Chapter 6 describes the demonstration of a deterministic single photon source by the aid of quantum memory and electronic feedback. Subsequently the generation of narrow-bandwidth entangled photons from independent atomic ensembles is presented

- Chapter 7 demonstrates a quantum-memory with long life time of milliseconds suitable for long-distance quantum communication. By the preparation of the atomic ensemble in first order magnetic field insensitive states and the additional generation of a long wavelength spin wave enables this significant improvement of the storage time. The observation of non-classical light from atomic ensemble confined in an optical dipole trap in another step in order to improve the quantum memory. By addressing the first-order magnetic-field insensitive states an improved lifetime of 60 μs is achieved.

- The last chapter summarizes the main results. In addition an outlook on future work is given.

The thesis concludes with appendices of theoretical details on the light shift and descriptions of electronic devices developed during the course of this thesis in cooperation with the workshops of the "Physikalisches Institut".

Chapter 2

Elements of Quantum Communication

The transfer of a quantum state from one location to another is a very challenging task. A transmission line which is suitable for the transfer of a quantum state is called a quantum channel. A quantum state is in general very sensitive to interaction with the environment. Any disturbance alters the state or even destroys it. The influence of the channel noise is therefore a critical parameter. As carrier of the quantum state for communication purposes photons are the "ideal" choice. They are fast and robust. In addition they can be guided in optical fibers or transmitted in free-space with optical elements like mirrors and lenses. Depending on the actual implementation, for example the type of fiber, the maximum communication distance for a secure connection varies. Typically this limit is several times of the absorption length of the medium, denoted by l_{att}. We recall that this restriction arises from the condition that the channel noise must be below a threshold [9].

This chapter starts with the possibilities to encode a qubit with photonic states. Then we review the quantum communication schemes of quantum key distribution, entanglement-based distribution and quantum teleportation and point out the fundamental difficulties to achieve quantum communication over long distance by these methods. Subsequently we take a look at a space based solution before we introduce the important concept of a *quantum repeater*.

2.1   Qubit

The smallest unit carrying quantum information is called a **qubit**. A pure qubit is a two-level system which can take any linear superposition of two basis states

$$|\Psi\rangle = \frac{1}{\sqrt{|\alpha|^2 + |\beta|^2}} \left(\alpha |0\rangle + \beta |1\rangle \right), \tag{2.1}$$

where $|0\rangle$ and $|1\rangle$ denote the basis and the complex numbers α and β are the probability amplitudes. Any quantum mechanical two-level system can be used to implement it, for example atoms and photons and ions. Each implementation has its advantages and disadvantages. For the transmission over long distances light, i.e. photons, is the "natural" choice as carrier of quantum information. Very often the quantum state is encoded in the polarization of the photons; then the base states of the qubit are substituted by the states of horizontal and vertical polarizations according to

$$|H\rangle = |0\rangle \quad |V\rangle = |1\rangle . \tag{2.2}$$

Instead of polarization we use the number of single photons in a single spatial mode. In the formalism of second quantization [79] we know that single photons can be described in the so-called Fock or number state basis. In this discrete basis the number in the Ket corresponds to the number of photons in the specified spatial mode, e.g. in a cavity mode. Then the basis vectors are

$$|0\rangle = |vac\rangle \tag{2.3}$$

$$|1\rangle = \hat{a}^\dagger |0\rangle , \tag{2.4}$$

where $\hat{a}^\dagger$ is the creation operator for the mode a. An arbitrary number of photons n is described by n-fold application of the creation operator on the vacuum:

$$|n\rangle \sim \left(\hat{a}^\dagger\right)^n |vac\rangle . \tag{2.5}$$

The commutation relation for the annihilation and creation operators is

$$\left[\hat{a} , \hat{a}^\dagger\right] = 1, \tag{2.6}$$

according to the bosonic properties of the photon.
The single photon basis is widely used in a dual rail representation of a qubit as well. Thus a superposition state of a photon in spatial mode a (or cavity a) and a photon in mode b is written as

$$|\Psi\rangle = \alpha |1\rangle_a |0\rangle_b + \beta |0\rangle_a |1\rangle_b = \alpha |10\rangle + \beta |01\rangle . \tag{2.7}$$

In terms of polarization this state reads as

$$|\Psi\rangle = \frac{1}{\sqrt{2}} \left(|HV\rangle - |VH\rangle\right), \tag{2.8}$$

which is a maximally entangled state (EME).

2.2 Quantum Communication schemes

2.2.1 Quantum key distribution

This area of quantum communication has drawn most attention in the past. The currently available and in the near future foreseeable technologies for quantum communication can not compete with classical communication in terms of bit-transmission rates. But the security which they provide is suitable for the absolute secure distribution of cryptographic keys.

The straight forward approach for transferring a quantum state is to send a qubit from the sender A or Alice to the receiver B or Bob with faint laser pulses. Photons used as qubits can be transmitted in free-space or by a fiber link. Sometimes this concept is referred to by the term "direct quantum communication". This approach was pioneered by Charles Bennett and Gilles Brassard in their famous BB84 protocol [7] which we have reviewed in the introduction part. Depending on the type of attack in order to gain information from the qubits send through the noisy channels, the upper limit for the QBER can be computed. For QBER < 11% [9] the communication is secure. To this error rate there are contributions from detector dark counts, the detection efficiency and imperfect photon sources. The technology has improved significantly in the last decade. An excellent review is given in [9]. The longest communication distance which so far has been achieved is 184.6 kilometers [80].

Entanglement-based distribution: An entangled pair of photons shared by Alice and Bob can be used for QKD as well [24]. A more sophisticated scheme is the use of EPR pairs which are shared between Alice and Bob . Firstly the security of the quantum channel is tested by violation of the Wigner inequality (CHSH-inequality can be used as well[8]). Then a variation of the BB84 is used in order to share the secret key. The most recent experiment between two Canary islands in 2007 achieved a distance of 144 kilometers [26].

A state of a composite system of two photons which not separable ($|\Psi\rangle \neq |\Psi\rangle_1 \bigotimes |\Psi\rangle_2$ with $|\Psi\rangle \in H_1 \bigotimes H_2$ and $|\Psi\rangle_i$ are pure states) is an entangled state. A pure entangled state is

$$|\Psi_{entang}\rangle = \frac{1}{\sqrt{2}} \left(|0\rangle_A \otimes |1\rangle_B - |1\rangle_A \otimes |0\rangle_B \right). \tag{2.9}$$

Such an entangled state, or Bell state, is usually referred to as Einstein-Podolsky-Rosen pair, for short **EPR** pair[14]. In fact equation (2.9) describes even a maximally entangled state, which means that there exists a local base such that the state can be written as a diagonal matrix. A measurement of one of the photons projects the joint state to one realization, such that the state of the remaining photon is instantaneously fixed. These non-classical correlations are used to sift a key.

The workhorse for the generation of entangled photons are sources using spontaneous
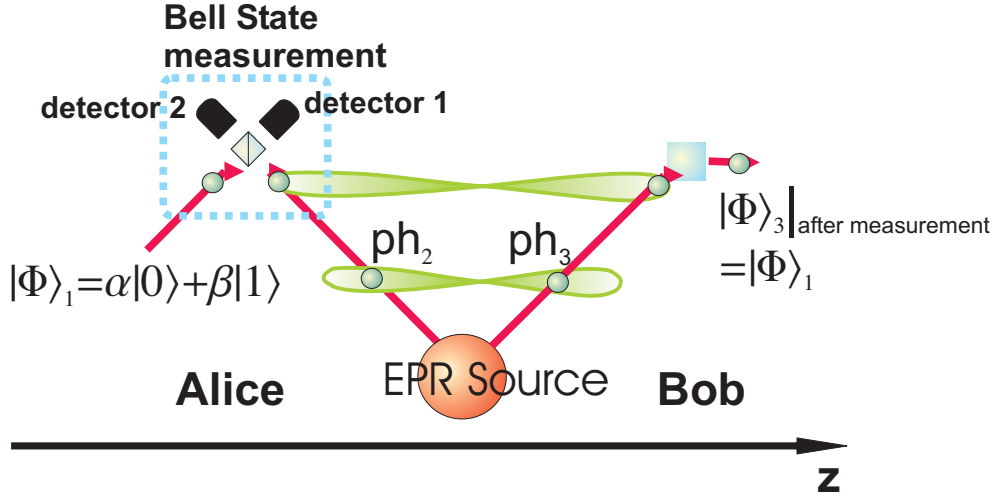
Figure 2.1: Schematic of the Teleportation principle: The EPR source sends pairs of entangled photons to Alice and Bob. Alice overlaps her photon with the photon carrying the quantum state which she wants to transmit. After a joint Bell-state measurement of the two photons on Alice side, the combined quantum state of all three particles collapses and besides a phase Bob receives Alice's quantum state. By a classical channel Alice can communicate her result of the Bell state measurement and by a unitary transformation Bob applies to his photon, he posses the quantum state which Alice wanted to send [3]. On her side the state is destroyed by the Bell state measurement, such that the no-cloning theorem cannot be violated. The schematic assumes $|\Phi^+\rangle$ as result of Alice's Bell state measurement, such that Bob does not need to apply any transformation in order to obtain the correct state.

parametric down-conversion (SPDC) [15]. The polarization entangled photon pairs

$$|\Psi\rangle = \frac{1}{\sqrt{2}} \left(|V\rangle_1 |H\rangle_2 + e^{i\phi} |H\rangle_1 |V\rangle_2 \right), \tag{2.10}$$

are generated by pumping a nonlinear crystal with UV light at a production rate of about $60,000$ pairs $\mathrm{s}^{-1}\mathrm{mW}^{-1}$ with a bandwidth of 5 nm. The photons are spontaneously generated by the decay of a pump photon into two with half of the energy and emitted into cones in the forward direction. By collecting the photons at two intersection points of the cones one obtains the two polarization entangled and spatially separated photons which can be send to Alice and Bob.

2.2.2 Teleportation

The entanglement distribution can be used as well to transfer a quantum with high quality by means of quantum teleportation. This is approach is different to QKD where non-classical correlations are used to sift a key. In case of teleporation an entangled pair shared by Alice and Bob is used to transfer an (unknown) quantum state. "An unknown quantum state $|\Psi\rangle$ can be disassembled and later reconstructed from, purely classical information and purely nonclassical Einstein-Podolsky-Rosen (EPR)

correlations" [31]. In order to send Alice's quantum state $|\phi_A\rangle_1 = \alpha |0\rangle_1 + \beta |1\rangle_1$ to Bob, she can make use of the entangled photon pair $|\phi^+\rangle_{23} = \frac{1}{\sqrt{2}} (|0\rangle_2 |0\rangle_3 + |1\rangle_2 |1\rangle_3)$. A Bell-state measurement on Alice's two photons $1, 2$ projects their state into one of the four Bell states:

$$\left|\phi^{\pm}\right\rangle_{12} = \frac{1}{\sqrt{2}} \left(|0\rangle_1 |0\rangle_2 \pm |1\rangle_1 |1\rangle_2\right) \tag{2.11}$$

$$\left|\psi^{\pm}\right\rangle_{12} = \left(|1\rangle_1 |0\rangle_2 \pm |0\rangle_1 |1\rangle_2\right). \tag{2.12}$$

Depending on the result of the Bell state measurement a unitary operation has to be applied on the state of photon 3 on Bob's site in order to recover the original state $|\phi_A\rangle_1$. Therefore the result of the Bell state measurement has to be transmitted in a classical channel from Alice to Bob. [16]
In an experiment in 2004 teleportation over 600 meters across the river Danube was achieved [81]. This scheme is affected as well by the limitations of the exponential increase in noise with the length of the transmission line. The fidelity of the EPR pair which needs to be delivered to Alice and Bob decreases with a similar scaling over distance.

2.3 Problems towards long-distance Quantum Communication

2.3.1 Photon Loss

The communication distance is limited by the absorption of photons in the fibre (or the atmosphere). Coherent states $|\alpha\rangle$ as well as single photon states $|n\rangle$ are attenuated according to the Lambert-Beer law [82]

$$
\begin{aligned}
|1\rangle &\longrightarrow \eta |1\rangle \langle 1| + (1 - \eta) |0\rangle \langle 0| \\
|\alpha\rangle &\longrightarrow \left|\sqrt{n}\alpha\right\rangle \\
\eta &= \exp\left(-L/L_{atten}\right)
\end{aligned} \tag{2.13a}
$$

and a typical attenuation length L_{abs}. The tolerable damping which allows secure quantum cryptography for a source rate $10 \cdot 10^6$ Hz is ~ 60 dB [1]. With an attenuation of $a = 0.195$dB/km^{-1} at 1550 nm, 65% detection efficiency, a dark count rate of 10 counts per second, a clock rate of 1 MHz and an damping of ~ 8 dB due to the detection optics a distance of ~ 140 kilometers has been achieved with sifted key bit rates of $\sim 10^0 - 10^{-1}$ [80]. The reported distance of ~ 180 kilometer has not been secure against all attacks. The acceptable damping of the fiber depends roughly

---

[1]According to reference [9] this limit is given by the dark count rate of present single photon detectors. Detection signals due to stray light in the signal channel can be integrated in this dark count rate. The rate of single photons from the source must be significantly higher than the noise due to the dark counts. For present detectors the dark count probabilities are $\sim 10^{-7}$.

on the detector dark counts and on the signal rate of source. The exponential absorption law means that these devices must be improved by orders of magnitude in order to provide security over long distances. In addition the sifted key bit rates decrease even more, such that communication becomes impractical. For free-space communication additional limitations apply. The violation of CHSH-inequality has been observed on Canary Islands over 144 kilometers of atmospheric absorption [26]. A further extension of this distance is problematic. Besides the above mentioned exponential photon loss, geographical features like the earth's curvature and atmospheric turbulence are the most serious issues.

Due to this absorption law intercontinental distances can not be connected by "direct communication".

2.3.2   Decoherence

Decoherence is the degradation of the quantum state due to its interaction with the environment. This means for an entangled state that it losses its quality, i.e. fidelity. The probability that the entanglement is completely destroyed grows with distance. A common model to describe this effect is the "depolarization channel". Suppose we have initially a single qubit state ρ. After the transmission it is with a probability of p replaced by the mixed state $\sigma_0^{(P)}/2$ and with probability $(1-p)$ it is unchanged. Here $\sigma_0^{(P)}$ denotes the first Pauli matrix which corresponds to the unity matrix I_d in d dimensions. The combined quantum system of the Qubit and the noise is then described by

$$\mathcal{E}(\rho) = \frac{pI_2}{2} + (1-p)\rho. \tag{2.14}$$

For a 4 dimensional system, i.e. an EPR pair, the mixed state in the equation is replaced by $I_4/4$. The probability $p = p_0 \exp\left(-l/L_{abs}\right)$ for the entanglement destruction scales exponential with the length channel length l, p_0 is the initial probability [83].

Thus the distribution of an entangled pair of photons for quantum communication does not change the scaling compared to the transmission of faint laser pulses.

2.3.3   Non-Deterministic Sources and Detectors

For all entanglement-based schemes, i.e. QKD and teleportation, the probabilistic nature of the currently known sources for entanglement generation represents an additional major problem. In section (2.5) we show that a straight-forward approach to use entanglement swapping to extend the communication distance is very limited because of this fact.

The single photon detectors which are currently available have an detection efficiency $\sim 50\%$. Since swapping and purification protocols (section (2.5)) with single photons are based on projective measurements, the non-deterministic detection need to be included in the scaling behavior shortly after.

2.4 Space Based Quantum Communication

In order to overcome the limitation of attenuation in the quantum channel in air or in fibers one can turn to make use of satellites. The damping in the atmosphere from a ground station to a satellite in a low orbit is comparable to 8 km in air at sea level [30]. From the satellite the signal can be relayed to the receiver's ground station [30]. This procedures works as long as both ground stations can have the satellite in their field of view or an extra satellite to satellite connection. Several orbiting satellites could establish quantum communication links around the globe. The free-space communication experiment between two Canary Islands over 144 kilometers has demonstrated the feasibility of a connection from a ground station to a satellite in principle [26]

2.5 Repeater based Protocols

The concept of entanglement swapping seems to be a solution to extend the communication distance of the protocols which rely on entanglement distribution. The probabilistic nature of the generation of entanglement (usually by parametric down conversion) is the key problem, why the scaling with distance of this approach is remains exponential. This can be demonstrated by a simple example.

Swapping: First one divides the total distance L into several equidistant segments of length l, such that their total number is $n = l/L$. Then one generates the entanglement between the ends of a segment, i.e. by sending the photons from an SPDC source to them. In the following one starts to connect adjacent segments by entanglement swapping. Two pairs of entangled photons can be connected by a joined Bell state measurement on one photon from each pair such that the two remaining photons are entangled. Two separated EPR sources emit the single pairs simultaneously (see figure (2.2)). Then the joint state of the four photons is given by

$$|\Psi\rangle_{1234} = \frac{1}{2} \left(|1\rangle_1 |0\rangle_2 - |0\rangle_1 |1\rangle_2 \right) \otimes \left(|1\rangle_3 |0\rangle_4 - |0\rangle_3 |1\rangle_4 \right) \qquad (2.15)$$

This can be rewritten into

$$|\Psi\rangle = \frac{1}{2} \left(\left|\Psi^+\right\rangle_{14} \left|\Psi^+\right\rangle_{23} + \left|\Psi^-\right\rangle_{14} \left|\Psi^-\right\rangle_{23} + \left|\Phi^+\right\rangle_{14} \left|\Phi^+\right\rangle_{23} + \left|\Phi^-\right\rangle_{14} \left|\Phi^-\right\rangle_{23} \right), \quad (2.16)$$

where $\left|\Psi^\pm\right\rangle_{i,j}$ and $\left|\Phi^\pm\right\rangle_{i,j}$ are the Bell states of photons i,j. A joint Bell state measurement on photons $2, 3$ projects photons $1, 4$ onto one of the Bell states, i.e. into an entangled state. By entanglement swapping [22] one can "entangle photons that never interacted."

In order to distribute an EPR state over the distance $L = 2n \times L_0$ we need to apply entanglement swapping n times (see figure (2.2)). Assume that χ is the probability
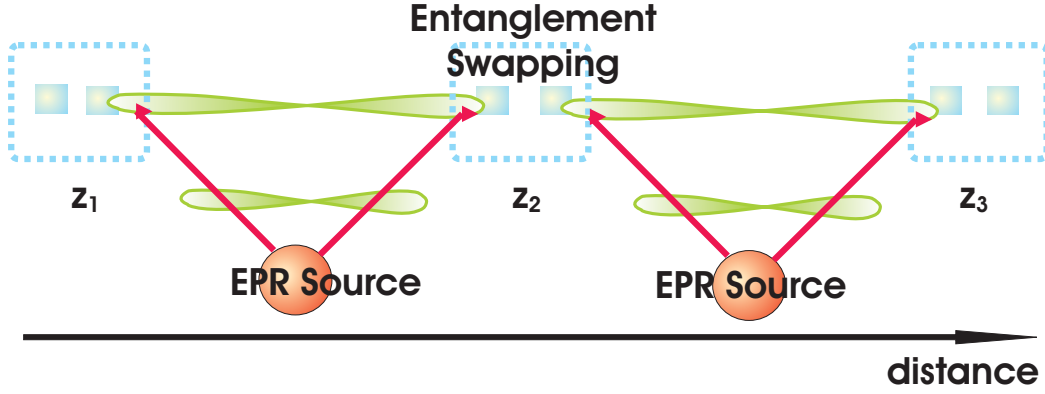
Figure 2.2: Schematics of entanglement swapping for a communication set-up: EPR-sources (SPDC [15]) emit pairs of entangled photons to the inter connection points z_i. At every point a joint Bell-state measurement on the two photons from adjacent pairs is applied and the entanglement is swapped. So in case of a measurement at z_2 the photons at this point are destroyed, but the photons at z_1 and z_3 are entangled by this process. At z_1 and z_3 additional swapping can be done with adjacent pair. Then entanglement distribution over distances can be implemented. Since the generation of the EPR pairs is probabilistic, the distribution across the complete distance can only take place if the EPR pairs at the connection points z_i are present at the same time (within their coherence length). As long as the entanglement of one segment cannot be stored at these nodes, the scaling of the connection time with the communication distance is exponential.

to generate entanglement in one trial, then the probability to create an EPR pair over the distance L is χ^n. We have assumed that all others resources (detectors, fibers, etc.) work perfectly.

Purification: The transmission of an EPR pair as well as the entanglement swapping reduces the quality of the EPR pair which is shared between both ends. In both cases the prepared pure entangled state $|\phi\rangle$ becomes a mixed state ρ. The fidelity F describes the quality of this mixed state with respect to the pure state:

$$F = \langle \phi | \, \rho \, | \phi \rangle , \qquad (2.17)$$

which is maximal if $F = 1$. The fidelity can be increased by distillation from a set of entangled pairs with low quality $F_1 > 1/2$ into a single pair with $F_2 > F_1$. This can be achieved by a sequence of local unitary operations using a CNOT gate [84] or by linear optics [21].
However various purification protocols account for different errors and vary in speed.

Problems of Swapping followed by Purification The minimal fidelity for entanglement purification is $F > 1/2$, which means that the segment length L must be chosen such that $L \simeq L_{abs}$. Therefore it not possible to distribute an entangled pair over $L \gg L_{abs}$ and subsequently purify it such that in can be used for quan-

tum communication. The scaling of the communication with distance obeys still an exponential law

$$p(L) = e^{-\frac{L}{L_{atten}}} \tag{2.18}$$

Therefore the average number of trials is

$$n_{av} = e^{\frac{L}{L_{atten}}} \tag{2.19}$$

if every segment is has a length of $l = L/N$ then the number of average trials for a successful preparation is

$$n_{avSwap} = \frac{N}{p(L/N)^N} = Ne^{L/L_{atten}}. \tag{2.20}$$

Thus the scaling remains exponential.

The concept of a *Quantum Repeater*   In classical communication, the problem of exponential attenuation can be overcome by using repeaters at certain points in the channel, which amplify the signal and restore it to its original shape. The **no-cloning theorem** does not allow amplification in quantum communication. But there exists the concept of a *quantum repeater*[41] which translates the classical approach into the quantum world. The distance between the parties A and B is divided into smaller segments such that on can send parts of maximally entangled pairs through each segment. Via entanglement swapping the segments are connected such that they establish entangled pairs over larger distances. Each connection process decreases the fidelity of the resulting entangled pair. It is important to note that even for a perfect connection the fidelity still decreases exponentially with distance. For example, we connect two pairs with fidelity $F = 0.95$ then the resulting pair has $F = (0.95)^2$. Therefore after connecting a few segments the fidelity is so low that it can no longer be increased by purification.

The core of a solution to this is to connect a string of (imperfect) entangled pairs (segments) by using nested purification protocol and thereby creating a single EPR pair of high fidelity which is shared by the parties A and B. The so-called *quantum repeater* scheme uses a nested combination of purification and entanglement swapping. The term "nested" refers to the application of these procedures in multiple stages during the connection of the segments, i.e. on different repeater levels. On the first level connecting the elementary EPR segments is done as long as the resulting entangled pair has sufficiently high fidelity for entanglement purification. Noisy local operations and measurements during the subsequent purification do not allow to purify one single maximally entangled pair from several copies. The fidelity can nevertheless be increased for remarkably high errors in the local operations and measurements in the order of percent. On the next level the resulting -more distant- pairs are connected and the purified by several copies obtained in the same way. Then the sequence of "connection and purification" is repeated until one has bridged the between the parties. The entangled pair which they now share can be used for QKD
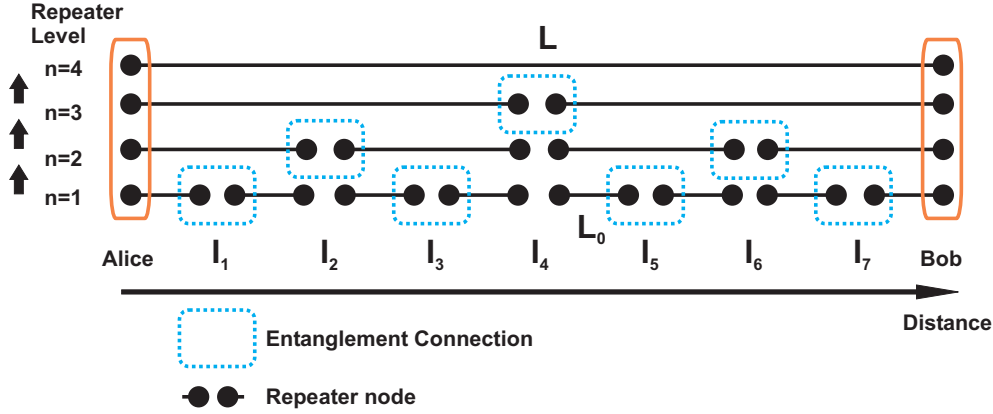
Figure 2.3: Quantum repeater scheme: The communication distance L between Alice and Bob is divided into segments of length L_0, the attenuation length of the quantum channel. I_i (i=1,..,7) are the intermediate nodes. On the basic repeater level the entanglement between the nodes of the segments are generated. In the subsequent step at the intermediate nodes with odd numbers the adjacent segments are connected. In the further steps the segments of increasing lengths are connected until Alice and Bob share a common entangled pair.

or teleportation. The main achievement of this scheme is that the physical and temporal resources scale logarithmical or polynomial with distance.

The details are as follows. The channel between sender A and receiver B is divided into N segments with connection points I_i (i.e. intermediate nodes) in between (see figure (2.3)). We create N elementary EPR pairs of fidelity F_1 between the nodes A and I_1, I_1 and I_2, ..., I_{N-1} and B.At each intermediate point the ends of two neighboring segments meet. The number of intermediate points N is chosen such that the fidelity of each segment is sufficiently high for purification $F_{min} < F_1 \lesssim F_{max}$. Subsequently, we connect these EPR pairs by making Bell measurements at the nodes I_i. By means of classical communication the resulting success or failure of the swapping is exchanged between the nodes. Eventually, the value of F_N drops below F_{min}, and therefore it will not be possible to increase the fidelity by purification. Therefore there is a maximum number of pairs $L \ll N$ that may be connected before purification is necessary restricted by the condition $F_L > F_{min}$. In order to derive an expression for the scaling properties let us assume for simplicity that $N = L^n$ for some integer n. On the first level of the repeater scheme, we simultaneously connect the pairs with initial fidelity F_1 at all of the intermediate points except at $I_L, I_{2L}, ..., I_{N-L}$. Then there are N/L pairs of length L and fidelity F_L between A and I_L, I_L and I_{2L}, and so on. A certain number M of copies on the segments A and I_L, I_L and I_{2L}, etc., is necessary in order to purify and obtain one pair on fidelity $\geq F_1$ on each extended segment. This restriction determines the (average) number of copies M that is needed. The exact value depend on the initial fidelity, the degradation of the fidelity under connections, and the efficiency of the purification protocol. The total number of elementary pairs involved in constructing one of the extended pairs of length L is LM. On the second level of the repeater scheme, we connect L of these more distant pairs at every connection point $I_{kL}(k = 1, 2, ..)$ except at

$I_{L^2}, I_{2L^2}, ..., I_{N-L^2}$. As a result we have N/L^2 pairs of length L^2 between A and I_{L^2}, I_{L^2} and I_{2L^2}, and so on, of fidelity $\geq F_L$. Again, we need M parallel copies of these pairs with length length L^2 to repurify up tot the fidelity $\geq F_1$. The total number of elementary pairs involved in constructing one pair of length L^2 us thus $(LM)^2$. Iteration leads to the total number of elementary pairs R which is given by

$$R = N^{\log_L M+1}. \tag{2.21}$$

This equation shows that the resources grow logarithmic with distance N. In order to evaluate M one needs to know the specific physical implementation of the quantum network.

The performance of the *quantum repeater* scheme naturally depend on the errors, the specific purification protocol, and the repeater metaprotocol, i.e. the distribution and number of repeater stations and their individual set-up. The repeater protocols range from the standard protocol where all pairs needed in the process are created initially as an ensemble (maximal physical, minimal temporal resources), over the "Innsbruck protocol" (physical resources scale logarithmical with the distance) to the "Harvard protocol" with minimal physical resources (two qubits per repeater station) but maximal temporal resources [43][44][45] [46] [47].

2.5.1   Memory in the repeater scheme

In the previous introduction to the *quantum repeater* concept we have assumed that the EPR pairs are present, whenever they are needed. But all available EPR sources or entanglement generation procedures are probabilistic. Therefore the scaling of the presented scheme implies a **perfect quantum memory**, which stores the EPR pairs until they are used. Even though photons have proven to be useful as carriers of the quantum state, they are on the opposite hard to store. The use of a fiber coil at each connection point, when one can heraldedly generate the basic EPR segments, introduces just a short delay, but at the expense of higher absorption probability and decoherence. Therefore another important ingredient is a light-to-memory interface in order to map the quantum state of the photons to a quantum memory

Quantum Repeater and Performance   As previously described the performance and scaling of the quantum repeater scheme depends on the actual implementation. As analyzed in [85] the type of entanglement purification is vital. A comparison of the schemes of Bennett et al. (Scheme A) [84], Deutsch et al. (Scheme B) [86] and a variation by Dür et al. [85] (Scheme C) in terms of physical and temporal resources show striking differences. These two quantities, which depend on the connection and purification protocol, characterize the performance of a quantum repeater scheme.

As physical resources we define the resources per segment needed to create the EPR pair between locations A and B. This is the number of parallel channels between two

	Continental scale		Intercontinental scale	
	resources	time [s]	resources	time[s]
A	$1.58 \cdot 10^9$	$3.88 \cdot 10^{-2}$	$9.01 \cdot 10^{12}$	0.298
B	329	$1.34 \cdot 10^{-2}$	4118	0.103
C	7	0.77	10	15.69

Table 2.1: Table from [85]: Depending on the purification protocol a shorter time is traded in for a larger amount of spatial resources.

intermediate points which are necessary for purification and it gives half of the particles which need to be stored at the I_i points. For the end points A and B it is the exact number. By the term temporal resources one refers to the total time needed to create an EPR pair over the entire distance. There are three time constants which need to be considered

1. The typical time τ_{op} which is needed to perform local operations at the I_i on single qubits, two qubits and for the Bell measurements.

2. In order to exchange the measurement results of the operations one needs to consider τ_{class} for classical communication between the nodes $\tau_{class} = \frac{l_{segment}}{c}$.

3. The typical time τ_{pair} to create an elementary pair. Assuming the fibers as absorption free channels (AFC) [87],[32] the model uses two classical transmissions and 5 operations:

$$\tau_{pair} = \tau_{AFC} = (5\tau_{op} + 2\tau_{class})e^{(\frac{l_{segments}}{l_0})} \tag{2.22}$$

The exponential term accounts for the photon absorption.

In order to compare the schemes A,B,C we make appropriate assumptions: error parameters of 1/2%, working fidelity of $F = 0.96$, a segment length of $l_{segment} \approx 10$ km, $\tau_{AFC} = 3.2 \cdot 10^{-4}$s, $\tau_{class} = 0.33 \cdot 10^{-4}$s and $\tau_{op} = 10^{-5}$s. Then $N = 128 = 2^7$ corresponds to a distance of ≈ 1000 km, which we will refer to as continental distance. Intercontinental is a communication distance of ≈ 10000km where $N = 1024 = 2^{10}$ connection points. Table (2.5.1) shows the physical resources per segment and the time needed for the creation of an EPR pair between the two locations. We can see that there are orders of magnitude differences in terms of physical resources needed, while achieving an increased speed. On the other hand more time is needed to establish a link, when fewer physical resources are used.

The comparison with a classical connection channel of 10000 km which needs only $T_{class} = \frac{10240km}{3 \cdot 10^5 km/s} = 0.034$s for the transmission of a signal underlines that quantum communication is not competitive in terms of bit-rates.

Chapter 3

Atom-Light Interface of the DLCZ-type protocols

The concept of a quantum repeater (section (2.5)) was proposed in 1998. A practical implementation seemed to be challenging and a long way down the road. A complete new and fast route was opened by the seminal proposal of a practical applicable scheme by Duan, Lukin, Cirac and Zoller [42] in 2001. It is called for short the **DLCZ** scheme.

In 2000 it was predicted that light can be "stopped" in atomic medium and subsequently retrieved by dynamic electromagnetic induced transparency (EIT) by M. Fleischhauer and M. Lukin [88]. In the year after the storage of light in an collective state of an atomic vapor could be successfully demonstrated [37]. In addition a proposal described that atomic ensembles can be entangled by trapping correlated photon states [89].

As carrier of choice for a quantum state photons are very robust, fast and easy to guide in a channel, i.e. a fiber. As we have seen in chapter (2) a quantum memory for the polynomial scaling of the quantum repeater scheme is necessary. Photons are easy to delay by sending them through a fiber, but hard to store. Therefore it is necessary to transfer the quantum state from the light to the memory and vice versa. This mapping should be of high fidelity and experimentally feasible. Based on the experimental and theoretical investigations of the atomic storage described above (for a review see [38]) DLCZ added the generation of correlated single photons by spontaneous Raman scattering and projective measurements and thus proposed a technical feasible atomic-light interface. The striking features of the usage of atomic ensembles and spontaneous Raman scattering was that two ingredients are within the limits of current technology: The use of linear optics and the availability of reliable single photon detectors on one hand, and well understood laser cooling and trapping techniques for alkali atoms. This atom-light interface is employed by the DLCZ protocol in order to enable long-distance quantum communication with quantum repeaters.

In the following we introduce to the atom-light interface used by DLCZ, its elegant

properties for a quantum repeater scheme and its application in order to connect distant quantum repeater sites. Successively we introduce an alternative theoretical model for the light storage, the polariton picture. Then we look at the performance of the DLCZ protocol and compare the DLCZ atom-light interface to other approaches.

3.1 Atom-Light Interface: Raman Scattering and Atomic Ensembles

In this section we will discuss in detail the atom-light Interface proposed by Lu-Ming Duan, Mikhail Lukin, Ignacio Cirac and Peter Zoller in the so-called DLCZ scheme. Improved variations of this protocol [43][44][45] [46][47] rely on that type of interface as well. The main building block of the DLCZ quantum repeater scheme are atomic ensembles, which are used for the generation of single photons and serve as memory. In the first section of this chapter, we discuss how the quantum state of light is mapped and retrieved: the so-called *write* and *read* processes. During the *write* process, single Raman scattered photons are detected. Upon a detection event, the atomic ensemble is projected onto a collective state. The *read* process allows to convert this collective state, in principle deterministically, into a single photon. The single photon states which are generated by these procedures are quantum mechanically correlated.

In order to verify the usefulness for the quantum repeater scheme we sketch how entanglement between different atomic ensembles can be generated or two entangled ensembles can be connected. By the measurement of non-classical correlations between the light fields emitted from the memory its performance is characterized.

It is useful to point out that there are various theoretical descriptions for the atom-light interface used. They differ in the simplifications in order to analyze various aspects. Very often, calculations are done by assuming a "bad" cavity encloses the atomic ensemble. Thus only one spatial mode, the cavity mode, needs to be considered. In that way one can obtain a one-dimensional description of the system. A more complex model treats the atomic ensemble in free space and thus accounting for multiple spatial modes. This situation is usually encountered in experiments. In order to shape the beams and collect the light with fiber couplers it is desirable to control the interface such that one mode is preferred without the technical challenges of controlling a cavity. We want to avoid the mathematical formalism of the free-space approach and focus on the physical consequences. Thus we describe the effect of spatial modes without a stringent formalism and give conditions for treatment with a single spatial mode. For the explanation of the electromagnetic transparency in the *read* process we assume a single mode, i.e. the "bad" cavity limit. Note that for reasons of clarity the normalization of the quantum states is omitted.
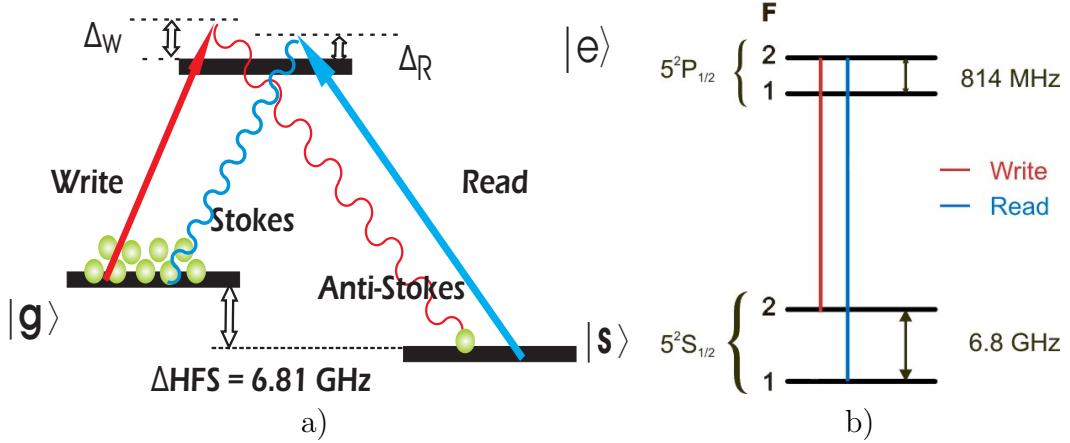
Table 3.1: Level schemes: a) Lambda level system with two ground states and excited state. The *write,read* pulses are are classical light fields. Stokes and Anti-Stokes are quantized fields. b) Level scheme of the D_1-line in ^{87} Rubidium.

3.1.1   The Write Process

In the *write* process the quantum state of a photon is mapped onto an atomic ensemble. The ensemble consists of N atoms with Λ-level structure as depicted in figure 3.1. In our experiment, we use ^{87}Rb which has two metastable ground states. The two hyperfine states $\left|5S_{1/2}, F = 1\right\rangle$ and $\left|5S_{1/2}, F = 2\right\rangle$ are the two ground states $|g\rangle$ and $|s\rangle$, and the $\left|5^2P_{1/2}, F' = 2\right\rangle$ state is the excited state $|e\rangle$. Further on we consider a pencil-shaped atomic cloud with its elongated axis in **z**-direction and its center in the origin. All the atoms are prepared in the state $|g\rangle$, and the ensemble is illuminated by a classical weak light pulse, which is detuned from the g-e transition by Δ_W. It propagates along **z**-direction through the cloud. This *write* pulse is described by $\mathbf{E}_W(\mathbf{r}, \mathbf{t}) = \hat{\epsilon}_W E_W(\mathbf{r}, t) \exp\left(\imath \mathbf{k}_W \cdot \mathbf{r} - \imath \omega_W t\right) + \text{H.c.}$. Here $\mathbf{k}_W = k_W \hat{\mathbf{z}}$ is the wave vector of the write light, $\omega_w = c k_W$ and $\hat{\epsilon}_W$ are the light frequency and the unit polarization vector respectively. Spontaneous Raman scattering [90] [91] transfers with a certain probability one atom from the state $|g\rangle$ to $|s\rangle$ and a single so-called Anti-Stokes photon is generated with frequency $\omega_{AS} = \Delta E_{es}/\hbar + \Delta_W$ and emitted in a solid angle of 4π. Here, ΔE_{es} is the energy difference between the excited state and the ground state $|s\rangle$. We adjust the detuning and intensity of the *write* such that the generated Anti-Stokes field is weak. Thus the operator for the quantized electromagnetic field is [79] $\hat{\mathbf{E}}_{AS}(\mathbf{r}, t) = \sum_{\mathbf{k}} \hat{\varepsilon}_{\mathbf{k}} \epsilon_{\mathbf{k}} \hat{a}_{\mathbf{k}} \exp\left(\imath \mathbf{k}_{AS} \cdot \mathbf{r} - \imath \omega_{\mathbf{k}_{AS}} t\right) + \text{H.c.}$. We summarize the normalization factor into $\varepsilon_{\mathbf{k}} = \sqrt{\frac{\hbar \omega_{\mathbf{k}}}{2\epsilon_0 V}}$ where V is the quantization volume, $\omega_{\mathbf{k}} = ck$ is the frequency of the Anti-Stokes light and $\hat{a}_{\mathbf{k}}$ is the annihilation operator of the mode $\mathbf{k}$. The sum over all possible wavevectors k_{AS} is necessary since the photon can be emitted into a solid angle of 4π. A big simplification can be made when we take our experimental situation into account. During typical pulse durations of the *write* light of several hundreds of nanoseconds the ultracold atoms barely move. Then we can assume that the atoms are fixed to their positions during the pulse duration. Their coordinates are denoted by $\mathbf{r}_i$ with $i = 1, ..., N$. After using

the rotating wave approximation (RWA) [92] the total Hamiltonian of the atom-light interaction is

$$
H = \sum_i^N \left\{ \hbar \Delta_W \sigma_{ee}^i + \left[-\hbar \Omega_W(\mathbf{r}_i, t) e^{(\imath \mathbf{k}_W \cdot \mathbf{r}_i)} \sigma_{eg}^i \right. \right.
$$
$$
\left. \left. + \sum_{\mathbf{k}} \hbar g_{\mathbf{k}} a_{\mathbf{k}} e^{(\imath \mathbf{k} \cdot \mathbf{r}_i - \imath \Delta \omega_{\mathbf{k}} t)} \sigma_{es}^i + \text{H.c.} \right] \right\}, \tag{3.1}
$$

where the detuning of the *write* is $\Delta_W = \omega_{eg} - \omega_W$ and the detuning of the Anti-Stokes $\Delta \omega_{\mathbf{k}} = \omega_{\mathbf{k}} - \omega_W - \omega_{sg}$. The energy differences of the atomic levels are $\omega_{eg} = \omega_e - \omega_g$ and $\omega_{sg} = \omega_s - \omega_g$. The atomic transition operators for the ith atom are denoted by $\sigma_{lm}^i = |l\rangle_i \langle m|$ $(l, m = e, g, s)$. The Rabi frequency of the classical write field is $\Omega_W(\mathbf{r}, t) = \frac{\mathbf{d}_{eg} \cdot \hat{\epsilon}_W E_W(\mathbf{r}, t)}{\hbar}$. The atomic dipole operator for the *write* field is $\mathbf{d}_{eg}$. In case of the Anti-Stokes light we use the coupling coefficient $g_{\mathbf{k}}$ of each mode $\mathbf{k}$ given by $g_{\mathbf{k}} = -\frac{\mathbf{d}_{es} \cdot \hat{\epsilon}_{\mathbf{k}} \epsilon_{\mathbf{k}}}{\hbar}$

The Hamiltonian can be simplified by application of the adiabatic level approximation, which eliminates the excited state and leads to an effective two-level system [93]. The approximation is justified since the Rabi frequency of the *write* pulse as well as the line width of the excited state $|e\rangle$ are significantly smaller than the detuning Δ_W. According to [94] the Hamiltonian is:

$$
H = \sum_i^N \left[\sigma_{sg}^i \frac{\Omega_W(\mathbf{r}_i, t) e^{\imath \mathbf{k}_W \cdot \mathbf{r}_i}}{\Delta_W} \sum_{\mathbf{k}} \hbar g_{\mathbf{k}} \hat{a}_{\mathbf{k}}^\dagger e^{-(\imath \mathbf{k} \cdot \mathbf{r}_i - \imath \Delta \omega_{\mathbf{k}} t)} + \text{H.c.} \right], \tag{3.2}
$$

where the AC Stark shift due to the *write* light is neglected. This ensemble of pseudo-two-level atoms has a transition frequency for the Anti-Stokes light of $\omega_{AS} = \omega_W - \omega_{sg}$ with a line width of the new "upper" state of $\Gamma' = \frac{\Omega_W^2}{\Delta^2} \Gamma$. In our case the pulse duration, i.e. the interaction time of the write is smaller that lifetime of this level. Thus the Anti-Stokes field can not be stimulated.

The simplified Hamiltonian (equation 3.2) can then be used in the first order approximation of the Schrödinger equation which is given by:

$$
|\Psi\rangle = \left(1 - \imath \int_0^T H(\tau) d\tau \right) |vac\rangle + O(p) \tag{3.3}
$$

The vacuum state is composed of the collective state of the atoms (A) $|0\rangle_A = \otimes_i |g\rangle_i$ and the light mode (L) $|vac\rangle = |0\rangle_A |0\rangle_L$. Evaluation of the integral over τ yields

$$
|\Psi\rangle = |0\rangle_A |0\rangle_L + \sum_i^N \frac{\Omega_W(\mathbf{r}_i) e^{\imath \mathbf{k}_W \cdot \mathbf{r}_i}}{\Delta} |g...s_i...g\rangle |1_{AS}\rangle, \tag{3.4}
$$

where $|1_{AS}\rangle = -\imath \int_0^T \sum_{\mathbf{k}} g_{\mathbf{k}} a_{\mathbf{k}}^\dagger e^{-(\imath \mathbf{k} \cdot \mathbf{r}_i - \imath \Delta \omega_{\mathbf{k}} t)} |0\rangle_L$ denotes the Anti-Stokes photon. We have assumed that the Rabi frequency is constant during the interaction time and constant over the spatial extend of the ensemble. The Rabi frequency is adjusted such
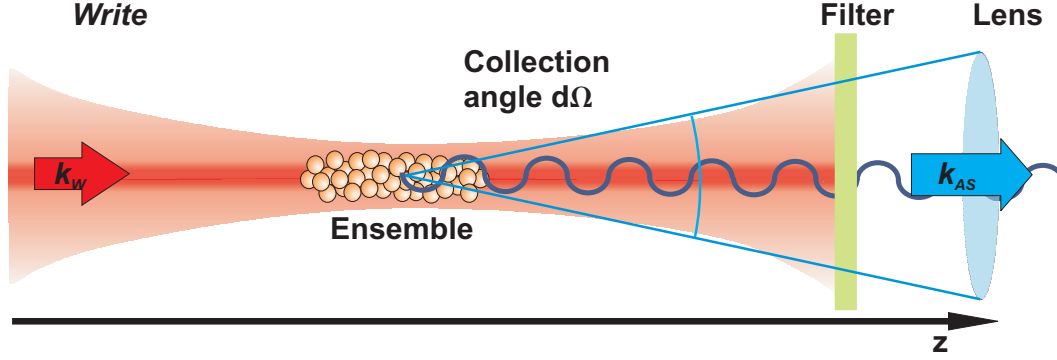
Figure 3.1: Illustration of the spatial light modes in the *write* process: The *write* light propagating along z direction generates Anti-Stokes photons by Raman scattering at the atomic ensemble. The detection mode is defined by the lens collecting the Anti-Stokes light in a collection angle $d\Omega$. We chose to detect Anti-Stokes photons which are emitted in z direction. A filter separates the *write* from the signal light.

that only one photon is generated. The spontaneous scattering of each individual atom is isotropic into the solid angle of 4π and independent from each other.

In [94] the electric field of an emitted Anti-Stokes photon from a pencil shaped atomic ensemble is evaluated in the paraxial approximation. The field incident at distance $\mathbf{r}_0$ on an observation plane emitted from the i-th atom is

$$
\begin{aligned}
E_i(\mathbf{r}_0) = & \ \frac{\epsilon_0}{z - z_i} \exp\left(\imath k_{AS}(z - z_i + \frac{x_i^2 + y_i^2}{2(z - z_i)} + \frac{x^2 + y^2}{2(z - z_i)} - \imath k_{AS} \frac{x_i x + y_i y}{z - z_i} \right) \\
\approx & \ \frac{\epsilon_0}{z} \exp\left(-\imath k_{AS} z_i\right) \exp\left[\imath k_{AS}\left(z + \frac{x_i^2 + y_i^2}{2z} + \frac{x^2 + y^2}{2z} - \frac{x_i x + y_i y}{z} \right) \right] \\
\times & \qquad \qquad \exp\left(\imath k_{AS} \left(\frac{x_i^2 + y_i^2}{2z^2} z_i + \frac{x^2 + y^2}{2z^2} z_i - \frac{x_i x + y_i y}{z^2} z_i \right) \right), \quad (3.5)
\end{aligned}
$$

assuming $|z_i| \ll z$. Let us introduce the diffraction angles $\Theta_{w_a} = \frac{1}{k_{AS} w_a}$ and $\Theta_l = \left(\frac{1}{k_{AS} l} \right)^{1/2}$, where w_a is the waist of the ensemble and l is its length. Then all phase factors with exception of $\exp\left(-\imath k_{AS} z_i\right)$ in equation (3.5) can be neglected as long as the detection angle is chosen to satisfy $\Theta \le \min\left(\Theta_{w_a}, \Theta_l\right)$. As a consequence one can treat the Anti-Stokes light $E_i(\mathbf{r})$ on the observation plane as one spatial mode described by

$$
\begin{aligned}
E_i(\mathbf{r}) \ & \simeq \ \frac{\epsilon_0}{z} \exp\left(\imath k_S \left(z + \frac{x^2 + y^2}{2z} \right) \right) e^{(-\imath k_{AS} z_i)}. && (3.6) \\
& = \ \zeta_{AS}(\mathbf{r}) e^{(-\imath \mathbf{k}_{AS} \cdot \mathbf{r}_i)}, && (3.7)
\end{aligned}
$$

where $\zeta_{AS}(\mathbf{r}) = \frac{\epsilon_0}{z} \exp\left(\imath k_{AS} \left(z + \frac{x^2 + y^2}{2z} \right) \right)$ denotes the detection mode of the Anti-Stokes light and $\mathbf{k}_{AS} = k_{AS} \hat{z}$ is the corresponding wave vector. Along this detection mode we can approximate the state of the Anti-Stokes photon by $|1_{AS}\rangle =$

$\sqrt{p}\hat{a}_{AS}^{\dagger}e^{(-\imath \mathbf{k}_S \cdot \mathbf{r}_i)}\left|0\right\rangle_L$. The single mode creation operator is labelled by $\hat{a}_{AS}^{\dagger}$ and the probability to scatter one Anti-Stokes photon into the solid angle $d\Omega$ of the detection mode is given by $p = \Gamma T \frac{\Omega_W^2}{\Delta^2} d\Omega$. In order to be in the single photon regime the generation probability must fulfill $p \ll 1$. Then we can write a combined atom-light state using $\Delta \mathbf{k} = \mathbf{k}_W - \mathbf{k}_R$ as

$$|\Psi\rangle = \left(1 + \sqrt{p}\left(\sum_i^N e^{\imath \Delta \mathbf{k} \cdot \mathbf{r}_i} \sigma_{sg}^i\right)\hat{a}_S^{\dagger}\right)|vac\rangle. \tag{3.8}$$

The equation can be simplified by defining a collective atomic state creation operator $S^{\dagger}$:

$$S^{\dagger} = \frac{1}{\sqrt{N}}\sum_i^N e^{\imath \Delta \mathbf{k} \cdot \mathbf{r}_i}\sigma_{sg}^i. \tag{3.9}$$

It obeys the bosonic commutation relation $\left[S, S^{\dagger}\right] \simeq 1$. So we simplify the state $|\Psi\rangle$ to

$$|\Psi\rangle = \left(1 + \sqrt{\chi}S^{\dagger}\hat{a}_S^{\dagger}\right)|vac\rangle. \tag{3.10}$$

Here $\chi = Np$ gives the probability to detect an Anti-Stokes photon. By the detection of this Anti-Stokes photon the combined atom-light state is projected into a collective atomic excited state. This superposition state holds in addition to the single excitation the phase information of the detected mode. Therefore we can speak of a spin wave which is imprinted onto the atomic ensemble.

Since we want to have the photon in a single spatial mode the Fresnel number $F = \frac{A}{\lambda l} \simeq 1$ has to be of the order of one ($A = \pi w_a^2$). Then the two diffraction angles are equal $\Theta_{w_a} \simeq \Theta_L$. Thus the detection solid angle is approximately $d\Omega \approx \lambda^2/A$. The total excitation probability for the Anti-Stokes light is $\chi = N\Gamma T\frac{\Omega_W^2}{\Delta^2}\frac{\lambda^2}{A} \sim \mathcal{D}\gamma_s T$. In the latter expression we have used the optical depth $\mathcal{D} \sim N\sigma_0/A$ and the new decay rate $\gamma_s \sim \Gamma\frac{\Omega_W^2}{\Delta^2}$.

3.1.2 Read Process

The single excitation which is stored in the spin wave can be converted back into a single photon state. We refer to this mapping of a stored atomic state into a photon state as *read* process. A classical light field is applied which couples the ground state which stores the excitation $|s\rangle$ to the excited state $|e\rangle$. Subsequently a Stokes photon is generated when the atom decays to $|g\rangle$. The emission of this photon is very different from the *write* process. Constructive interference from all atoms results in a directed emission of Stokes light. If the detection mode is spatially mode-matched to the mode of the Anti-Stokes the stored excitation is recovered with high efficiency. Electromagnetic induced transparency (EIT) (see section (3.1.3)) enables the Stokes photon to leave the atomic cloud without absorption.

The classical *read* field $\mathbf{E}_R(\mathbf{r}, \mathbf{t}) = \hat{\epsilon}_R E_R(\mathbf{r}, t)\exp\left(\imath \mathbf{k}_R \cdot \mathbf{r} - \imath\omega_R t\right) + \text{H.c.}$ is counter propagating to the *write* light $\mathbf{k}_R = -k_R\hat{z}$. In case the *read* pulse is resonant to the $|s\rangle \to |e\rangle$ transition, the generated Stokes photon is resonant to $|e\rangle \to |g\rangle$. The
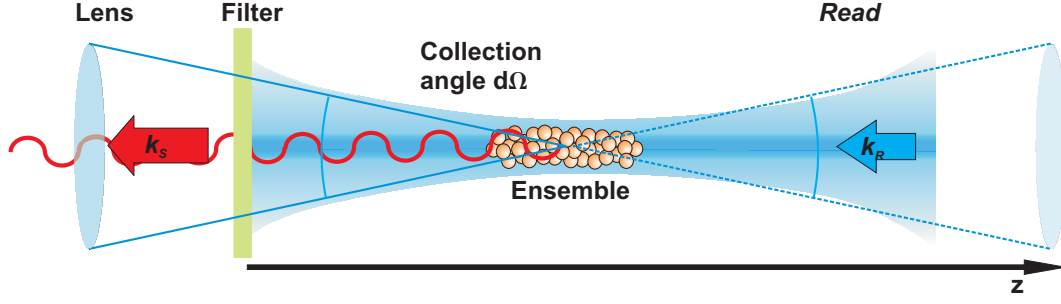
Figure 3.2: Illustration of the spatial light modes in the *read* process: The *read* light propagating opposite to the z direction generates Stokes photons. The detection mode is defined by the lens collecting the Stokes light in a collection angle dΩ. If the detection mode of the Stokes photons is selected opposite to the Anti-Stokes detection mode, the retrieve efficiency is highest. Due to the satisfaction of the mode match condition the constructive interference of the contributions of all atoms the detection of an Stokes photon in opposite z direction is highly correlated with the previous detection of the Anti-Stokes photon in z direction.

spatial mode of the quantized Stokes field at detection point $\mathbf{r}'$ is given by

$$E_S(\mathbf{r}') = \frac{1}{\sqrt{N}} \sum_i^N e^{i\Delta\mathbf{k}\cdot\mathbf{r}_i} e^{i\mathbf{k}_R} \cdot \mathbf{r}_i \frac{1}{|\mathbf{r}' - \mathbf{r}_i|} e^{i\mathbf{k}_S \cdot (|\mathbf{r}' - \mathbf{r}_i|)}. \tag{3.11}$$

The contribution of the atoms with position $\mathbf{r}_i$ is largest if the wave vectors fulfill the mode match condition:

$$\mathbf{k}_W - \mathbf{k}_S + \mathbf{k}_R - \mathbf{k}_{AS} = 0 \tag{3.12}$$

If we fix the observation plane of the Stokes light opposite to the detection plane of the Anti-Stokes light while the *write*, *read* beams are counter-propagating, the retrieval of the stored excitation into a Stokes photon has maximal efficiency. By application of the paraxial approximation then we get [94]:

$$E(\mathbf{r}') \simeq \sqrt{N} \int d\mathbf{r}'' n(\mathbf{r}'') \frac{1}{z'} e^{-i k_S (z' + \frac{x'^2 + y'^2}{2z'})} \tag{3.13}$$

The mode of the Stokes field can be written in analogy to equation (3.7) as

$$\zeta_S(\mathbf{r'}) = \frac{\epsilon_0}{z'} \exp\left(-i k_S \left(z' + \frac{x'^2 + y'^2}{2z'}\right)\right), \tag{3.14}$$

thus $E_S(\mathbf{r}') = \sqrt{N}\zeta_{AS}(\mathbf{r}')$. In this approximation it is a Gaussian mode as well.

This result is correct as long as the detection angle is $\Theta' \leq min(\Theta_{w_a}, \Theta_l)$ and the Rabi frequencies are constant across the atomic ensemble. From equation (3.14) we can see that there is an enhancement of the *read* out into the detection mode by the atom number N. The intensity is proportional to the solid angle of the detection

mode $d\Omega$ in the direction of the constructive interference and the atom number N. We introduce the retrieval efficiency η_{retr} which is a measure for the probability to retrieve a single excitation, previously stored in the atomic ensemble, into a Stokes photon

$$\eta_{retr} \sim \frac{\gamma N d\Omega}{\gamma N d\Omega + \gamma} = \frac{N d\Omega}{N d\Omega + 1}. \tag{3.15}$$

Then the scattering into the optimal detection mode is $\gamma N d\Omega$ whereas into all other directions it is given by the decay rate of the excited state γ.

In the single mode regime the solid angle of the detection can be approximated by $d\Omega \sim \frac{\lambda^2}{A}$. Then it can be shown that the retrieval efficiency $\eta_{retr} \sim 1 - \frac{1}{d_0}$ depends only on the optical depth of the ensemble.

3.1.3   EIT in the Read-Out

Electromagnetically induced transparency (EIT) is a phenomena first investigated in a three level atomic system with two ground states, one excited state and a strong coherent light field on one transition [38]. The atomic medium becomes under certain conditions transparent for a weak probe field on the other transition due to quantum mechanical interference [79]. In the *read* process this effect is present and it is responsible that the single photons generated in any part of the atomic cloud can leave the ensemble. Thus they are not absorbed by the majority of the atoms in the state $|g\rangle$. In order to reduce the mathematical complexity we treat the system with one spatial mode, i.e. one-dimensional problem. As mentioned in the introduction to this chapter we can assume the pencil shaped atomic ensemble enclosed by a "bad" cavity ($\kappa \gg g\sqrt{N}$) along its longitudinal direction or we can assume that our detection modes are matched accordingly. Recall that the uniform atomic ensemble consists as previously of N atoms in a lambda-type configuration. After the *write* pulse and the subsequent detection, most of the atoms are still in the $|g\rangle$ state.

Equations of motion for a three level lambda system   In the semiclassical model one can derive the equations of motion for the lambda system interaction when two classical light fields are present: the *read* field with strong intensity Ω_R and the Stokes fields as a weak probe field with Rabi-frequency Ω_S. The time evolution of the system is given by the von-Neumann equation for the density matrix ρ by $i\hbar\dot{\rho}_{ij} = [\rho_{ij}, H_{int}]$, where ρ_{ij} are the i, j matrix element of the density matrix and H_{int} denotes the interaction Hamiltonian. The equations of motions for the coupled

system are [79] [1]:

$$\dot{\rho}_{es} = \left(-\frac{\Gamma}{2} + \imath\omega_{es}\right)\rho_{es} - \frac{\imath}{2}\Omega_R^*(\rho_{ss} - \rho_{ee}) - \frac{\imath}{2}\Omega_S^*\rho_{gs}$$

$$\dot{\rho}_{eg} = \left(-\frac{\Gamma}{2} + \imath\omega_{eg}\right)\rho_{eg} - \frac{\imath}{2}\Omega_S^*(\rho_{gg} - \rho_{ee}) - \frac{\imath}{2}\Omega_R^*\rho_{sg}$$

$$\dot{\rho}_{sg} = \imath(\omega_{eg} - \omega_{es})\rho_{sg} - \frac{\imath}{2}(\Omega_R\rho_{eg} - \Omega_S^*\rho_{se}) \tag{3.16}$$

The frequency differences between the levels are labelled by ω_{ij}. Since the Rabi-frequencies have usually only a real part, i.e. $\Omega = \Omega^*$ the remaining elements are given by

$$\rho_{es} = \rho_{se}^*; \quad \rho_{eg} = \rho_{ge}^*; \quad \rho_{sg} = \rho_{gs}^*; \tag{3.17}$$

The derivation of these equations in second quantization accounts for the non-classical Stokes field, but the main conclusions hold as well.

We assume for simplicity that the Rabi-frequencies are time-independent. Only if the Rabi-frequencies are small such that the atomic system can follow adiabatically this solution works for the time-dependent Rabi-frequencies as well, but it results in lengthy equations.

An additional assumption is that nearly all atoms are in the state $|g\rangle$ and therefore we take all other levels initially as unoccupied which means

$$\rho_{gg}^{(0)} = 1, \ \rho_{ss}^{(0)} = \rho_{ee}^{(0)} = \rho_{se}^{(0)} = 0 \tag{3.18}$$

By introducing slowly varying quantities $\rho_{eg} = \tilde{\rho}_{eg}e^{-\imath\omega_S t}$ and $\rho_{sg} = \tilde{\rho}_{sg}e^{-\imath(\omega_S+\omega_R)t}$ one obtains two coupled equations. Introducing $\delta = \omega_{eg} - \omega_S$ as the detuning of the Stokes light from the atomic transition and solving them yields

$$\rho_{eg}(t) = \frac{\imath\mathbf{d}_{eg}\mathcal{E}e^{-\imath\omega_S t}(\imath\delta + \Gamma)}{2\hbar[(\Gamma + \imath\delta)\imath\delta + \Omega_R^2/4]} \tag{3.19}$$

The polarization of an atomic medium is given by

$$\mathcal{P} = n_0[\mathbf{d}_{ge}\rho_{ge} + \mathbf{d}_{se}\rho_{se} + c.c.] \tag{3.20}$$

We use $\mathcal{P} = \epsilon_0\chi E$ where the linear susceptibility is a complex quantity $\chi = \chi' + \imath\chi''$ and evaluate it. We choose the *read* light to be on resonance ($\Delta_R = 0$). The real part of the linear susceptibility for the Stokes field is

$$\chi' = \frac{|\mathbf{d}_{gs}|^2 n_0}{\epsilon_0\hbar} \times \left[\frac{4\delta(\Omega_R^2 - 4\delta^2 - \Gamma^2)}{|\Omega_R^2 + (\Gamma + \imath 2\delta)(\Gamma + \imath 2\delta)|^2}\right] \tag{3.21}$$

Since $E_{out} = E_{in}\exp\left(\imath k_S l\chi'/2\right)$ the transmission T is then given by

$$T = \frac{E_{out}^2}{E_{in}^2} = \exp\left(\imath k_S l\chi'\right). \tag{3.22}$$

---

[1]We assume the decay rate for ρ_{eg} and ρ_{es} to be equal and denote it by Γ.

In case the linewidth in the medium is inhomogeneous broadened the collective spin wave can still be retrieved with a high efficiency [95] if the two-photon detuning satisfies the condition

$$\delta \ll \delta_{2ph} = \frac{g\sqrt{N}}{\sqrt{\Gamma t_{tr}}}, \tag{3.23}$$

where g is the coupling constant, Γ the decay from the excited state and t_{tr} the transfer time. Therefore a rather large two-photon detuning can be tolerated in an optically thick medium.

EIT Window   The EIT effect is not limited to a narrow frequency, but a range of frequencies. This range is called the transparency window of the EIT. For the determination of its width we simplify χ' of a homogenous medium with a resonant *read* field by

$$\chi' = \frac{n_g}{kc}\frac{|\Omega_R|^2\delta}{|\Omega_R|^2 - \delta^2 - \imath\Gamma\delta} \approx \frac{n_g}{kc}\left[\delta + \imath\delta^2\frac{\Gamma}{|\Omega_R|^2} + O(\delta^3)\right], \tag{3.24}$$

where $\delta = \nu - \omega_{se}$ is the detuning of the Stokes field. If we assume a homogeneous drive field, we find that the transmission can then be written as

$$T(\delta) = \exp\left(-kz\text{Im}[\chi]\right) \approx \exp\left(-\delta^2/\Delta\omega_{tr}^2\right), \tag{3.25}$$

where the transmission window ω_{tr} is defined as

$$\Delta\omega_{tr} = \left[\frac{c}{\Gamma l}\frac{|\Omega_R|^2}{n_g}\right]^{1/2} = \frac{|\Omega_R|^2}{\Gamma}\frac{1}{\sqrt{\mathcal{D}}}. \tag{3.26}$$

The optical depth $\mathcal{D} = \tilde{n}\sigma_0$ and the Rabi-frequency of the *read* beam are the adjustable parameters.[2] One recognizes that the transparency width decreases with an increasing group index n_g which is given by

$$n_g(z) = \frac{g^2 N}{|\Omega(z)|^2}. \tag{3.27}$$

Let us express the transparency width in terms of the pulse delay time $\tau_d = n_g l/c$ for the medium. This yields

$$\Delta\omega_{tr} = \sqrt{\mathcal{D}}\frac{1}{\tau_d}. \tag{3.28}$$

Hence large delay times imply a narrow transparency window, which in turn requires a long pulse time. When the group velocity becomes so small that the spectral width of the pulse (Fourier transform of the pulse in frequency space) is smaller than the window width, then the light pulse is absorbed. Hence there is an upper bound for

---

[2]$\sigma_0 = 3\lambda^2/(2\pi)$ is the resonant light absorption cross section and $\tilde{n}$ is the integrated atomic density along the direction of the propagation. In case of a homogeneous medium it is $\tilde{n} = n \cdot l$, i.e. the atomic density n times the length of the medium l.
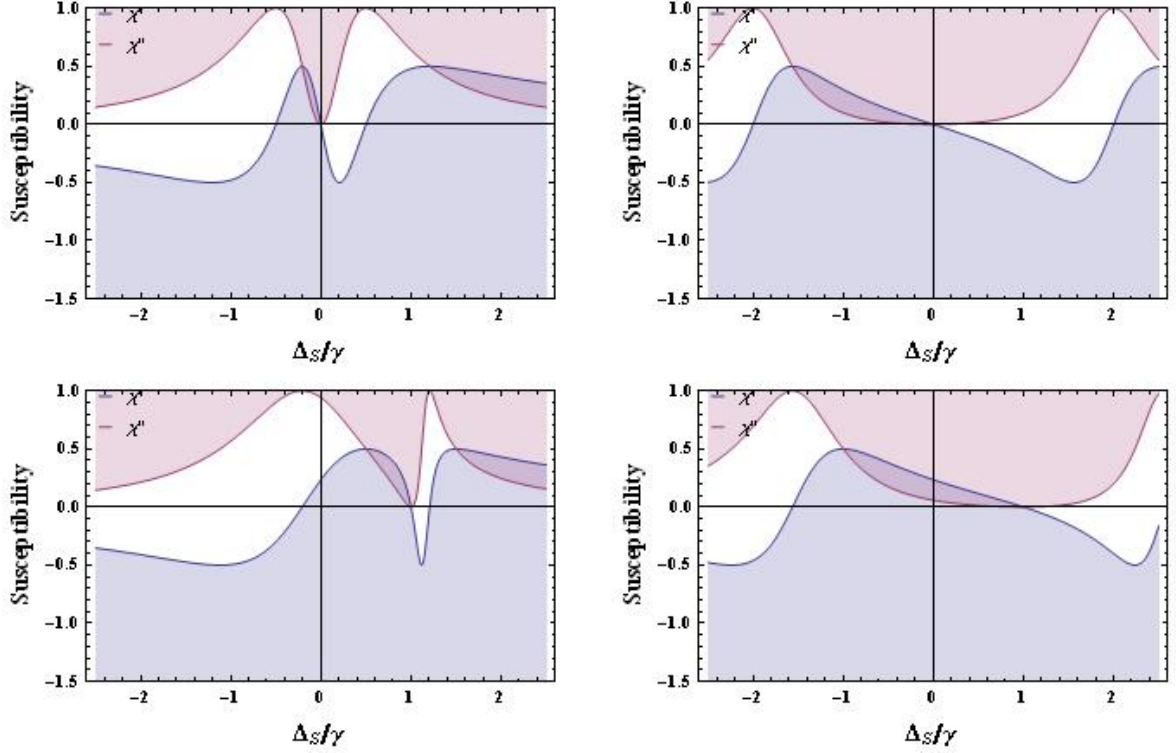
Figure 3.3: EIT window: Real χ' and imaginary χ'' parts of the susceptibility χ for various parameters of the detuning and power of the *read* light. a) $\Omega_R = 1/2\Gamma$ on resonance b) $\Omega_R = 2\Gamma$ on resonance c) $\Omega_R = 1/2\Gamma$ with a detuning of Γ d) $\Omega_R = 2\Gamma$ with a detuning of Γ. The EIT window becomes wider for a higher intensity of the *read* light.

the ratio of achievable delay time to the initial pulse length of a photon wave packet,

$$\frac{\tau_d}{\tau_p} \leq \sqrt{\mathcal{D}} \quad \text{and} \quad \tau_d \leq \Gamma_{\gamma_{se}}^{-1}. \tag{3.29}$$

Because our *read* pulse is short, the pulse length is limiting the minimal EIT bandwidth. Let us assume a Gaussian pulse shape

$$I(t) = I_0 \exp\left(-\frac{t^2}{\tau^2}\right), \tag{3.30}$$

where τ denotes the pulse length. The Fourier transformation into frequency space (Δ) yields

$$F(\Delta) = \int_{-\infty}^{\infty} I(t) \exp\left(\imath 2\pi \Delta t\right) dt = I_0 \sqrt{\pi} \tau \exp\left(-\pi^2 \tau^2 \Delta^2\right). \tag{3.31}$$

The convolution of this pulse with the transmission of the cloud leads to:

$$T_\tau(\Delta_R) = \int_{-\infty}^{\infty} T_\tau(\Delta')F(\Delta_P - \Delta')d\Delta' \tag{3.32}$$

3.1.4   Collective Atomic States and Atomic Mode

We recall that an atomic ensemble of N atoms with a lambda level system is considered. The photonic excitation which has been written into the ensemble is stored in a quantum-mechanical superposition state of the atoms. We write the initial collective atomic state as

$$|0\rangle_A = |gggg...g\rangle_A\,, \tag{3.33}$$

where all atoms are in the ground state $|g\rangle$. The application of the collective spin operator from equation (3.9) $S^\dagger = \frac{1}{\sqrt{N}}\sum_i^N e^{i\Delta\mathbf{k}\cdot\mathbf{r}_i}\sigma_{sg}^i$ onto this collective state corresponds to a single stored excitation, i.e.

$$|1\rangle_A = S^\dagger|0\rangle_A\,. \tag{3.34}$$

Expanding the sum in the spin operator yields

$$|1\rangle_A = \frac{1}{\sqrt{N}}\left(|eg...g\rangle + |ge...g\rangle + ... + |g...e\rangle\right), \tag{3.35}$$

which indicates that the collective atomic state is a superposition state of all possible realizations. Every atom i at position $\mathbf{r}_i$ carries a phase factor $e^{i\Delta\mathbf{k}\cdot\mathbf{r}_i}$ which is imprinted during the *write* process. Multiple excitations are represented by multiple application of the spin operator

$$\begin{aligned} |2\rangle_A &\sim \left(S^\dagger\right)^2|0\rangle \\ |n\rangle_A &\sim \left(S^\dagger\right)^n|0\rangle \\ |N\rangle_A &= |eee...e\rangle\,, \end{aligned} \tag{3.36}$$

where the collective states $|n\rangle$ are Dicke-like states [96]. In the following section (sec. 3.1.5) we see how the photon generated in the *write* process and the photon generated by the *read* process are nonclassical correlated. The atomic ensemble serves therefore as a quantum memory. Our treatment assumes the atoms are fixed in space without interaction between themselves and with the environment (besides the vacuum) and the three level system is perfect, conditions which are obviously not experienced in experiments. All these effects contribute to the decoherence of the quantum superposition stored in the state. The result is a finite lifetime of the spin wave, which means after a certain observation time the written excitation cannot be "recovered". In the next chapter we will look in detail into the limitation of the lifetime of such a quantum memory.

3.1.5 Nonclassical correlation of Single Photons

In order to see the statistical connection between the Anti-Stokes and Stokes photons we write a combined state for both fields, even though they cannot be present at the same time. We need to detect the Anti-Stokes before we can retrieve a Stokes photon. Nevertheless we can write a quantum mechanical state for both light fields (if we neglect the vacuum contributions) by

$$|\Psi\rangle_L = \left(1 + \sqrt{\chi}\hat{a}_{AS}^{\dagger}\hat{a}_S^{\dagger} + \chi\hat{a}_{AS}^{2\dagger}\hat{a}_S^{2\dagger}/2\right)|vac\rangle$$
$$= |0_S 0_{AS}\rangle + \sqrt{\chi}|1_S 1_{AS}\rangle + \chi|2_S 2_{AS}\rangle , \qquad (3.37)$$

where $|i_{AS}j_S\rangle$ with $i,j = 0,1,2...$ are the numbers of single photons in the Fock basis. We have assumed a retrieval efficiency of 1. The Cauchy-Schwarz inequality [97]

$$\left[g_{S,AS}^{(2)}\right]^2 \leq g_S^{(2)}g_{AS}^{(2)} \qquad (3.38)$$

is fulfilled for classical light fields. The cross-correlation of the Stokes and Anti-Stokes photons, i.e. $g_{S,AS}^{(2)} = \langle\hat{a}_S^{\dagger}\hat{a}_{AS}^{\dagger}\hat{a}_S\hat{a}_{AS}\rangle/\left(\langle\hat{a}_S^{\dagger}\hat{a}_S\rangle\langle\hat{a}_{AS}^{\dagger}\hat{a}_{AS}\rangle\right)$, must be less than the product of the autocorrelation functions of the individual Anti-Stokes and Stokes fields $g_{AS}^{(2)} = \langle\hat{a}_{AS}^{2\dagger}\hat{a}_{AS}^2\rangle/\langle\hat{a}_{AS}^{\dagger}\hat{a}_{AS}\rangle^2$ and $g_S^{(2)} = \langle\hat{a}_S^{2\dagger}\hat{a}_S^2\rangle/\langle\hat{a}_S^{\dagger}\hat{a}_S\rangle^2$ respectively, normalized to the intensities.

The maximum value for the autocorrelation functions in our case is 2, because they are thermal light states. In order to observe nonclassical correlations equation (3.38) is violated. From the combined light state (equation (3.37)) we can see that $g_{S,AS}^{(2)} = 1/\chi$. On the other hand the product of the autocorrelation function $g_S^{(2)} = g_{AS}^{(2)} = 2$ is 4, i.e. the Cauchy-Schwarz inequality (3.38) is violated if $g_{S,AS}^{(2)} > 2$. When the excitation probability is $\chi < 0.5$, then the Anti-Stokes and Stokes photons are quantum mechanically correlated. Since the storage of the collective atomic state in the ensemble is responsible for the observation of the nonclassical correlation, we speak of the atomic ensemble as quantum memory for a light state. For further details on the experimental implementation we refer to the supplement of reference [98].

3.2 DLCZ atom-light interface in a quantum repeater scheme

The atom-light interface which we have investigated is suitable for the application in a quantum repeater scheme. We show how the entanglement generation and connection is achieved and that a purification against errors due to photon loss is built-in in the original DLCZ protocol [42].
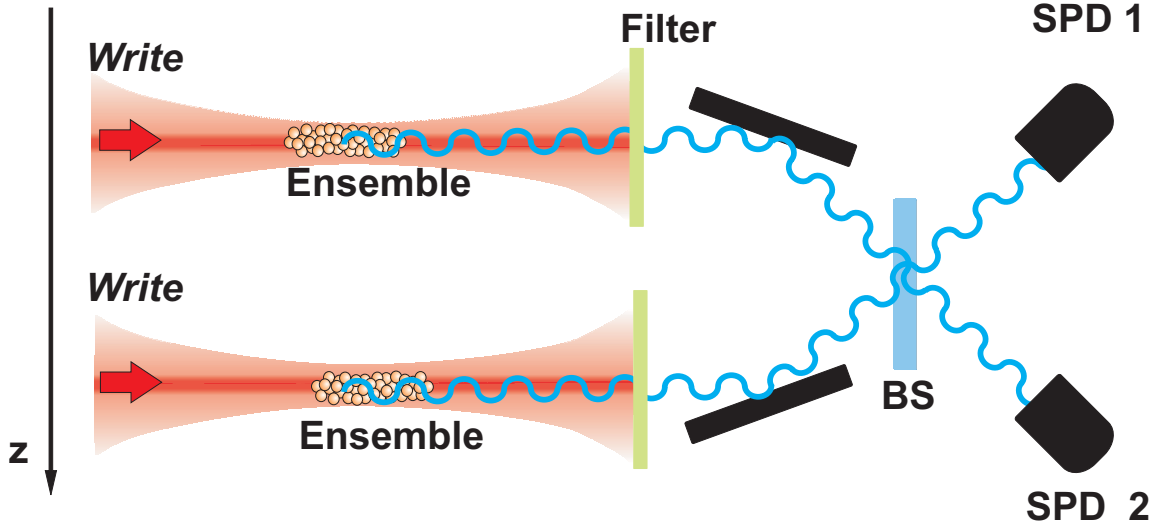
Figure 3.4: Entanglement generation according to DLCZ: A joint projective measurement of the Anti-Stokes fields of both ensembles generates the entanglement between the two spatially separated atomic ensembles.

3.2.1   Entanglement Generation

We follow the original DLCZ scheme [42], since it is more instructive than the improved versions. Entanglement between two sites separated by distance L_0 should be created. Note that the separation $L_0 \leq L_{att}$ may not exceed the attenuation length of the channel L_{att} . At each site A and B we have an atomic ensemble as described in the previous sections. On both sites two *write* pulses are applied simultaneously (see figure (3.4)). After several trials an Anti-Stokes photon is generated at one site. It is collected and overlapped at a beam splitter (BS) with the vacuum mode from the other ensemble:

$$\left(|0,0\rangle_{A,L} + \sqrt{\chi}\,|1,1\rangle_{A,L}\right)\left(|0,0\rangle_{B,L} + \sqrt{\chi}\,|1,1\rangle_{B,L}\right) \tag{3.39}$$

By the detection of the photon with single photon detectors (SPD) at one of the output ports of the BS the combined atom-light state is projected and the atomic ensembles at site A and B are entangled. This is described by the state

$$|\Psi_{\phi_{AB}}\rangle_{A,B} = |1,0\rangle_{A,B} \pm e^{\imath\phi_{AB}}\,|0,1\rangle_{A,B} = (S_A^\dagger + e^{\imath\phi_{ab}}S_B^\dagger)/\sqrt{2}\,|vac\rangle\,. \tag{3.40}$$

ϕ_{AB} denotes an unknown phase due to the difference between the length of the two channels. The success probability for the generation (assuming perfect SPDs) is

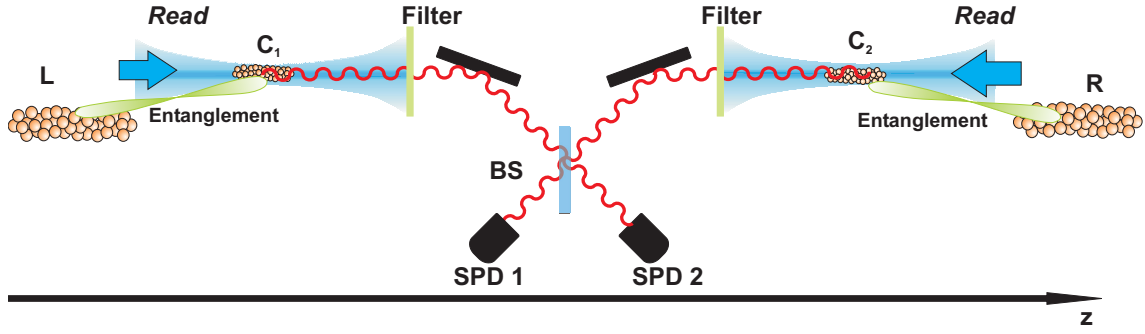$$\chi\eta_l \text{ with } \eta_l = \exp\left(-L_0/L_{att}\right). \tag{3.41}$$

Figure 3.5: Entanglement connection according to DLCZ: Two entangled pairs of atomic ensembles are initially prepared (pair (L,C_1) and pair pair (C_2,R)). A joint projects measurement of the Stokes fields *read* out of both intermediate ensembles (C_1 and C_2) connects the two atomic ensembles L and R whereas the ensembles C_1 and C_2 are traced out of the joint entangled state. BS denotes the beamsplitter and SPD is the abbreviation for single photon detectors.

Then the average time T_{egen} for the successful entanglement generation is given by

$$T_{egen} = t_{comm}/\chi\eta_l \sim (L_0/c)\exp(L_0/L_{att})/\chi, \tag{3.42}$$

where t_{comm} is the classical communication time between the sites needed to verify the success or start another trial.

3.2.2 Entanglement Connection

When two neighboring segments of length L_0 are prepared as previously described, we can use entanglement connection between these two pairs of entangled ensembles in order to extent the communication length. One pair which connects sites L and C is $\rho_{L,C1}$, the other one connects sites R and C labelled by $\rho_{C2,R}$. At the center of the total distance two ensembles $C1, C2$ are located. A *read* pulse is applied simultaneously on both of them. The generated Stokes photon (assume unit retrieve efficiency) is collected and overlapped with the vacuum component of the other ensemble on a BS. The click at one of the SPDs at the output ports prepares the ensembles L and R in an effective maximally entangled state (EME) (see figure (3.5)). Mathematically the entanglement connection is described by

$$|\Psi\rangle_{LC_1}|\Psi\rangle_{RC_2} \xrightarrow{\text{read}} \left(|\Psi\rangle_{LC_1}\langle\Psi|\right)\left(|\Psi\rangle_{RC_2}\langle\Psi|\right)\xrightarrow{click}|\Psi\rangle_{LR} \tag{3.43}$$

Cascading this method to more ensembles leads to a further increase of communication length L_n. For the distance $L_n = 2^n L_0$ the overall time needed for the generation of an entangled state is $T_n = T_0 \prod_{i=1}^{n}(1/p_i)$. The success probability for the connection is denoted by p_i and independent of the distance.

3.2.3 Purification

In entanglement connection schemes without purification the entanglement fraction decays usually exponentially with distance. In the DLCZ scheme the decay is linear due to an in-built entanglement purification. Let us look how noise modifies the entanglement generation. In this case the dominant influence is the loss of photons which has origins in the channel attenuation, spontaneous emission of the atoms, coupling inefficiencies of the Anti-Stokes light into the (fiber) channels and the detection efficiencies of the SPDs. When separating the channel attenuation from other noise contributions η_P' the overall efficiency is given by $\eta_P = \eta_P' e^{-L_0/L_{att}}$, i.e. the loss probability is $1 - \eta_P$. Then the probability to detect a photon click is $\eta_P \chi$, but it has no effect on the entangled state. On the other hand the dark counts in the SPDs can generate a click even though there was no photon, which we denote by the probability p_{dc}. The so-called vacuum coefficient $c_0 = p_{dc}/(\eta_P \chi) \ll 1$ is included in the generated entangled state ρ_{AB} which accounts for the noise by

$$\rho_{AB}(c_0, \phi) = \frac{1}{c_0 + 1}(c_0 \left|00\right\rangle_{AB} \left\langle 00\right| + \left|\Psi\right\rangle_{AB} \left\langle \Psi\right|). \tag{3.44}$$

Since the vacuum term is projected out in this protocol it does not affect the state. The source of noise which affects it are the higher order excitations. They decrease the fidelity and the fidelity imperfection can be estimated by $\Delta F_0 \approx \chi$.

The treatment of the influences of noise on the entanglement swapping can be done in analogy. Then the noise sources which do not change the fidelity of the quantum state can be summarized into a vacuum-coefficient $c_i \approx (L_i/L_0 - 1)(1 - \eta_s)$ (as long as $c_0 \ll 1 - \eta_s$), where i indexes the number of entanglement connections and η_s is the overall efficiency in the entanglement swapping (like η_P for the generation). Each time the entanglement is connected the final state can be written as in equation (3.44) where the component c_0 is replaced by c_i. This can be understood that a detection click removes part of the vacuum noise and the higher vacuum noise results just in more repetitions in order to do the swapping. It implies that the entanglement fraction decreases only linearly with distance instead of the exponential decrease in connection schemes without purification. Therefore one can speak of an built-in purification. But it is important to note that this effect only applies to noise due to photon loss. In contrast to purification protocols for EME states of light [20] [84] the fidelity is not improved. The fidelity of the atomic ensembles' EME state decreases by $\Delta F_n \approx 2^n \Delta F_0 \approx (L_N/L_0)\Delta F_0$ after n entanglement connections.

3.2.4 Quantum Memory

Quantum memory is required at each site to store and process states. Errors in local operations and finite memory time is critical. Long lived ground states of matter provide a natural storage medium. The atomic mode stores the quantum state until it is *read* out. The light-matter interface must provide a faithful and efficient mapping between the light and the atomic quantum state. It is important

to note that the quantum memory is crucial for the sub-exponential scaling of the DLCZ protocol. In the next chapter we will analyze what limits the storage process.

3.3   Polariton Picture and Phase Coherence

An alternative, but equivalent approach to the picture of a spin wave is the description as dark-state polaritons. A polariton is a quasi-particle and describes a mixture of an electromagnetic excitation with collective excitations of spin transitions. By diagonalizing the Hamiltonian of the atom-light interaction in a lambda level system one gets two new eigenstates: the bright and the dark state polariton. A bright state polariton (BSP) $\hat{\Phi}(z,t)$ and a dark state polarition (DSP) $\hat{\Psi}(z,t)$ are described according to [38] by:

$$\hat{\Psi}(z,t) \;=\; \cos\left(\Xi(t)\right)\hat{\mathcal{E}}(z,t) - \sin\left(\Xi(t)\right)\sqrt{N}\hat{\sigma}_{sg}(z,t)e^{(\imath\Delta kz)} \qquad (3.45a)$$

$$\hat{\Phi}(z,t) \;=\; \sin\left(\Xi(t)\right)\hat{\mathcal{E}}(z,t) + \cos\left(\Xi(t)\right)\sqrt{N}\hat{\sigma}_{gs}(z,t)e^{(\imath\Delta kz)} \qquad (3.45b)$$

By changing the so-called mixing angle $\Xi(t)$, i.e. the Rabi-frequency Ω_R, one can change the spin wave part of a DSP into a light field and back. In our case we write a DSP into the ensemble by the spontaneous Raman scattering, but we recover it into a "light" DSP by application of the *read* pulse. The mixing angle is given by

$$\tan^2\Xi(t) = \frac{g^2 N}{\Omega_R^2(t)} = n_g(t), \quad g = |\mathbf{d}_{eg}|\sqrt{\frac{\omega_1}{2\hbar\epsilon_0 V}}, \qquad (3.46)$$

thus it can be controlled by changing the intensity of the *read* field. g is the atom-field coupling constant of the Stokes light. The simplest dark state polariton for a number state is

$$\left|D_n^k\right\rangle = \frac{1}{\sqrt{n!}}\left(\hat{\Psi}_k\right)^n |0\rangle_L |g_1...g_N\rangle_A. \qquad (3.47)$$

The description is extended by the inclusion of the Zeeman hyperfine levels in the states of the lambda-system [62] which we sketch. The DSP operator for helicity α and *read* polarization β [3] represented in wave number q is

$$\hat{\Psi}_\alpha(q,t) = \frac{\imath\Omega_R(t)\hat{a}_{k,\alpha} - \sqrt{Np}\kappa^* \sum_m R_{m\alpha}(\beta)\hat{S}^{g\,m}_{s\,m+\alpha-\beta}(q,t)}{\sqrt{\Omega_R(t)^2 + Np|\kappa|^2 \sum_m |R_{m\alpha}(\beta)|^2}}, \qquad (3.48)$$

where $R_m = C^{F_g 1 F_e}_{m1m-1}/C^{F_s 1 F_e}_{m1m+1}$ is a ratio of Clebsch-Gordan coefficients and p is computed by $p = 1/(2F_b + 1)$. The collective spin wave annihilation operator is

$$\hat{S}^{g\,m}_{g'\,m+\alpha-\beta} \equiv (1/\sqrt{Np}) \sum_\mu \hat{\sigma}^{(i)}_{gm,g'm'} \cdot e^{-\imath(qz_i + (\Delta_{HFS})(t - z_i/c))}, \qquad (3.49)$$

---

[3]For a circular polarization of the *read* field: $\beta = \pm 1$

where the atomic level transition operator includes the Zeeman manifold with magnetic quantum number m and is labelled by $\hat{\sigma}^i_{gm,sm}(0) = |g,m\rangle_i \langle s,m|$. The frequency of the hyperfine splitting is denoted by Δ_{HFS} The time evolution of the DSP in the presence of an homogenous external magnetic field $\mathbf{B}$ along $\mathbf{z}$ direction is given by $\hat{S}^{g\,m}_{s\,m+\alpha-\beta}(q,t) = \sum_{m_1=-F_g}^{F_g} \sum_{m_s=-F_s}^{F_s} \mathcal{D}^{(g)\dagger}_{m_1 m}(t) \mathcal{D}^{(s)}_{m+\alpha-\beta,m_2}(t) \hat{S}^{g\,m_1}_{g'\,m_2}(q,0)$. $\mathcal{D}^{(j)}_{m,m'}(t) = \langle j,m| \exp\left(-\imath g_j \mathbf{\Omega_B} \cdot \hat{\mathbf{F}}(t)\right)|j,m'\rangle$ is a matrix element of the rotation matrix for the states $j = g,s$. $\hat{F}$ is the total angular momentum and Larmor-frequency is $\mathbf{\Omega}_B = \mu_B \mathbf{B}/\hbar$. The number of DSPs at time T_s is $\langle \hat{N}(T_S)\rangle = \sum_q \langle \hat{\Psi}^\dagger(q,T_s) \hat{\Psi}(q,T_s)\rangle$. The retrieval efficiency is given by the ratio

$$\frac{\langle \hat{N}(T_s)\rangle}{\langle \hat{N}(0) = \left|\sum_{m_1 m_2} \frac{R_{m_1} R_{m_2}}{\sum_m |R_m|^2} \mathcal{D}^{(g)\dagger}_{m_2 m_1}(T_s) \mathcal{D}^{(s)}_{m_1,m_2}(T_s)\right|^2 \rangle}. \tag{3.50}$$

By using the approximation for an alkali atom $g_{s,m} = -g_{g,m}$ the phases in the DSP with a Larmor period of $(2\pi/|g_g\mathbf{\Omega}_B|)$. Thus the retrieve efficiency of the DSP is time dependent and experiences -no damping assumed- collapses and revivals.

3.4 Performance and Drawbacks of the original DLCZ repeater scheme

The DLCZ scheme has opened a feasible path to enable long-distance quantum communication, since it scales sub-exponential with the communication length L. According to [47] the time for the successful creation of an entangled pair is given by

$$T_{tot} = \frac{L_0}{c} \frac{1}{P_0 P_1 ... P_n P_{pr}} \left(\frac{3}{2}\right)^{(n+1)}. \tag{3.51}$$

The length of a segment is $L_0 = L/2^n$ and n is the nesting level. The factor $\frac{L_0}{c}$ accounts for the photon propagation and for the classical communication time to broadcast the success. P_0 is the success probability for entanglement generation in an elementary segment. P_i is the connection probability in the i-th level which is a constant. P_r is the probability for projection into a maximally entangled state. The factor $3/2$ is due to fact that two segments must be entangled before they are connected. Only $P_0 \propto \eta_{L_0}$ depends on the channel loss η_{L_0}. It is a fixed value computed by $\eta_{L_0} = e^{-L_0/L_{att}}$, since the segment length L_0 is fixed. Thus with increasing L only the maximum nesting level n increases and the total time T_{tot} clearly scales not exponentially.

Despite the nice scaling the original DLCZ protocol has some drawbacks when considering practical application. It is mainly designed to compensate for photon loss, but it cannot correct any error. In contrast, it is sensitive to multiple photon generation. In addition the phase factor arising due to the path length difference of the channels in the entangled state makes a practical implementation unrealistic. In [94] it is shown that the path difference during the entanglement generation process
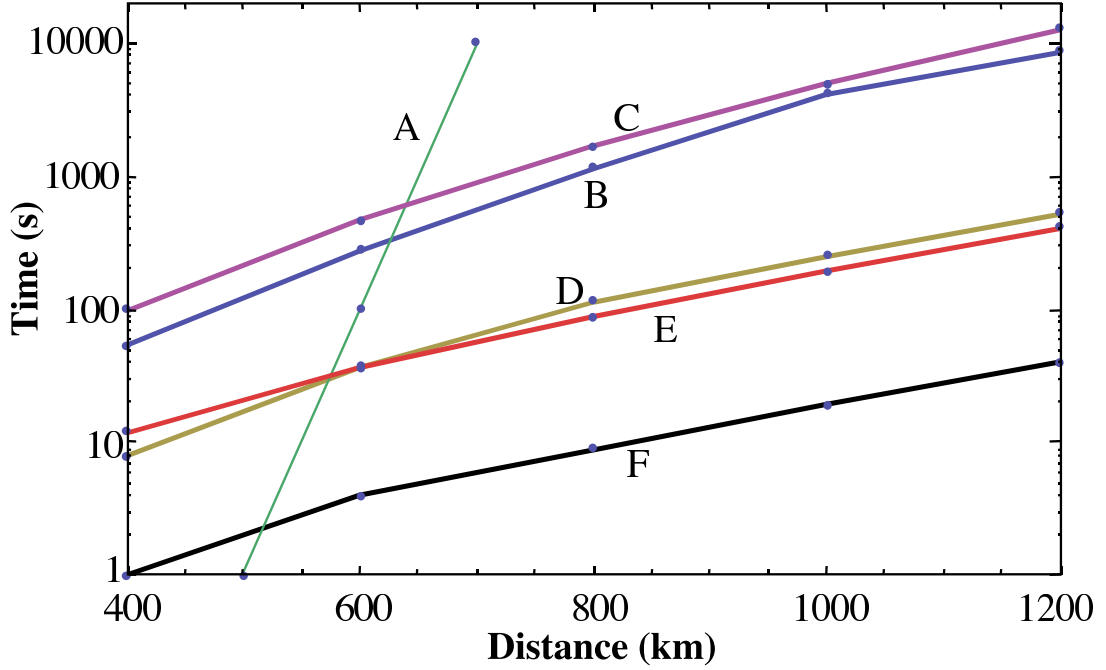
Figure 3.6: Time needed for entanglement generation over communication distance L for various protocols (taken from [45]): The original DLCZ scheme is labelled by A. The scaling is subexponential, even though the three points suggest to be on a straight line. The other protocols (B,..F) are improvements of the DLCZ scheme. Line F is for the protocol proposed in reference [45].

must be stabilized to $\delta x \leq 0.1$ μm, which is not practical for a length $L_0 > 10$ km. Another drawback is that the generated entangled pairs cannot be further purified by distillation of entanglement from other pairs [84].

In order to overcome the drawbacks of the original scheme a variety of protocols [43][44][45] [46] [47] have been proposed, based on the DLCZ scheme. In figure (3.6) the time needed to generate entanglement is plotted for various types of protocols over the communication distance. In terms of temporal resources the improved versions of the DLCZ scheme perform better. Note that the time scales determine the memory time needed as well. The increased performance with respect to communication time is offset by an increased need of spatial resources, i.e. the number of atomic ensembles at each site.

For practical applications various parameters besides the effects of errors influence the performance as well. The detection efficiency of single photon detectors for a wavelength of 795 nm is approximately $p_{detect} \sim 40$ percent. If N detectors are necessary for the communication distance the success probability to detect all photons is p_{detect}^N. The availability of photon-number resolving detectors could help in solving the problem with multi-excitations.

It is important to note that the detection efficiency can be combined with the retrieve efficiency to $p_{detect}\eta_{retrieve}$ into a single parameter. Thus it is obvious that for an optimal scaling a high retrieve efficiency is crucial.

Other imperfections and noise sources are the detector dark counts, non-stationary

channel noise and set-up asymmetries.

3.5   Other Atom-Light Interfaces and Protocols

The DLCZ type atom-light interface is not the only interface to map a quantum state of light onto matter and vice versa. We summarize at this point their properties in order to put the usefulness of the DLCZ approach for long-distance quantum communication into perspective. We describe below quantum memories types which are investigated with great efforts and successes. We sketch why they are currently not considered for practical implementations of quantum communication.

Cavity   The atom-light interface by the weak Raman scattering described above has the principle disadvantage that it is non-deterministic, because of the probabilistic *write* process. Multiple trials are needed for the successful photon generation even if the retrieval works perfectly. Naively the better approach seems to be the conversion of a single photon into the excitation of a single atom and subsequent retrieval with high efficiency. This is the so-called strong atom-light coupling regime. The interaction Hamiltonian of a two-level atom with an electromagnetic field is

$$V = g \left(|e\rangle \langle g| \, a + |g\rangle \langle e| \, \hat{a}^{\dagger} \right), \tag{3.52}$$

with the coupling constant $g^2 = (\sigma/A)F\gamma\kappa$. Cavity QED [34] predicts strong coupling for $g^2 \gg \kappa\gamma$. This is possible if the Finesse is large $F \sim c/L\kappa$. A high Finesse cavity with a single atom is technically non-trivial [99, 35].

Solids   For commercial applications a quantum memory implementation in solid state systems seems to be more practical. Unfortunately in solid state systems quantum states are harder to control and prepare. So far stopped light has been achieved in a crystal for up to 10 seconds. The light states stored have been classical pulses and no quantum mechanically states yet [100].
The use of photon echos in erbium doped fibers is another way to store a quantum state. Its currently main advantage is the storage of multiple temporal modes in a single quantum memory by a technique called: Controlled Reversible Inhomogeneous Broadening (CRIB)[101]. The drawbacks up to now are that the fibers have to be placed in a cryostat and storage times of only 1.6 μs have been achieved [102] [103].

Stopped Light   By reducing the group index of equation (3.27) with a time varying control field, one can slow down a single photon in an atomic medium and stop it by mapping the corresponding DSP onto a pure spinwave. In that way classical pulses can be stopped and stored in atomic ensembles for several hundred microseconds in thermal ensembles and for a few milliseconds in Bose-Einstein condensates [38]. For quantum communication it would be crucial to store single entangled photon

states. The EPR pairs generated by SPDC sources have not a bandwidth narrow enough to be stored in atomic ensembles with a relatively small line width. Single photons generated from the DLCZ-type interfaces have a narrow bandwidth and can therefore be stored [104] [105]. Even the storage of entanglement has been demonstrated [71]. In fact we have shown that the *read* out of the darkstate polariton corresponds to the retrieval of a stopped light pulse. Only the *writing* of a single excitation into a spin wave by Raman scattering is different [4] in contrast to the stopping of a single photon. But since only the DLCZ-type quantum memories can provide deterministic single sources (chapter 7, [74], [57]) of sufficiently small bandwidth, the stopped light approach for long-distance quantum communication can only work in connection with the DLCZ-type memories.

Encoding in Continuous Variables   Another way to encode quantum information is the use of the quadrature amplitudes of the light field. The atom-light interface uses a different interaction and the quantum state is stored by spin squeezing of collective atomic spin states. The quantum state of the light is not encoded in discrete photon number states, but in the quadrature amplitudes of the electromagnetic field. By using thermal atomic ensembles in magnetic shields a quantum memory with a decay constant $\beta = 0.09$ ms^{-1} has been observed. Due to a verification light pulse the observed life time is up to 8 milliseconds (40-400 ms without the pulse) [107][108]. The state stored in the atoms can be verified but not retrieved. A proposal [109] for the read-out has not been implemented yet.

This memory cannot be used for long-distance quantum communication, since the entanglement connection of the memories is sensitive to photon loss. That means that the exponential law for the absorption of the photons limits the scaling of this approach.

---

[4]This difference has important consequences for the optimization of the retrieval [106].

Chapter 4

Atomic Ensembles as Quantum Memory

In the previous chapter the DLCZ-type atom-light interface has been presented. There the quantum memory has been treated as a perfect unit. In this chapter we take practical considerations into account and look at the physical processes the atoms experience during the storage of the quantum state.The important mechanisms which are limiting the storage time in current experiments are described and simulated. Concepts for overcoming this limits are described in the end of this chapter.

4.1   Requirements on Quantum Memory

According to the quantum repeater scheme the memory time needs to be sufficiently long in order to allow the preparation of all communication segments. Despite the reduction of used memories during the entanglement connection steps, the memories of the sender and receiver must maintain their quantum states during total duration of the process for creating a distant entangled pair. Depending on the protocol type (3) the generation time for a distant entangled pair over only 1000 kilometers can be more than 10,000 seconds [45]. Assuming that DLCZ-type protocols can still be improved and technologies advance, e.g. that the single-photon detection efficiency increases, one can make a rough estimate for the minimal memory time needed. As lower limit we take time a single photon propagates through a fiber over an intercontinental distance of about 10,000 kilometers. The speed of light in fiber of about 2/3 of the speed of light in vacuum and a factor of two for the confirmation signal. Thus the necessary memory time is about 100 milliseconds.

The fidelity of the quantum memory is very important, which means that the quantum state must not be altered during storage. In [110] for fidelities of $F = 0.5$ to $F = 0.9$ the bounds on the error probabilities are computed for various communication distances. It can be necessary to make them as low a $1 - \eta < 0.001$.

The protocols of the DLCZ-type are optimized against photon loss at the expense of an increase sensitivity to multiple photon events. The excitation probability χ for the Raman scattered Anti-Stokes photons must be adjusted to a low value. The second order contribution in equation(3.37), i.e. the probability to generate two photons at the same time is proportional to χ^2. Let us take for example an excitation probability χ of about 1%[1], then the two-photon component triggered on the detection of the first one is smaller than 0.1%.

As we have seen in the previous chapter that matching the mode of the Anti-Stokes detection to the Stokes mode is necessary in order to observe the correlations. This is important for the set-up of the detection optics. There mode-matching is to adjust the detection mode of the optics as well as possible to the signal mode of the emitted light from the ensemble. We have seen in the previous chapter 3, that the mode is approximately a single mode Gaussian beam. A Fresnel number $F \leq 1$ is required [90] in that case. Such a mode can be coupled into a single-mode fiber with high efficiency. There are two situations which have to be considered:

1. The atomic ensemble has a larger radius than the waist of the detection mode. Then the Fresnel number is determined atoms in the mode of the detection optics.

2. If the diameter of the atomic ensemble is smaller than the detection mode, then the Fresnel number is determined by the dimensions of the ensemble. They must be matched to have a Fresnel number ≤ 1 in order to be be in the single-mode regime. Nevertheless the detection mode should be matched to the ensemble in order to reduce noise, i.e. detected photons which are not related to an atomic excitation. Let us consider the case where the dimensions of the ensemble are such that $F << 1$, i.e. the ensemble is very elongated. The detection angle for the correlations $\theta' \leq \min(\theta_{w_a}, \theta_L)$ is then determined by $\theta_L = \sqrt{\frac{1}{k_s L}}$. In order to achieve the Fresnel number of one, one can either reduce the length or increase the width of the ensemble. The retrieve efficiency is proportional to the solid angle $d\Omega$. Therefore it is more favorable to reduce the length and thereby increase θ_L.

The retrieve efficiency is indeed a very important quantity. As shown in [106] the retrieval efficiency of any stored spin wave only depends on the optical depth of the medium.

In case the two metastable ground states are not degenerate, then after an increase of the optical depth $\mathcal{D}$ the length of the ensemble must be adapted in order to achieve an optimal retrieve efficiency [111].

So far we have assumed that the atoms are fixed to their positions. Since our atomic ensemble is an ensemble of a dilute gas, the atoms have a velocity according to the Maxwell-Boltzmann distribution. A general requirement is that the atoms do not leave the interaction region during the storage time. This can be achieved in several ways. A more detailed discussion is given in section (4.3).

---

[1]In actual experiments it is by 2 orders lower

4.2   Errors in Atomic Memories

The atomic mode which we use as storage is a collective state. Naively, one might think that with increasing number this state becomes more sensitive to external influences. It was shown in [112], that for memory errors the decoherence of this collective state is not enhanced by the number of atoms N. In the following we summarize the must important results valid for a single atom. In order to obtain the total error for the ensemble, the number of atoms must multiplied.

- The imperfect preparation of the atomic ensemble in state $|g\rangle$ can introduce an error when such an excitation is read out. But it can be shown that for a small probability ($\ll 1$) to find an atom in in the wrong state $|s\rangle$ means that number of initial spin-waves arising from the preparation is similar small.

- A random spin flip from $|g\rangle \rightarrow |s\rangle$ of an individual atom for a stored Fock state $|n\rangle$ ($n \ll N$ leads to a decrease of fidelity f given by

$$f = 1 - \frac{n+1}{N} + \mathcal{O}\left(\frac{1}{N^2}\right). \tag{4.1}$$

- A random symmetric spin flip $|g\rangle \leftrightarrow |s\rangle$ leaves the Fock state in the quantum memory with a fidelity according to

$$f = 1 - \frac{1}{N} + \mathcal{O}\left(\frac{1}{N^2}\right). \tag{4.2}$$

- A flip of the phase of an atom in the collective state depends on the average number of spin waves n_{sw} stored the fidelity scales as

$$f = 1 - \frac{n_{sw}}{N} + \mathcal{O}\left(\frac{1}{N^2}\right). \tag{4.3}$$

- The loss of atom from the collective state leaves the Fock state $|n\rangle$ with a fidelity

$$f = 1 - \frac{n}{N}. \tag{4.4}$$

- The thermal motion of the atoms mixes the spatial phase information imprinted during the *write* process. If D is the characteristic diffusion coefficient and we consider a single Fock state $|n = 1\rangle$ stored in the collective state then the fidelity f decreases with time t according to

$$f = \frac{1}{N}\left(1 + (N-1)e^{-Dt}\right) \sim e^{-Dt}. \tag{4.5}$$

That means there is no disadvantage in using collective atomic states compared to single atoms. The effect of an error of a single atom on the fidelity is $\propto \frac{1}{N}$ and thus

can be reduced with increased atom number. The reason is that there many equivalence classes of the spinwave present. In the picture of the polaritons (section (3.3)) all states with every combination of dark state and bright state polaritons present in the complete system is equivalent as long as their projections on a dark state polariton mode are the same. Since the dark state polaritons do not interact with each other and perturbations on the bright state polariton of a specific combination do not affect the dark state polaritons mode, a family of equivalence classes is rather robust.

So far the analysis of the quantum repeater scheme has assumed a perfect memory. The storage and readout can be done with high fidelity and without introducing noise into the quantum state. The effect of memory errors in quantum repeater scheme changes the scaling of the scheme and has been treated in ref. [110]. A main conclusion is that the fidelity of the quantum memory can limit the total communication distance. This boundaries depend not only on the error probability alone but in connection with the memory time and the minimal fidelity for purification. It limits the maximal achievable fidelity of the long-distance entangled pair as well. The treatment of imperfections of the memory for the DLCZ scheme is analyzed in ref. [113].

4.3   Selection of atomic species and its temperature regime

The DLCZ protocol [42] provided a way for a suitable experimental implementation of an atom-light interface. The requirements are very general and there are several options to make use of. The first choice to do is the selection of an appropriate atomic species. The experiments with stopped light in thermal cells with ^{87}Rubidium have shown that low coherence times 300 μs are feasible. Since these experiments also influenced the proposal of the DLCZ protocol the use of thermal Rubidium glass cell seemed natural [51]. ^{87}Rubidium provides on the D_1-line a closed lambda system [114]. Isotopic ^{87}Rubidium together with a certain amount of buffer gas is filled into a glass cell, which usually has flat end faces of high quality optical glass. In order to achieve a larger optical density and therefore a stronger signal the cell is heated. The buffer gas reduces the diffusion of the hot Rubidium atoms out of the interaction region with the *write* and *read* fields [115]. In order to prevent the splitting of atomic levels due to the Zeeman effect induced by stray magnetic fields a multiple layer magnetic shield is build around the cell. For a typical temperature of $\sim 70°$ C the Doppler width (FWHM) given by

$$\delta\omega_D = \frac{\omega_0}{c}\sqrt{(8k_B T)/m}, \tag{4.6}$$

is about 537 MHz. This is large compared to the natural line width of $2\pi \cdot 5.7$ MHz. In order to achieve Raman scattering with low fluorescence background detunings of typically 1 GHz are necessary.

Even though progress with this approach was fast the maximal reported storage time is about 3 μs [52]. Thorough investigation by [53] showed that there is an additional incoherent light part which affects the detection of the nonclassical Stokes and Anti-Stokes photons. The incoherent contribution is due to collisions in the excited state by the *write* pulses (with 1 μs duration) which is also stored. This incoherent process takes place during the *read* out as well [116]. The quality of the correlations can be increased by employing narrowband Fabry-Perot cavities as the expense of an increased time overhead. Larger detuning of the *write* and *read* light helps as well, but causes difficulties for filtering leakage light by pumped filter cells. A reduction of the buffer gas pressure reduces the probability of collisions during the Raman processes. The drawback is an increased diffusion length. The diffusion can be compensated by using expanded beams and paraffin-coated inside of the cell in order to control collisions with the wall. In summary the technical complexity will be significantly increased.

On the other hand laser cooled atoms produced in a magneto-optical trap(MOT) have become a standard tool in the field of quantum gases. At an approximate temperature of ~ 120 μK he Doppler broadening of cold atoms is about 310 kHz. A detuning for Raman scattering is therefore technically not challenging. In addition there is no need for buffer gas, since their velocity in the range of $v \sim 1$cm/s is so low that diffusion out of the interaction region is not a main concern. Magnetic shielding of a ultra-high vacuum chamber with need for good optical access is difficult. In chapter 5 we will see how to overcome this problem. In addition the variety of tools which have been developed for ultracold quantum gases make them as a system for the principal investigation of quantum memory and demonstration of the DLCZ protocol a good choice. The first experiments for the generation of nonclassical light in a MOT have been done with cesium [54]. Historically our group has acquired experience with rubidium. The other reason for our choice to continue with rubidium is that is better ratio elastic/inelastic scattering properties, which can be useful for future investigation.

4.4 Optimal Retrieval

The importance of the efficiency and fidelity for the storage process has been been pointed out already. Various theoretical publications [117] [111] [106] have analyzed strategies for the optimal retrieval. By optimization of the pulse shape during storage and retrieval of the *write* and *read* pulses. In case of single photons stopped in the ensemble the optimal efficiency is always achieved when the *read* process is the time reversed of the storage process. For that reason the retrieval opposite to the direction of the *write* is favorable in our case, too. But we will see in the following that there is a subtlety. In case of optimized pulse shapes the retrieval efficiency depends only on the optical depth.

A qualitative argument from [111] gives an approximate dependency. A field emitted from a mode with cross section A covers a solid angle of $\gamma\lambda^2/A$. The decay of a single atom into this mode has a probability $\sim \lambda^2/A$. During the *read* N atoms contribute

coherently in this direction which gives $\gamma_c \sim \gamma N \lambda^2 / A$. The ratio between the decay from the desired signal γ_c to the noise contribution γ yields the retrieve efficiency as $\eta = \gamma_c/(\gamma_c + \gamma) \sim 1 - 1/\mathcal{D}$. The result by using the optimization strategy is $1 - \eta \approx 2.9/\mathcal{D}$. This increase of the retrieve efficiency with optical depth is only correct if the spin wave does not have any discontinuities. Otherwise the retrieve efficiency is improved only by $1/\sqrt{\mathcal{D}}$. The reason for this effect is the pulse that must be retrieved can be transformed into Fourier space. A square pulse has more Fourier components than a smooth one. In frequency space the EIT window of the *read* process has only a certain width. If higher frequency components are cut off, then the impact of the optical depth is reduced. A spin wave generated by spontaneous Raman scattering is flat and the error scales as $\sqrt{2\pi}/\sqrt{\mathcal{D}}$[111].

The non-degeneracy of the two ground states $|g\rangle$ and $|s\rangle$ has a negative effect on the maximal achievable retrieve efficiency. Then the quantity $\Delta k L$ must be adjusted with increasing optical depth in order to maintain the optimal retrieve efficiency.

4.5 Decoherence Processes in Quantum Memory

The lifetime of the quantum memory is due to the interaction of the atomic ensemble with the environment, with the trap and due to interaction of atoms of the ensemble with each other. All these effects influence the stored spin wave. We have seen that the collective atomic state is more robust than an individual atomic state to several types of errors. Since we want to store a quantum mechanical state and we want to achieve a sufficiently long storage time, we must isolate, investigate and control all mechanisms which lead to decoherence. In this section we describe the mechanisms limiting current experiments.

In equation (3.9) we have introduced the spin wave as a collective state with phase factors $c_i \equiv e^{i \Delta \mathbf{k} \cdot \mathbf{r}_i}$ for every atom i. The factors c_i are determined by the momentum $\Delta \mathbf{k}$ and the position of the atom $\mathbf{r}_i$. For the time evolution an additional phase $c_i'(t) = e^{-\frac{i}{\hbar} H_{pertub} t}$ due to external perturbations H_{pertub}. In case they are position dependent, i.e. $H_{pertub} = E_{pertub}(\mathbf{r}_i)$ the spin wave state is given by

$$|S,t\rangle = \frac{1}{\sqrt{N}} \sum_{i=1}^{N} e^{-(\frac{i}{\hbar} E_{pertub}(\mathbf{r}_i))t} |\tilde{s}_i\rangle , \qquad (4.7)$$

where $|\tilde{s}_i\rangle$ the initial state of an atom in the spinwave. The retrieval efficiency is given by the overlap with initial spin wave:

$$R(t) := |\langle S,t\,|S,t=0\rangle|^2 = \frac{1}{N^2} \left| \sum_{i=1}^{N} e^{-\frac{i}{\hbar} E_{pertub}(\mathbf{r}_i)t} \right|^2$$

$$\approx \left| \int n(\mathbf{r}) e^{-\frac{i}{\hbar} E_{pertub}(\mathbf{r}_i)t} \right|^2 \qquad (4.8)$$

Reversible Dephasing

4.5.1   Collapse and revival of dark-state polaritons

By application of a constant and uniform magnetic field along the atomic ensemble the phase factors of each atom from this coherent collective state the retrieve efficiency for the non-classical correlations changes periodically with the delay time between the *write* and *read* pulses. As long as the damping of theses oscillations is small, such a collapse and revival phenomenon of a quantum mechanical system, usually introduced in textbooks [79] for two-level atoms, can be nicely experimentally observed [105]. The evolution of the phase factor due to the interaction with the magnetic field is different for each hyperfine component. The Larmor period changes with the magnetic quantum number. As a consequence the collective spin wave looses its coherence and the retrieve efficiency decays to zero. During the evolution time all of the hyperfine components can have rephased (no damping assumed) at a certain time. The collective state has revived and the retrieve efficiency is maximal again. The Larmor frequencies of the components are different by an integer value such they are in phase at specific times. For magnetic fields of approx. 0.5 G and various orientations of the field with respect to the *write* and *read* axis the collapses and revivals with a period of 2.3 μs could be measured for multiple times. The observation of the revivals are limited to the storage time which has been measured previously.

Despite the application of an external influence, i.e. uniform magnetic field, the quantum state was not destroyed more rapidly, but it could be altered in a controlled fashion. The main reason was that the **dephasing** of the components is reversed by a **rephasing** during evolution in time. This is certainly not the case for all external or internal interactions of the atomic ensemble. Therefore we must isolate and control each one in order to achieve the desired storage time.

Irreversible Dephasing

4.5.2   Dephasing of Magnetic Substates

The main decoherence process limiting the life time in previous experiments is the dephasing of the Zeeman sublevels due to external magnetic fields.

The description of the atom-light interface in previous chapter (3) does not take into account any "structure" of the ground states. The situation occurring in experiments is different. Rubidium and Cesium, which are used, have two meta-stable ground states due to the hyperfine interaction. They are the $|g\rangle$ and $|s\rangle$ states in the lambda system. Each hyperfine state with quantum number F has a manyfold of Zeeman sublevels with magnetic quantum number $m_F = -F, ..., F$. Any kind of external magnetic or electric field will lift the degeneracy of these Zeeman levels. The influence of magnetic fields is in typical laboratory environments dominant compared to the electric fields. The focus of our analysis is on the first ones. The first experiments

with cold atoms achieved only a memory time of about 250 ns [54]. The cooling and repumping light was switched off, but due to a desirable high repetition rate of the experiment, the magnetic quadrupole field of the MOT was not switch off during the experimental trials. A fast switch capable of switching high currents with big inductive loads overcomes this problem. The effect of remaining stray magnetic fields on the freely expanding atomic cloud was compensated by three sets of Helmholtz coils. They are not able to compensate gradient fields, such that typically a gradient of 10 mG over the size of the ensemble remains. In the subsequent experiments, life time measurements of 15 μs are consistent with that technical limit.

The theory of this dephasing mechanism is given in [66]. The theory has been adopted to our experimental situation and a MATHEMATICA code was written in order to simulate the decay of the cross correlation function over time. In the following paragraph we summarize the key points of the theoretical model.

For the subsequent considerations ($F \leq 1$) we treat the problem one-dimensionally and neglect the small angle of the detection channels to the *write* and *read* beams. The atomic ensemble has a uniform distribution and a cylindrical shape due to the symmetry of the problem. In order to include the Zeeman structure into the Hamiltonians we represent the F_j manifold for the ith atom by the state $|m_j\rangle_i$. An additional generalization is introduced by the employment of four-level atoms, i.e. with an extra excited state. In principle this allows the modelling of a *read* out transition different to the *write* transition. The complete Hamiltonian for the system is $\hat{H}(t) = \hat{H}_0 + \hat{V}(t)$. The free-atom Hamiltonian reads as

$$
\hat{H}_0 = \sum_{i=1}^{N} \left(\sum_{m_s=-F_s}^{F_s} (\mu_B g_s m_s B_{z_i}) |m_s\rangle_i \langle m_s| + \right.
$$
$$
\left. \sum_{m_g=-F_g}^{F_g} \mu_B g_g m_g B_{z_i} |m_g\rangle_i \langle m_g| + \sum_{m_a=-F_a}^{F_a} \hbar\omega_a |m_a\rangle_i \langle m_a| + \sum_{m_b=-F_b}^{F_b} \hbar\omega_b |m_b\rangle_i \langle m_b| \right).
$$
$$(4.9)$$

The interaction Hamiltonian is

$$
\hat{V}(t) = \sum_{i=1}^{N} \left(\sum_{m_a=-F_a}^{F_a} \sum_{m_g=-F_g}^{F_g} (-\mathbf{d}_{m_a,m_g} \cdot \mathcal{E}) |m_a\rangle_i \langle m_g| \right.
$$
$$
+ \sum_{m_s=-F_s}^{F_s} \sum_{m_a=-F_a}^{F_a} (-\mathbf{d}_{m_s,m_a} \cdot \mathcal{E}_{sa}^{\dagger}) |m_s\rangle_i \langle m_a|
$$
$$
+ \sum_{m_b=-F_b}^{F_b} \sum_{m_s=-F_s}^{F_s} (-\mathbf{d}_{m_b,m_s} \cdot \mathcal{E}_{sb}) |m_b\rangle_i \langle m_s|
$$
$$
\left. + \sum_{m_g=-F_g}^{F_g} \sum_{m_b=-F_b}^{F_b} (-\mathbf{d}_{m_g,m_b} \cdot \mathcal{E}_{gb}^{\dagger}) |m_g\rangle_i \langle m_b| \right) .
$$
$$(4.10)$$

We do not include the Zeeman splitting of the the excited state, since we want to investigate a situation were it is small compared to the natural line width. The *write* and *read* fields are

$$\mathcal{E}_{ga}(\mathbf{r}, t) = \mathbf{e}_{p_w} u_w(\mathbf{r}, t) e^{\imath(k_w z - \omega_w t)} \tag{4.11}$$

$$\mathcal{E}_{sb}(\mathbf{r}, t) = \mathbf{e}_{p_r} u_r(\mathbf{r}, t) e^{\imath(k_r z - \omega_r t)} \tag{4.12}$$

The two Raman fields are:

$$\hat{\mathcal{E}}_{sa}(\mathbf{r}, t) \propto \sum_{p_1} \int d\mathbf{k}_1 \hat{a}_{\mathbf{k}_1, p1} e^{\imath(\mathbf{k}_1 \cdot \mathbf{r} - \omega_{\mathbf{k}_1} t)} \mathbf{e}_{p_1} \tag{4.13}$$

$$\hat{\mathcal{E}}_{gb}(\mathbf{r}, t) \propto \sum_{p_2} \int d\mathbf{k}_2 \hat{b}_{\mathbf{k}_2, p2} e^{\imath(\mathbf{k}_2 \cdot \mathbf{r} - \omega_{\mathbf{k}_2} t)} \mathbf{e}_{p_2} \tag{4.14}$$

The annihilation operators for the Raman fields are denoted by $\hat{a}_{\mathbf{k}_1, p1}, \hat{b}_{\mathbf{k}_2, p2}$, where p_i represents the polarization of the field and the frequency $\omega_{\mathbf{k}_i} = |\mathbf{k}_i| c$. The state of a spontaneously generated photon for the field $i = 1, 2$ is then $|1_{\mathbf{k}_i, p_i}\rangle$.

The temporal evolution of the combined system of atoms and Raman fields, a density matrix $\hat{\rho}(t)$, can be described by in the interaction picture by:

$$\hat{\rho}_I(t) = \hat{U}_I(t) \hat{\rho}(0) \hat{U}_I^\dagger(t). \tag{4.15}$$

We skip the further derivation of [66] and present the final equation.

The values of the so-called coupling constants of the transitions K_{m_i, m_j} are computed by the decomposition of the atom-light dipole interaction into the constant and the mode function $u(\mathbf{r}, t)$. For the *write* light this is

$$-\mathbf{d}_{m_e, m_g} \cdot \mathcal{E} = K_{m_e, m_g} u_W(\mathbf{r}, t) e^{\imath(k_w z_i - \omega_W t)}. \tag{4.16}$$

By multiplication of the coupling constants for the *write*, field 1, *read*, field 2 transitions for various m_F state we receive

$$d(m_g, m_s) = \sum_{m_b=-F_b}^{F_b} \sum_{m_a=-F_a}^{F_a} K_{m_g m_b}^{\mathbf{k}_2 p_2} K_{m_b m_s}^{r} K_{m_s m_a}^{\mathbf{k}_1 p_1} K_{m_a m_s}^{w} \tag{4.17}$$

which is the strength of a specific excitation pathway. D_{m_g} is the distribution of the m_F states in the initial ground state. The mode functions $u(\mathbf{r}, t)$ can be further decomposed into a spatial mode $q(\mathbf{r})$ and a slowly varying envelope $f(t)$ written as

$$u(\mathbf{r}, t) = q(\mathbf{r}) f(t). \tag{4.18}$$

The phase-matching condition

$$k_r z_i + k_w z_i - \mathbf{k}_1 \cdot \mathbf{r}_i - \mathbf{k}_2 \cdot \mathbf{r}_i = 0 \tag{4.19}$$

is taken into account as well. Then a function $F(t, z_i)$ is defined which can be taken as time propagator and is given by

$$
F(t, z_i) = \underbrace{\int_0^t dt' e^{\imath(-\Delta_r + a_{ig})t'}}_{Stokes} \underbrace{\int_0^{t'} dt'' f_r(t'') e^{\imath(\Delta_r - a_{is})t''}}_{Read}
$$

$$
\times \underbrace{\int_0^{t''} dt''' e^{\imath(-\Delta_w + a_{is})t'''}}_{Anti-Stokes} \underbrace{\int_0^{t'''} dt'^{\nu} f_w(t'^{\nu}) e^{\imath(\Delta_w - a_{ig})t'^{\nu}}}_{Write} \tag{4.20}
$$

We assume that the pulse shapes of the *write* and *read* light $f_w(t)$, $f_r(t)$ are square:

$$
f_w(t) = \theta(t) - \theta(t - T_p), \tag{4.21a}
$$
$$
f_r(t) = \theta(t - T_R) - \theta(t - T_p - T_R), \tag{4.21b}
$$

where $\theta(t)$ is the step function. Both pulses have the same duration T_P and a relative delay T_R. The function $F(t, z_i)$ can then be computed as (when $\Delta_r, \Delta_w \gg T_P^{-1}, a_g, a_s$)[118]

$$
F(z) = -\frac{\theta(T_R - T_P)}{\Delta_r \Delta_w} F_1(z) - \frac{\theta(T_P - T_R)}{\Delta_r \Delta_W} F_2(z). \tag{4.22}
$$

The functions F_1 and F_2 are

$$
F_1(z) = \delta_{a_s, a_g} T_p^2 + (1 - \delta_{a_s, a_g})
$$
$$
\times \left[\frac{e^{\imath(a_g - a_s)(T_P + T_R)} - e^{\imath(a_g - a_s)T_R}}{a_g - a_s} \right] \left[\frac{e^{\imath(a_g - a_s)T_R} - 1}{a_g - a_s} \right], \tag{4.23}
$$

and

$$
F_2(z) = \delta_{a_s a_g} \left(\frac{T_P^2}{2} + T_P T_R - \frac{T_R^2}{2} \right) + (1 - \delta_{a_s a_g}) \times
$$
$$
\left\{ \left[\frac{e^{\imath(a_g - a_s)T_P} - e^{\imath(a_g - a_s)T_R}}{a_g - a_s} \right] \left[\frac{e^{-\imath(a_g - a_s)T_R} - 1}{a_g - a_s} \right] + \right.
$$
$$
\left[\frac{e^{\imath(a_g - a_s)(T_P + T_R)} - e^{\imath(a_g - a_s)T_P}}{a_g - a_S} \right] \left[\frac{e^{-\imath(a_g - a_s)T_P} - 1}{a_g - a_s} \right] +
$$
$$
\left. \frac{\imath(T_P - T_R)}{a_g - a_s} - \left[\frac{e^{\imath(a_g - a_s)(T_P - T_R)} - 1}{(a_g - a_s)^2} \right] \right\} \tag{4.24}
$$

Since we vary T_R as the delay time between *write* and *read* pulse, there is an implicit time dependence in this equation. The a_g and a_s terms a dependent on the position of the atom, such there is an implicit dependence on z as well.

The probability $p_{12}(t)$ for the detection of a second photon after a time interval t

after a first click is given by

$$p_{12}^{th}(t) = C \left| \sum_{m_g=-F_s}^{F_g} \sum_{m_s=-F_s}^{F_s} D_{m_g} d(m_g, m_s) \int_{-L/2}^{L/2} \frac{dz}{L} F(t, z) \right|^2, \qquad (4.25)$$

where the constant C is defined as

$$C = N^2 |\langle q_r(x, y) q_w(x, y) \rangle|^2, \qquad (4.26)$$

where N is the number of atoms and q_r and q_w denote the spatial modes of the *read* and *write* beams, respectively. Even though we have not taken into account the complete description in terms of spatial modes as in the previous chapter, mode matching is still important.

As model for the magnetic fields we take a gradient field B_z along the z axis with its zero at $z = 0$, which is taken as the center of the atomic ensemble with length of L as well. The parameters for the $|g\rangle$ and $|s\rangle$ states are then given by

$$a_g = 2\pi K m_g \left(\frac{z}{L} \right) \qquad (4.27\text{a})$$

$$a_s = 2\pi K m_s \left(\frac{z}{L} \right) \qquad (4.27\text{b})$$

The constant K is computed by

$$K = \frac{\mu_B g_g B_z L}{h}. \qquad (4.28)$$

Therefore the product $K m_F$ gives an estimate for the inhomogeneous broadening of the magnetic field.

In addition a homogenous bias field B_{bias} can be added. This is important when considering the second order differential Zeeman-shift between the $|F = 1, m_F = -1\rangle$ and $|F = 2, m_F = 1\rangle$ states which is [119]

$$\Delta \nu_{gs} \approx 431.359 \text{ Hz/G}^2 (B - B_0)^2, \qquad (4.29)$$

where the constant B_0 is $B_0 \approx 3.229$. Since this pair of states is in first order magnetic field insensitive, the second order needs to be considered for the simulation of the dephasing. Due to our selection of polarizations it can be neglected compared to the first order shift for other sets of pair.[2]

In order to use the probability function $p_{12}^{th}(t)$ for the prediction of the decay of the cross correlation function $g_{1,2}$ we scale the probability function p_{12} by a factor ξ according to

$$\tilde{p}_{12}(t) = \xi p_{12}^{th}(t) + 1. \qquad (4.30)$$

The scaling factor ξ is found by comparison with the experimental data of $g_{1,2}$ at time delay $\Delta t = 0$.

---

[2]By proper selection of polarization the pair $|F = 1, m_F = 0\rangle$ and $|F = 2, m_F = 0\rangle$ can be addressed. It is insensitive in first order to the magnetic field as well.
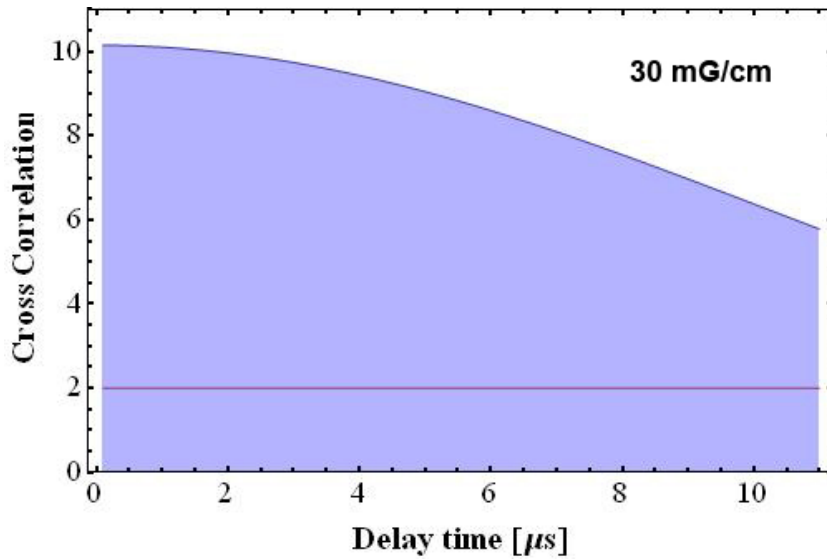
Figure 4.1: Simulation for a Cesium ensemble after the release from MOT: The atoms are initially in the $|F = 4\rangle$ state and all Zeeman sublevels are equally distributed. The *write* and the *read* light have orthogonal linear polarizations. The magnetic field gradient is 30 mG/cm.

At first we have simulated the dephasing of Cesium width the experimental conditions given in [66]. The first reason was the testing of the code by comparison with the results given in the reference. Secondly we want to be able to compare the properties between this atomic species and ^{87}Rubidium [1]. A horizontal line at a cross correlation of 2 indicates the classical limit.

The simulations in figures (4.1), (4.2),(4.3)) treat a Cesium cloud released from a MOT with $|g\rangle = |F = 4\rangle$. Despite a Zeeman shift for a single sublevel which is half of that of ^{87}Rubidium the magnetic field gradient can be larger in Rubidium. The observation time of the non-classical light is comparable (fig. (4.6)). The origin can be seen in the larger manifold of Zeeman sublevels in Cesium. The dephasing of the nine components is faster to the five components of the $|F = 2\rangle$ states in ^{87}Rubidium. As shown in fig. (4.4) a gradient comparable to the Cesium experiments shows a longer observation time.

The data measured in our experiment (chapter 6) matches best to figure (4.7) with a gradient of 40 mG/cm which corresponds to a gradient of about 15 mG across the ensemble. A homogenous magnetic bias field applied in addition to a gradient field does not lead to a faster dephasing (figure (4.9)). In figure (4.10) the situation is simulated if the quadrupole field of the MOT is not switched off during the experiment. Non-classical correlations could only be observed for several hundred of nanoseconds. In this simulation we also show the situation if the *read* pulse is applied during the *write* pulse. The pulse width which we considered is 100 ns.

Then we simulated the situation in an optical dipole trap with parameters as the set-

---
[1]With exception of one plot the read out during the write pulse has not been plotted.
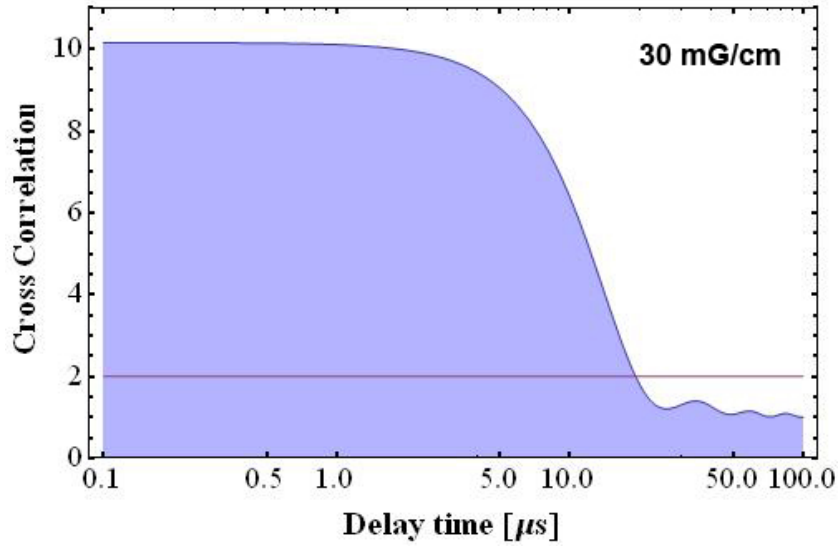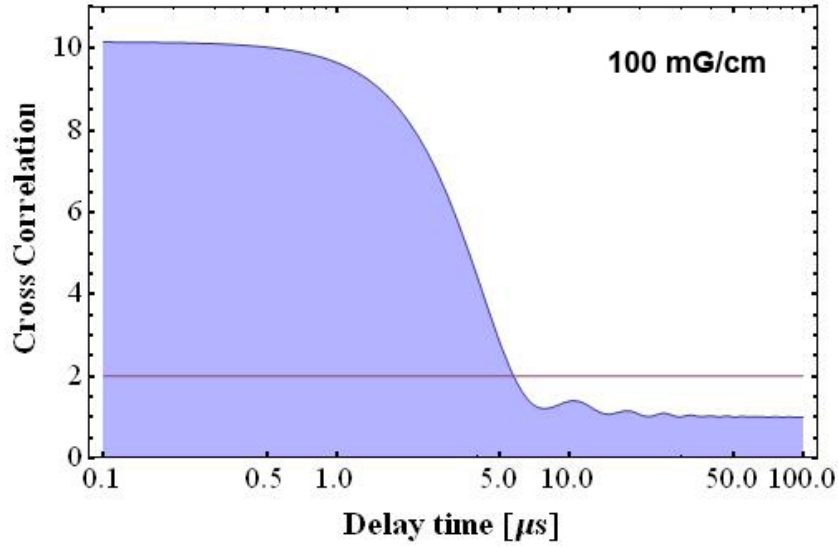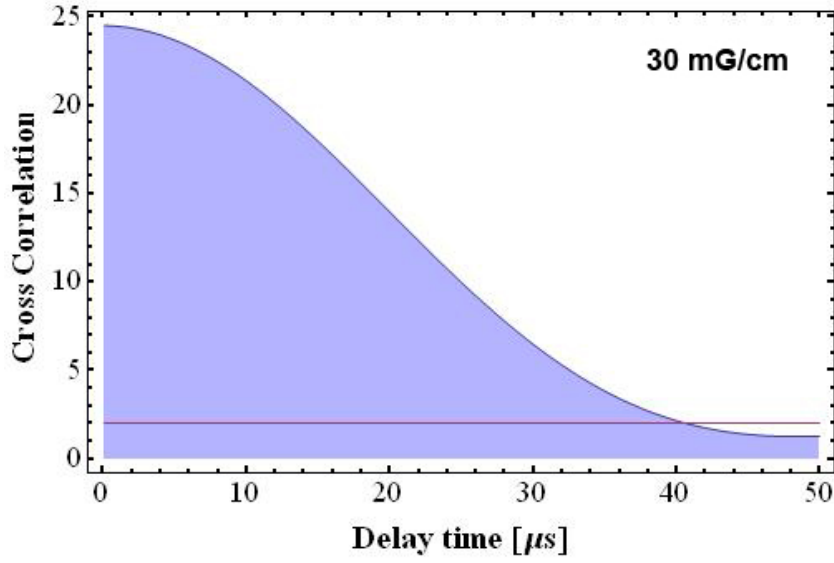
Figure 4.2: Simulation in a semi-logarithmic plot for a Cesium ensemble after the release from MOT: The atoms are initially in the $|F = 4\rangle$ state and all Zeeman sublevels are equally distributed. The *write* and the *read* light have orthogonal linear polarizations. The magnetic field gradient is 30 mG/cm.
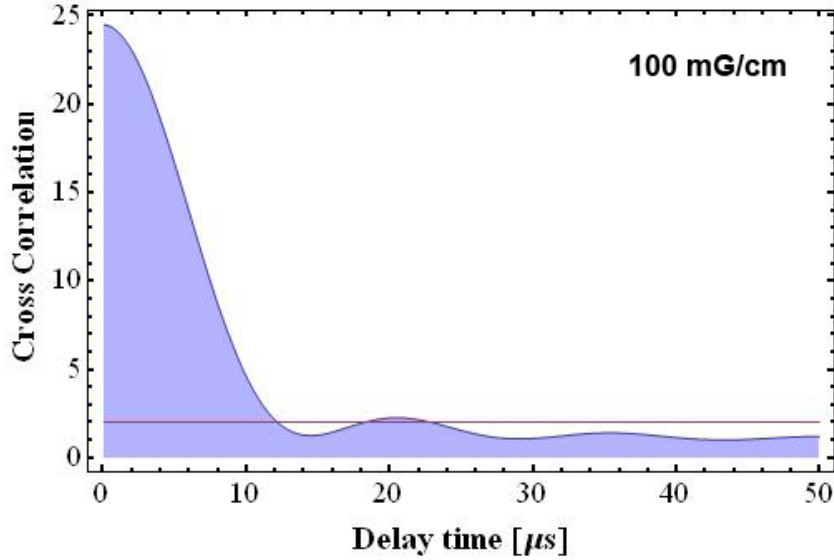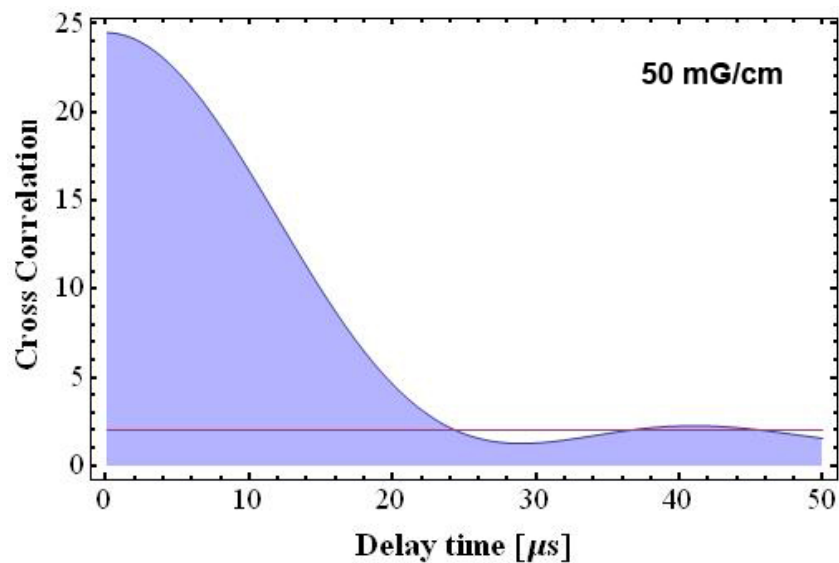

Figure 4.3: Simulation for a Cesium ensemble after the release from MOT: The atoms are initially in the $|F = 4\rangle$ state and all Zeeman sublevels are equally distributed. The *write* and the *read* light have orthogonal linear polarizations. The magnetic field gradient is 100 mG/cm.
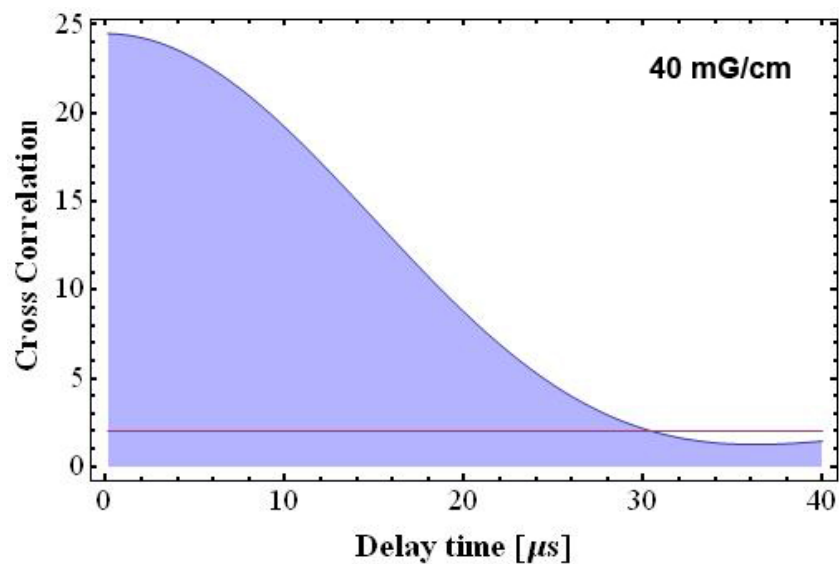
Figure 4.4: Simulation for a Rubidium ensemble after the release from MOT: The atoms are initially in the $|F = 2\rangle$ state and all Zeeman sublevels are equally distributed. The *write* and the *read* light have orthogonal linear polarizations. The magnetic field gradient is 30 mG/cm.
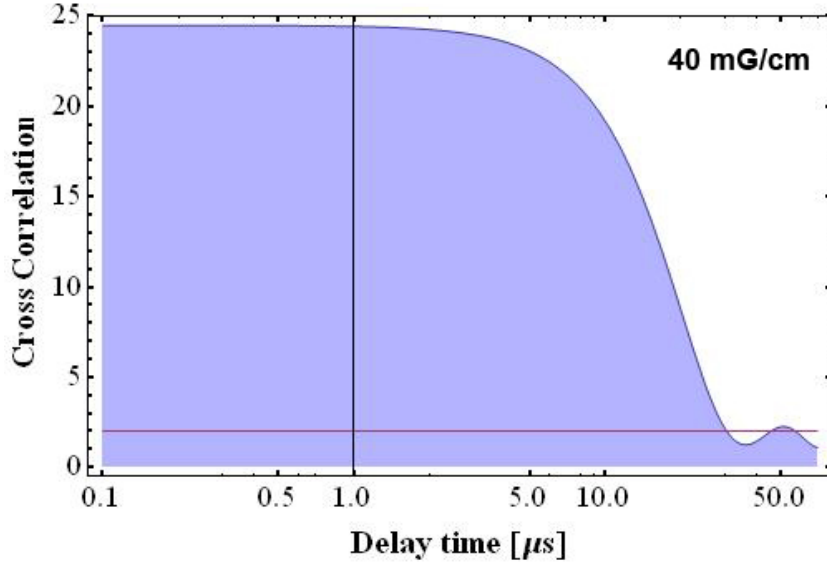

Figure 4.5: Simulation for a Rubidium ensemble after the release from MOT: The atoms are initially in the $|F = 2\rangle$ state and all Zeeman sublevels are equally distributed. The *write* and the *read* light have orthogonal linear polarizations. The magnetic field gradient is 100 mG/cm.

Figure 4.6: Simulation for a Rubidium ensemble after the release from MOT: The atoms are initially in the $|F = 2\rangle$ state and all Zeeman sublevels are equally distributed. The *write* and the *read* light have orthogonal linear polarizations. The magnetic field gradient is 50 mG/cm.
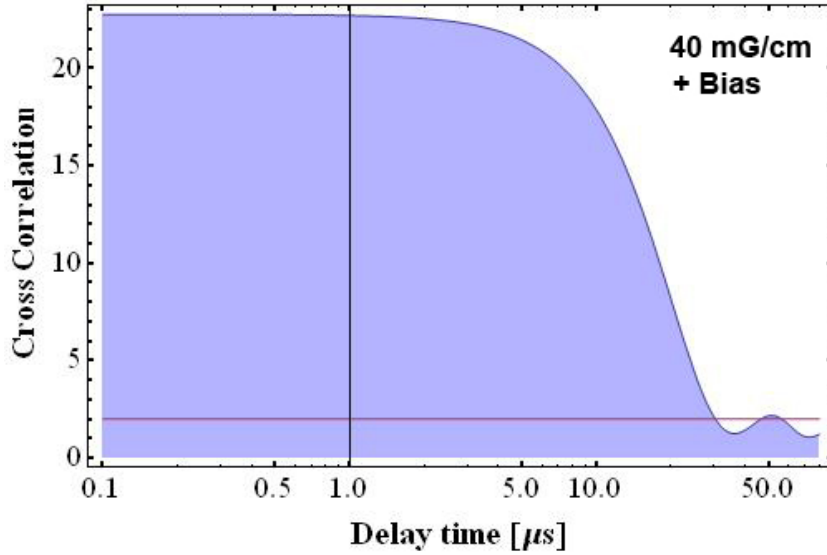

Figure 4.7: Simulation for a Rubidium ensemble after the release from MOT: The atoms are initially in the $|F = 2\rangle$ state and all Zeeman sublevels are equally distributed. The *write* and the *read* light have orthogonal linear polarizations. The magnetic field gradient is 40 mG/cm.
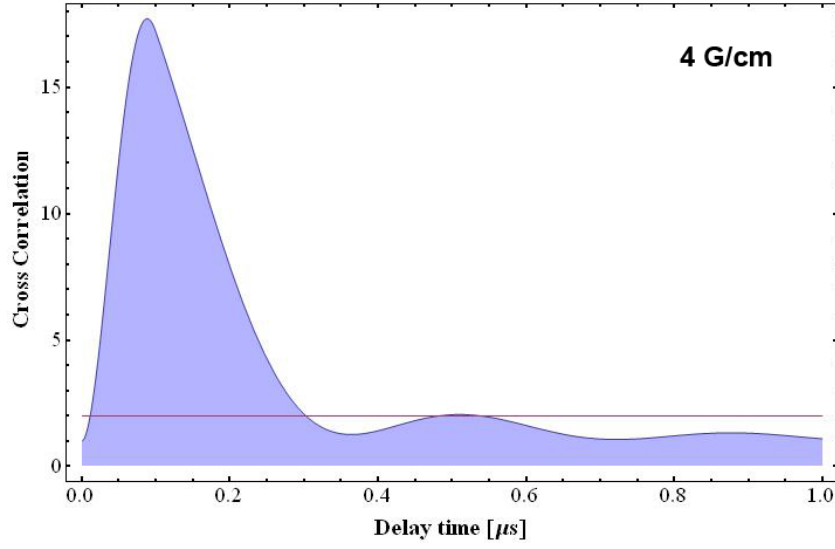
Figure 4.8: Simulation for a Rubidium ensemble after the release from MOT: The atoms are initially in the $|F = 2\rangle$ state and all Zeeman sublevels are equally distributed. The *write* and the *read* light have orthogonal linear polarizations. The magnetic field gradient is 40 mG/cm.

Figure 4.9: Simulation for a Rubidium ensemble after the release from MOT: The atoms are initially in the $|F = 2\rangle$ state and all Zeeman sublevels are equally distributed. The *write* and the *read* light have orthogonal linear polarizations. The magnetic field gradient is 40 mG/cm. The homogenous magnetic bias field is taken to be 3.23 Gauss.

Figure 4.10: Simulation for a Rubidium ensemble after the release from MOT: The atoms are initially in the $|F = 2\rangle$ state and all Zeeman sublevels are equally distributed. The *write* and the *read* light have orthogonal linear polarizations. The magnetic field gradient of 4 G/cm simulates the magnetic quadrupole field of the MOT. The increase in correlations depicts the situation when *read* light is applied during the *write* pulse.
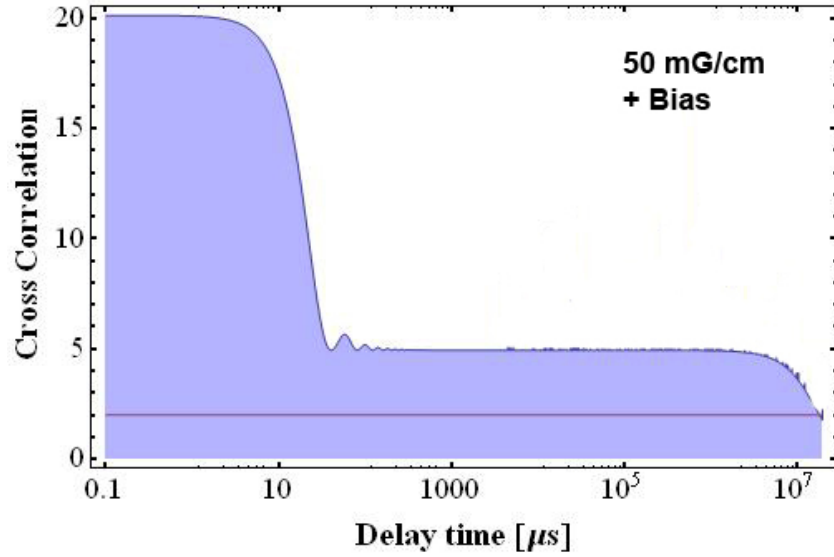

Figure 4.11: Simulation for the atoms in the ODT: The atoms are initially in the $|F = 1\rangle$ state and all Zeeman sublevels are equally distributed. The *write* and the *read* light have orthogonal circular polarizations. The magnetic field gradient is 50 mG/cm. The homogenous magnetic bias field is taken to be 3.23 Gauss. It is oriented along the trapping beam axis.

up which is described in chapter 7. Since the life time of atoms in the $|F = 1\rangle$ in an ODT is significantly longer, this state is selected as initial state $|g\rangle$. The polarization
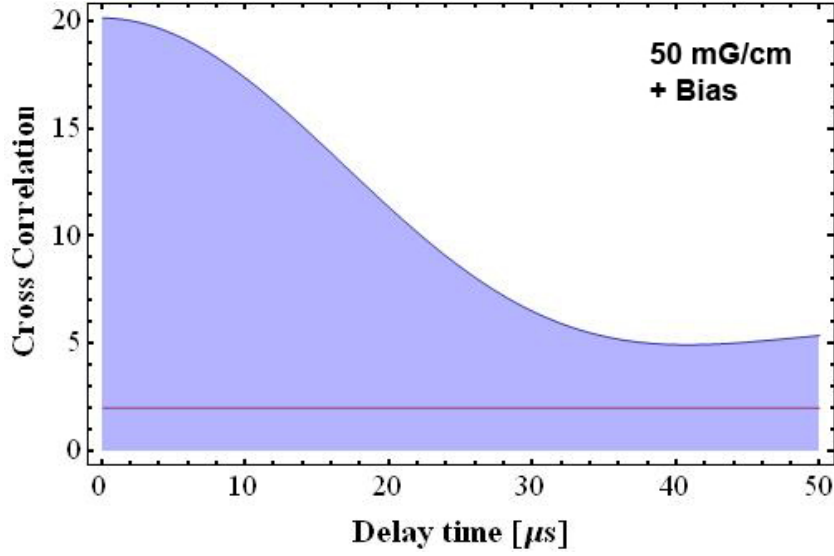
Figure 4.12: Simulation for the atoms in the ODT: The atoms are initially in the $|F = 1\rangle$ state and all Zeeman sublevels are equally distributed. The *write* and the *read* light have orthogonal circular polarizations. The magnetic field gradient is 50 mG/cm. The homogenous magnetic bias field is taken to be 3.23 Gauss. It is oriented along the trapping beam axis.
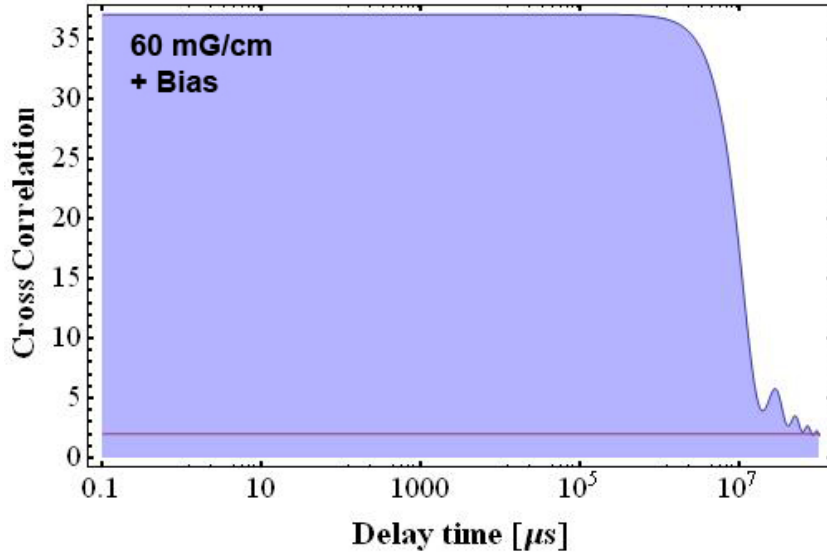

Figure 4.13: Simulation for the atoms in the ODT: The atoms are initially in the $|F = 1, m_F = -1\rangle$ state. The *write* and the *read* light have orthogonal circular polarizations. The magnetic field gradient is 60 mG/cm. The homogenous magnetic bias field is taken to be 3.23 Gauss. It is oriented along the trapping beam axis.
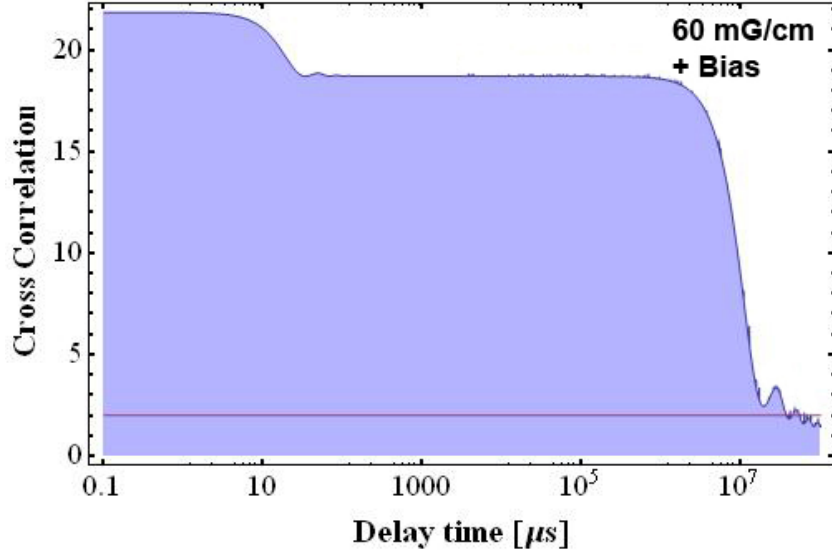
Figure 4.14: Simulation for the atoms in the ODT: Simulation for the atoms in the ODT: The atoms are initially in the $|F = 1\rangle$ state and all Zeeman sublevels are populated 0.7 to 0.15 to 0.15 . The *write* and the *read* light have orthogonal circular polarizations. The magnetic field gradient is 60 mG/cm. The homogenous magnetic bias field is taken to be 3.23 Gauss. It is oriented along the trapping beam axis.

of the *write* and *read* light is chosen as circular as well as the detected Raman light in order to address the clock states introduced above. Figure (4.11) shows the expected dephasing. Two time constants can be observed. The fast one is due to the non-clock state components which dephase similar than in the computations with the ensembles released from a MOT. The slow decay is due to the clock states whose dephasing is only affected by the second order Zeeman shift. An observation time of several seconds is predicted by this model. In figures (4.13) and (4.14) the effect of optical pumping with a complete and partially preparation of a single Zeeman state ($|F = 1, m_F = -1\rangle$) is simulated. In case of a perfect preparation only one time constant is observed and the signal, i.e. the degree of the cross correlation, is higher, as long as the number of atoms does not change. If the preparation is not optical two time constants can be observed and the ratio between both components depend on the distribution of the population of the Zeeman sublevels and the number and strength of the transitions contributing to the signal.

4.5.3 Traps for atomic ensembles

When considering the use of thermal atoms, it is quite clear that the Rubidium atoms must be embedded in a glass cell in order to prevent the Rubidium vapor from mixing with the air. The optical access is provided by such a solution as well. In the context of cold atoms, it is also obvious for the reader familiar with quantum gases, that a vacuum chamber is needed. Since the cold atoms are prepared from

a thermal source by laser cooling, during this process the atoms are confined in a trap. Usually a magneto-optical trap (MOT) [120] is employed for this process of preparation of cold atoms. This is not the issue which should be discussed here. The key question is if the cold atomic ensemble should be trapped during the experiment, i.e. during the storage. The somewhat "straight forward" answer to this is: yes, of course. At a second glance one should have doubts, since every trapping method relies on the interaction of the ensemble with the environment. Let us continue to consider the MOT as preparation tool. During the experiment we need have to prepare in a certain ground state and during storage the atoms have to maintain their states. This is one reason, why we have to switch off the cooling laser light during the storage. The other one is that are working on a single photon level and thus we are sensitive to strong light. This means that the confinement of the atoms is gone as well. If one keeps the magnetic field on as well, we have seen in section (4.5.2), that this affects the storage as well. In the subsequent sections we see that any kind of nowadays used trap will affect the storage. The logical consequence seems to be that one uses the atomic ensemble during free expansion after the MOT phase. This approach provides atomic ensembles for approximately 8 ms, then the atomic clouds has expanded significantly and the remaining density is to low to continue. This limit (it is not the only one) is sufficient to conduct proof-of-principle experiments, for example [71] [77] [78], but it is not sufficient for practical implementation of quantum communication over continental or even intercontinental distances. In order to achieve storage times with cold atoms in the necessary regime of seconds one needs to add a confinement to the atoms. For this reason it is necessary to understand the dephasing/decoherence mechanisms in the traps, design one suited for the purpose of a quantum memory and employ techniques to compensate the remaining influences.

4.5.4 Dephasing of Spin Wave Induced by Atomic Random Motion.

We have seen in chapter 3 that every atom carries a phase in this collective state. We have treated the effect of interactions with magnetic fields. By selecting ultra cold atoms we have reduced the influence of loss of atoms from the interaction region. Here we want to consider the effect on the stored spin wave if the atoms move due to thermal motion within the ensemble. Assume the j-th atom moves to $\mathbf{r}_j(\delta t) = \mathbf{r}_j + \mathbf{v}_j \delta t$ after a storage time of δt. The collective state or spin wave (SW) freely evolves according to

$$|\psi_{\mathrm{D}}\rangle = \frac{1}{\sqrt{N}} \sum_j e^{i\Delta\mathbf{k}\cdot\mathbf{r}_j(\delta t)}|g...s_j...g\rangle, \qquad (4.31)$$

where we have neglected the effect of magnetic field for simplicity. The retrieval efficiency is given by the overlap between the original SW and the perturbed one,

$$\gamma(\delta t) \sim |\langle\psi|\psi_{\mathrm{D}}\rangle|^2 = |\frac{1}{N}\sum_j e^{i\Delta\mathbf{k}\cdot\mathbf{v}_j\delta t}|^2 = |\int f(\mathbf{v})e^{i\Delta\mathbf{k}\cdot\mathbf{v}\delta t}|^2 d\mathbf{v} \qquad (4.32)$$

with $f(\mathbf{v})$ the velocity distribution. In the temperature regime we are considering it is reasonable to assume $f(\mathbf{v}) \sim e^{-\frac{m\mathbf{v}^2}{2k_B T}}$ is a Boltzmann distribution at temperature T. Integrating over all possible velocity, we obtain $\gamma(\delta t) \sim e^{-\delta t^2/\tau_D^2}$, with the lifetime $\tau_D = \frac{1}{\Delta k v_s}$ and $v_s = \sqrt{\frac{k_B T}{m}}$ as average speed in one dimension. This diffusion is due to spatial motion of the atoms if we neglect gravity.

4.5.5 Differential Light Shift

The application of an optical dipole trap (ODT) (5.3) for the confinement of the atoms adds another dephasing mechanism. The potentials for the ground states which we use for the storage are slightly different and cause therefore in an unequal time evolution of the states $|g\rangle$ and $|s\rangle$

The so-called differential light shift δ_0 between the two hyperfine ground states of Rubidium is given by:

$$\hbar\delta_0 = U_0(\Delta_{eff}) - U_0(\Delta_{eff} + \omega_{hfs}), \tag{4.33}$$

where Δ_{eff} labels the effective detuning of the trapping light $\Delta_{eff} = \left(\frac{2}{\Delta_{D2}} + \frac{1}{\Delta_{D1}}\right)$ from D_2 and D_1 line. The maximum potential depth U_0 will be computed later (5.3). In our considerations we assume a depth of $U_0 = k_B \times 0.6$ mK. The ground hyperfine splitting in ^{87}Rb is $\omega_{hfs} = 2\pi \cdot 6.8$ GHz. For a wavelength of 1030 nm the hyperfine splitting is much smaller than the effective detuning $\omega_{hfs} \ll \Delta_{eff}$. The differential light shift can then be considered as proportional to the maximum light shift U_0, and we can write

$$\hbar U_0 = \eta U_0. \tag{4.34}$$

We introduce a scaling factor $\eta = \omega_{hfs}/\Delta_{eff}$. In figure (4.15) we have plotted the differential light shift between the $\left|5S_{1/2}, F = 1\right\rangle$ and $\left|5S_{1/2}, F = 2\right\rangle$ ground states of ^{87}Rb for a fixed beam waist and a single trapping beam with a wavelength of 1030 nm and for various powers.

In the red-detuned trap the shift for an individual atom is position dependent. The trapped atomic ensemble experiences in the semiclassical limit only an average shift. Let us calculate the average light shift of the two ground state for an ensemble [121]. In a red-detuned trap a hotter atom experiences a lower laser intensity than a cold one. Consequently its averaged differential light shift is smaller. The energy distribution of the atomic ensemble can be described by a three dimensional Boltzmann distribution with the probability density given by

$$p(E) = \frac{E^2}{2(k_B T)^3} \exp\left(-\frac{E}{k_B T}\right). \tag{4.35}$$

The total energy $E = E_{kin} + U$ is the sum of kinetic and potential energy. In a harmonic trap the viral theorem is applicable if $k_B T \ll U_0$. Then the potential energy carries half of the total energy $U = E/2$. The average light shift for a single
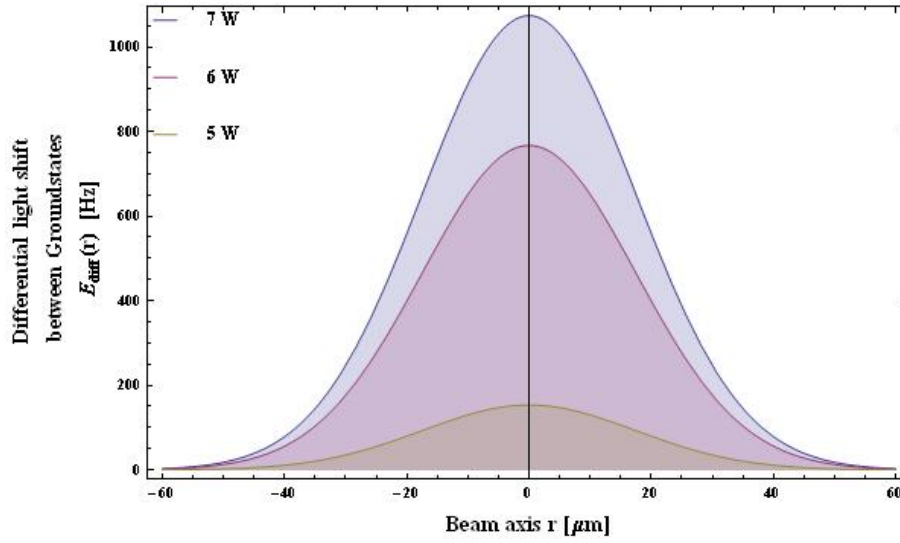
Figure 4.15: Differential light shift between the $F = 1$ and $F = 2$ hyperfine states of the $5S_{1/2}$ ground state for various powers of the trapping laser. The calculations assumes the trap parameters described in section (5.3).

atom with energy E can be computed by:

$$\delta_{ls}(E) = \delta_0 + \frac{\eta E}{2\hbar}, \tag{4.36}$$

where $\delta_0 < 0$ is the maximum shift in the center of the trap. When taking the energy distribution into account the light shift has a distribution according to:

$$\tilde{p}_{ls}(\delta_{ls}) = \frac{K^3}{2}(\delta_{ls} - \delta_0)^2 \exp\left[-K(\delta_{ls} - \delta_0)\right]. \tag{4.37}$$

The temperature dependence is absorbed in the parameter $K = \frac{2\hbar}{\eta k_B T}$. Integration of the product $\tilde{p}_{ls} \cdot \delta_{ls}$ yields the average shift for the ensemble.

For an ensemble at a temperature of 45 μK and a trapping laser power of 7 Watts at a wavelength of 1030 nm the the shift computes to $\approx 2\pi \cdot 1192$ Hz.
The inhomogeneity of the energy shift is comparable to the magnetic gradient field. Then the averaged shift for 7 Watts corresponds to a dephasing time of $\tau \sim 840\ \mu$s.

4.5.6 Cold Collisions

Collisions are affecting the spin wave stored in an atomic ensemble in several ways. They lead to loss of atoms from the ensemble/trap, they can change the internal states of the atoms and they are responsible for the dephasing of the collective state by the diffusion. Thus they are potential source of memory errors which must be considered.

Elastic collisions of ground state atoms:

It is important for thermalization of the ensemble. Especially for the technique of evaporative cooling it is a very important quantity. In ultracold atoms the elastic collisions are dominated by s-wave scattering. This type does not change the internal state of the atoms. For identical bosons the scattering length is given by [122]

$$\sigma_s(k_c) = 2 \cdot \frac{4\pi a_s^2}{1 + k_c^2 a_0}, \tag{4.38}$$

where a_s is the scattering length, a_0 the Bohr radius and k the wavevector of the scattered wave. In the limit $k \to 0$ the scattering cross section is $\sigma_{sc} = 8\pi a_s^2$. The collision rate is given by

$$\Gamma_{coll} = n_0 \sigma_{sc} v, \tag{4.39}$$

where n_0 is the atomic density and v is the average velocity. The scattering length a_s is for ^{87}Rb $a_s \sim 109$ a$_0$ [114]. The average velocity is

$$v = \sqrt{\frac{k_B T}{m}} = 0.11 \frac{\text{m}}{\text{s}}. \tag{4.40}$$

With a peak atomic density of $n_0 \approx 10^{11}\text{cm}^{-3}$ then the collision rate computes to $\Gamma_{sc} \sim 46.6$ s^{-1}. The elastic collisions contribution to the diffusion of atoms of the spinwave from their initial position. At present there is no quantitative model available to describe the effect on the life time.

Collisions with Background gas Due to the ultra-low temperatures of the trapped ensembles collisions of atom with room temperature background gas will lead to a rapid loss of atoms from the trap. According to [123] the loss rate of a trap is given by

$$\Gamma_{BG} \simeq n_{BG} \sigma_{BG} v_{BG}, \tag{4.41}$$

where n_{BG} is the density of the background gas and σ_{BG} is the cross section for the dominant atomic species. In case of water molecules evaporating from the vacuum chamber the cross section is $\sigma_{BG} = 2 \cdot 10^{-18}\text{m}^2$ and in case of ^{87}Rb from the atomic source it is $\sigma_{BG} = 2.5 \cdot 10^{-17}\text{m}^2$ [123]. The operation of a MOT needs a vacuum better than 10^{-9} mbar. In contrast to the other dephasing we can therefore neglect these collisions even though the atomic source in our experiments produces Rubidium vapor with about 100° C. For a storage time of seconds a switched source or double vacuum chamber set-up with a differential pumping stage should be considered [124].

Inelastic ground state collisions

These types change the internal state of the atoms and needs consideration for the lifetime of the spinwave. The lambda system in ^{87}Rubidium which we use consists amongst others of the two hyperfine states $\left|5^2 S_{1/2}, F = 2\right\rangle$ and $\left|5^2 S_{1/2}, F = 1\right\rangle$ as

ground states. Collisions between the atoms during the storage time can change the hyperfine state of the atoms and can therefore lead to memory errors.

Hyperfine changing collisions   In this case the total spin number of the collision system is preserved. The rate is typically in the order of 10^{-11}cm^3/s in a MOT, but in magnetic trap many orders smaller 2.2×10^{-14}cm^3/s [125]. Compared to the other inelastic collisions this process is dominant.

Spin-dipole interactions   There is another type of inelastic collisions where the total spin is not conserved. The rate has been measured for $|F = 2, m_F = 2\rangle$ and $|F = 1, m_F = -1\rangle$ in magnetic traps to $\sim 1 - 2 \times 10^{-15}cm^3/s$ [126].

Collisions with singly excited states

This type of collisions has to be considered if many atoms are excited to the electronically excited state [127]. In thermal atoms this is an important effect [53]. The cross sections for these collisions can be many orders of magnitude larger than the ones in the ground state. They are the dominant loss mechanisms in a MOT. But if the excitation rate[3] during the *write* process is high, then they can occur in this process as well, not only in the loading phase.

Radiative Escape [128]:   When one of two ground state atoms is excited during their approach the potential changes and the atoms are accelerated onto each other. Before the collision the atom is deexcited and a red-shifted photon is emitted. The energy gain is shared between the two collision partners. Multiple absorption and emission processes in one approach lead to the escape of the atoms at the collision. This loss type is mainly present in the MOT and in the loading phase of an optical dipole trap. As long as the detuning of the trapping light of ODT is large it can be neglected during storage.

Fine structure changing collisions   This type of collisions, for example from $P_{3/2} \to P_{1/2}$, is present in a MOT. The gain of kinetic energy for each atom is half of the fine structure energy difference which is sufficient to leave trap. It can happen during the *write* and *read* process as well, but its affect is in current experiments negligible.

Hyperfine state changing spontaneous Raman scattering by trap light The scattering of far-detuned light from the trap laser heats up the ensemble. In

---

[3]The excitation rate of the detected single photons can be nevertheless small, if the detection optics collects only a fraction of the light.

addition it can also change the internal hyperfine state of an atom. An atom can be transferred from state $|F = 2\rangle \rightarrow |F = 1\rangle$. The total scattering rate introduced by the trap light can be decomposed into a part for Rayleigh scattering and a part for Raman scattering according to

$$\Gamma = \Gamma_{Rayleigh} + \Gamma_{Raman}. \tag{4.42}$$

The Kramers-Heisenberg formula [129] which is valid for a small population of the excited state gives the total scattering rate according to

$$\Gamma_{i \rightarrow f} = \frac{\alpha^2 \omega^3 \mathcal{E}_0^2}{3\hbar c} \cdot \left| \sum_{e, \epsilon_{\mathbf{r}}} \frac{\langle f| \, \epsilon_{\mathbf{r}}^* \cdot \mathbf{r} \, |e\rangle \, \langle e| \, \epsilon \cdot r \, |f\rangle}{\omega_e - \omega} + \frac{\langle f| \, \epsilon^* \cdot \mathbf{r} \, |e\rangle \, \langle e| \, \epsilon_r \cdot \mathbf{r} \, |f\rangle}{\omega_e + \omega} \right|^2, \tag{4.43}$$

where $\epsilon_{\mathbf{r}}$ is the polarization of the radiated light. The Rayleigh part is $\Gamma_{Rayleigh} = \Gamma_{i \rightarrow i}$ and the Raman part the summation over the remaining states f. A calculation shows that [130] for alkali atoms in a far red-detuned trap the ratio scales as

$$\frac{\Gamma_{Raman}}{\Gamma_{Rayleigh}} \approx \frac{8}{9} \left(\frac{\Delta_{fs} \omega_{trap}}{\omega_0^2} \right)^2 \tag{4.44}$$

For Rubidium and an assumed trapping frequency of 1030 nm the ratio is ~ 0.00018. This means that most of the scattering events lead to Rayleigh scattering. The inclusion of the hyperfine splitting changes the result only by a very small amount.

4.6 Extension of Memory Time: Concepts

From our considerations on the requirements and decoherence processes we derive a design strategy for a long-life time quantum memory.

Optical Density We have seen that the retrieve efficiency depends on the optical depth, which means in free space a large number of atoms.
A large number of atoms does not necessarily mean a high atomic density. More important is, within the geometric conditions of mode matching, the number of atoms in the interaction region. The appropriate quantity we want to maximize is the optical density with is for resonant light $\mathcal{D} = \sigma_0 \tilde{n}$. The cross section for resonant light is $\sigma_0 = 3\lambda^2/2\pi$ and $\tilde{n}$ is the atomic density integrated along the propagation direction of the light. That means that one can balance the effects of a high atomic density which has a higher collision rate as disadvantage and a bigger ensemble length which more difficult to control and protect from external influences. We have seen as well that a large optical density improves the retrieve efficiency as well. The drawback of a high optical density is that optical pumping becomes more difficult. In order to reduce the absorption of *write* light its detuning from the atomic resonance has to be increased. The power of the *read* light must be increased as well in order to make the ensemble transparent by EIT during the retrieval.
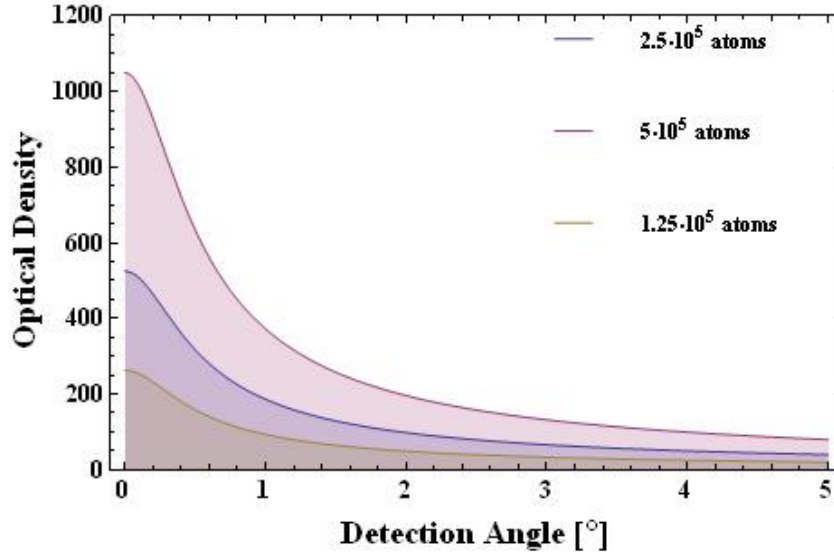
Figure 4.16: Computed optical density of the optical dipole trap set-up described in chapter (5) on the D_1 line: The detection angle is given with respect to the symmetry axis of the elongated ensemble. The parameters are as in figure (5.16).

Temperature A low temperature reduces the diffusion of atoms out of the interaction region. Further on it reduces the collisions between the atoms. A small velocity means a small Doppler shift and all atoms experience the same Rabi frequencies. Lower temperatures reduce the diffusion of the spin-wave which dominates the dephasing mechanism when the magnetic-field effects are reduced. When trapping the atomic ensemble various heating processes have to be taken into account, like scattering of trap light.

Confinement in a Red-detuned Optical Dipole trap A red-detuned optical dipole trap can provide the necessary confinement for the atomic ensemble. The light is detuned far from the atomic transitions and can therefore be filtere out well. By adjusting the intensity of the light or changing the waist of the trapping beam the density of the atoms can be increased.
The drawback is the differential light shift which introduces a dephasing between the hyperfine ground states. Since this shift depends on the intensity of the trap light, the cooling of atoms enables the reduction of the trap depth and subsequently of the differently light shift.

First-order Magnetic Field Insensitive States The effect of inhomogeneous magnetic fields is dominant is previous experimental set-ups. ^{87}Rb offers sets of state which are first-order insensitive to magnetic fields. For simplicity we will use the expression "clock states" to describe them. The use of this term is not unambiguous. It describes as well the $|F, m_F = 0\rangle$ and $|F', m_F = 0\rangle$ states which are usually used for the atomic clocks as the combination of $|1, m_F = -1\rangle$ and $|2, m_F = +1\rangle$ states
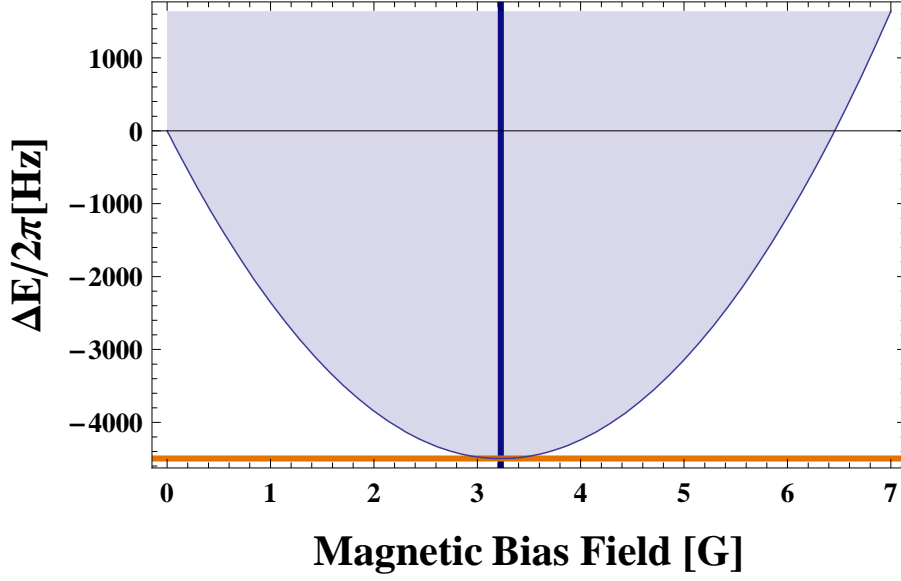
Figure 4.17: Differential energy of the $|F = 1, m_F = -1\rangle$ and $|F = 2, m_F = 1\rangle$ clock states of Rubidium 87. The minimum of the parabola is at a magnetic field of $B_0 = 3.228917$ Gauss. There the sensitivity to magnetic field variations is smallest. The overall energy difference compared to the free-space hyperfine splitting has no significant influence on the life time.

of Rubidium 87. We will make use of the latter states since their second order shift due to a magnetic field is slightly lower. The energy shift of the Zeeman manifold of the ground states $|5S_{1/2}, F = 2\rangle$ and $|5S_{1/2}, F = 1\rangle$ due to the interaction with an intermediate magnetic field B can be described by the Breit-Rabi Formula:

$$E_{|J=1/2,m_J,I,m_i\rangle} = -\frac{\Delta E_{hfs}}{2(2I+1)} + g_I \mu_B m B \pm \frac{\Delta E_{hfs}}{2} \left(1 + \frac{4mx}{2I+1} + x^2\right)^{1/2}. \quad (4.45)$$

ΔE_{hfs} denotes the energy of the hyperfine splitting, I the nuclear spin, μ_B is the Bohr magneton, g_I is the nuclear g-factor, g_J labels the Landé factor for the quantum number J, m is the mass and x is given by the expression

$$x = \frac{(g_J - g_I)\mu_B B}{\Delta E_{hfs}}. \quad (4.46)$$

For the $|F = 2, m_F = +1\rangle$ and the $|F = 1, m_F = -1\rangle$ the first order (linear) Zeeman shift vanishes. Then only the second order contribution remains for the so-called clock transition. The energy difference due to an external magnetic field between the states $|F = 1, m_F = -1\rangle$ and $|F = 2, m_F = +1\rangle$ is

$$\Delta\omega(\mathbf{r}) \approx 429 \, \frac{\text{Hz}}{\text{G}^2} \, (B(\vec{r}) - 3.23 \text{ G})^2 + \text{const.} \quad (4.47)$$

Thus by application of a homogeneous magnetic bias field of $B_0 = 3.228$ G, the sensitivity of the time evolution of the spinwave to spatial inhomogeneities is reduced

and becomes first order insensitive to temporal fluctuation of the field.

From the Breit-Rabi formula one can derive the second-order Zeeman shift for the $m_F = 0$ pair of states which have a vanishing first order shift as well. The quadratic dependence of the energy shift in case of weak magnetic fields is given by [114]:

$$\Delta\omega_{shift} = \frac{(g_J - g_I)^2 \mu_B^2}{2\hbar \Delta E_{hfs}} B^2 \sim 2\pi \cdot 575.15 \text{ Hz/G}^2. \tag{4.48}$$

It is indeed larger than for the other set of states.

4.6.1 Compensation Laser

The main reason for the dephasing due to the light shift is that the two ground states experience a different trapping potential. One way to overcome that is the use of a compensation laser [131]. It should generate an "opposite potential" without lifting the trapping. The additional light with power $I'(\mathbf{r})$ and a frequency in the center of the hyperfine splitting reduces the deviation of the hyperfine frequency due the atom light-interaction $\tilde{\omega}_{HF}(\mathbf{r})$ from the free space frequency ω_{HF} according to

$$\tilde{\omega_{HF}}(\mathbf{r}) - \omega_{HF} = \frac{\Pi c^2 \gamma \omega_{HF}}{\omega_0^3} \left[\frac{I(\mathbf{r})}{\Delta_{eff} - \left(\frac{\omega_{HF}}{2}\right)^2} - \frac{I'(\mathbf{r})}{\left(\frac{\omega_{HF}}{2}\right)^2} \right], \tag{4.49}$$

where $\Delta_{eff} = (\delta_{2,F=1} + \delta_{2,F=2})/2$ effective detuning with respect to the center of the hyperfine splitting. In case the compensation beam is spatially mode-matched, i.e. $I'(\mathbf{r}) = \eta \times I(\mathbf{r})$ then the ratio of powers η is given by

$$\eta \approx \left(\frac{\omega_{HF}}{2\Delta_{eff}}\right)^2. \tag{4.50}$$

For the set-up described in chapter (5) the intensity necessary is in the order of hundred nanoWatts.

4.6.2 Blue-detuned Trap

A second approach is to avoid a differential light shift of the two hyperfine ground states by using a blue-detuned trap. The potential minimum is not in the maximum of intensity but at minimum intensity of the trapping light. One cannot use a Gaussian TEM$_{00}$ mode but a higher order Languerre-Gaussian beam, LG$_{01}$ [132][133]. This is a circular beam with a minimum in its center.

Let us assume for the Languerre gaussian beam a light wall of waist w [129]. The potential of the wall is given by

$$U(x) = U_0 e^{(-x^2/8w^2)}. \tag{4.51}$$

The resulting phase shift on an atoms during the collision with the wall can be computed by

$$\Delta\Phi = \frac{2}{\hbar} \int_{\infty}^{x_t} \frac{U(x)dx}{\sqrt{\frac{2}{M}[U_i - U(x)]}} = U_i t_{ph}/\hbar. \tag{4.52}$$

The integration is carried up to the classical turning point x_t, where the condition $U(x_t) = U_i$ is satisfied. It is important to note that this equation defines the dephasing time t_{ph}. The traversing time at the wall is $t_{tr} = w/v$. An atom confined by two walls separated by distance d experiences an average trapping potential due to thermal motion according to [129]

$$\langle U \rangle_{th} \sim \frac{t_{ph}}{t_{tr}} \frac{w}{d} k_B T. \tag{4.53}$$

One can show that $t_{ph}/t_{tr} \sim 0.4$ for $U_0/U_i > 5$. Then an optimal trap configuration is given if the separation between the walls is much larger than their waists $d \gg w$ and in addition $mgw \ll k_B T$ is fulfilled. Thus in a blue-detuned trap the average trapping potential energy which is felt by the atoms can be smaller than their thermal energy, which means that the average differential light shift is negligible.

More complex and powerful approaches are the employment of a box from light sheets [134] or using axicons with blue-detuned light.

4.6.3 Optical Lattice

An important contribution to irreversible dephasing is the diffusion of atoms. The construction of a very tight optical traps is possible [121], but comes with the disadvantages of a smaller volume which means less atoms and a more difficult to collect the light emitted from the small ensemble. A more feasible alternative is the use of an optical lattice. The spacing between the potential minima is half of the wavelength of the trapping beam, i.e. in the order of several hundreds of nanometers. This significantly restricts the motion of atoms and if the potential is deep enough the tunnelling between the lattice sites can be sufficiently suppressed.

4.6.4 Cavity

The retrieval can be increased by defining a spatial mode. The use of a cavity can increase the cooperativity C of the ensemble in the *read* out. This is equivalent to an increased optical depth. The retrieval efficiency is independent of the pulse shape of the *read* light and is equal to $C/(1 + C)$ [117].

The cooperativity is connected to the finesse F of the cavity in case of a single atom by

$$C = \frac{F}{2\pi} \frac{\sigma_0}{A}, \tag{4.54}$$

where σ_0 is the atomic absorption cross section and the beam cross section A in the cavity can be computed by $A = \frac{\pi}{4} w_0^2$. The finesse does not to be very high since it not necessary to achieve the challenging strong coupling regime. Nevertheless the use of a cavity increases the complexity of any experimental set-up. It must support the two different frequencies and it must be stabilized. The *write* and *read* light is in the same mode as the signal light which requires that they must be separated before the detection. The distortion of the signal outputs should be minimal in order to achieve a high coupling efficiency to the single photon detectors. The cavity must of course be aligned to the atomic ensemble which can tedious.

Chapter 5

Technology and Procedures

The work which is described in the chapters 6 and 7 is based on three experimental set-ups: a single-MOT set-up, a double-MOT set-up and an optical dipole trap set-up. As atomic ensembles we use ultracold, dilute atomic gas clouds of Rubidium 87. In order to prepare these ensembles we use magneto-optical traps (MOT). By means of laser cooling with a spatially dependent friction force ultracold ensembles of dilute gases[1] are prepared in an ultra-high vacuum vessel. Nowadays the MOT is a standard technology in the research area of ultra-cold quantum gases. For its working principle we refer to textbooks, for example [120].

5.1   Single MOT Set-Up

In figure (5.1) the schematic experimental set-up is outlined. The core of the system is an ultra-high vacuum chamber made from stainless steel. The vacuum is necessary to avoid collisions of thermal gas particles with the cold atomic ensemble and thus removing them from our trap. The inner core of the chamber is a six-way cross with CF-40 Conflat flanges. In one plane four CF-16 flanges arranged as cross tilted by 45 degrees with respect to cross of CF-40 ports. At all flanges in this plane viewports of quartz glass are mounted, i.e. four CF-40 and four CF-16. Two of the latter ones, which we use for shining in the *write* and *read* beams have a broadband anti-reflection coating. On top of this inner core a six-way cross with CF-63 flanges is attached. Connected to this are the ion-getter pump (25 l) [2], a titanium sublimation pump[3], an ion gauge, a valve and three Rubidium dispensers which serve as source of atoms. On top of the cross a CF-63 viewport is mounted which serves in connection with the CF-40 viewport on the bottom side of the core as optical axis for a pair of MOT-beams. A vacuum pressure of $\sim 1 \times 10^{-10}$ mbar is achieved if the dispensers

---

[1]Since laser cooling requires a closed transition the gases are mostly alkali atoms. Molecules are produced from these ensembles by more advanced methods.
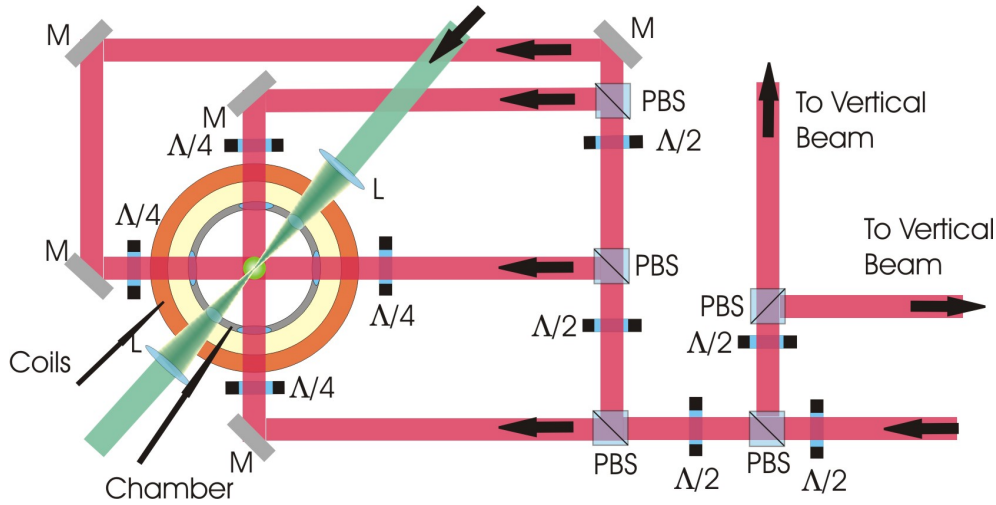[2]Thermionics PS-100
[3]Varian TSP

Figure 5.1: Single-MOT set-up: The red beams are the cooling beams of the MOT. Two of them are directed such that they counter-propagate in the axis perpendicular to the sketching plane and intersect the the others in center of the chamber (after two additional quarter wave plates). By the adjustment of the halfwave plates the intensity balance between the beams can be adjusted. The quarterwave plates turn the linear polarized light into circular polarized. The orange ringe indicates one of the coils for the quadrupole field. The green beam shows the axis where the *write* and *read* beams are focused and directed onto the atoms.

are off. In order to get a dense and large trapped atom cloud the configuration of six independent cooling beams was preferred over a three beam retro-reflected design. The beams intersect in the center of the core chamber which is also the center of the magnetic quadrupole field. Each of the cooling beams has a one inch diameter. The two coils in Anti-Helmholtz configuration with ten windings each are directly glued on the core chamber.   For reasons of stability and smaller currents we have glued 2 times 10 turns of copper wire ($\varnothing$ 2 mm) on the steel tubes to the two vertical CF-40 flanges with a separation of about 5 cm. At approximately 8 Amperes the gradient of the magnetic field is 10 G/cm.   The usual operation current is 4.85 A. A low noise DC current source provides the current [4]. The control of the current by connecting its analog input to a computer controlled analog-out card is not fast enough for switching the coils within some tens of microseconds. A home-built switch from our electronics workshop can switch off the small inductive load of our coils within 30 μs by a TTL signal. It can switch up to 60 Amperes with an inductive load of 120 μH.

Three sets of coils in Helmholtz configuration form a cube of approximately 50 $\times$ 50 $\times$ 50 cm^3. With currents of up to 1.7 A one can compensate the residual magnetic field to a few tens of milliGauss [5].

For the cooling beams the D_2 line of ^{87}Rb at 780 nm is used, since it has a higher efficiency compared to the D_1 line. A 500 mW high power external cavity diode

---
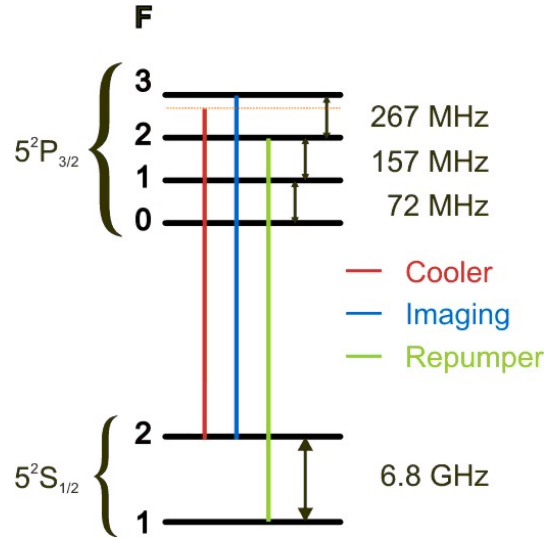
[4] Agilent 6573 A

[5] Agilent 6612C

Figure 5.2: Level scheme of the D_2 line of ^{87} Rubidium at 780 nm: The transitions for the cooler, repumper and imaging beams.

laser in Littrow configuration has been used for the cooling light, but it turned out as not very reliable. Then a new 1 W external cavity diode laser [6] was installed and its power divided and fiber coupled to two experimental set-ups. The laser is FM-locked [135] with Doppler free saturation spectroscopy on the Rubidium transition. The lock point is chosen such that after passing an acousto-optical modulator (AOM) [7] the cooling light is 20 MHz red-detuned from the $F = 2 \rightarrow F' = 3$ of the D_2 line. After the AOM used for fast switching of the light, the beam passes a telescope with a power of typically 45 mW. Before the telescope the repumper light is overlapped by a polarized beam splitter (PBS) with the cooling beam. Thus only one telescope for expanding both beams is needed. The repumper laser is a commercially available device[8]. It is locked in the same way as the cooler laser, but to a different transition, such that the light after an AOM [9] is resonant with the $F = 1 \rightarrow F' = 2$ transition. Before the telescope its intensity is typically 20 mW.

The lasers[4] for the *write* and *read* light are working at a wavelength of 795 nm, the D_1 line. The frequency of the *write* light is 10 MHz blue detuned to the $F = 2 \rightarrow F' = 2$ transition. The *read* light is resonant with the transition $F = 1 \rightarrow F' = 2$. Two AOMs [10] for each beam are necessary to achieve an extinction ratio of $\sim 10^{10}$. In order to generate short light pulses radio-frequencies (rf) of 250 MHz and 260 MHz have been selected.

The linear *write* and *read* light are overlapped on a Glan-Laser prism (GL), co-propagate and are focused on the ensemble with a lens $f = 150$ mm. In order to

---

[6]Toptica: DLX 110 RockSolid

[7]AA MT110-B30A1-IR

[8]Sacher Lasertechnik: TEC 120 Littrow Laser System: LYNX

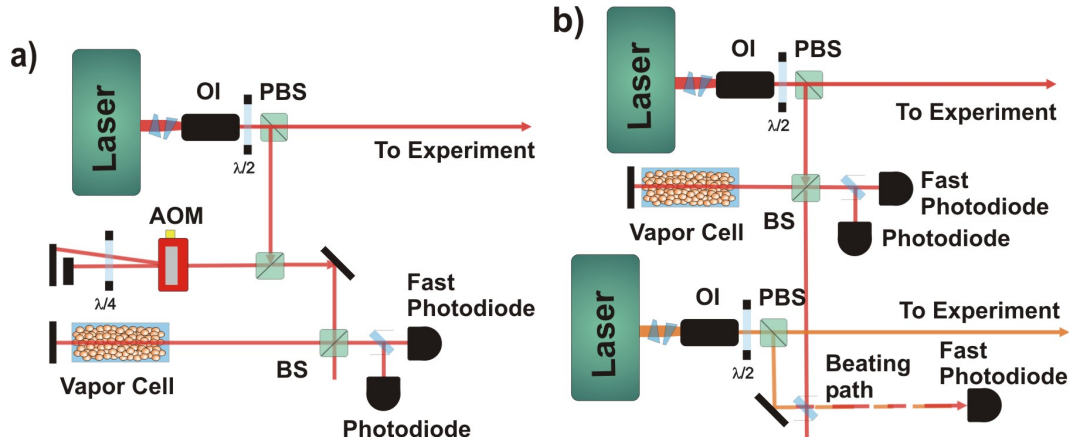[9]AA MT80-B30A1-IR

[10]AA MT250-B100A0-IR

Figure 5.3: Schematic set-up of the optics for Laser frequency stabilization: a) Frequency Modulation (FM) lock: The laser current is modulated with a fixed frequency $\omega_{mod} = 20$ MHz and sidebands with frequencies $\omega_L \pm \omega_{mod}$ are generated. The laser light passes an anamorphotic prism pair wich changes the beam profile from an elliptical into a circular shape. It passes an optical isolator (Isowave Optical Isolator: > 60dB) (OI) before a part of the light is branched off for the locking. Then optionally follows an acousto-optical modulator (AOM) in a double-pass configuration. The light frequency is then shifted by twice the frequency of the sound wave (ω_{rf}). The frequency can be changed without displacement of the beam. Thus the laser frequency can be locked relative to an atomic line with a frequency difference of $2 \cdot \omega_{rf}$. After the optional AOM path a Doppler-free saturation spectroscopy follows. The sidebands and the carrier experience different indices of refraction around the atomic resonances since they have different frequencies. The signal is picked up by two photo diodes. One detects only the slow part which is used to display the transmission spectroscopy during scanning the laser frequencies. The fast photodiode picks up the signal of the modulated sidebands and compares it to the reference oscillator which is used for the current modulator. From the phase difference an error signal is generated by an electronic circuit with its center at the atomic transition. The voltage signal is connected to the input of PI controller which uses the piezo of an extended Laser cavity in Littrow configuration as feedback unit. b) Frequency off-set (FO) lock: The light from a stabilized laser is overlapped with the light of the laser which needs to be stabilized. The beating signal of the two laser fields which corresponds to their frequency difference is detected by a fast photodiode and the electric signal is feed into an electric circuit. The circuit compares the frequency of the beating signal with a reference oscillator. This voltage controlled oscillator (VCO) can be tuned between 50 to 400 MHz. The comparison results in a voltage signal indicating the frequency difference. The voltage is used as error signal for a PI-controller which gives a feedback to the piezo of the laser. Thus the feedback loop stabilizes the second laser such that the beating signal has the same frequency as the VCO. This means that the second laser has a frequency difference to the so-called master laser by the VCO frequency. Due to electronic circuit there are more points in the error signal which can be used for locking. Therefore a part of the beating signal is feed into a frequency counter in order to adjust the desired frequency difference. In order to see the frequency of this laser to the atomic resonance a Doppler-free saturation spectroscopy is used [136].
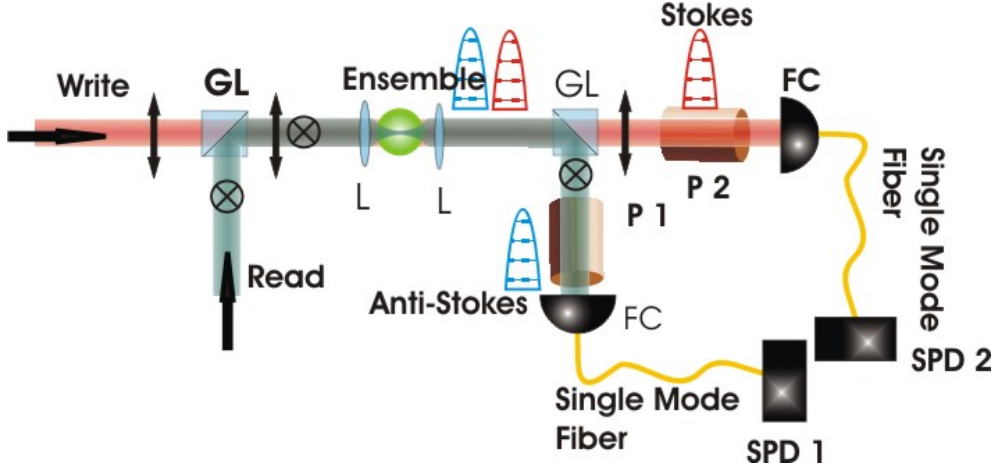
Figure 5.4: Filtering in the Co-propagating configuration: The *write* and *read* light is overlapped with orthogonal polarizations on a Glan-Laser prism (GL) and focused by a lens (L). The Raman fields are detected in orthogonal polarizations and separated by a second GL from the classical pulses. Pumped filter cells (P1,P2) with Rubidium and buffer gas filter out leakage light after the GL originating from the classical pulses. An interference filter (not depicted) after the cell blocks stray pumping light better than 1 : 100. The fiber coupler detects only a single spatial mode which is guided in the fibers to the single photon detectors (SPD1 and SPD2).

separate the co-propagating Raman light fields from the classical light pulses various filter stages are needed as depicted in figure (5.4). The frequency difference between the classical fields and the single Raman photons is only ~ 7 GHz. The polarization filtering achieves an extinction ratio of $\sim 10^{-6}$. The extinction ratio of a pumped filter cell is $\sim 10^{-4}$, but the transmission efficiency of filter cell for (Anti-)Stokeslight is $\sim 80\%$. Due to the detection within a solid angle of 0.15 additional spatial filtering is employed. Gating of the single-photon detectors counts only the events within the 500 ns gate time. The time resolution of 2 ns from the multiscaler card [11] enables a further temporal selection of the counted events.

In order to achieve a high repetition rate a PCI-card with an FPGA is used[12]. A home-built driver unit converts the signal into non-standard TTL signal capable of driving 50 Ω loads. Since our pulse can be as short as 100 ns the signal cables must be determined with the impedance of the lines in order to prevent back-reflections. A Labview [13] programm accesses a DLL in order to communicate with the FPGA chip. The program takes the user input and downloads the parameters with the VHDL program for the FPGA chip onto the PCI card. The clock speed of 40 MHz determines the time resolution to 25 ns.

The single photon detectors (SPD) which we use are gatable silicon avalanche pho-

---

[11]FastComTec P7888

[12]CESYS Gesellschaft für angewandte Mikroelektronik mbH

[13]National Instruments Labview

todiodes with $\approx 40\%$ quantum efficiency at 795 nm[14]. If a gate signal is applied, for every single photon detected, an electronic pulse is generated. A fast counter card with 2 ns time resolution [15] is used to count the pulses within a predefined sweeptime. The data with the countrate and the time stamps from each channel is analyzed by a Labview program [137]. It calculates and displays the excitation probability χ, the cross correlation function $g^2_{as,s}$ and the retrieve efficiency η.

5.2 Double-MOT Set-up

In terms of lasers this set-up is similar to the set-up described before. The cooling light is shared with the single-MOT set-up (section (5.1)). For the repumper light a FM-locked home-built laser with a maximum power 20 mW seeds a tapered amplifier chip [16] capable of delivering 500 mW of optical power. In order to receive a clean mode it is fiber coupled. The *write* and *read* lasers are home-built. Another difference is that only a single 260 MHz AOM is used to switch these beams. This is due to the beam configuration which is depicted in figure (5.5).

The vacuum set-up consists of two glass cells[17] which are horizontally attached on two opposite flanges of a stainless steel cross carrying a 27 liter ion-getter pump [18], an ion gauge, the Rubidium dispensers and a valve. Each glass cell has its own set of quadrupole field coils with a diameter of ~ 7 cm in a carrier structure of plastic fitted to the outer dimensions of the cell and mounted on the optics breadboard. Each cell has three sets of Helmholtz coils for independent magnetic field compensation. Six cooling beams intersect in the center of a glass cell. Since the two sites are controlled independently, two telescopes are used for the beam expanding before the light distribution into the individual MOT beams. The set-up of the switching AOMs is mirrored as well. The intensity of the cooling and repumping light in front of a telescope is ~ 20 mW and ~ 10 mW, respectivly.

In order to achieve a higher retrieve efficiency and reducing the effort of filtering a counter-propagating configuration was employed [73]. In figure (5.5) a schematic of the set-up is drawn. *Write* and *read* beams are overlapped and counter-propagating. The fiber couplers are focused onto the ensemble. Due to the mode-matching condition (see equation (3.12)) the correlated Anti-Stokes and Stokes fields are emitted in opposite directions. The axis for the detection is tilted by ≈ 3 degree in order to suppress leakage from the classical light fields into the detection. The Anti-Stokes field is coupled into a single mode fiber and filtered by an additional pumped filter cell. Thus Rayleigh scattering can be filtered out and nonclassical correlations are typically increased by a factor of two.

---

[14]PerkinElmer SPCM-AQR-13

[15]Fastcomtec P7888 1 GHz Multistop TDC

[16]Toptica Boos TA

[17]Japan Cells: 25mm × 25mm × 100mm glass cuvette on a glass to metal adapter with CF-40.
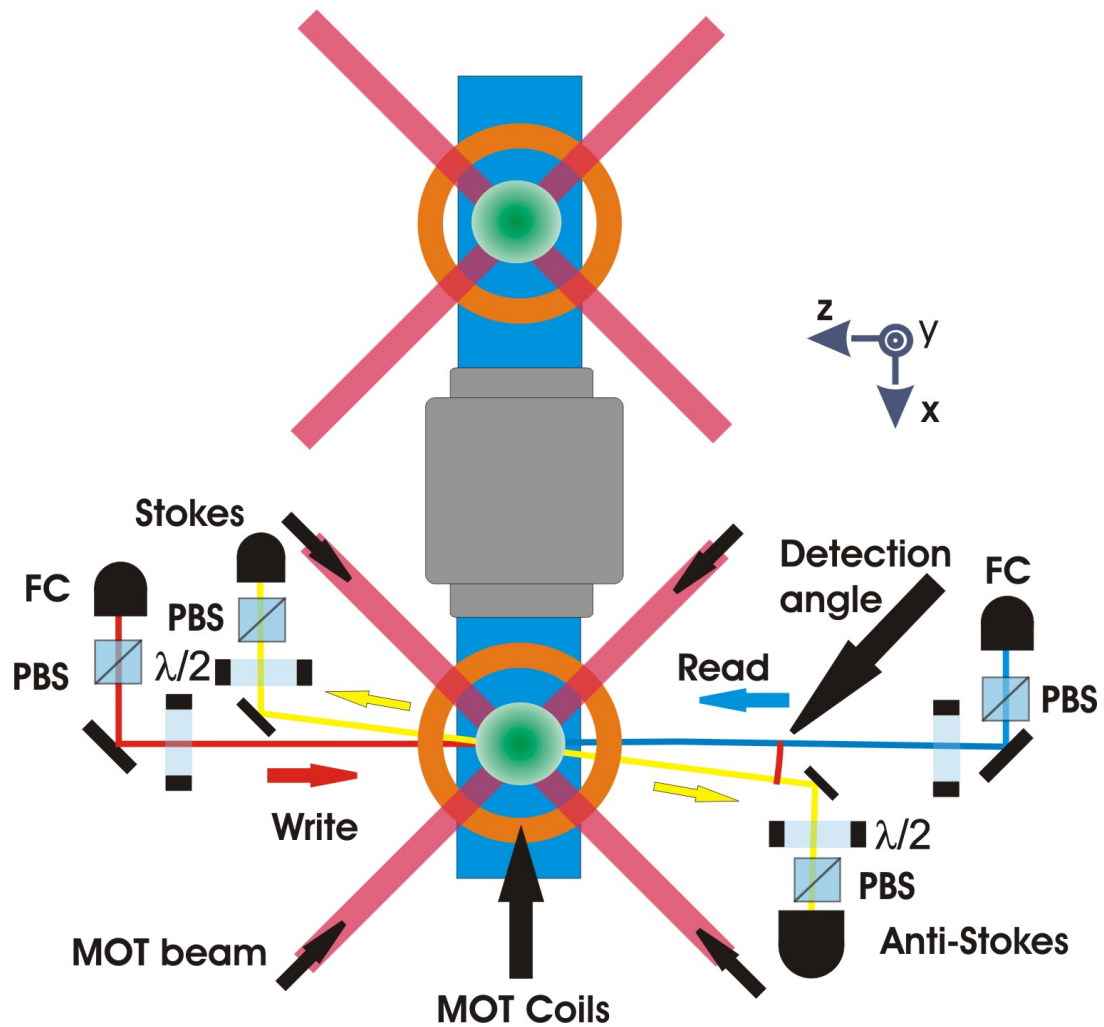
[18]Varian VacIon Plus20

Figure 5.5: Double MOT set-up with counter-propagating configuration: The two glass cells are attached to stainless steel flange cross. The fiber couplers (FC) with single mode fibers focus the beams onto the ensembles and detect the single photons generated. The fiber couplers are all of the same type using an aspheric lens. Thus a good mode match is achieved. Coupling efficiencies between corresponding couplers $> 80\%$ are possible.

5.3   Dipole Trap Set-up

In section 7.2 we describe an experiment with an atomic ensemble confined by an optical dipole trap (ODT). For this purpose we extended the single MOT set-up from section (5.1) by adding an optical dipole trap and absorption imaging. We have decided to use an optical dipole trap which is loaded right from a magneto-optical trap (MOT) by a dark MOT phase (see section (7.2)). Due to availability of reliable commercial lasers with sufficiently enough power the complexity compared to magnetic traps is greatly reduced. We describe in the following the principle of such a trap, before we turn to the implemented design.

Classical Oscillator Model   In an optical dipole trap the dipole force arises due to induced dipole moment and its dispersive interaction with a gradient light field [138]. The potential is conservative which means that it can be used for trapping. A trapping laser field with an electrical field amplitude of $\mathcal{E}$ and its polarization vector given by $\hat{\epsilon}$ induces an atomic dipole moment $\mathbf{d}$ according to

$$\mathbf{d} = \alpha(\omega)\mathcal{E}. \tag{5.1}$$

The polarizability $\alpha(\omega)$ is a complex number which depends on the frequency ω of the trapping field. The dipole potential in this field of intensity $I = 1/2\epsilon_0 c\mathcal{E}^2$ is

$$U_{ODT} = \int_0^{\mathcal{E}} -\mathbf{d}(\mathcal{E}) \cdot \delta\mathcal{E} = -\frac{1}{2}\langle \mathbf{d} \cdot \mathcal{E}\rangle = -\frac{1}{2\epsilon_0 c}\alpha I. \tag{5.2}$$

The factor of 1/2 has its origin in the induced dipole moment under the assumption that the atom responds linear to the electric field [82]. proportional to the gradient of the potential and therefore to the gradient of a spatially varying intensity $I = I(\mathbf{r})$ as well:

$$F_{OPT} = -\nabla U_{ODT} = \frac{1}{2\epsilon_0 c}\alpha\nabla I \tag{5.3}$$

Depending on the sign of the polarizability the atoms are pushed to a higher or a lower intensity. Thus they are trapped either in an intensity maximum or minimum.

Semi-Classical Approximation   In order to evaluate the polarizability $\alpha(\omega)$ we consider the atom as a two-level quantum system and the laser as a classical radiation field with frequency ω. The quantum mechanical perturbation theory of multi-level system gives [139]

$$\alpha(\omega) = \sum_{|f\rangle} \frac{1}{\hbar\Delta_{if}} \left| \langle i|\hat{\mathbf{d}} \cdot \mathcal{E}|f\rangle \right|^2, \tag{5.4}$$

where $|i\rangle$ represents the state we are interested in and $|f\rangle$ all possible states which can undergo by an induced dipole transition $\hat{\mathbf{d}}\mathcal{E}$ into it. The detuning is computed by $\frac{1}{\Delta_{if}} = \frac{1}{\omega_{if}-\omega} + \frac{1}{\omega_{if}+\omega}$. For a two-level atom with a single atomic transition ω_0 and an incident linear laser field ω_L the optical dipole trap (ODT) potential U and the

scattering rate Γ_{scatt} is given as [140]

$$U_{ODT}(\mathbf{r}) = -\frac{3\pi c^2}{2\omega_0^3}\left(\frac{\Gamma}{\omega_0 - \omega_L} + \frac{\Gamma}{\omega_0 + \omega_L}\right)\cdot I(\mathbf{r}) \tag{5.5a}$$

$$\Gamma_{Scatt}(\mathbf{r}) = \frac{3\pi c^2}{2\hbar\omega_0^3}\left(\frac{\omega_L}{\omega_0}\right)^3\cdot\left(\frac{\Gamma}{\omega_0 - \omega_L} + \frac{\Gamma}{\omega_0 + \omega_L}\right)^2\cdot I(\mathbf{r}). \tag{5.5b}$$

For large detunings $|\Delta| = |\omega_L - \omega_0| \ll \omega_0$ and in the rotating wave approximation (RWA) [97] the equations simplify to:

$$U_{ODT}(\mathbf{r}) = -\frac{3\pi c^2}{2\omega_0^3}\left(\frac{\Gamma}{\Delta}\right)\cdot I(\mathbf{r}) \tag{5.6a}$$

$$\Gamma_{Scatt}(\mathbf{r}) = -\frac{3\pi c^2}{2\hbar\omega_0^3}\left(\frac{\Gamma}{\Delta}\right)^2\cdot I(\mathbf{r}) \tag{5.6b}$$

Multi-Level atoms Real atoms have a multi-level structure with fine and hyperfine interactions. Their level scheme exhibits multiple very close transitions which need to be taken into account. For alkali atoms like Rubidium the spin-orbit coupling of the excited state results in a D-line doublet ($^2S_{1/2} \rightarrow ^2P_{1/2}, ^2P_{3/2}$ and $\hbar\Delta'_{FS}$) [140]. In the case of Rubidium the wavelength of the D_1 line is 795 nm and the D_2 line is at 780 nm. The coupling of the orbit to the nuclear spin splits the ground state into two separated by $\hbar\Delta_{HFS}$ and the excited state into multiple with a total splitting energy of $\hbar\Delta'_{HFS}$. The relation of the splitting energies is $\hbar\Delta'_{FS} \gg \hbar\Delta_{HFS} \gg \hbar\Delta'_{HFS}$. As long as the detuning of the trapping laser fulfills the condition $|\Delta| = |\omega_L - \omega_0| \gg \Delta'_{HFS}$, the hyperfine states are unresolved. Then the trapping potential can be written as

$$U_{ODT}(\mathbf{r}) = \frac{\pi c^2 \Gamma}{2\omega_0^3}\left(\frac{2 + q\cdot g_F m_F}{\Delta_{2,F}} + \frac{1 - q\cdot g_F m_F}{\Delta_{1,F}}\right) I(\mathbf{r}), \tag{5.7}$$

where $\Delta_{2,F}$ and $\Delta_{1,F}$ are the detunings from the D_2 and the D_1 line respectively. The parameter q takes on values of 0 for linear and ± 1 circular polarized light. The D_2 and D_1 lines have the strongest contributions to the polarizability of the $\left|5S_{1/2}\right\rangle$ ground states and give in our case of a far red-detuned optical dipole trap a sufficiently accurate value.

For a general derivation one needs to consider the dressed state picture [141]. In addition to the quantum-mechanically treatment of the atom the light field is quantized. In this picture the trapping light leads to an energy shift of the atomic level $|i\rangle$ according to

$$\Delta E_i = \pm\frac{\mathcal{E}^2}{4\hbar}\sum_{f\neq i}|\langle i|\mathbf{d}|f\rangle|^2\frac{1}{\Delta_{eff}} \tag{5.8}$$

The plus and minus sign indicates that the excited and the ground state, respectively, are shifted oppositely (see also figure (5.11)). This energy shift is referred as *light shift* or *AC-Stark shift*. The transition matrix elements $\langle i|\mathbf{d}|f\rangle$ depend on the quantum
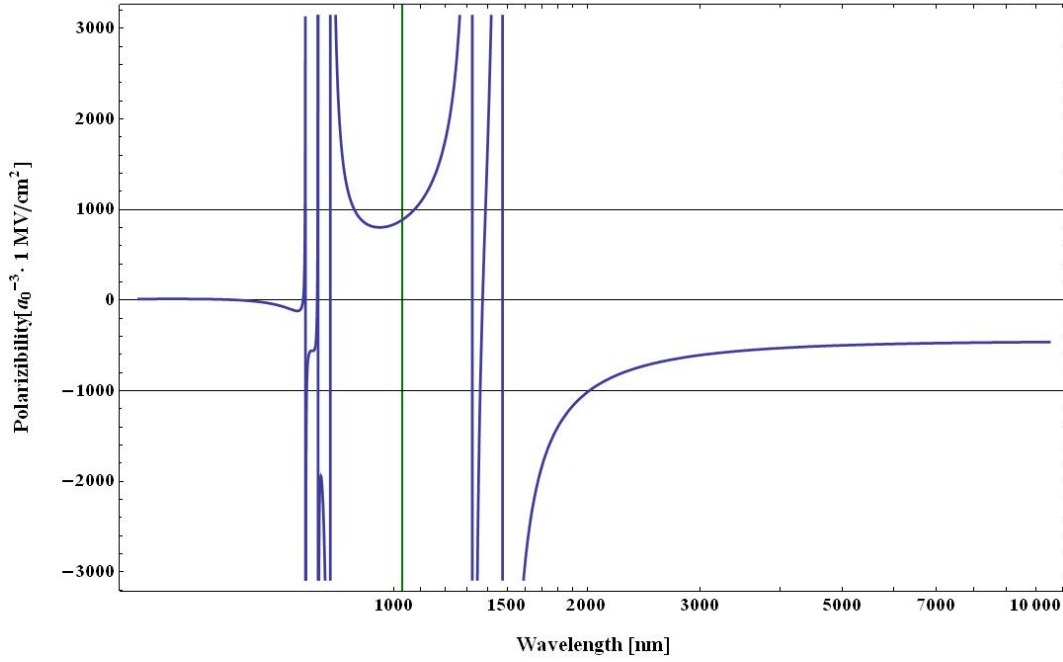
Figure 5.6: Polarizability for the excited $5P_{1/2}, F = 2, m_F = 0$ of the D1 line in dependence of the wavelength for the trapping light.

numbers n, J, F, m_F and the polarization of the laser field ϵ. In appendix B it is shown that the matrix elements can be rewritten by using the Wigner-Eckart theorem. Plugging this expression into equation (5.8) and comparing it with the classical picture $U = -\frac{1}{4}\alpha|\mathcal{E}|^2$ shows that the polarizability is given by

$$\alpha(\omega) = \frac{3e^2}{2m_e}(2J+1)(2F+1)\sum_{f=n',J',F',m'}(2F'+1)\frac{f_{if}}{\omega_{if}\Delta_{if}}\begin{pmatrix} F & 1 & F' \\ -m & q & m' \end{pmatrix}^2 \begin{Bmatrix} J & F & I \\ F' & J' & 1 \end{Bmatrix}^2 .$$

$$(5.9)$$

The summation over $|f\rangle$ indicates that all possible transitions into $|i\rangle$ are included. In practice one can neglect weaker ones their contributions do not affect the polarizability much, as long as the wavelength of the trapping light is not close to such one. The oscillator strength of the $i = nJ \longrightarrow f = n'J'$ transition is defined by

$$f_{if} = \frac{2m_e\omega_{if}}{3\hbar e^2(2J+1)}|\langle nJ|d|n'J'\rangle|^2 ,$$

$$(5.10)$$

and can be looked up for example in data bases.

Gaussian Trap Beams   As we have previously mentioned the sign of $\alpha\omega$ depends on the wavelength of the trapping light. In case of a detuning to red of the atomic resonance frequency, an intensity maximum is necessary in order to trap the atoms. The TEM$_{00}$ mode of a Laguerre-Gaussian beam has an intensity distribution which
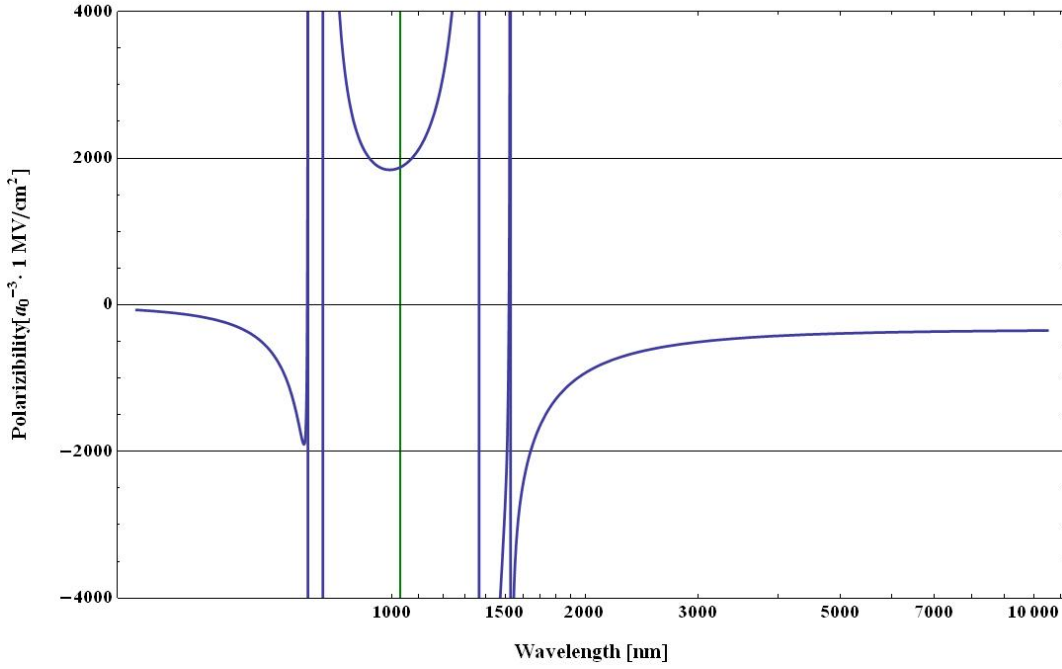
Figure 5.7: Polarizability for the excited state $5P_{3/2}, F = 2, m_F = 0$ of the D2 line in dependence of the wavelength for the trapping light.

is given by

$$I(r, z) = I(z) \cdot e^{-\left(\frac{2r^2}{w(z)^2}\right)} = I_0 \cdot \frac{1}{1 + \left(\frac{z}{z_0}\right)^2} \cdot e^{-\left(\frac{2r^2}{w(z)^2}\right)}, \tag{5.11}$$

where $I_0 = 2P/w_0^2\pi$ is the maximum intensity, and the waist is

$$w(z) = w_0 \sqrt{1 + \left(\frac{z}{z_0}\right)}. \tag{5.12}$$

The Rayleigh range z_0 can be computed by

$$z_0 = \frac{\pi w_0^2}{\lambda} \tag{5.13}$$

When using a single beam the optical potential is given by:

$$U_{ODT}(\mathbf{r}) = \frac{\pi c^2 \Gamma}{2\omega_0^3} \cdot I_0 \cdot \left(\frac{2 + q \cdot g_F m_F}{\Delta_2, F} + \frac{1 - q \cdot g_F m_F}{\Delta_1, F}\right) \frac{1}{1 + \left(\frac{z}{z_0}\right)^2} \cdot e^{-\left(\frac{2r^2}{w_0^2(1 + \left(\frac{z}{z_0}\right)^2)}\right)} \tag{5.14}$$

or

$$U(z, r) = -U_0 \frac{w_0^2}{w(z)^2} e^{-2r^2/w^2(z)}, \tag{5.15}$$

where U_0 is the maximum trap depth. The trapping potential can be approximated by a harmonic potential when the energy of the trapped atoms is a fraction of the maximal potential depth $k_B T \ll U_0$. If z is the symmetry axis the harmonic potential is written as

$$U_{harm}(r,z) = \frac{m}{2}(\omega_r^2 r^2 + \omega_z^2 z^2) \tag{5.16}$$

where we have used the radial and axial trapping frequencies $\omega_r = \sqrt{\frac{4\hat{U}_0}{mw_0^2}}$ and $\omega_z = \sqrt{\frac{2\hat{U}_0}{mz_R^2}}$. These quantities are usually employed in order to describe the steepness of traps for neutral atoms. Typical values for our single beam red-detuned trap are about $2\pi \cdot 2$ kHz for the radial and $2\pi \cdot 10$ Hz for the axial trapping frequency.

Ground State Polarizability The atoms are trapped in the ground state, so we need this polarizability. It can be computed by

$$\alpha_g(\omega) = -\frac{\pi c^3 \epsilon_0}{2}\left(\frac{2\Gamma_{3/2}}{\omega_{3/2}^3 \Delta_{3/2}} + \frac{\Gamma_{1/2}}{\omega_{1/2}^3 \Delta_{1/2}}\right) \tag{5.17}$$

where ω_J and Γ_J are the transition frequency and line width of the excited $5^2 P_J$ state ($J = 1/2, 3/3$). It is $\alpha = -1.21325 \cdot 10^{-38}\frac{\text{C}^2\text{s}^2}{\text{kg}}$. This result is already included in equation (5.7).

Excited State Polarizability The polarizability of the excited state is important when considering the interaction of the trapped atoms with additional incident laser fields, e.g. for imaging or state manipulation. For a trapping wavelength 1030 nm the polarizability of the excited state $5^2 P_{3/2}$ is then computed to $\alpha = -2.6094 \cdot 10^{-38}\frac{\text{C}^2\text{s}^2}{\text{kg}}$ (see figure (5.7)). The polarizability of the excited state $5^2 P_{1/2}$ is then computed to $\alpha = -1.31518 \cdot 10^{-38}\frac{\text{C}^2\text{s}^2}{\text{kg}}$ (see figure (5.6)).

5.3.1 Inhomogeneous AC Stark Broadening

For a two-level atom in a red-detuned optical dipole trap (FORT) the ground and excited state experience a light shift opposite to each other. Since the trapping laser beam is usually a Gaussian beam, the level shifts are position-dependent as seen in figure (5.11). Thus the transition is inhomogeneous broadened. If the broadening is too large then upper hyperfine states mix (e.g. on the D_2 line), since their separation is in the order of a two hundred MHz. On the D_1 line we use for the Raman scattering, the separation of about eight hundred MHz is well enough. We can therefore consider the *write* and *read* transitions separately.

The width of the broadening needs to be averaged over all atoms in the trap. For a thermalized ensemble in a trap the occupation of the motional trap states is given

by the Boltzmann distribution

$$P(E_n) \propto \exp\left(-\frac{E_n}{k_B T}\right), \tag{5.18}$$

where the energy eigenstates of the three dimensional harmonic potential are determined by $E_n = (n_x + 1/2)\hbar\omega_x + (n_y + 1/2)\hbar\omega_y + (n_z + 1/2)\hbar\omega_z$. The density of states $g(E)$ of a 3D harmonic oscillator can be approximated by [142]

$$g(E) = \frac{E^2}{2h^3\omega_x\omega_y\omega_z}, \tag{5.19}$$

For the atoms with thermal energies larger than the energy steps of the oscillator $k_B T \gg \hbar\omega_1$, the number density is given by

$$\mathcal{N}(E) = g(E) \times \mathcal{P}(E) = \frac{E^2}{2h^3\omega_x\omega_y\omega_z} \times \exp\left(-\frac{E}{k_B T}\right). \tag{5.20}$$

Convolution with the natural line width and a subsequent fit to data leads to the broadened line width. We have estimated the line width for our set-up [143] to approximately 14 MHz.

Due the inhomogeneous broadening the the detuning of the light from resonance in the *write* and *read* processes depends on the position of the atom. This can be compensated by an additional light field like reported in ([144]) for Cesium and for Rubidium in [145] which has been used for improved loading from a MOT into an optical dipole trap. In case of the *write* pulse we must choose a larger detuning in order to suppress the unwanted Rayleigh scattering.

5.3.2 Vector Light Shift

The vector light shift is an additional shift induced by circular components of the trapping light [146]. This frequency shift is linear in m_F, the projection of F onto the quantization axis. In other words this means that the Zeeman sublevels experience various light shifts (see equation (5.7)). The ground state is affected as well, therefore the potential for the atoms depends on their internal state. The influence of this effect can be reduced by the suppression of the non-linear components of the trapping light. For this reason we employ in our set-up a polarizing beam splitter after the fiber. It ensures a ratio of linear polarized light to other contributions of better than 300:1. Therefore this contribution can be neglected.

5.3.3 Tensor Light Shift

Hyperfine interaction in the excited state causes tensor shifts quadratic in the quantum number m_F even for a linear polarization of light. Since the quantum memory makes use of the superposition of the ground states the storage time is not affected

by this effect. There is no effect during the *write* and *read* process since we use the transitions on the D_1 line. Only our imaging beam and the pumping beams on the D_2 line are effected. $\alpha_2 = -9.43837 \cdot 10^{-39} \frac{\mathrm{C^2 s^2}}{\mathrm{kg}} \times C$ with $C = \left(\frac{5j_v(2j_v-1)}{6(j_v+1)(2j_v+1)(2j_v+3)} \right)^{1/2}$ defined as in appendix (B).

5.3.4 Implemented Design

In chapter (4) we have seen the critical parameters for a quantum memory based on an atom ensemble. For the design of the optical dipole trap these parameters are our design criteria. In practice one usually has to restrain the optimal design due to predetermined restrictions. In our case we had to employ the vacuum chamber which has been available. The trapping laser was available as well. The maximum output power of 45 W and the wavelength is 1030 nm [19]. It has a linewidth according to the specification sheet of ~ 2 GHz. Due to the limited optical access of the vacuum chamber and the fact that the optical depth is more critical than the atomic density we decided to use a single beam trap (travelling wave).

Computed potential   As basis of our computations we take a beam waist of $w_0 = 36$ μm. Thus the maximum trap depth at $P = 7$ Watts is $U_0 = 0.63822$ mK. This is sufficient to load the atoms from the MOT. The photon scattering rate at the trap center is $\Gamma \approx 6$ s^{-1}. The axial trap frequency $\omega_z = 2\pi \cdot 15.8$ Hz and the radial one is $\omega_z = 2\pi \cdot 2313.8$ Hz. This means a tight radial confinement with a steep slope, but only a weak axial confinement. The atomic cloud will very elongated, which is not too critical from the point of optical depth. But it makes further evaporative cooling very ineffective. Assuming an achievable temperature of 45 μK the trap volume is $V_{trap} = 2.12464 \cdot 10^{-7}$cm^{-3}. In figures (5.8), (5.9) and (5.10) the computed potential is depicted in a axial cut, a radial cut and a two dimensional cut, respectively.

Optical Set-up of the trapping beam   We used a commercial optics design program [20] in order to select the correct lenses for achieving the beam waist. The light beam exits a fiber coupler as collimated beam. Due to space limitation around the vacuum chamber we have to use a focussing lens with $f = 300$ mm. Between the fiber coupler and this lens the telescope lenses with $f = 70$ mm and $f = 300$ mm were matched in order to achieve the desired beam waist. After compensation of the imaging and lens errors the diffraction limited beam waist was computed to $w_0 \approx 39$ μm. After the set-up it is necessary to compare the actual beam parameters with the designed values. An extensive overview on the characterization of the trapping beam is found in [143]. The measured waist of 37$\pm$1 μm is in nice agreement with the prediction.

The trapping laser is fiber coupled into a polarization maintaining photonic crystal

---

[19]ELS Versadisk 1030-40
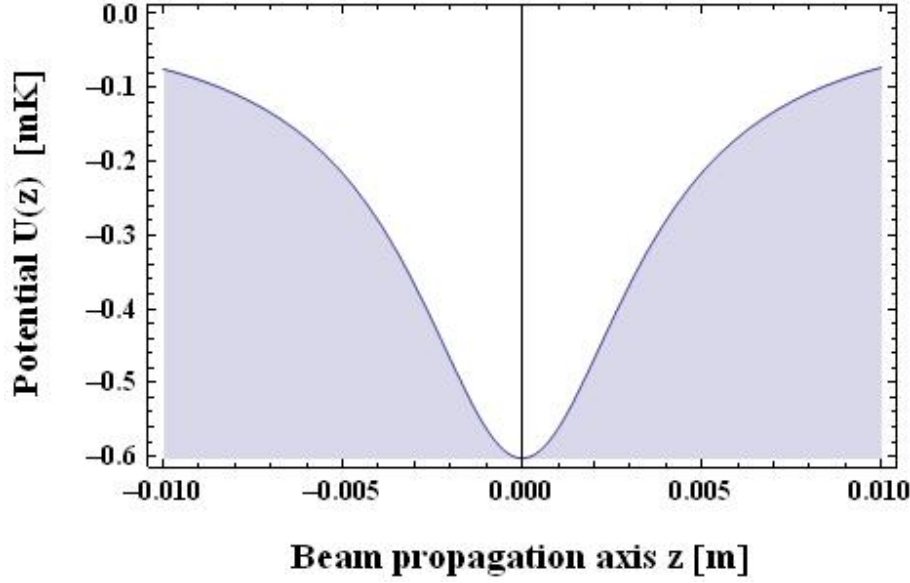[20]OSLO-EDU edition from Lambda research cooperation

Figure 5.8: Optical dipole trap potential: $z = 0$ corresponds to the focal point.

single mode fiber[21]. The coupling efficiency of the TEM_{00} mode is only $\sim 50\%$ since the lens in the coupler does not match it well enough to the fiber mode with waist diameter of 13.0 ± 1.0 μm. The fiber coupling provides a fixed beam position for the beam expanding telescope. In addition it translates pointing instabilities of an 80 MHz AOM [22] into intensity fluctuations at the output coupler, which can be controlled.

For this purpose an intensity stabilization circuit is used. From the beam after the output coupler light leaking through a mirror is picked up by a photodiode with a current-to-voltage converter. A differential amplifier compares the output voltage with a control voltage from an analogue output card of a computer. The differential signal is used as error-in signal for a home-built PI-controller[23]. Its output is connected to the external rf-level[24] control of the AOM driver. In that way the PI-card controls by the rf-power the intensity of the trapping laser. More details are found in [143].

Density distribution of the atomic ensemble in the ODT   By using the harmonic approximation for the trapping potential we can write the Gaussian atomic density distribution as

$$n(\mathbf{r}) = n_0 \exp\left(-\frac{1}{2}\left(\frac{x^2}{\sigma_x^2} + \frac{y^2}{\sigma_y^2} + \frac{z^2}{\sigma_z^2}\right)\right), \tag{5.21}$$

---

[21]Crystal Fibre LMA-PM 16

[22]Intraaction ATM-803DA6M

[23]PI stands for **P**roportional and **I**ntegral

[24]Radiofrequency (rf) at a transducer generates the soundwave in the AOMs crystal.

[25]OSLO optics design program from Lambda research cooperation, EDU edition
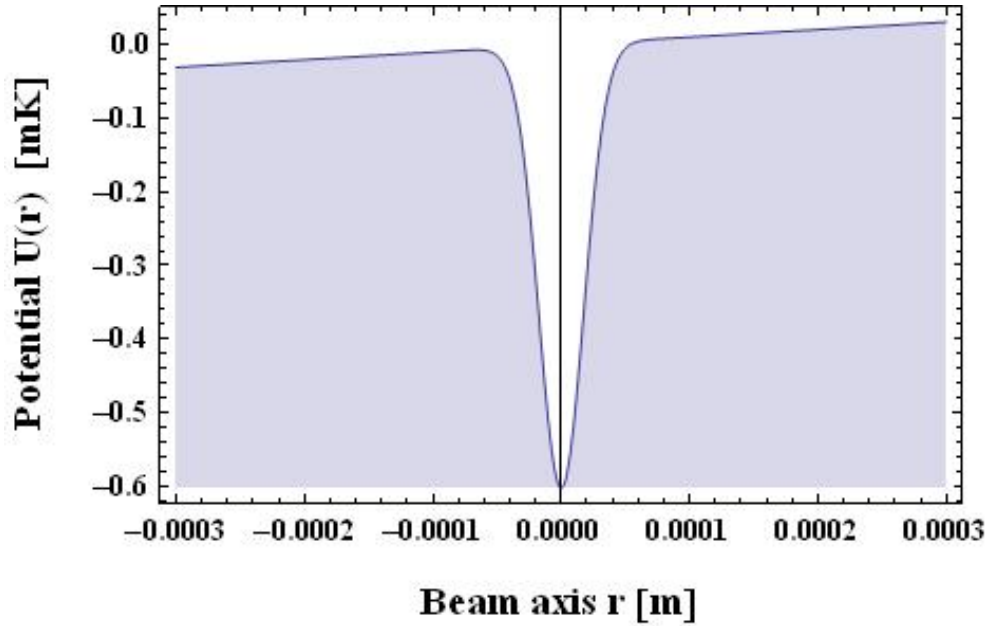
Figure 5.9: Optical dipole trap potential: cut through beam profile at focus. $R = 0$ corresponds to beam center. The slope is due to gravity.

with peak intensity $n_0 = \frac{N}{(2\pi)^{3/2}\sigma_x\sigma_y\sigma_z}$ with N atoms. The cloud widths are calculated by $\sigma_i = \sqrt{\frac{k_B T}{m\omega_i^2}}$, where the index $i = x, y, z$ denotes the spatial directions and ω_i are the corresponding trap frequencies.

Optical depth of the atomic ensemble in the ODT   A probe beam incident on an atomic ensemble propagating in **z**-direction is attenuated according to

$$I(x,y) = I_0(x,y)e^{-\mathcal{D}(x,y)}, \tag{5.22}$$

with I_0 as initial intensity and $\mathcal{D}$ is the optical depth which we have already introduced. For a resonant probe light ($\Delta_P = 0$) the scattering cross section is $\sigma_0 = \frac{3\lambda_0^2}{2\pi}$. From the atomic density distribution $n(x, y, z)$ one can compute the optical depth for a fixed number of atoms N and various temperatures. The atomic density along the propagation axis is integrated and the optical depth is given by

$$\mathcal{D}(x,y) = \sigma_0 \int_{-\infty}^{\infty} Nn(x,y,z)dz. \tag{5.23}$$

In figures (5.16),(5.17),(5.18),(5.19),(5.20) we have computed the resonant optical depth for our trap parameters and atom numbers, as well as temperatures, typically measured in our experiments.
The conclusions are that we can achieve very high optical depth compared to $\mathcal{D}_{max} \sim 5$ in the MOT. The optical depth drops quickly with increasing detection angle, but at an angle of 3 degree it is still $\mathcal{D} \sim 100$. The effect of the temperature range
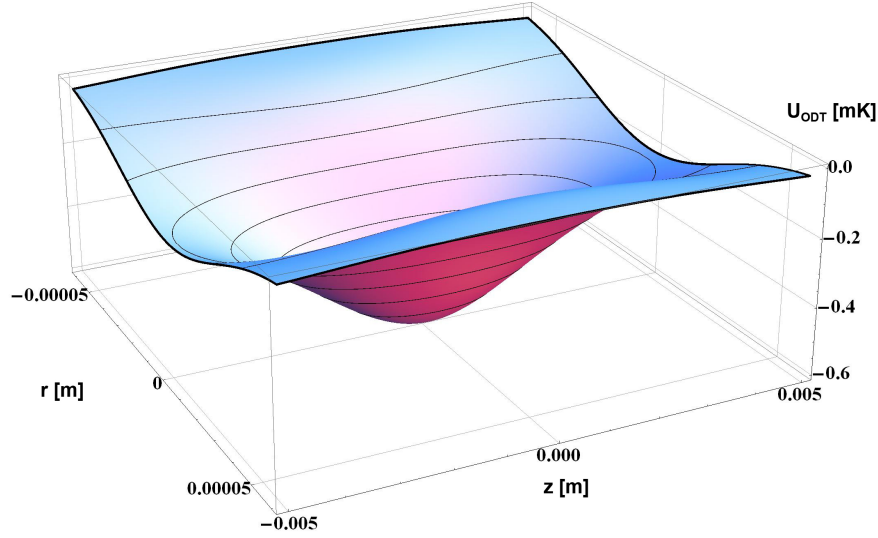
Figure 5.10: Optical dipole trap potential: Plot of the trap potential including gravity in axial z and radial r direction. The single Gaussian beam propagates along z.

encountered on the optical depth is larger than a moderate variation of the trapping power. This assumes that the atom number is constant when varying these conditions which is in experiment typically not the case.

Heating effects

Heating processes in the trap are undesired since can they increase the loss of atoms from the trap and increase the decoherence of the quantum memory.

Pointing instability of the trapping laser   The pointing instability of the trapping laser can induce a significant heating of the trapped atomic ensemble. In order to avoid this effect the trapping laser is fiber coupled. After the light leaves the coupler on the other end of the fiber it is directed onto the beam expanding telescope. The telescope optics is mounted on solid lens mounts on a one centimeter thick stainless steel board machined by our workshop. For the alignment of the focusing lens an adjustable lens mount was employed on a stable linear translation stage. In [143] the standard deviation of the focus' position was measured to 0.8 μm at a resolution of 0.5 μm. Compared to the measured beam waist of 36 μm it is a very small deviation.

Scattering of trap light   Let us estimate the heating rate due to the scattered trap light photons. One photon recoil increases the kinetic energy of an atom by

$$E_{rec} = \frac{p^2}{2m} = \frac{\hbar^2 k^2}{2m}. \tag{5.24}$$
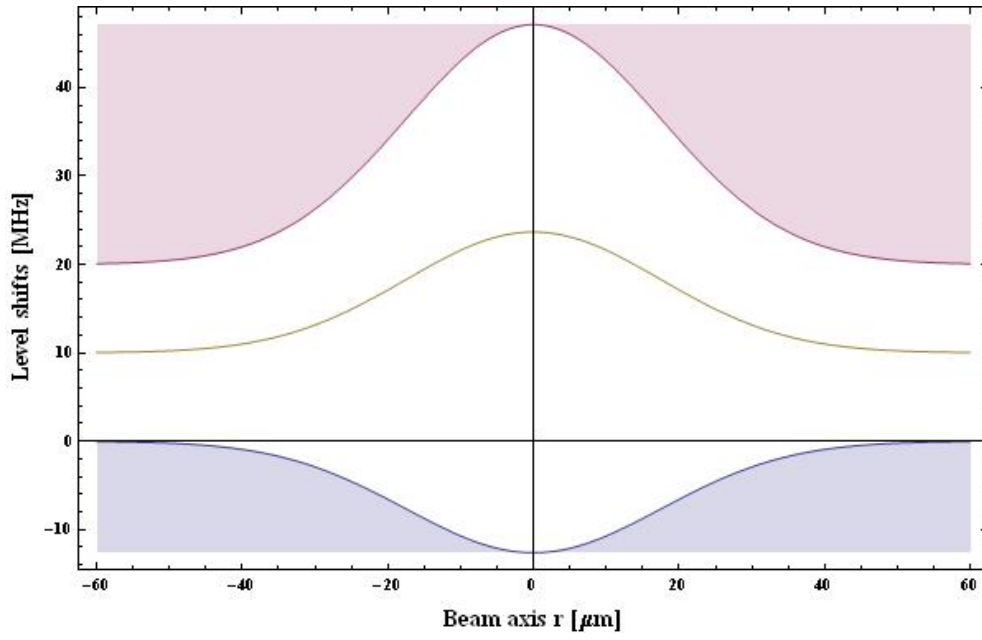
Figure 5.11: Lightshifts across the beam cross section for the ground state $S_{1/2}$, $P_{1/2}$, $P_{3/2}$. For better distinction there is an offset added to $P_{1/2}$, $P_{3/2}$ of 10 MHz and 20 MHz respectively.
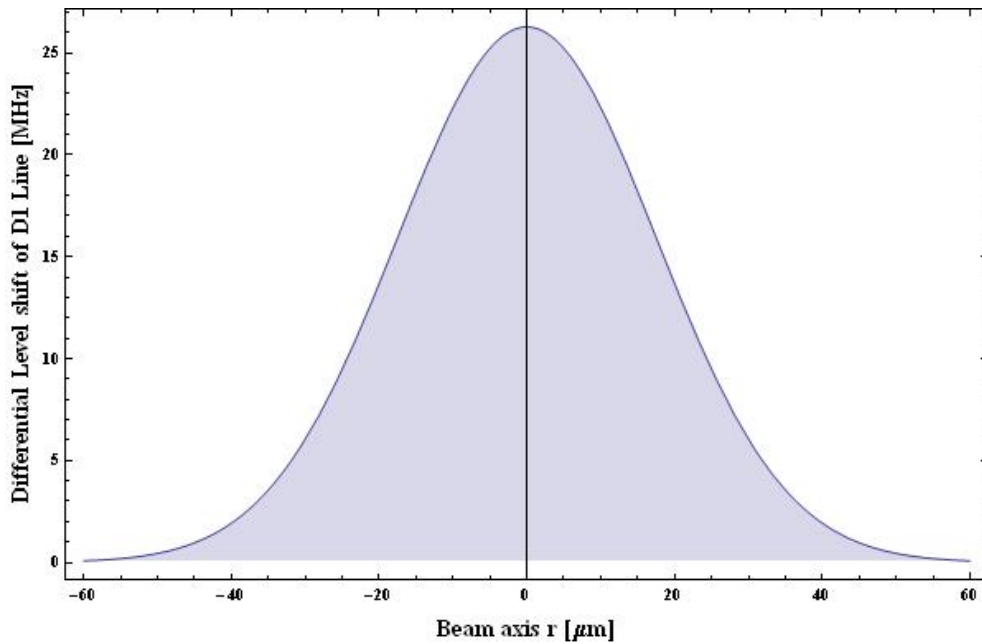

Figure 5.12: Detuning from the resonance frequency due to the lightshifts between the ground state $S_{1/2}$ and the excited state $P_{1/2}$ of the D1 line across the cross section of the trapping beam.
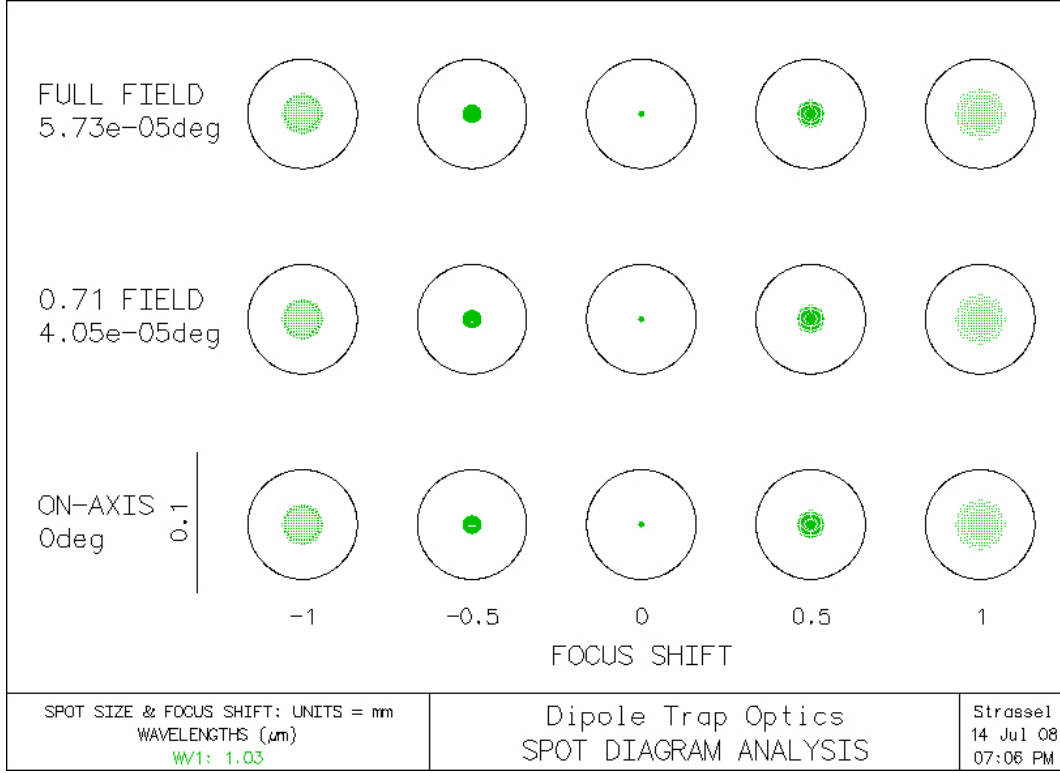
Figure 5.13: OSLO [25] spot diagram at the focus of the trapping optics: The black circle represents the Airy disk. All the beams of the geometrical raytracing correspond to the green dots in the focal plane. The points lie within the Airy disk, which means that the optics is diffraction limited. The computed waist w_0 is 39 μm.

The recoil temperature is defined by $k_B T_{rec} = 2E_{rec}$. A simple derivation for the heating rate in a 3D trap yields [140]:

$$\frac{dT}{dt} = \frac{T_{rec}}{3} \bar{\Gamma}_{sc} \tag{5.25}$$

$\bar{\Gamma}_{sc}$ is the average scattering rate of the trapping light of an optical dipole trap. The average scattering rate can be calculated by using the virial theorem [140] as

$$\bar{\Gamma}_{sc} = \frac{\Gamma}{h\Delta} \left(U_0 + \frac{3}{2} k_B T \right) \tag{5.26}$$

The computed value for our case (T=45 μK) is 1.09 s^{-1}. For a recoil temperature of 208 nK, the heating rate is $\frac{dT}{dt} \approx 76$ nK/s.

Bias Field Coils For the generation of the homogenous bias field of ≈ 3.23 G a set of Helmholtz coils is installed with the magnetic field along the **z** axis, the propagation direction of the trapping light. Each of the two coils has 23 turns with a size of 50×50 cm^2 and their separation is 25 cm. The ratio of the B-field to

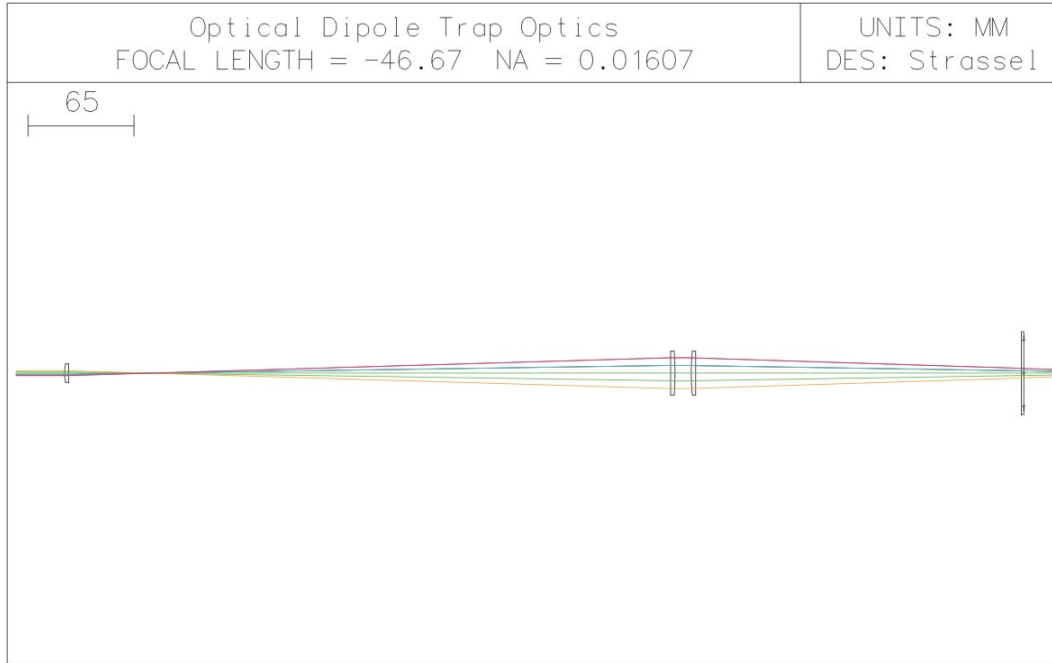**Figure 5.14:** OSLO[25] ray tracing for the optical set-up of the trapping beam: The light from the fiber coupler (not drawn) enters from the left side and passes the two telescope lenses. The collimated beam is then focused by a lens through the vacuum window onto the image plane.

the current is linear and its slope is $\sim 1 \, \frac{\mathrm{G}}{\mathrm{A}}$. A low noise power supply provides the current. It is switched by a home-built switch.

Counterpropagating set-up   In figure (5.21) the counter-propagating set-up is depicted. In contrast to the double MOT set-up (section (5.2)) additional dichroic mirrors have been used in order to overlap the *write*, *read* and pumping beams with the trapping beam at 1030 nm. The dichroic mirrors transmit the signal and pumping light on the D_1 and D_2 line (transmittance for 795 nm $\approx$ 70%) and reflect the dipole trap light at 1030 nm (reflectivity $> 99\%$). The fiber couplers focus the beams onto the trapped ensemble with a $1/e^2$ radius of 250 μm and collect the single photons with a $1/e^2$ mode radius 75 μm into the single-mode fibers. The maximum coupling efficiency between the Stokes and Anti-Stokes couplers is $\sim$ 93% which ensures a good mode match.

Computer Control   The computer control consists of in total four computers. One computer controls the analog[26] and digital outputs [27] for the operation of the MOT and the ODT. The second one controls the CCD camera used for the absorption imaging of the atomic cloud. Since the camera control "blocks" most of

---

[26]National Instruments PCI 6371
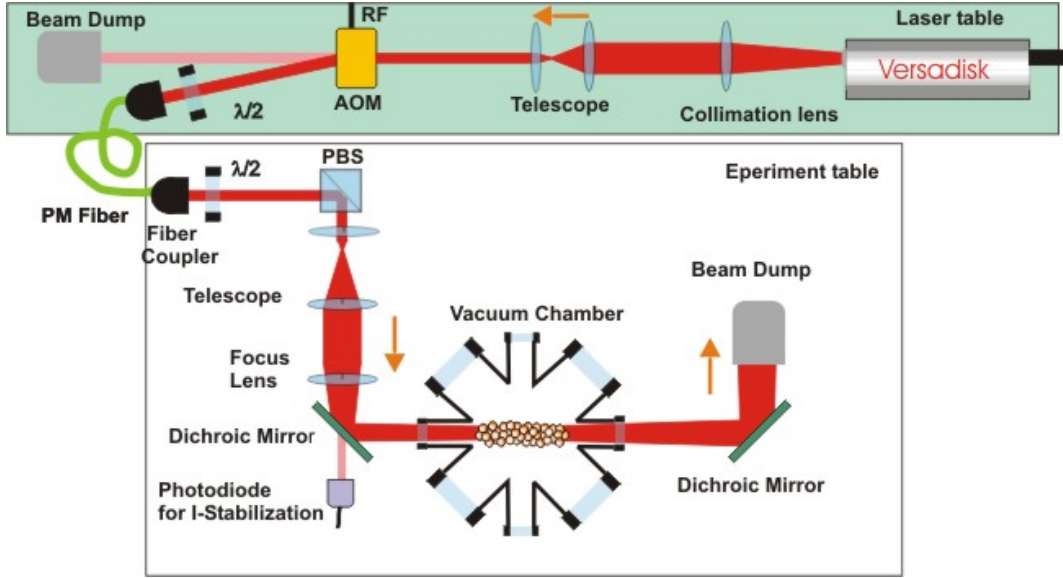[27]ADLink PCI 7300A Rev. B

Figure 5.15: Schematics of the optics for the trapping beam: The 1030 nm laser stands on an extra table. The slight divergence of the beam is compensated by a collimation lens. A telescope reduces the beam size in order to achieve a better diffraction efficiency at the acousto-optical modulator (AOM). The first-order diffracted beam is coupled into a polarization maintaining (PM) single mode photonic crystal fiber which can handle the high power. After leaving the second fiber coupler a polarizing beam splitter (PBS) is used in order to reduce fluctuations of the polarization. The telescope expands the beam such that it can be focused by a lens with focal length $f = 300$ mm to the correct spot size. The focal point is at the center of the vacuum chamber, where the MOT is located. The trapping beam leaves the chamber and is directed into a beam dump. The dichroic mirrors (DM) allow the overlap of the *write* and *read* light with the trapping light. One of the dichroic mirrors is used to couple out a small fraction of the light for the intensity stabilization.
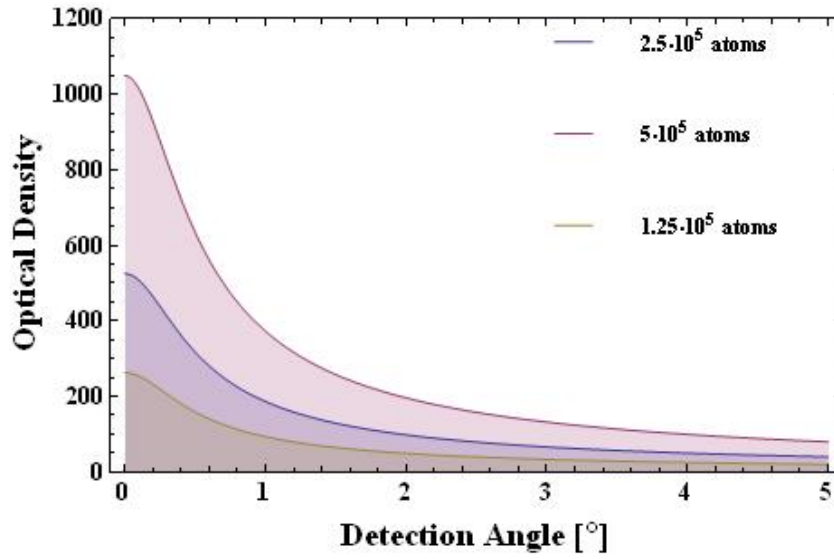
Figure 5.16: Optical density as a function of the detection angle with respect to the elongated axis: The trapping power is 7 Watts, the number of atoms is $1.25 \cdot 10^5$, $2.5 \cdot 10^5$, $5 \cdot 10^5$ at a temperature of 45 μK.

Figure 5.17: Optical density as a function of the detection angle with respect to the elongated axis: The trapping power is 7 Watts, the number of atoms is $1.25 \cdot 10^5$, $2.5 \cdot 10^5$, $5 \cdot 10^5$ at a temperature of 20 μK.
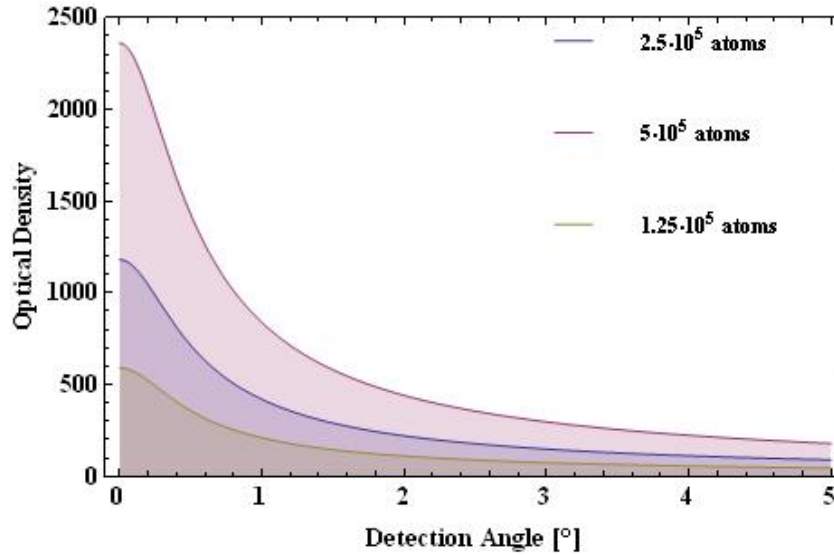
Figure 5.18: Optical density as a function of the detection angle with respect to the elongated axis: The trapping power is 5 Watts, the number of atoms is $1.25 \cdot 10^5$, $2.5 \cdot 10^5$, $5 \cdot 10^5$ at a temperature of 45 μK.
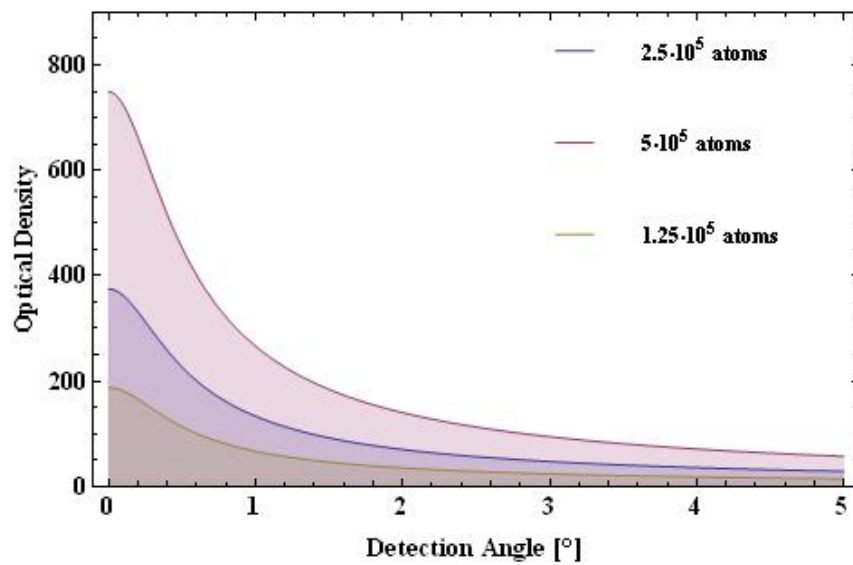

Figure 5.19: Optical density as a function of the detection angle with respect to the elongated axis: The trapping power is 8 Watts, the number of atoms is $1.25 \cdot 10^5$, $2.5 \cdot 10^5$, $5 \cdot 10^5$ at a temperature of 45 μK.
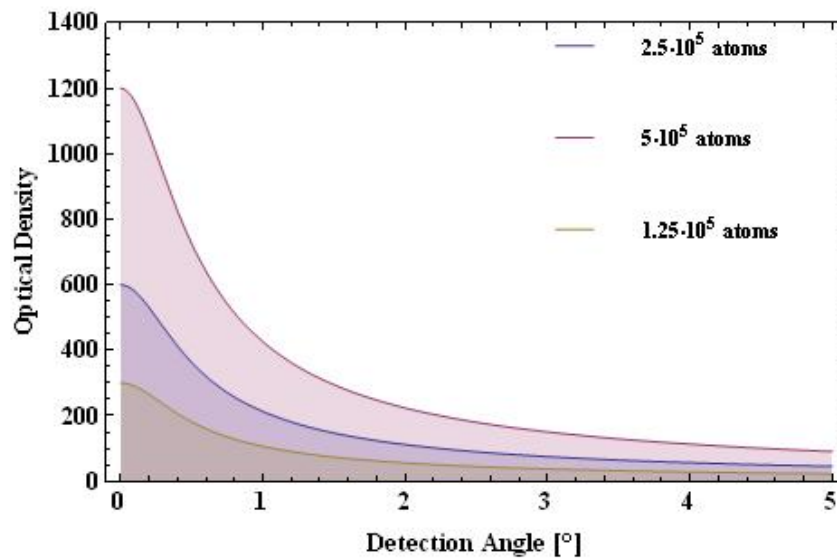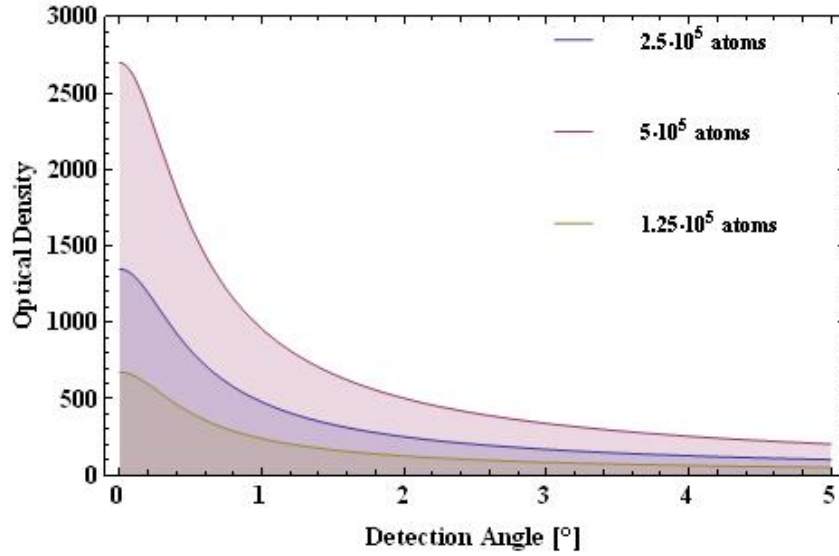
Figure 5.20: Optical density as a function of the detection angle with respect to the elongated axis: The trapping power is 8 Watts, the number of atoms is $1.25 \cdot 10^5$, $2.5 \cdot 10^5$, $5 \cdot 10^5$ at a temperature of 20 μK.
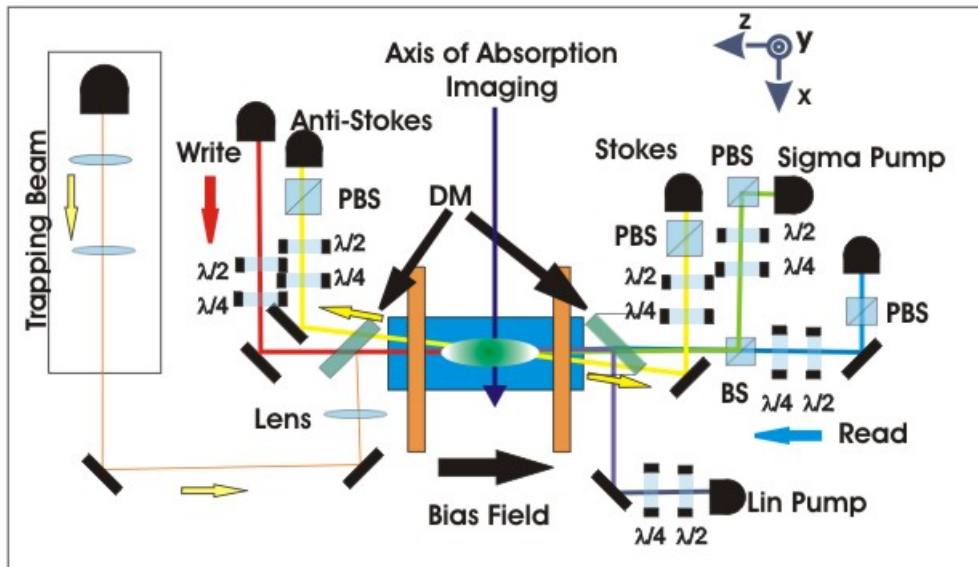

Figure 5.21: Schematic set-up: The *write* and *read* beams are counter propagating. The pumping beams are overlapped with these beams. The dichroic mirrors (DM) are used to overlap these four beams with the trapping beam. The polarizing beam splitters (PBS) guarantee a linear polarization after the fiber couplers. The half- and quarter wave plates are necessary in order to achieve a good circular/linear polarization after the DMs which alter any polarization state. The axis of the detection optics is tilted by 2 degree with respect to the *z*-axis. In the Stokes and Anti-Stokes channel there is an additional DM which is not drawn in order to remove leakage light from the optical dipole trap.

the computer's resources for transferring the images from the camera to the hard drive, an additional computer analyzes the images with a Matlab[28] program [143]. It computes the number of atoms, the size of the cloud and the atomic density. A fourth computer controls a LogicBox built by our workshop which generates the fast pulses for the actual experimental trials. The box has a 40 MHz clock and a FPGA chip generating the signal pulses. By the help of a Labview toolbox the VHDL code is prepared and downloaded by USB to the logic box. The computer houses the multiscaler card for analysis of the signals from the single photon detectors as well.

---

[28]Mathworks

5.4   Experimental Procedures

In this section we describe experimental procedures which are important tools for preparing the experiments. Since the work with the optical dipole trap (ODT) is more complex that the experiments with the MOT there is the need for a larger "toolbox" in order to characterize the atomic ensemble.

5.4.1   Imaging

For adjustment and optimization of the experimental parameters one needs information of the atomic ensemble like position, atom number, temperature and internal state. The detection of light emitted or absorbed by the atoms is a standard way to gain the necessary information. There are three well investigated methods available: fluorescence-, absorption- and phase contrast imaging [147].
In our experiments we have used fluorescence imaging for a rough determination of the atom number in the MOT. The number of atoms N can be estimated from the intensity of the light scattered from the trap. The light within a solid angle Ω is collected by a lens and detected with a calibrated photo diode. The light is converted into an electrical current with efficiency α. Then the number N is given by

$$N = \frac{2\tau}{\hbar\omega} \times \frac{I}{\alpha} \times \frac{4\pi}{\Omega}, \qquad (5.27)$$

where τ is the life time of the excited state and ν the corresponding transition frequency. This equation assumes that the transition is not saturated.
A more advanced method is absorption imaging which can provide in addition spatial information on the ensemble's properties. Let us consider N two-level atoms with a three-dimensional density distribution $n(\mathbf{r})$. A light beam with intensity I is absorbed by atoms during its propagation along direction z according to

$$dI = -I\sigma_{abs}(\delta, I)n(\mathbf{r})dz, \qquad (5.28)$$

where σ_{abs} is the general absorption cross section which depends on the detuning δ and the intensity:

$$\sigma_{abs}(\delta, I) = \frac{\alpha\sigma_{abs}^0}{1 + \alpha I/I_s + 4\delta^2/\Gamma^2} \qquad (5.29)$$

The resonant absorption cross section for a two level atom ($\lambda = 780.240$ nm) is $\sigma_{abs}^0 = 3\lambda^2/2\pi = 2.9 \cdot 10^{-13} m^2$. The saturation intensity is $I_S \approx 1.6$ mW/cm². The correction factor is $\alpha = 7/15$ if all atoms are equally distributed over the Zeeman manifold [124].
The transmission after passing the ensemble along $\mathbf{z}$ direction is given by the ratio of the final to the initial light intensity:

$$T(x, y) = \frac{I_f(x, y)}{I_0(x, y)} = \exp\left(\sigma_{abs}\int_{-\infty}^{+\infty} n(\mathbf{r})dz\right). \qquad (5.30)$$

It depends on the integrated column density $\tilde{n}(x,y) = \int_{-\infty}^{+\infty} n(\mathbf{r})dz$. Thus by measuring the two-dimensional transmission with a camera, we can calculate for small probe intensities the atomic density distribution integrated along $\mathbf{z}$ by

$$\tilde{n}(x,y) = \frac{1}{\sigma_{abs}^0} \left(1 + \frac{4\delta^2}{\Gamma^2}\right) \ln\left(\frac{I_f(x,y)}{I_0(x,y)}\right). \tag{5.31}$$

After integration over the remaining two dimensions we obtain the total number of atoms. Mainly due to intensity fluctuations of the imaging beam, background light and interference fringes we have fluctuations in the number of atoms of $\pm 5\%$.

From time of flight (TOF) images, i.e. images of the atoms after their release from the trap, one can determine the temperature of the ensemble. During the time of flight the width of the cloud increases as simulated in figure (5.22). The density distribution of the ensemble is a Gaussian function with an initial radial width $\sigma_r(0)$. After the release the width evolves according to

$$\sigma_r(t) = \sqrt{\sigma_r(0)^2 + \sigma_v(t)^2} = \sqrt{\sigma_r(0)^2 + \frac{k_B T t^2}{m}}, \tag{5.32}$$

depending on the temperature T, where t is the time of flight after the release. Thus by determining the ensemble width for various times t and subsequent fitting of equation (5.32) one can compute the temperature of the ensemble in the trap.

Figure (5.23) shows the experimental set-up implemented for the absorption imaging. The CCD camera [29] has a back-illuminated CCD chip with 1024×1024 pixels of size $13~\mu$m $\times$ $13~\mu$m and an image depth of 16 bit. The quantum efficiency at 780 nm is $\sim 90\%$. It can be triggered externally, but it does not have a frame transfer mode. The camera is TEC-cooled to $-70°$ C in order to obtain a small dark count rate. The transfer of the image to the control computer is done by USB. A Matlab program described in [143] analyzes the three images (light with atoms, light, background) taken and displays the fitting results.

5.4.2   Loading the Dipole trap

The optical dipole trap has a potential depth of ≈ 0.6 mK. In order to trap atoms in it they must be precooled. Since our trapping laser provides sufficient power to enable that trap depth we can load the atoms from a MOT into the trap. A MOT typically collects $\sim 10^8$ atoms with a temperature of $\sim 100~\mu$K. An obstacle is that the volume of the dipole trap is much smaller than the MOT. Therefore increasing the density of the precooled atoms before loading into the dipole trap is needed. Secondly radiative collisions enhanced by the strong MOT lights complicate an effective loading [148].

We use three stages in order to prepare a sufficiently large and cold ensemble in the optical dipole trap: loading of the MOT, a dark-MOT phase for increasing the density and a short molasses cooling as last phase [149][150]. In figure (5.24) the
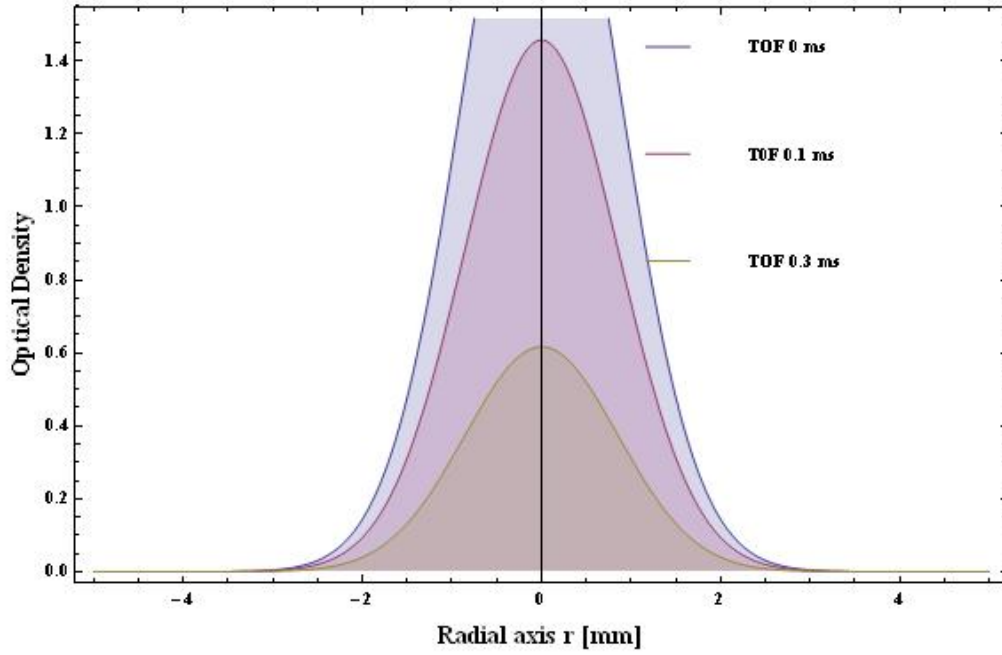
---

[29] Andor Ikon-M

Figure 5.22: Simulation of the optical density perpendicular to elongated axis for various TOF points. The trapping power is 7 Watts, the number of atoms is $5 \cdot 10^5$ at a temperature of 45 μK. It agrees well with the observed data.
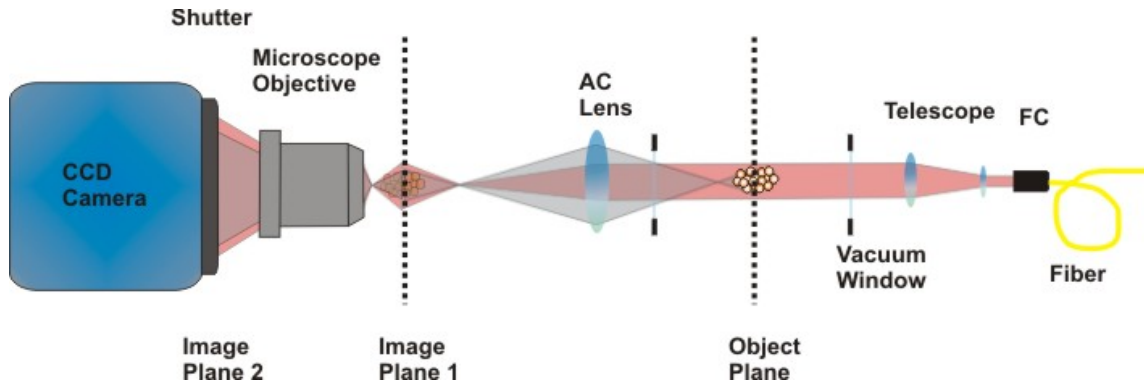

Figure 5.23: Schematic set-up of the absorption imaging: The imaging light is guided by a fiber to the chamber. A telescope expands the beam which exits the fiber coupler to ~ 1 inch diameter. It enters the vacuum chamber trough a CF 16 viewport. The atom cloud is imaged by an achromatic lens outside the chamber with a focal length of $f \sim 16$ cm. It creates a real image by a 1:1 magnification which is magnified by an aspheric microscope objective. It has a magnification of $M = 4$ and creates the image on CCD chip of the camera. Since the internal shutter of the camera induces vibrations and cause interference patterns in the processed images an external shutter is used. It is suspended from the steel rack above the optical table. The diffraction limited resolution of the imaging is ≈ 3.25 μm per camera pixel.
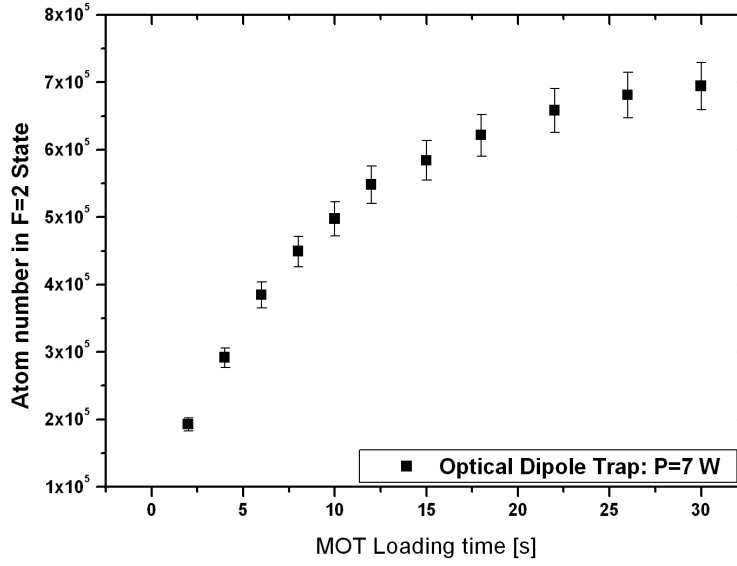
Figure 5.24: Number of atoms in the Dipole trap (P=7 Watts) over the MOT loading time: after 30 seconds the saturation limit is reached.

dependence of the number of atoms in the optical dipole trap as a function of the MOT loading time is depicted. After ~ 30 seconds loading time the saturation limit is reached with a number of $\sim 7 \cdot 10^5$ atoms in the dipole trap. In order to obtain a high repetition rate for our experiments we typically restrict the MOT loading time to 2 seconds resulting in $\sim 2 \cdot 10^5$ trapped atoms.

Determination of heating Various heating mechanisms in an optical dipole trap increase the temperature of the atomic ensemble. As we have seen in chapter 4 an increased temperature can accelerate the dephasing of the spin wave. By measurement of the ensemble's temperature when varying the trap time T we can estimate the heating rate. From figure (5.25) it can be read that the temperature is roughly constant with an average value of 45 μK. Even for lower temperatures down to 20 μK no significant heating has been observed.

Determination of lifetime The lifetime of the atoms in the trap is a measure how long an atomic ensemble can be confined. As already mentioned different collisions and heating processes trigger the escape of atoms from the trap. In figure (5.26) the life time of the atomic ensemble is depicted. In order to prepare over 95 % of the atoms in the $|F = 1\rangle$ state the repumper light is switched off in the loading phase 3 milliseconds before the cooler. After the trapping time T the repumper is switched on for 1 millisecond before the imaging light which is resonant on the transition $F = 2 \rightarrow F' = 3$. From figure (5.26) we determine an exponential decrease of the
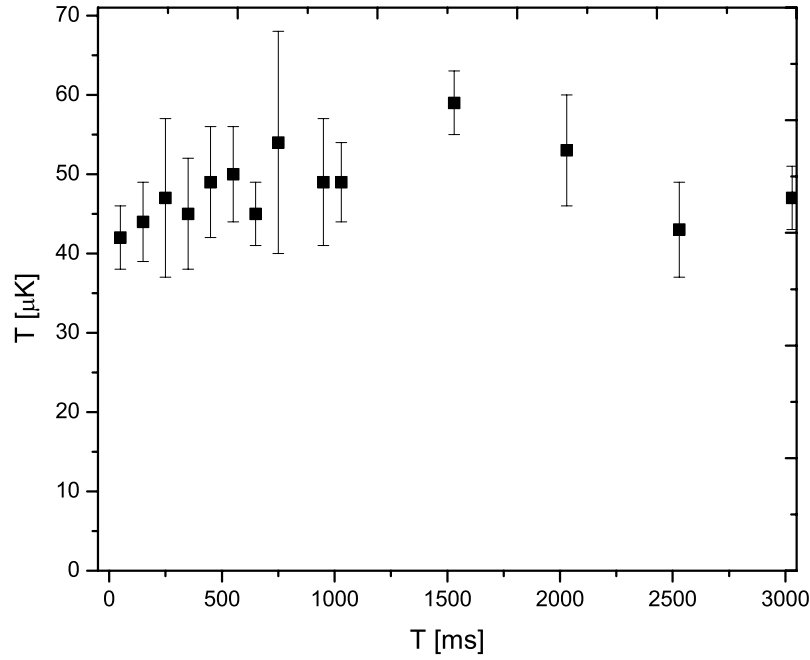
Figure 5.25: Temperature of the trapped atoms for various trapping times: within the errors the temperature is constant over 3 seconds.

number of atoms with time constant $\tau_{F=1} = 19 \pm 2$ s which is mainly due to collisions with the background gas. By switching off the dispensers during the trap time, they could be further reduced.

In the case when all atoms are prepared in the $|F = 2\rangle$ ground state there is an additional loss mechanism present. The loss of atoms can be described by the model [140]:

$$\frac{dN(t)}{dt} = -\frac{N(t)}{\tau} - \beta N(t)^2. \tag{5.33}$$

A bi-exponential fit to the data [143] yields the two decay times of $\tau_{F=2} = 14 \pm 1$ s and $\beta = 2.6 \pm 0.5$ s^{-1}.

In summary, we are able to confine the atoms for tens of seconds without significant heating. But it is important to prepare the ensemble in the $|F = 1\rangle$ state in contrast to the MOT experiments.

5.4.3 Microwave Spectroscopy: Magnetic Field Measurement and State Population

The optical pumping into a single Zeeman-sublevel of the ground state is necessary in order to prevent dephasing between the components and obtain a long life time (see section (4.5.2)). For the magnetic bias fields we can apply with our coils of ≈ 5 G it is not possible to resolve the population of the individual Zeeman sublevels with single photon transitions. In order to have a Zeeman splitting which is larger than the natural linewidth one needs more than 10 G.
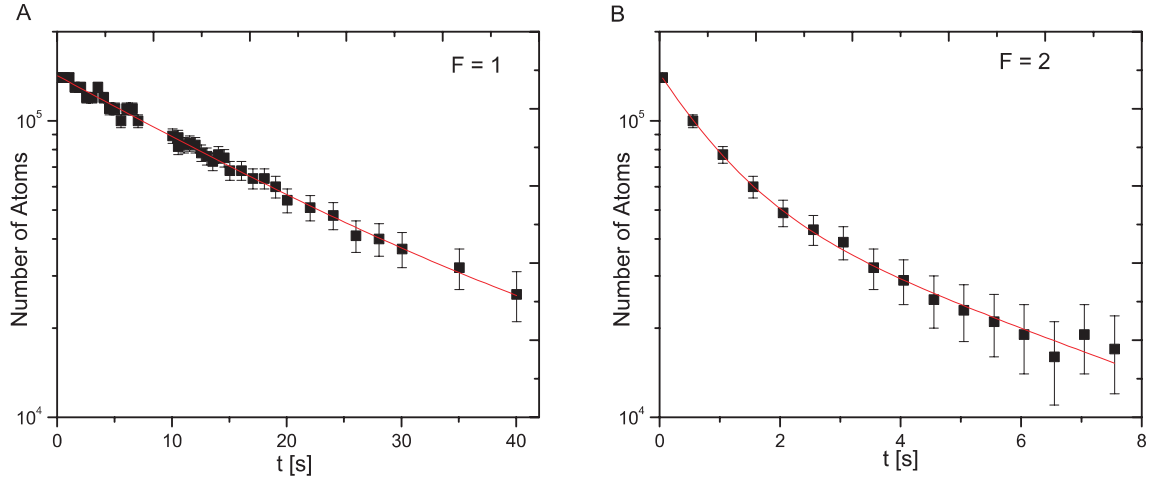
Figure 5.26: Life time of atoms in the ODT: A) During the trap time t all the atoms are in the $|F = 1\rangle$ ground state. B) If all the atoms are in groundstate $|F = 2\rangle$, the loss from the trap is significantly higher.

We use microwave spectroscopy in the experiments with the optical dipole trap in order to determine the population of the individual Zeeman sublevels. As one can see from figure (5.28) the linewidth of the transitions is of the order of 10 kHz which is sufficient to resolve a Zeeman splitting even at low magnetic fields. A home-built helical microwave antenna is adjusted at a 45 degree angle with respect to the axis of the magnetic bias field. A commercial[30] 10 Watt amplifier with a fixed gain of 54 dB provides the power. At its input a TTL-controlled microwave switch[31] opens for a pulse of 100 μs 1 millisecond before the atoms are released from their confinement and imaged. A microwave frequency synthesizer[32] generates the microwave signal corresponding to the hyperfine splitting of ν_0 =6.834680 GHz. It is connected via GPIB to the experimental control computer. Thus it can be detuned from the frequency ν_0 in steps of 10 kHz and its output power can be changed.

Let us consider the atomic ensemble is trapped in the $|F = 1\rangle$ state and a bias field of 0.8 G is applied until the end of the experimental cycle. The Zeeman degeneracy of the sublevels is lifted according to $\Delta E_{|F,m_F\rangle} = \mu_B g_F m_F B_{bias}$ and there are 9 possible transitions between the sublevels in $|F = 1\rangle$ and $|F = 2\rangle$ (see figure (5.27)). Since two pairs are degenerate there are seven different transition frequencies. Our imaging beam is tuned to the transition $F = 2 \rightarrow F' = 3$. Thus we adjust the microwave frequency to one of the resonances and adjust the output power of the synthesizer to transfer the corresponding population of the $|F = 1, m_F = i\rangle$ level to the $|F = 2, m_F = j\rangle$ level by the microwave pulse. Then the atoms are imaged and their number is computed. In figure (5.28) the blue data shows the number of atoms in the $|F = 2\rangle$ over the detuning of the microwave from the hyperfine splitting ν_0. The ensemble has not been optically pumped, therefore for all seven transition frequencies atoms are detected. The height of the peaks does not only depend on

---

[30]Miteq: AMF-5B-0680-39P-TTL
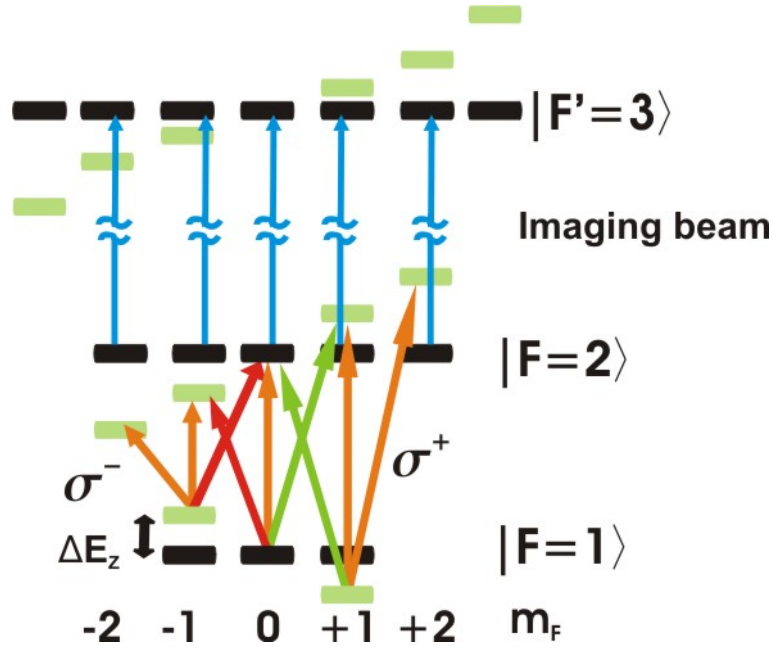[31]Miteq: N136A-D-F-1
[32]Wiltron 6747A-20

Figure 5.27: Transitions for the microwave spectroscopy: All atoms are prepared in the $|F = 1, M_F = -F, .., +F\rangle$ manifold. If the microwave field contains all polarizations all the transitions can be addressed by varying the microwave frequency. The red transitions are degenerate as well as he two green transitions. Thus there are seven distinct transition frequencies. The imaging beam on the D_2 line is resonant with the transition $|F = 2\rangle \rightarrow |F' = 3\rangle$. The frequency is adjusted to compensate the AC-Stark shift. For small magnetic fields the Zeeman splitting can be neglected compared to the natural linewidth. Since there is no closed cycling transition the atom number has to be corrected by taking the corresponding transition probabilities into account.

the initial distribution of the population across the Zeeman sublevels, but on the transition strength as well.

The red data in figure (5.28) shows the distribution of the population. Before the microwave pulse linear pump light resonant to the $F = 2 \rightarrow F' = 2$ and a simultaneous $\sigma^{(-)}$ pump light resonant to the $F = 1 \rightarrow F' = 1$ transition is applied for 8 milliseconds along the propagation axis. The intensities are of the order of the saturation intensity for the transition, but the detuning is not very well optimized to compensate the light shift of the optical dipole trap. The red data shows only three transitions and the total atom number is similar to the one when the magnetic field is not on during the imaging. This conclusion is, that we have optically pumped the atoms in the $|F = 1, m_F = -1\rangle$ state.
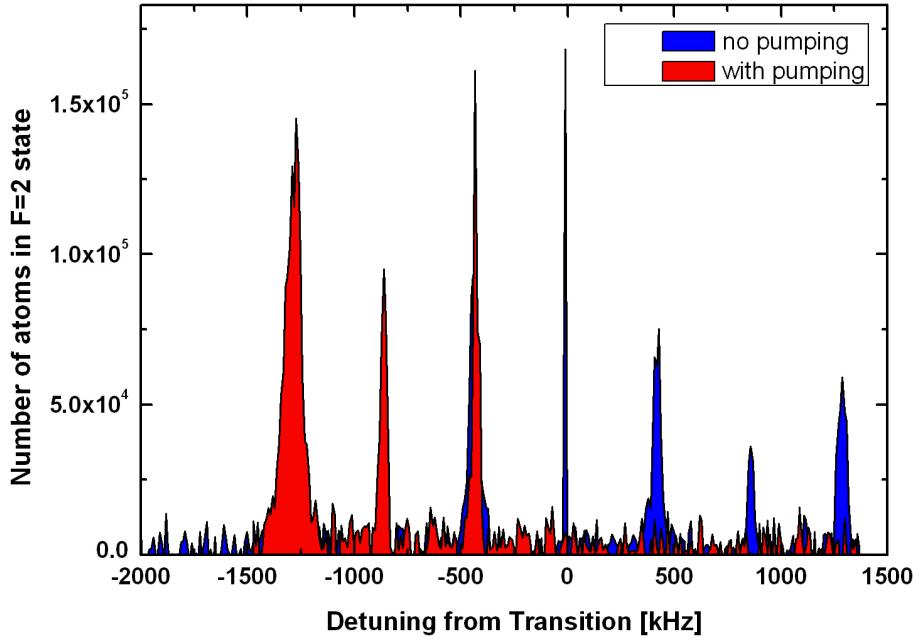
Figure 5.28: Microwave spectroscopy in the optical dipole trap: The transition frequency on the left side corresponds to the $|F = 1, m_F = -1\rangle \rightarrow |F = 2, m_F = -2\rangle$ transition. The next one to the right is the $|F = 1, m_F = -1\rangle \rightarrow |F = 2, m_F = -1\rangle$ transition. The next peak corresponds to the degenerate transitions $|F = 1, m_F = -1\rangle \rightarrow |F = 2, m_F = 0\rangle$ and $|F = 1, m_F = 0\rangle \rightarrow |F = 2, m_F = -1\rangle$. The center frequency corresponds to the $|F = 1, m_F = 0\rangle \rightarrow |F = 2, m_F = 0\rangle$ transition which is first-order magnetic field insensitive. $|F = 1, m_F = 0\rangle \rightarrow |F = 2, m_F = 1\rangle$ and $|F = 1, m_F = 1\rangle \rightarrow |F = 2, m_F = 0\rangle$, $|F = 1, m_F = 1\rangle \rightarrow |F = 2, m_F = 1\rangle$ and $|F = 1, m_F = 1\rangle \rightarrow |F = 2, m_F = 2\rangle$ correspond to the remaining three peaks.

Chapter 6

Quantum memory based Single Photon Sources and Application

In this chapter we describe the experiments demonstrating the performance of single photon sources based on DCLZ-type quantum memories.

6.1 Deterministic Single Photon Source

6.1.1 Motivation

Although weak coherent beams can be used as a pseudo single-photon source, the advent of quantum information processing (QIP) has placed stringent requirements on single photons either on demand or heralded [151]. In particular, linear optical quantum computation [48] depends on the availability of such single-photon sources. The single-photon nature guarantees unconditional security and high efficiency in quantum cryptography [9]. Different approaches have been attempted in the last decade to develop an on-demand single-photon source, such as quantum dots [152, 153], single atoms and ions [99, 154], and color centers [155]. However, all of them are confronted with different challenges. For example, the single-atom implementation provides spectrally narrow single photons with a well defined spatial mode, but the manipulation of single atoms requires sophisticated techniques and expensive setups [99]. Quantum dots are a potential source with high single-photon rate, but the requirement of spectral filtering entails inevitable losses. It is very difficult to prepare truly identical sources due to inhomogeneities in both the environment of the emitters and the emitters itself [156]. Color centers are excellent sources, even at room temperature, however, the high peak intensities of a pulsed excitation can lead to complex and uncontrollable dark states [151]. So it has been taken as a formidable task to develop a promising deterministic single-photon source.

Moreover, an important challenge in distributed QIP is the controllable transfer of

quantum state between flying qubit and macroscopic matter. Starting from a recent proposal for long-distance quantum communication with atomic ensembles [42], it is possible to implement both a single-photon source on demand and controllable transfer of quantum state between a photonic qubit and macroscopic matter, provided that proper feedback is applied. A single spin excitation can be generated in an atomic ensemble by applying a series of subsequent clear (optical pumping) and write pulses stimulating spontaneous Raman scattering. The successful generation of a spin excitation is indicated by the detection of a corresponding Raman photon. This information is used as feedback to stop the sequence, and further on to start the next process, for example to convert the spin excitation back into a single photon. Such a sequence can be taken as having a feed-forward ability for the deterministically converted single photon.[58]

Recently, significant experimental progresses have been achieved in demonstration of quantum storage and single-photon sources [54, 63, 58, 104], and even entanglement between two atomic ensembles [55, 157] has been generated. However, coincidence-based post-selection was used in these experiments. No feedback was applied and consequently the requirement of resources would increase exponentially with each new step of operation. This significantly limits the scalability of the schemes [48, 42].

6.1.2   Experiment

In this section, we present an experimental realization of a deterministic and storable single-photon source. Single spin excitations in an atomic ensemble are generated by detecting anti-Stokes photons from spontaneous Raman scattering. This detection allows to implement feed-forward and convert the spin excitations into single photons at a predetermined time. It is shown that the single-photon quality is conserved while the production rate of single photons can be enhanced significantly by the feedback circuit. In principle, the spatial mode, bandwidth, and frequency of single-photon pulses are determined by the spatial mode, intensity and frequency of the retrieve laser [104]. It is feasible to integrate such a single-photon source with the storage medium, atomic ensembles. Together with the technology developed in previous experiments [54, 63, 58, 104, 55, 157], our controllable single-photon source potentially paves the way for the construction of scalable quantum communication networks [42, 41] and linear optical quantum computation [48].

The basic concept of our experiments is shown in Fig. 6.1. Cold atoms with Λ-type level configuration (two ground state $|a\rangle$, $|b\rangle$ and an excited state $|e\rangle$) collected by a magneto-optical trap (MOT) are used as the media for quantum memory. The atoms are initially optically pumped to state $|a\rangle$ by a pump laser. Then a weak classical *write* pulse, with the Rabi frequency Ω_W, close to the resonance of transition $|a\rangle$ to $|e\rangle$ is introduced in the atomic cloud. Due to the spontaneous Raman process, a photon of anti-Stokes field $\hat{a}_{AS}$ is emitted into the forward scattering mode. Simultaneously, a collective spin excitation corresponding to the mode of the anti-Stokes field $\hat{a}_{AS}$
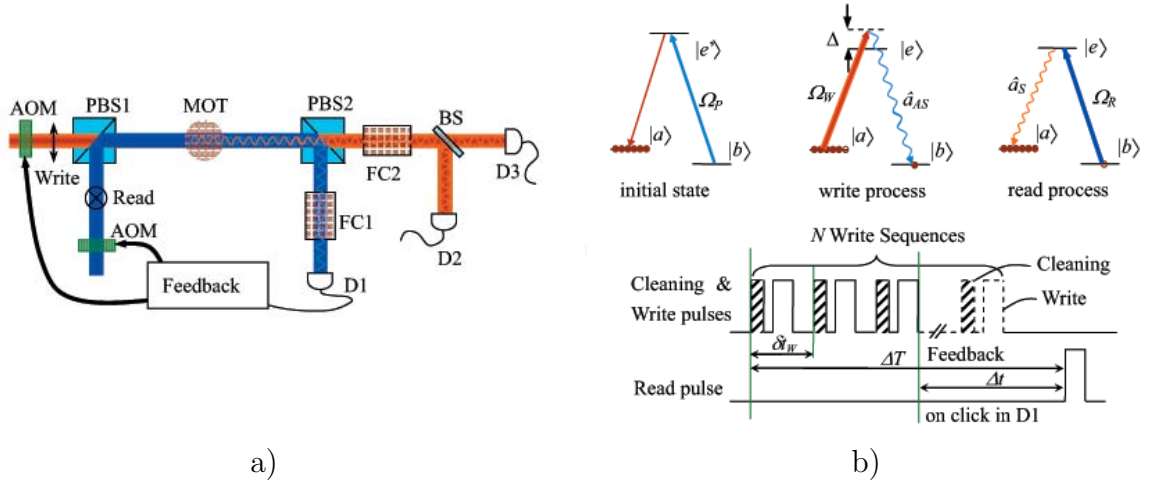
a) b)

Figure 6.1: Illustration of the experimental setup (a) and the time sequence with the feedback circuit for the *write* and *read* process (b). The atomic ensemble is firstly prepared in the initial state $|a\rangle$ by applying a pump beam resonant with the transition $|b\rangle$ to $|e'\rangle$. A write pulse with the Rabi frequency Ω_W is applied to generate the spin excitation and an accompanying photon of the mode $\hat{a}_{AS}$. Waiting for a duration Δt, a read pulse is applied with orthogonal polarization and spatially overlap with the write beam in PBS1. The photons, whose polarization is orthogonal to that of the write beam, in the mode $\hat{a}_{AS}$ are spatially extracted from the write beam by PBS2 and detected by detector D1. Similarly, the field $\hat{a}_S$ is spatially extracted from the Read beam and detected by detector D2 (or D3). Here, FC1 and FC2 are two filter cells, BS is a 50/50 beamsplitter, and AOM1 and AOM2 are two acousto-optic modulators.

is generated in the atomic ensemble [42, 158]. The state of the field $\hat{a}_{AS}$ and the collective spin state of the atoms can be expressed by the superposed state

$$|\Psi\rangle \sim |0_{AS}0_b\rangle + \sqrt{\chi}|1_{AS}1_b\rangle + \chi|2_{AS}2_b\rangle + O(\chi^{3/2}), \qquad (6.1)$$

where χ is the excitation probability of one spin flip, $|i_{AS}i_b\rangle$ denotes the i-fold excitation of the anti-Stokes field and the collective spin. Ideally, conditioned on detecting one and only one anti-Stokes photon in detector D1, a single spin excitation is generated in the atomic ensemble with certainty. After a controllable time delay δt (in the order of the lifetime τ_c of the spin excitation), another classical *read* pulse with the Rabi frequency Ω_R, which is on-resonance with the transition from $|b\rangle$ to $|e\rangle$, is applied to retrieve the spin excitation and generate a photon of Stokes field $\hat{a}_S$.

In our present experiment, more than 10^8 ^{87}Rb atoms are collected by the MOT with an optical depth of about 5 and the temperature of about $100\,\mu$K. The earth magnetic field is compensated by three pairs of Helmholtz coils. The two ground states $|a\rangle$ and $|b\rangle$ and the excited state $|e\rangle$ in the Λ-type system are $|5S_{1/2}, F = 2\rangle$, $|5S_{1/2}, F = 1\rangle$, and $|5P_{1/2}, F = 2\rangle$, respectively. The write laser is tuned to the transition from $|5S_{1/2}, F = 2\rangle$ to $|5P_{1/2}, F = 2\rangle$ with detuning of $+10$ MHz and the read laser is locked on resonance to the transition from $|5S_{1/2}, F = 1\rangle$ to $|5P_{1/2}, F = 2\rangle$. By using orthogonal polarizations, write and read beams are spatially overlapped on

a polarized beam splitter (PBS1), and then focused into the cold atoms with the beam waist of 35 μm. After passing the atomic cloud, the two beams are split by PBS2 which serves as the first stage of filtering the write (read) beam out from the anti-Stokes (Stokes) field. The leakage of write (read) field from PBS2 propagating with the anti-Stokes (Stokes) field will be further filtered by a thermal cell filled with ^{87}Rb atoms, in which the rubidium atoms are prepared in state $|5S_{1/2}, F = 2\rangle$ ($|5S_{1/2}, F = 1\rangle$) initially. Coincident measurements among D1, D2 and D3 are performed with a time resolution of 2 ns.

After switching off the MOT, the atoms are optically pumped to the initial state $|a\rangle$. The write pulse containing about 10^4 photons with a duration of 100 ns is applied onto the atomic ensemble, to induce the spontaneous Raman scattering via $|a\rangle \to |e\rangle \to |b\rangle$. The state of the induced anti-Stokes field and the collective spin in Eq. (6.1) is generated with a probability $\chi \ll 1$. After a controllable delay of δt, the read pulse with the duration of 75 ns is applied for converting the collective excitation into the Stokes field. In comparison, the intensity of the read pulse is about 100 times stronger than that of the write one.

Assume the probability to have an anti-Stokes (Stokes) photon is p_{AS} (p_S), and the coincident probability between the Stokes and anti-Stokes channels is $p_{AS,S}$, then the intensity correlation function $g^{(2)}_{AS,S} = p_{AS,S}/(p_{AS}p_S)$. We measured the variation of $g^{(2)}_{AS,S}$ as a function of p_{AS} shown in Fig. 6.2(a) with a time delay of $\delta t = 500$ ns. Considering the background in each channel, we obtain

$$p_{AS} = \chi\eta_{AS} + B\eta_{AS}, \tag{6.2a}$$

$$p_S = \chi\gamma\eta_S + C\eta_S, \tag{6.2b}$$

$$p_{AS,S} = \chi\gamma\eta_{AS}\eta_S + p_{AS}p_S. \tag{6.2c}$$

Here, η_{AS} and η_S are the overall detection efficiencies in the anti-Stokes and Stokes channels respectively, which include the transmission efficiency η_t of filters and optical components, the coupling efficiency η_c of the fiber couplers, and the quantum efficiency η_q of single photon detectors (η_{AS} includes an additional spatial mode-match efficiency η_m [58]), γ is the retrieve efficiency which is a time-dependent factor, and B (C) is determined by the background in the anti-Stokes (Stokes) channel. The red curve in Fig. 6.2(a) is the least-square fit result according to Eq. (6.2), assuming $B = 0$ for simplicity. The efficiency in the anti-Stokes channel is observed as $\eta_{AS} \sim 0.07$ and the retrieve efficiency $\gamma \sim 0.3$. The largest correlation $g^{(2)}_{AS,S}$ (101 ± 6) appears at the lowest excitation probability p_{AS} (3.5×10^{-4}).

The finite lifetime of the spin excitation results from the dephasing of the collective state due to the Larmor precession of the spins in the residual magnetic field. It can be characterized by the decay of the retrieve efficiency $\gamma(\delta t) = \gamma_0 \exp(-\delta t^2/\tau_c^2)$ [58], where τ_c is the lifetime of the collective state. It can be determined from the decay of the measured intensity correlation function $g^{(2)}_{AS,S}(\delta t)$ as shown in Fig. 6.2(b), taken
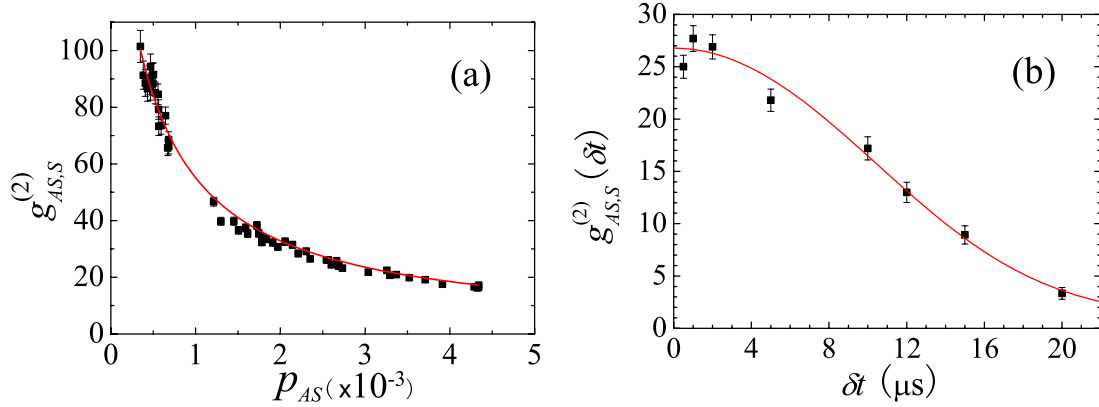
Figure 6.2: Intensity correlation function $g^{(2)}_{AS,S}$ along the excitation probability p_{AS} with $\delta t = 500$ ns (a) and along the time delay δt between read and write pulses with $p_{AS} = 3 \times 10^{-3}$ (b). The black dots are obtained from current experiment and the curves correspond to a least-square fit procedure according to Eq. (6.2) and (6.3). The observed lifetime is $\tau_c = 12.5 \pm 2.6$ μs.

at $p_{AS} = 0.003$. Using Eq. (6.2), the intensity correlation function reads

$$g^{(2)}_{AS,S}(\delta t) = 1 + \frac{\gamma(\delta t)}{(B + \chi)\gamma(\delta t) + D}, \tag{6.3}$$

where C is absorbed by the new constant D. Our data give a lifetime of $\tau_c = 12.5 \pm 2.6$ μs. The cross correlation of the first point is slightly lower which might be caused by noise arising from the elastic scattering of the write beam.

In order to increase the efficiency of the single-photon source we apply a feedback protocol. As shown in Fig. 6.1(b), in the time interval ΔT, N independent write sequences with a period of δt_W are applied to the atomic ensemble. Each write sequence contains a cleaning pulse (the optical pumping to the initial state) and a write pulse. Once an anti-Stokes photon is detected by D1 the feedback circuit stops the further write sequence and enables the read pulse to retrieve the single Stokes photon after a time delay Δt. The maximum number of trials (N) is given by the life time of the excitation. The feedback protocol enhances the production rate of Stokes photons according to the new excitation probability $P_{AS} = \sum_{i=0}^{N-1} p_{AS}(1 - p_{AS})^i$ while the single-photon quality is conserved.

Our protocol can be executed in different modes. In a first mode, one can fix the retrieve time ΔT. Therefore, the delay Δt varies because the spin excitation is created randomly by one of the write sequences. Single photons are produced at a given time with a high probability, ideally approaching unity if $N \gg 1$. Furthermore, the retrieve efficiency could be improved significantly by an increased optical depth of the atomic ensemble and an optimal retrieve protocol [106]. This mode serves as a deterministic single-photon source. In a second mode, we retrieve the single photon with a fixed delay Δt after a successful write. More general the imprinted single excitation can be converted into a single photon at any given time with the
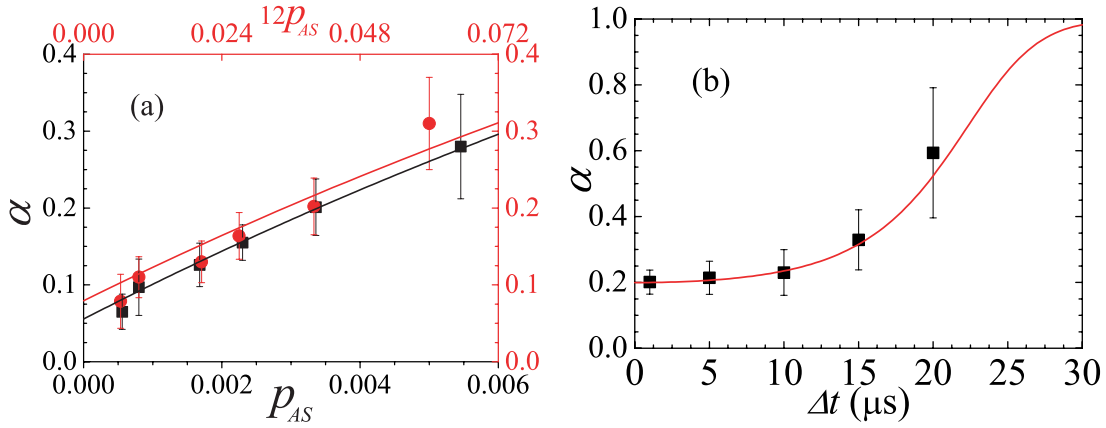
Figure 6.3: The anti-correlation parameter as a function of p_{AS} (a) and Δt (b). In Fig (a), the data in black correspond to the experiment without feedback circuit, in which each write sequence is followed by one read pulse. The data in red correspond to the experiment with feedback circuit, in which 12 successive write sequences are followed by one read pulse. The red curve is the theoretical evaluation taking into account the fitted background of the black dots. In Fig (b), 12 write sequences were applied in each trial while measuring. The excitation probability is fixed to $p_{AS} \approx 3.5 \cdot 10^{-3}$.

life time τ_c. This is well suited for a quantum repeater [41, 42] where one needs to synchronize the nodes.

In the first experiment, we fixed $\Delta T = 12.5$ μs and $\delta t_W = 1$ μs, and $N = 12$ subsequent write sequences were applied. The quality of the single-photon source can be characterized by the anti-correlation parameter α [159], which is equivalent to the second-order auto-correlation function $g_{s,s}^{(2)}$ of the Stokes photon on the condition of an anti-Stokes photon is detected. When we use N write pulses and the feedback protocol, the detection probabilities in D2, D3 and the coincidence detection probability D23 conditioned on a registration of an anti-Stokes photon in D1 are

$$P_{m|AS} = \frac{\sum_{i=0}^{N-1} p_{AS}(1 - p_{AS})^i p_{m|AS}(\Delta T - n \cdot \delta t_w)}{\sum_{i=0}^{N-1} p_{AS}(1 - p_{AS})^i}, \tag{6.4}$$

where $m = 2$, 3, 23 and $p_{m|AS}(\Delta T - n \cdot \delta t_w)$ is a time-dependent probability conditioned on a click in the anti-Stokes channel. The anti-correlation parameter α is given by $P_{23|AS}/(P_{2|AS}P_{3|AS})$.

Fig. 6.3(a) shows the measured α as a function of the excitation probability p_{AS}. For $N = 1$ (black) the variation of α is nearly linear in the region of $p_{AS} = 0 \sim 0.006$. The black curve is the fit according to Eq. (6.4). When using 12 successive write sequences, we plot α versus $12p_{AS}$ as red dots. The red line is a no free parameter calculation from Eq. (6.4), taking the fitted parameters from $N = 1$ setting $N = 12$. We note that, for $p_{AS} \to 0$ the value of α is 0.057 ± 0.028, which in principle should be 0. This offset comes from noise including residual leakage of the write and read beams, stray light, and dark counts of the detectors. However, the advantage of the

feedback protocol is not degraded by such noise. It is verified that α is conserved even with enhanced excitation probability. If the lifetime of the spin excitation is sufficiently long to allow many write sequences, the excitation probability can reach unity while the single-photon nature is still conserved. Then the generation efficiency then only depends on the retrieve efficiency itself.

In the second experiment, we use $\delta t_W = 1$ μs and $N = 12$. Fig. 6.3(b) shows the measured α as a function of Δt. For every Δt, ΔT varies due to the random creation of the spin excitation by the N write sequences. The behavior of $\alpha(\Delta t)$ is related to a reversed profile of $g_{AS,S}^{(2)}(\delta)$ in Fig. 6.2(b). For the delay $\Delta t < \tau_c$, the value of α stays at a low level and varies slowly. For $\Delta t > \tau_c$, $\alpha(\Delta t)$ increases towards 1. But even for a delay of 20 μs ($\sim 2\tau_c$) we find $\alpha \sim 0.6$. A satisfying agreement is observed between the theoretical curve and the experimental data.

Typically, the single spin excitation can be produced at a rate of 600 per second, while with a detected success probability per trial is 2.5%, the overall detection rate of single-photon production is $\sim$15 s^{-1}. As demonstrated in the present work, the lifetime of collective states is important for the quality and production rate of single photons. In the atomic ensemble, the coherence time of the collective state suffers from the residual magnetic field around the MOT and the thermal motion of the atoms. The latter effect is negligible because of the very low temperature of the atomic cloud. Using a better compensation of residual magnetic field or using field insensitive clock states we can significantly increase the lifetime of the collective state. Moreover, by further improving the control circuit, i.e. reducing the period of write pulses, we can apply more write pulses within the lifetime. In particular, in the case with $p_{AS} = 0.003$ and a write period of 300 ns, we can obtain a single-photon source with a probability as high as 95% within a lifetime of 300 μs.

6.1.3 Discussion

In conclusion, we have demonstrated an experimental realization of an controllable single-photon source with atomic storage. The lifetime of the collective spin excitation reaches 12.5 μs. A feedback circuit was constructed to control the generation of the spin excitation and the storage time δt. Being a key device in the scalable quantum communication network, this circuit also shows a promising performance in the enhancement of the excitation probability while the single-photon quality is conserved. This single-photon source is able to work at either a deterministic mode or a time controllable mode heralded by the feedback circuit. The single-photon source based on atomic ensemble has the advantages of narrow band, high quality and controllable character, which is helpful for the construction of scalable quantum information processing system in the future. A related experiment is described in [57].

6.2   Synchronized Independent Narrow-band Single Photons and Efficient Generation of Photonic Entanglement

6.2.1   Motivation

Synchronized generation of either deterministic and storable single photons or entangled photon pairs is essential for scalable linear optical quantum information processing (LOQIP). With the help of quantum memory and feed-forward, one can thus achieve long-distance quantum communication [41, 20, 42] and efficient quantum computation [48, 160, 49, 161]. Very recently, interfering synchronized independent single photons [162] and entangled photon pairs [163] have been experimentally achieved with two pulsed spontaneous parametric down-conversion sources pumped by two synchronized but mutually incoherent femto-second lasers. However, due to the absence of quantum memory for broad-band (a few nm) single photons no feedback was applied in the above experiments, single photons or entangled photon pairs were merely generated probabilistically in each experimental run, i.e. with a small probability p. Thus, in an experiment concerning manipulation of N synchronized single (or entangled) photon sources, the experimental efficiency will decrease exponentially with the number of sources (proportional to p^N). Moreover, the short coherence time of down-converted photons ($\sim$ a few hundred fs, defined by the bandwidth of interference filters) also makes hard the overlap of photon wavepackets coming from two distant sites. These two drawbacks together make the above experiments inappropriate for scalable LOQIP.

Following a recent proposal for long-distance quantum communication with atomic ensembles [42] (see also the improved schemes [43][44][46]), it is possible to generate narrow-band single photons or entangled photon pairs in a deterministic and storable fashion. In the past years, significant experimental progresses have been achieved in demonstration of quantum storage and single-photon sources [58, 104], and even entanglement in number basis for two atomic ensembles has been demonstrated experimentally [64]. Moreover, deterministic narrow-band single-photon sources have been demonstrated most recently with the help of quantum memory and electronic feedback circuits [57, 68, 74].

6.2.2   Experiment

In this section, we develop further the techniques used in Ref. [74] to implement synchronized generation of two independent single-photon sources from two remote atomic ensembles loaded by magneto-optical traps (MOT). The two synchronized single photons are further used to demonstrate efficient generation of entangled photon pairs. Since our single-photon sources are generated in-principle in a deterministic and storable fashion, with the help of feed-forward the experimental methods

can be used for scalable generation of photonic entanglement. Moreover, compared to the short coherence time of down-converted photons in Refs. [162, 163] the coherence time of our synchronized narrow-band single photons is about 25 ns, four orders longer, which makes it much easier to overlap independent photon wavepackets from distant sites for further applications of LOQIP. Finally, it is worth noting that the read and write lasers used for different single-photon sources are fully independent to each other. The synchronization was achieved by separate electronic signals generated by the control electronics.

The basic concept of our experiment is illustrated in Fig. 6.4. Atomic ensembles collected by two MOT's 0.6 m apart function as the media for quantum memories and deterministic single-photon sources. Each ensemble consists of about 10^8 ^{87}Rb atoms. The two hyperfine ground states $|5S_{1/2}, F = 2\rangle = |a\rangle$ and $|5S_{1/2}, F = 1\rangle = |b\rangle$ and the excited state $|5P_{1/2}, F = 2\rangle = |e\rangle$ form a Λ-type system $|a\rangle$-$|e\rangle$-$|b\rangle$. The atoms are initially optically pumped to state $|a\rangle$. Shining a weak classical *write* pulse with the Rabi frequency $\Omega_{\rm W}$ into the atoms, creates a superposed state of the anti-Stokes field $\hat{a}_{\rm AS}$ and a collective spin state of the atoms,

$$|\Psi\rangle \sim |0_{\rm AS}0_b\rangle + \sqrt{\chi}|1_{\rm AS}1_b\rangle + \chi|2_{\rm AS}2_b\rangle + O(\chi^{3/2}), \tag{6.5}$$

where $\chi \ll 1$ is the excitation probability of one spin flip , and $|i_{\rm AS}i_b\rangle$ denotes the *i*-fold excitation of the anti-Stokes field and the collective spin. Ideally, conditioned on detecting one and only one anti-Stokes photon, a single spin excitation is generated in the atomic ensemble with certainty. In practice, considering photon loss in the detection, this condition can be fulfilled by keeping $\chi \ll 1$ so as to make the multi excitations negligibly small. After a controllable time delay $\delta t_{\rm R}$ (in the order of the lifetime τ_c of the spin excitation), another classical *read* pulse with the Rabi frequency $\Omega_{\rm R}$ is applied to retrieve the spin excitation and generate a photon in the Stokes field $\hat{a}_{\rm S}$. If the retrieve efficiency reaches unity, the Stokes photon is no longer probabilistic because of the quantum memory and feedback control [74, 68, 57], which now can serve as a deterministic single-photon source. As shown in Fig. 6.4, Alice and Bob both have such a source. They prepare collective spin excitations independently and the one who finishes the preparation first will wait for the other while keeping the collective spin excitation in her/his quantum memory. After they agree that both have finished the preparation, they retrieve the excitations simultaneously at anytime they want within the lifetime of the collective state. Therefore the retrieved photons arrive at the beam splitter with the required timing.

Compared to a probabilistic photon source, the present implementation with atomic ensembles contributes a considerable enhancement to the coincidence rate of single photons coming from Alice and Bob. For instance, we consider a similar setup but without feedback circuit, where Alice and Bob apply write and read in every experimental trial and thereafter measure the four-fold coincidence of anti-Stokes and Stokes photons in the four channels D1, D2, C1 and C2. Assume the probability to have an anti-Stokes photon in channel D1 (D2) is $p_{\rm AS1}$ ($p_{\rm AS2}$) and the corresponding retrieve efficiency for conversion of the spin excitation to a Stokes photon
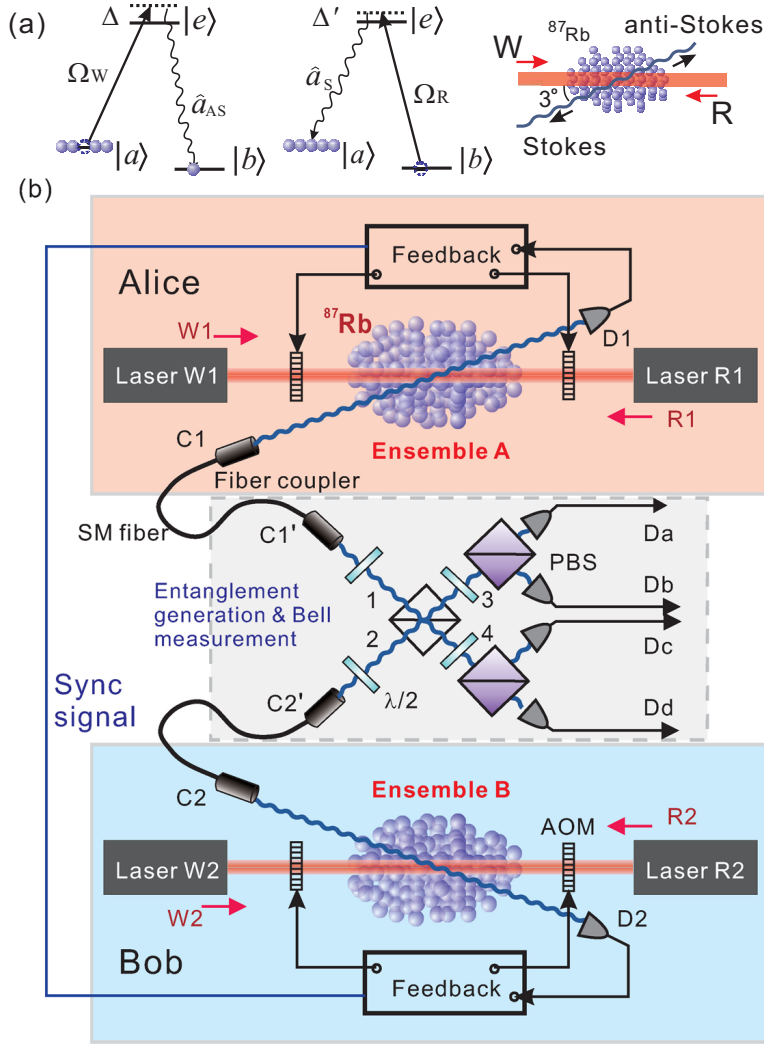
Figure 6.4: Illustration of the relevant energy levels of the atoms and arrangement of laser beams (a) and the experimental setup (b). (a) ^{87}Rb atoms are prepared in the initial state $|a\rangle$. A write pulse Ω_W with the detuning of $\Delta = 10$ MHz and a beam diameter about 400 μm is applied to generate the spin excitation and an accompanying photon of the anti-Stokes field $\hat{a}_{AS}$ with a beam diameter about 100 μm. The mode $\hat{a}_{AS}$, tilted $3°$ from the direction of the write beam, is coupled in a single-mode fiber (SMF) and guided to a single-photon detector. Waiting for a duration δt_R, a read pulse is applied with orthogonal polarization and spatially mode-matched with the write beam from the opposite direction. The spin excitation in the atomic ensemble will be retrieved into a single photon of the Stokes field $\hat{a}_S$, which propagates to the opposite direction of the field $\hat{a}_{AS}$ and is also coupled in SMF. (b) Alice and Bob each keeps a single-photon source at two remote locations. As elucidated in Ref. [74], Alice applies write pulses continuously until an anti-Stokes photon is registered by detector D1. Then she stops the write pulse, holds the spin excitations and meanwhile sends a synchronization signal to Bob and waits for his response (This is realized by the feedback circuit and the acousto-optic modulators, AOM). In parallel Bob prepares a single excitation in the same way as Alice. After they both agree that each has a spin excitation, each of them will apply a read pulse simultaneously to retrieve the spin excitation into a light field $\hat{a}_S$. The two Stokes photons propagate to the place for entanglement generation and Bell measurement. They overlap at a 50:50 beam splitter (BS) and then will be analyzed by subsequent half-wave plates ($\lambda/2$), polarized beam splitters (PBS) and single photon detectors Da, Db, Dc, and Dd.

coupled into channel C1 (C2) is $\gamma_1(\delta t_\mathrm{R})$ [$\gamma_2(\delta t_\mathrm{R})$], then the probability of four-fold coincidence is $p_{4c} = p_\mathrm{AS1}\gamma_1(\delta t_\mathrm{R})p_\mathrm{AS2}\gamma_2(\delta t_\mathrm{R})$. This has to be compared with using the feedback circuits shown in Fig. 6.4, where we can apply at most N (limited by the lifetime of the quantum memory and the speed of the feedback circuit) write pulses in each trial. Then the probability of four-fold coincidence becomes

$$
\begin{aligned}
P_{4c} &= \Big\{ \textstyle\sum_{i=0}^{N-1} p_\mathrm{AS1}(1-p_\mathrm{AS1})^i \sum_{j=i}^{N-1} p_\mathrm{AS2}(1-p_\mathrm{AS2})^j \\
&\quad \times \gamma_2(\delta t_\mathrm{R})\gamma_1[(j-i)\cdot\delta t_\mathrm{W} + \delta t_\mathrm{R}] \Big\} + \big\{ \cdots \big\}_{1\leftrightarrow2},
\end{aligned}
\tag{6.6}
$$

where δt_W is the time interval between the sequential write pulses [74] and $\{\cdots\}_{1\leftrightarrow2}$ is the same as the first term with index 1 and 2 being exchanged. Assume $p_\mathrm{AS1} \ll 1$ and $p_\mathrm{AS2} \ll 1$ and a long lifetime τ_c, we obtain $P_{4c} \sim N^2 p_\mathrm{AS1}\gamma_1(\delta t_\mathrm{R})p_\mathrm{AS2}\gamma_2(\delta t_\mathrm{R})$ for a definite number N. So the probability of four-fold coincidence is enhanced by N^2 for each trial. For our case $p_\mathrm{AS1} \approx p_\mathrm{AS2} = 2.0 \times 10^{-3}$ (the relevant cross correlation $g^{(2)}_\mathrm{AS,S} = 30$), $N = 12$, $\tau_c \sim 12~\mu\mathrm{s}$, $\delta t_\mathrm{W} = 800$ ns, $\delta t_\mathrm{R} = 400$ ns, and $\gamma_1(0) \approx \gamma_2(0) = 8\%$, the enhancement is 136.

The four lasers in Fig. 6.4 are independently frequency stabilized. The line widths of W1 and R1 are about 1 MHz while those of W2 and R2 are about 5 MHz of the full width at half maximum (FWHM). However, they will be broadened to more than 20 MHz because the laser pulse modulated by the AOM is a Gaussian-like profile with width about 40 ns FWHM. The line width of the retrieved single photons is determined mainly by the line width and intensity of the read lasers. So we try to make the profile of the two independent read pulses identical to each other.

In order to verify that the two Stokes photons coming from Alice and Bob are indistinguishable, we let them overlap at a BS with the same polarization (horizontal in our case) and measure the quantum interference indicated by the the Hong-Ou-Mandel (HOM) dip [164]. Having observed the high visibility of HOM dip in both time domain and frequency domain, we are confirmed that the two independent photons are indistinguishable. Then we put one of the two photons to vertical polarized before they enter the BS. By coincidence measurement at the two outputs of the BS, we generate the Bell state $|\Psi^-\rangle_{12} = \frac{1}{\sqrt{2}}(|H\rangle_1|V\rangle_2 - |V\rangle_1|H\rangle_2)$, which is verified by the measurement of violation of Bell's Inequality.

The measurement of HOM dip. We did two measurements to obtain the HOM dip in time domain and frequency domain respectively. To make the photons indistinguishable, the polarizations of the anti-Stokes photons were set to horizontal with two half-wave plates before they enter the BS as shown in Fig. 6.4. The other two half-wave plates after the BS were set to $0°$.

In the first measurement, we measured the four-fold coincidence among detectors D1, D2, Da and Dd while changing the time delay between the two read pulses (Fig. 6.5, left panel). The excitation probabilities $p_\mathrm{AS1} \approx p_\mathrm{AS2} = 2.0 \times 10^{-3}$. The coincidence rate is varied with the delay. Ideally, there should be completely destructive
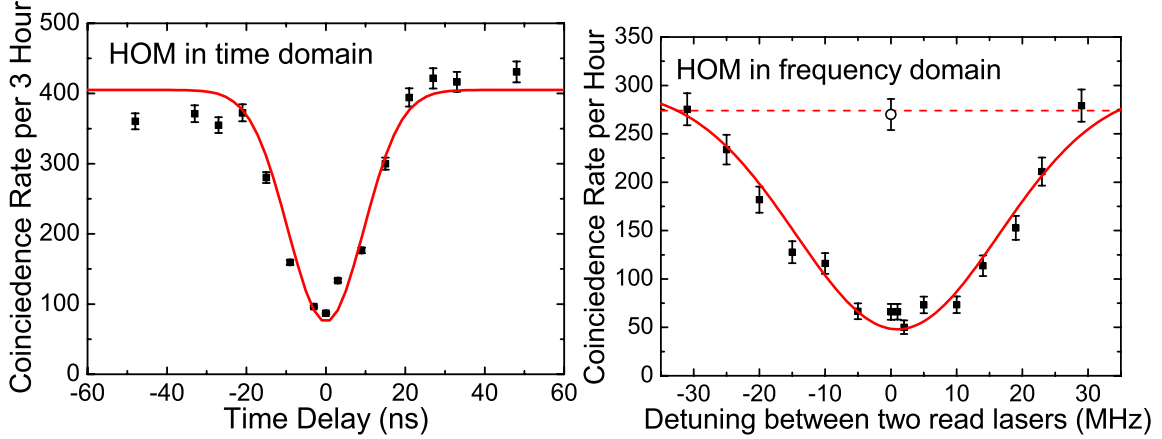
Figure 6.5: Hong-Ou-Mandel dips in time domain (left panel) and frequency domain (right panel). The circle in the right panel was obtained by setting the polarization of the two photons perpendicular to each other and zero detuning between two read lasers. The Gaussian curves that roughly connect the data points are only shown to guide the eye. The dashed line shows the plateau of the dip. Error bars represent statistical errors, which are ± one standard deviation.

interference if the wave packets of the two photons overlap perfectly. However, it is hard to make the two wave packets absolutely identical or exactly overlapped in practice. We obtained the visibility of the dip $V = (C_{\mathrm{plat}} - C_{\mathrm{dip}})/C_{\mathrm{plat}} = (80 \pm 1)\%$, where C_{plat} is the non-correlated coincidence rate at the plateau and C_{dip} is the interfering coincidence rate at the dip. The asymmetry of the profile at negative delay and positive delay shows that the two wave packets are (a) not perfectly identical, (b) not symmetric themselves. Assume the HOM dip is a Gaussian-type profile, we estimate the coherence time is 25±1 ns FWHM.

In the second measurement, we measured the four-fold coincidence among detectors D1, D2, Da and Dd while changing the frequency detuning between the two read pulses (Fig. 6.5, right panel). It is the first time to measure HOM dip in frequency domain at single-photon level. The excitation probabilities are $p_{\mathrm{AS1}} \approx p_{\mathrm{AS2}} = 3.0 \times 10^{-3}$, higher than those in time domain. Because of the limit of the current setup, the detuning can be varied from -30 MHz to 30 MHz. In order to verify the coincidence rate at largest detuning reached the plateau of HOM dip, we measured the coincidence by setting the polarization of the two photons perpendicular to each other and zero detuning between two read lasers (shown as a circle in Fig. 6.5). The consistence of this data with those two at largest detunings shows that we have achieved the plateau of HOM dip. The visibility is $(82 \pm 3)\%$ which agrees well with that obtained in time domain. The width of the HOM dip is 35±3 MHz FWHM, in accordance with the coherence time 25 ns. Therefore, the narrow-band characteristic of the present source is verified directly by the HOM dip in the frequency domain.

Besides the imperfect overlap of the single-photon wave packets, the two-photon components in each of the single-photon sources affect the visibility as well. The quality of single-photon source is characterized by the anti-correlation parameter $\alpha =$

$2P_{\mathrm{II}}/P_{\mathrm{I}}^2$ [74], where P_{I} (P_{II}) is the probability of generating one (two) photon(s) for each source (the higher orders are negligible small). If the two wave packets do not overlap at all, there is no interference between them. Then we obtain the non-correlated coincidence rate $C_{\mathrm{plat}} = P_{\mathrm{I}}^2/2 + P_{\mathrm{II}}$ between Da and Dd. If they overlap perfectly, there is destructive interference leading to a coincidence rate $C_{\mathrm{dip}} = P_{\mathrm{II}}$. So the visibility of the HOM dip is $V = 1/(1 + \alpha)$. In our experiment, $\alpha = 0.12$ for the source prepared later (the spin excitation is retrieved immediately) and $\alpha = 0.17$ for the source prepared earlier (it has to wait for the other one). This leads to an average visibility of 87%. In the frequency domain, the average visibility is around 83% because of higher excitation probabilities.

Efficient entanglement generation. As shown in Fig. 6.4, we set orthogonal polarizations (horizontal and vertical) of the Stokes photons with the two half-wave plates before the BS. Then the state of the two photons will be projected to $|\Psi^-\rangle_{12}$ if there is coincidence between the two output port 3 and 4. With another two half-wave plates and two PBS after the BS, the entanglement of the two photons can be verified by a Clauser-Horne-Shimony-Holt (CHSH) type inequality [165], where $S \leq 2$ for any local realistic theory with

$$S = |E(\theta_1, \theta_2) - E(\theta_1, \theta_2') - E(\theta_1', \theta_2) - E(\theta_1', \theta_2')|. \qquad (6.7)$$

Here $E(\theta_1, \theta_2)$ is the correlation function where θ_1 and θ_1' (θ_2 and θ_2') are the measured polarization angles of the Stokes photon at port 3 (4). The observed values of the correlation functions are listed in Table 6.1 resulting in $S = 2.37 \pm 0.07$, which violates Bell's Inequality by 5 standard deviations. This clearly confirms the quantum nature of the entanglement state.

With our imperfect sources we do not create a perfect $|\Psi^-\rangle_{12}$. If we consider the two photon component in the photon sources the created state will be:

$$|\Psi_{\mathrm{eff}}\rangle_{12} = \begin{cases} P_{\mathrm{I}}^2/2, & 1/\sqrt{2}(|H\rangle_1|V\rangle_2 - |V\rangle_1|H\rangle_2); \\ P_{\mathrm{II}}/2, & |H\rangle_1|H\rangle_2; \\ P_{\mathrm{II}}/2, & |V\rangle_1|V\rangle_2. \end{cases} \qquad (6.8)$$

From the quality of the single photons generated from the two ensembles, $\alpha = 0.12$, 0.17 and Eq. (6.8), we estimate the expected violation of Bell's Inequality is around 2.3, which is in good agreement with our measured value. It is interesting to note that a violation of Bell's Inequality needs a single photon source with $\alpha < 0.24$ according to Eq.(6.8). In order to minimize α, further improvements, e.g., a higher optical couple efficiency, a lower photon loss, a lower excitation probability and a higher retrieve efficiency, will be made in our future investigations.

6.2.3 Discussion

In conclusion, we realized synchronized generation of narrow-band single photons with two remote atomic ensembles. The Hong-Ou-Mandel dip was observed in both

Table 6.1: Correlation functions E and the resulting S.

E	$\theta_1 = 0°$	$\theta_1' = 45°$	S
$\theta_2 = 22.5°$	-0.613 ± 0.037	0.575 ± 0.039	
$\theta_2' = -22.5°$	0.606 ± 0.038	0.579 ± 0.039	2.37 ± 0.07

time domain and frequency domain with a high visibility for independent photons coming from two distant sites, which shows the indistinguishability of these photons. By virtue of quantum memories and feedback circuits, the efficiency of generating entangled photon pairs was enhanced by a factor of 136, which claims our single-photon source as a promising candidate for the future implementation of scalable quantum computation based on linear optics [48, 160, 49, 161]. The present spatially-distributed independent single-photon sources (with fully independent write and read lasers) are pre-requirements for the long-distance quantum communication [41][43][44][46]. The narrow-band property (which makes the overlap of the photon wave packets at the order of nanoseconds) of single photons and high efficiency of entanglement generation also profit the present source to serve as an ideal candidate for large scale communications, e.g., satellite-based quantum communication. There is still potential to improve our single-photon source. We can improve the retrieve efficiency close to unity by increasing the optical density of the atomic ensemble. A better compensation of the stray magnetic field will help the extension of the lifetime up to 100 μs. If we want an even longer lifetime, a good solution is to confine the atoms in an optical trap, which also benefits to a much higher optical density.

Two related experiments are described in [67, 60].

Chapter 7

Quantum Memory: Extension of Storage Time

In order to enhance the performance of the previously described single photon sources an extension of the memories storage time is necessary. A long storage time is also vital for enabling quantum communication over long distances.

7.1 Long Life Time: A millisecond quantum memory for scalable quantum networks

7.1.1 Motivation

Quantum repeaters with atomic ensembles and linear optics have attracted broad interest in recent years, since they hold the promise to implement long-distance quantum communication and distribution of entanglement over quantum networks. Following the protocol proposed by Duan *et al.*[42] and the subsequent improved schemes[44, 43, 46], significant progresses have been accomplished, including coherent manipulation of the stored excitation in one atomic ensemble[57, 74] and two atomic ensembles[67, 60, 75], demonstration of memory-built-in quantum teleportation[77], and realization of a building block of the quantum repeater[78, 65]. In these experiments, the atomic ensembles serve as the storable and retrievable quantum memory, where the collective state is used to store qubits and entanglement. Despite the advances achieved in manipulating atomic ensembles, scalable quantum networks with atomic ensembles remain challenging due to the short coherence time of the quantum memory. For example, to directly establish entanglement between two memory qubits over a few hundred kilometers, one needs a memory with a storage time of a few hundred microseconds. More seriously, in scalable linear optical quantum computation and quantum communication, one has to asynchronously prepare many deterministic single-photon sources[48] or number-state entanglement sources[42]. In

this case, the coherence time of the quantum memory must be significantly longer than the manipulation time, since when one source is ready, it has to be held until all the other sources are prepared[41, 48, 42, 44, 43, 46]. Again, this would need a storage time of a few hundred microseconds, a prerequisite for large-scale quantum information processing. However, the longest storage time reported so far is only on the order of 30 μs[57, 74, 65, 166]. It is long believed that the short coherence time is mainly caused by the residual magnetic field[66, 71]. Thereby, storing the collective state in the superposition of the first-order magnetic-field-insensitive state[167], i.e. the "clock state", is suggested to inhibit this decoherence mechanism[66]. A numerical calculation shows that the lifetime of the collective excitation stored in the "clock state" is on the order of seconds.

Here we report our investigation on prolonging the storage time of the quantum memory for single excitations. In the experiment, we find that only using the "clock state" is not sufficient to obtain the expected long storage time. We further analyze, isolate and identify the distinct decoherence mechanisms, and thoroughly investigate the dephasing of the spin wave (SW) by varying its wavelength. We find that the dephasing of SW is extremely sensitive to the angle between the write and detection mode, especially for small angles. Based on this finding, by exploiting the "clock state" and increasing the wavelength of the SW to suppress the dephasing, we succeed in extending the storage time from 10 μs to 1 ms, which for the first time allows for the quantum memory of single excitations to persist for times comparable to the propagation of light over 100 kilometers. Our work has opened the door to the first steps in building a quantum repeater, and thus provides an essential tool for long distance quantum communication.

7.1.2   Experimental Details

The architecture of our experiment is depicted in Fig. 1a and 1b. A cold ^{87}Rb atomic ensemble in a magneto-optical trap (MOT) at a temperature of about 100 μK serves as the quantum memory. The two ground states $|g\rangle$ and $|s\rangle$, together with the excited state $|e\rangle$ form a Λ-type system. A bias magnetic field of about 3 G is applied along the axial direction to define the quantization axis. Note that there are three pairs of "clock states" for the ground states of ^{87}Rb atom, i.e. ($|1, 1\rangle$, $|2, -1\rangle$), ($|1, 0\rangle$,$|2, 0\rangle$), and ($|1, -1\rangle$, $|2, 1\rangle$), where we have defined $|i, j\rangle = |5S_{1/2}, F = i, m_F = j\rangle$. In a timescale of milliseconds, we can use any of them to store the collective excitation, because the decoherence of the "clock states" caused by magnetic field is negligible. In our experiment, we prepare the atoms in $|1, 0\rangle$ to exploit the clock state ($|g\rangle = |1, 0\rangle$, $|s\rangle = |2, 0\rangle$). An off-resonant σ^- polarized write pulse with wave vector $\mathbf{k}_\mathrm{W}$ is applied to the atomic ensemble along the axial direction, inducing spontaneous Raman scattering. The Stokes photon with σ^- polarization and wave vector $\mathbf{k}_\mathrm{S}$ is collected at an angle of $\theta = 3°$ relative to the write beam, as in most of the previous experiments[57, 60, 76, 65, 77, 67]. The beam waist of the detection mode is about 100 μm in the atomic ensemble. Conditional on detecting a Stokes photon, a collective excited state or a SW is imprinted in the atomic ensemble[42],

described by

$$|\psi\rangle = \frac{1}{\sqrt{N}} \sum_j e^{\imath \Delta \mathbf{k} \cdot \mathbf{r}_j} |g...s_j...g\rangle, \qquad (7.1)$$

with $\Delta \mathbf{k} = \mathbf{k}_\mathrm{W} - \mathbf{k}_\mathrm{S}$ the wave vector of the SW, and $\mathbf{r}_j$ the coordinate of the j-th atom. After a controllable delay δt, a strong σ^+ polarized read light, counter-propagating to the write light, converts the collective excitation into an anti-Stokes photon, which is σ^+ polarized and spatially mode-matched with the Stokes photon from the opposite direction. The Stokes (anti-Stokes) photon and the write (read) light are spatially separated.

In the experiment, the MOT is loaded for 20 ms at a repetition rate of 40 Hz. The trapping magnetic field and repumping beams are then quickly switched off. After 0.5 ms, the bias magnetic field is switched on, whereas the cooler beams stay on for another 0.5 ms before being switched off to prepare the atoms in the $|5S_{1/2}, F = 1\rangle$ ground state. Then, within another 4 ms, experimental trials (each consisting of pumping, write and read pulses) are repeated with a controllable period depending on the desired retrieval time. In order to optically pump the atoms to the desired sub-level, we switch on two pumping beams in each experimental trial before write and read process: one couples the transition $|5S_{1/2}, F = 2\rangle \rightarrow |5P_{3/2}, F' = 2\rangle$ with linear polarization for 2 μs, and the other couples the transition $|5S_{1/2}, F = 1\rangle \rightarrow |5P_{1/2}, F' = 1\rangle$ for 1.7 μs, which is linearly (σ^+) polarized for $|1, 0\rangle$ ($|1, 1\rangle$). From the experimental result, we estimate more than 80% of the atoms are prepared to the desired state.

In our experiment, more than 10^8 ^{87}Rb atoms are collected by the MOT with an optical depth of about 5 and a temperature of about 100 μK. The write pulse with a detuning of $\Delta = 20$ MHz and a beam diameter of about 400 μm is applied to generate the SW and the Stokes photon. The Stokes mode is coupled into a single-mode fiber (SMF) and guided to a single-photon detector. After a controllable delay, the strong read pulse with a detuning of $\Delta = 6$ MHz is applied to retrieve the SW. The stored SW is converted into the anti-Stokes photon, which is also coupled into a SMF and detected by a single-photon detector.

In the experiment, for $\theta = 3°, 1.5°$ and $0.6°$, the Stokes (anti-Stokes) photon and the write (read) light can be spatially separated and thus we can choose any of the three pairs of "clock states". Because the retrieval efficiency is proportional to the coupling strength of the transition $|e\rangle \rightarrow |g\rangle$, we choose the clock state $(|1, 0\rangle, |2, 0\rangle)$ to get higher retrieval efficiency. While for smaller angles $\theta = 0.2°$ and $0°$, the two beams with the same polarization cannot be spatially separated, and thereby we have to use the other two "clock states". In this case, we choose the "clock state" $(|1, 1\rangle, |2, -1\rangle)$, since the energy level $|1, 1\rangle$ is lower than $|1, -1\rangle$ under the bias magnetic field and the pumping effect is better. The overall retrieval efficiency, including transmission efficiency of filters and optical components, the coupling efficiency of the fiber coupler, and the detector quantum efficiency, are about 2% for $(|1, 0\rangle, |2, 0\rangle)$ at $\theta = 3°, 1.5°$ and $0.6°$, and 1% for $(|1, 1\rangle, |2, -1\rangle)$ at $\theta = 0.2°$, and 0.8% for $(|1, 1\rangle, |2, -1\rangle)$ at $\theta = 0°$. The retrieval efficiency at $\theta = 0°$ is a little bit lower
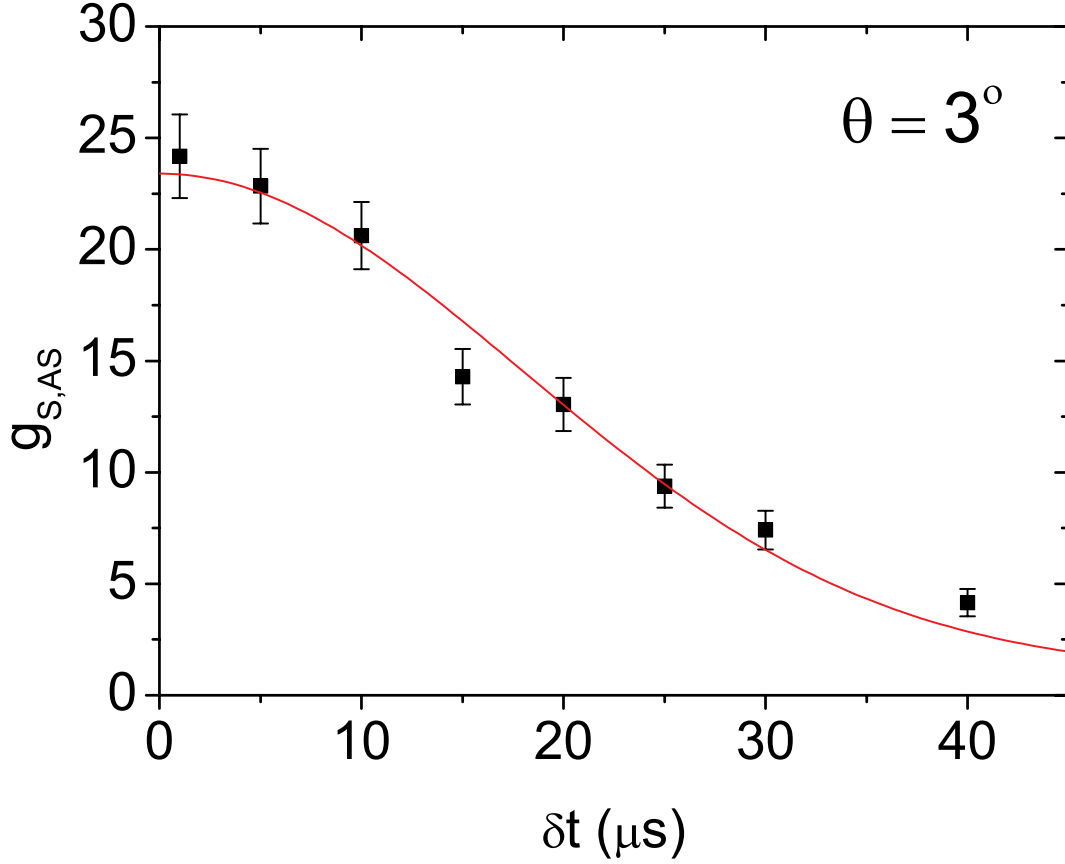
Figure 7.1: Fig. 2. The cross correlation $g_{\text{S,AS}}$ versus the storage time δt for $(|1,0\rangle, |2,0\rangle)$ at $\theta = 3°$. The data are fitted by using $g_{\text{S,AS}}(\delta t) = 1 + C \exp(-\delta t^2/\tau_{\text{D}}^2)$. Our data give a lifetime of $\tau_{\text{D}} = 25 \pm 1$ μs, which is much less than the theoretical estimation for the "clock state". Error bars represent statistical errors.

than at $\theta = 0.2°$, because one more etalon was used to filter the excitation beams. These correspond to 15% and 10% of original retrieval efficiency for $(|1,0\rangle, |2,0\rangle)$ and $(|1,1\rangle, |2,-1\rangle)$, respectively. The low overall retrieval efficiency is caused by the transmission loss, the mode mismatch, the imperfect pumping, and the imperfect polarization of the write and read light.

In the experiment, to evaluate the coherence time of the quantum memory, we measure the cross correlation $g_{\text{S,AS}} = p_{\text{S,AS}}/(p_{\text{S}} \cdot p_{\text{AS}})$ as a function of the time delay, with p_{S} (p_{AS}) the probability of detecting a Stokes (anti-Stokes) photon and $p_{\text{S,AS}}$ the coincident probability between the Stokes and anti-Stokes channels. The time dependent cross correlation can be described by[74]

$$g_{\text{S,AS}}(\delta t) = 1 + C\gamma(\delta t), \tag{7.2}$$

with C a constant determined by the excitation probability and background noise, and $\gamma(\delta t)$ the time dependent retrieval efficiency. The experimental result is shown in Fig. 2, where the data are fitted by using $g_{\text{S,AS}}(\delta t) = 1 + C \exp(-\delta t^2/\tau_{\text{D}}^2)$, with τ_{D}

the lifetime of the collective state. Below the expectation, our data only give a lifetime of $\tau_D = 25 \pm 1$ μs, which is far from the theoretical predication for the "clock state". One might think this is caused by the atoms moving out of the interaction region. However, the decoherence due to loss of atoms gives a lifetime of a few hundred microseconds under the present condition. This can be estimated by calculating the average time for the atoms flying out of the pencil shaped interaction region, where the thermal motion in radial direction dominates. At temperature T, an atomic cloud with a cross section radius r_0 expands according to $r^2(\delta t) = r_0^2 + v_r^2 \delta t^2$, with the average speed in radial direction $v_r = \sqrt{\frac{2k_B T}{m}}$. The retrieval efficiency can be given by $\gamma(\delta t) = r_0^2/r^2(\delta t) = 1/(1 + \frac{v_r^2}{r_0^2}\delta t^2)$. Thereby, when $\gamma(\tau_L) = 1/e$, only $1/e$ of the atoms remain in the interaction region, giving a lifetime of $\tau_L \simeq \frac{1.31 r_0}{v_r}$. For $r_0 = 100$ μm as the waist of the detection mode and $T = 100$ μK, we have $\tau_L = 950$ μs, which is much longer than our result.

We carefully analyze the decoherence mechanism of the quantum memory and find that the short lifetime could be explained by the dephasing of the SW induced by atomic random motion[112]. This decoherence mechanism is in fact a dominating decoherence mechanism in this experiment and most of the previous experiments[57, 60, 76, 65, 77, 67]. However, it has not been noticed before.

The dephasing can be understood as follows. As shown in Fig. 1c, assume a SW is stored in the atomic ensemble and will be retrieved out after a time delay δt. In this interval, each atom randomly moves from one point to another along the wave vector direction. The internal states or the spin of the atoms are conserved since collisions can be safely neglected at a low temperature and density. However, the atomic motion leads to a perturbation on the phase of the SW. Consequently, the projection of the perturbed SW on the original one gradually decreases as the delay of the retrieve becomes longer. In other words, the atomic random motion leads to a random phase fluctuation in the SW and thus causes decoherence. The timescale of the dephasing can be estimated by calculating the average time needed for the atoms to cross $\frac{1}{2\pi}$ of the wavelength of the SW, giving a lifetime of $\tau_D \sim \frac{\lambda}{2\pi v_s}$, with $v_s = \sqrt{\frac{k_B T}{m}}$ the one dimensional average speed and $\lambda = \frac{2\pi}{\Delta k}$ the wavelength of the SW. A more detailed calculation gives $\gamma(\delta t) \sim e^{-\delta t^2/\tau_D^2}$, with the lifetime $\tau_D = \frac{1}{\Delta k v_s}$. In our case, there is an angle θ between $\mathbf{k}_W$ and $\mathbf{k}_S$, and thus we have $\Delta k = |\mathbf{k}_W - \mathbf{k}_S| \simeq k_W \sin\theta$. For $\theta = 3°$, a simple calculation gives $\lambda = 15$ μm and then $\tau_D = 25$ μs, which is consistent with the experimental result.

The above analysis also suggests that in order to suppress this dephasing and extend the storage time, we have to increase the wavelength of the SW by decreasing the detection angle (see Fig. 1d). Thereby, we reduce the angle by choosing $\theta = 1.5°$, $0.6°$, and $0.2°$. Note that, for $\theta = 0.2°$, the two beams with the same polarization can not be spatially separated, and thereby we use another "clock state" ($|g\rangle = |1, 1\rangle$, $|s\rangle = |2, -1\rangle$) by preparing the atoms in $|1, 1\rangle$. In this case, the Stokes (anti-Stokes) photon is σ^+ (σ^-) polarized. The write (read) and Stokes (anti-Stokes) lights have orthogonal polarizations and are separated by a Glan-Laser prism.

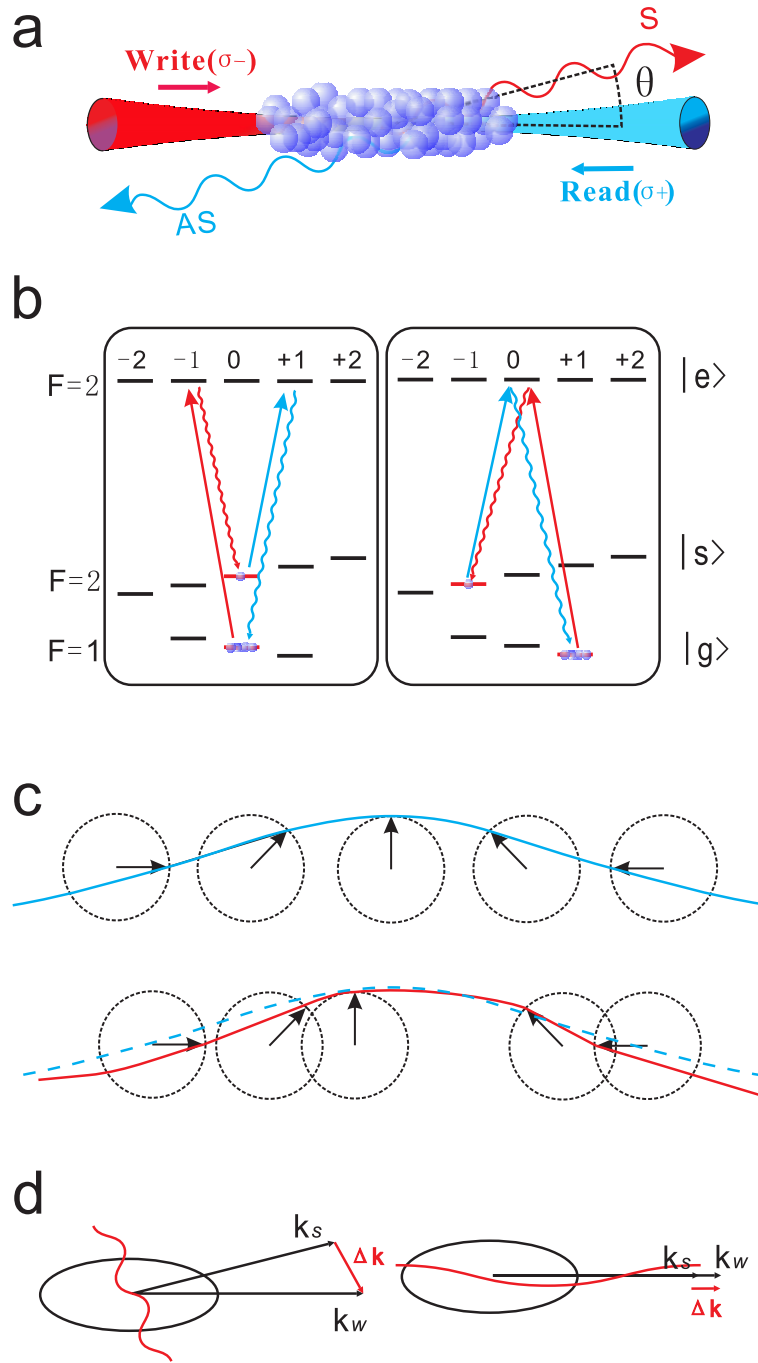**Figure 7.2: Fig. 1.** (a) Schematic view of the experiment. The atoms are initially prepared in $|g\rangle$. A weak σ^- polarized write pulse is applied to generate the SW and Stokes photon via spontaneous Raman transition $|g\rangle \to |e\rangle \to |s\rangle$. The Stokes photon are detected at an angle of θ relative to the write beam. After a controllable delay, a strong σ^+ polarized read light induces the transition $|s\rangle \to |e\rangle \to |g\rangle$, converting the SW into an anti-Stokes photon. (b) The structure of atomic transitions (^{87}Rb) under a weak magnetic field. The left panel corresponds to the experiment with $(|1,0\rangle, |2,0\rangle)$. The right one corresponds to the experiment with $(|1,1\rangle, |2,-1\rangle)$. (c) Illustration of the SW dephasing induced by atomic random motion. The blue curve represents the SW initially stored in the quantum memory. The atoms randomly move along the wave vector direction, resulting in a phase fluctuation. The perturbed SW is represented by the red curve. (d) The wavelength of the SW can be controlled by changing the detection configuration. In the collinear case, we have the maximum wavelength.

The experimental results are displayed in Fig. 3a-3c. As expected, the dephasing of the SW dominates in our experiment, where the effect of magnetic field is inhabited by using the "clock state". The lifetime increases from 25 μs to 283 μs by reducing θ or, in other words, increasing the wavelength of SW. Our results clearly show that the long-wavelength SW is robust against the dephasing induced by atomic random motion. Note that, for $\theta = 0.2°$, the data are fitted by taking into account the effect of loss of atoms. The measured lifetime τ_D is shown in Fig. 3d as a function of angle θ. The solid line is the theoretical curve $\tau_D = \frac{1}{\Delta k v_s}$, with $v_s = 0.1$ m/s corresponding to a temperature of $T \simeq 100$ μK. The good agreements between theory and experiment imply that our work provides an alternative approach to measure the temperature of an atomic ensemble. Moreover, since the lifetime is only sensitive to the velocity of the atoms in the interaction region, which is determined by the waist of the detection mode and is controllable, one can also use our method to measure the velocity distribution of the atomic ensemble by performing measurement in different regions.

To achieve a longer storage time, we use the collinear configuration ($\theta = 0°$), where we have the maximum wavelength of the SW $\lambda \simeq 4.4$ cm and thus $\tau_D \simeq 72$ ms. In this case, the decoherence due to loss of atoms becomes the principal decoherence mechanism. The experimental result is shown in Fig. 4, where the "clock state" ($|1, 1\rangle$, $|2, -1\rangle$) is also used. Our data give a lifetime of $\tau_L = 1.0 \pm 0.1$ ms, when the retrieval efficiency has dropped to $1/e$. The experiment result is in good agreement with theoretical estimation.

7.1.3   Discussion

In our experiment, we have isolated and identified different decoherence mechanisms of the quantum memory for single excitations and thoroughly investigated the dephasing of the stored SW by varying its wavelength. Moreover, we have successfully realized a long-lived quantum memory for single collective excitation by exploiting the "clock state" and long-wavelength SW. The storage time of 1 ms is 30 times longer than the best previous results reported so far [74, 57, 65, 166], and is long enought for photons transmission over 100 kilometers. In our experiment, the coherence time of the quantum memory is limited by the decoherence due to loss of atoms, which can be suppressed by lowering the temperature via optical molasses. A storage time of 3 ms is achievable by reducing the temperature to 10 μK. This will be the upper limit for the atomic memory in MOT, since longer storage time is prohibited by the free falling of the atoms under gravity. Further improvement might be achieved by trapping the atoms in an optical dipole trap[66, 140], where the decoherence due to loss of atoms and the dephasing induced by atomic random motion can both be suppressed. In this case, the principal decoherence mechanism is the diffusion caused by collisions, which will give a lifetime of a few tens of milliseconds. To inhibit the collision-induced diffusion, one has to trap the atoms in a deep optical lattice[168], where each atom is tightly confined in a single site and collisions are avoided. The optical lattice has the potential to store the collective
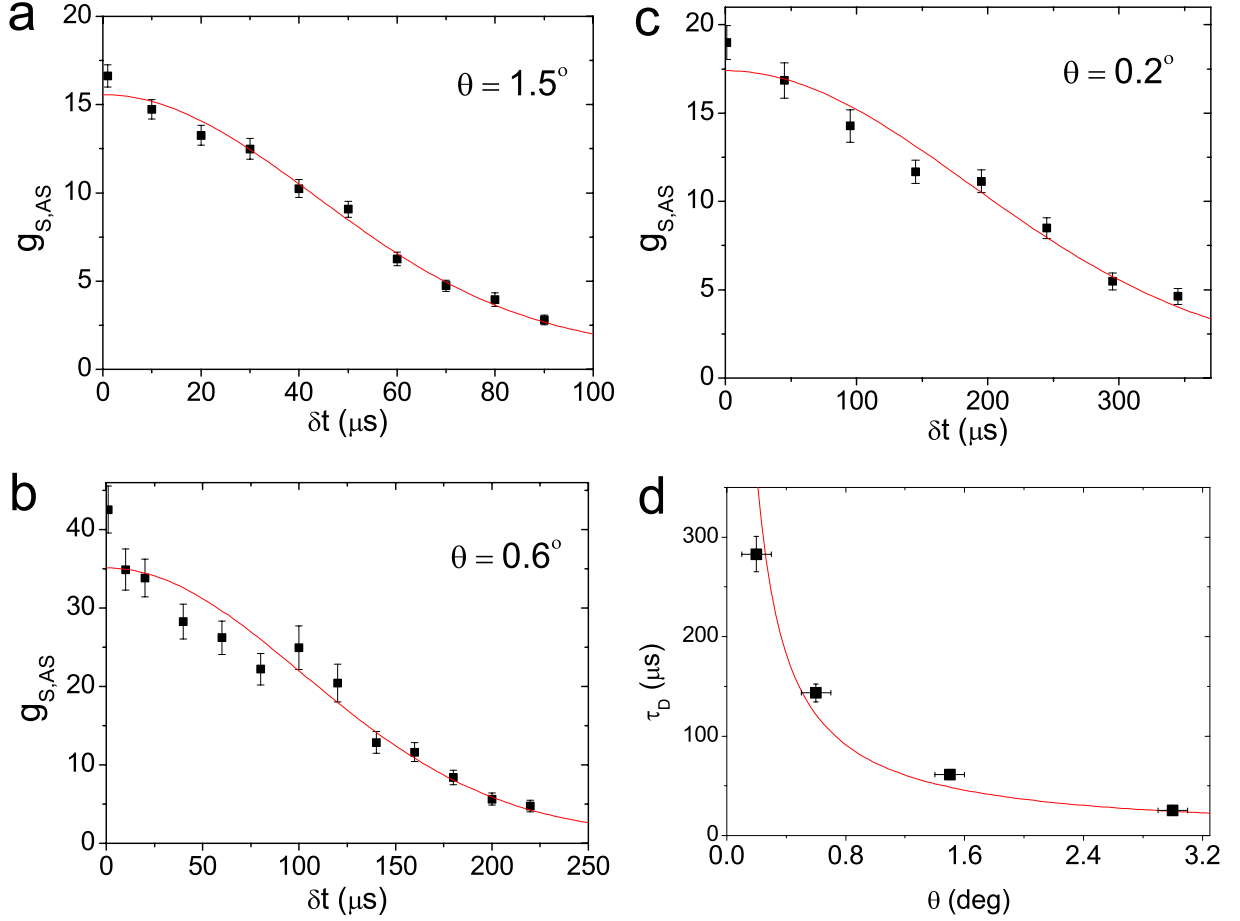
Figure 7.3: Fig. 3. The cross correlation $g_{S,AS}$ versus the storage time δt for different angles (a)-(c) and the measured lifetime τ_D as a function of detection angle θ (d). Panels (a) and (b) are for $(|1,0\rangle, |2,0\rangle)$ at $\theta = 1.5°$ and $0.6°$, respectively. The data are fitted by using $g_{S,AS}(\delta t) = 1 + C\exp(-\delta t^2/\tau_D^2)$, where τ_D is the lifetime due to dephasing. Panel (c) is for $(|1,1\rangle, |2,-1\rangle)$ at $\theta = 0.2°$. In this case we take into account the effect of loss of atoms and fit the data by using $g_{S,AS}(\delta t) = 1 + C\exp(-\delta t^2/\tau_D^2)/(1 + A\delta t^2)$, with A the fitting parameter obtained from the collinear configuration. The fitted lifetime for each case is: (a) $\tau_D = 61 \pm 2$ μs, (b) $\tau_D = 144 \pm 9$ μs, (c) $\tau_D = 283 \pm 18$ μs. The first data are a little bit higher than the fitted curves, which might be caused by the imperfection in the pumping process. By reducing the angle, the lifetime is increased from 25 μs to 283 μs, which implies the decoherence is mainly caused by the dephasing induced by atomic random motion. Panels (d) depicts the measured lifetime τ_D as a function of detection angle θ, where the horizontal error bars indicate measurement errors in the angles. The solid line is the theoretical curve with $T \simeq 100$ μK. The experimental results are in good agreement with the theoretical predications. The vertical error bars indicate statistical errors.
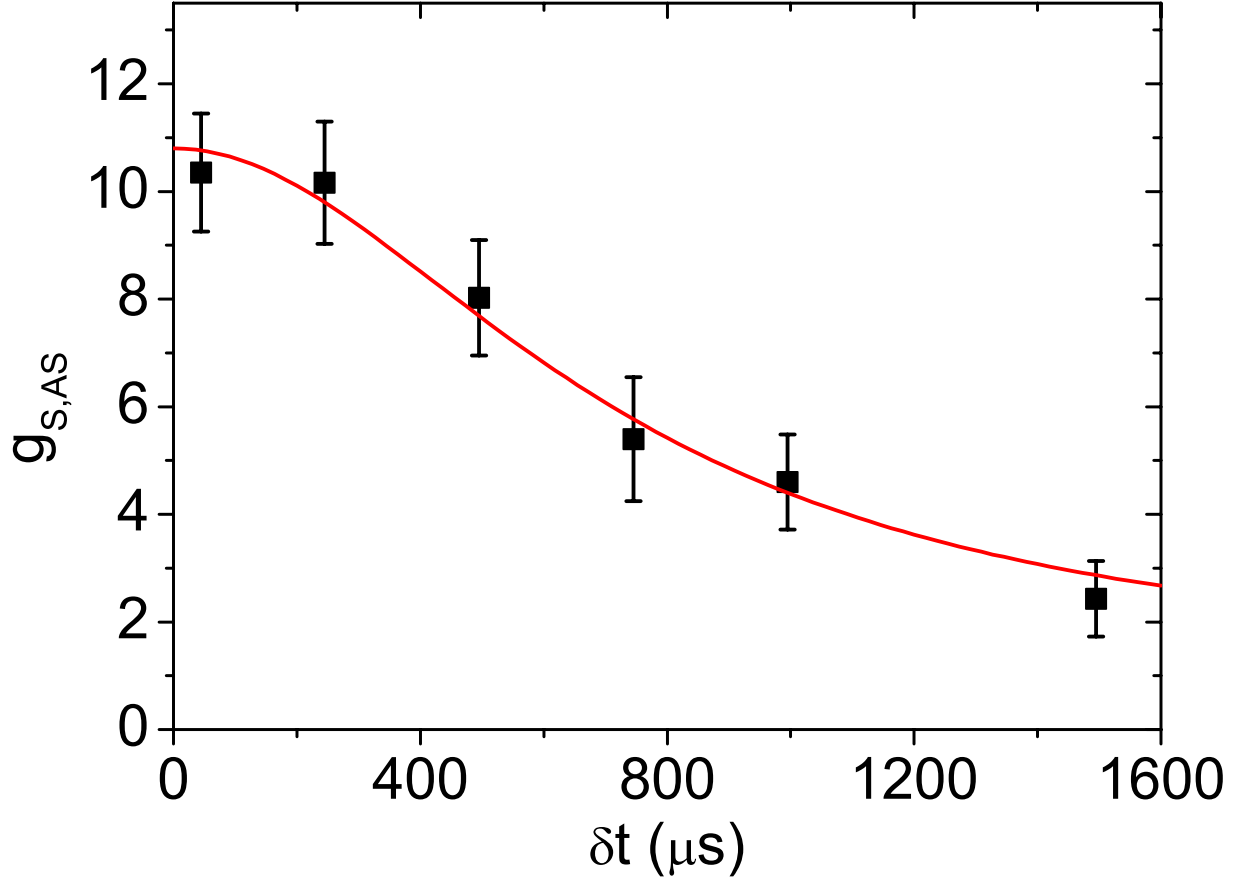
Figure 7.4: Fig. 4. The cross correlation $g_{\mathrm{S,AS}}$ versus the storage time δt for $\theta = 0°$ and $(|1,1\rangle, |2,-1\rangle)$. The data are fitted by using $g_{\mathrm{S,AS}}(\delta t) = 1 + \frac{C}{1+A\delta t^2}$, with A the fitting parameter. Our data give a lifetime of $\tau_{\mathrm{L}} = 1.0 \pm 0.1$ ms, when the retrieval efficiency $\gamma(\delta t) = \frac{1}{1+A\delta t^2}$ has dropped to $1/e$. Error bars represent statistical errors.

excitation for a few tens of seconds, which will reach the requirement in the storage time for a robust and efficient quantum repeater with atomic ensembles[45]. The idea presented in this work can also be applied to the quantum memory based on electromagnetically induced transparency[88, 58, 71]. By using the same method as in our experiment, a storage time of a few hundred microseconds can be expected.

Our work opens up the exciting possibility to implement many tasks of quantum information processing. Combined with the techniques developed in recent years, one can implement a high-quality on-demand single-photon source, deterministic preparation of multi-qubit entanglement, generation of entanglement between two remote atomic memory qubits over a few hundred kilometers, and even construction of long-lived quantum nodes for scalable quantum networks. More generally, our work presents an experimental investigation on the decoherence of the SW at single quanta level. It is clearly shown that a long-wavelength SW is robust against dephasing. Besides, our work also provides an approach to measure the temperature or the velocity distribution of an atomic ensemble. Furthermore, since the decoherence of the SW is controllable, one can measure certain important physical quantities by introducing additional physical mechanisms. For example, when performing experiments in optical dipole trap, the lifetime is determined by collision between atoms[112]. Thereby, the s-wave scattering cross section or scattering length might be measured using our approach.

7.2 Quantum Memory with Optically Trapped Atoms

7.2.1 Motivation

A quantum memory, a storage device for quantum states, is requisite to a scalable quantum repeater [41] for the realization of long-distance quantum communication [169]. In the quantum repeater protocol, the transmission channel is divided into several segments with lengths comparable to the channel attenuation length. Entanglement is then generated and purified [84] for short distances before being extended to a longer distance by entanglement swapping [170]. The entanglement creation, purification, and connection are probabilistic, thereby requiring the successfully entangled segment state to be stored in a quantum memory while waiting for the others to generate. Once the entanglement is distributed over the transmission channel, it can be used for quantum teleportation [31] or cryptography [10]. A quantum memory with long storage time is therefore crucial to achieve scalable quantum communication networks with a manageable time overhead. Various schemes were proposed for implementing quantum repeaters [42][46][44] in which the scalability stems from the entanglement between a sent photon and the quantum state stored in the quantum memory. The quantum state is stored in a collective state of an atomic ensemble where a superposition between two ground states is shared among all the atoms. The key issue to a quantum memory is that the stored state, which could be later read out by converting into another photon, keeps its quantum correlation with the sent photon. This correlation also allows an arbitrary state to be written into the quantum memory by quantum teleportation. Significant progress has been made toward realization of quantum repeaters in recent years. Non-classical correlation has been observed between Raman scattered photons and the consequent collective excitations in an atomic ensemble [54, 51, 73, 74]. Number-state entanglement has also been generated between two ensembles of atoms [55, 64]. Most recently, quantum teleportation with a built-in quantum memory [77] and entanglement swapping [78] have been demonstrated. Despite these advances, the storage times of the quantum memories reported to date are primarily limited by inhomogeneous broadening of the ground state due to magnetic fields [66]. As a result, the quadrupole magnetic field of the magneto-optical trap (MOT) used to confine the atoms is switched off during the storage. Nevertheless, the residual magnetic field still limits the lifetime (see below) of the quantum memory to only $\sim 10~\mu$s [74, 77, 66]. Moreover, without confinement the atoms simply diffuse out of interaction region ($\sim 100~\mu$m) after a few hundred microseconds. For a quantum memory in a MOT, the atomic diffusion imposes a strict limitation on the storage time, which in turn limits the maximum distance for quantum communication in practical applications. On the contrary, a quantum memory confined in a far-detuned optical dipole trap [140] can simultaneously achieve long coherence and confinement as widely discussed in the recent literature [54, 77, 73, 78, 66]. In an optical trap, the large detuning efficiently suppresses photon scattering, which results in a non-dissipative confinement for the

atoms without introducing magnetic fields. Furthermore, coherent manipulation of atomic internal states for seconds has been demonstrated in such traps [134]. A quantum memory of this sort thus has a potential storage time of seconds. However, realization of a memory in an optical trap is extremely challenging and, to the best of our knowledge, has not been achieved.

7.2.2   Experiment

We experimentally demonstrate a quantum memory in a focused-beam optical trap that has a long trap lifetime ($\tau_{trap} = 20$ s) and a negligible photon scattering rate ($\Gamma = 4$ s^{-1}). In addition to optical trapping, we also make use of the first-order magnetic-field-insensitive state (clock state). For the clock state, we choose the superposition state of the magnetic sublevels, $|c_1\rangle = |5S_{1/2}, F = 1, m_F = -1\rangle$ and $|c_2\rangle = |5S_{1/2}, F = 2, m_F = 1\rangle$, of ^{87}Rb. These states experience the same first-order Zeeman shift at a magnetic field of ~ 3.23 G (see paragraph (4.6)). Hence, an atomic ensemble in a superposition of this state pair is, to first-order, insensitive to the spatial inhomogeneity and temporal fluctuation of the magnetic field [167][171]. Our quantum memory is therefore robust against the principal decoherence process experienced in previous experiments and provides an additional confinement during quantum storage.

A schematic of our apparatus is shown in Fig. 7.5 (a). The experiment begins with a standard MOT. During 2 s of loading, 5×10^6 ^{87}Rb atoms, with a temperature of about 100 μK, are loaded from the background vapor. We then change the configuration of the MOT to a temporal dark MOT, followed by molasses cooling, to maximize the transfer of atoms into the optical trap. In the dark MOT phase, the frequency of the cooling light, f_{cool}, is shifted to the red of the $|5S_{1/2}, F = 2\rangle \rightarrow |5P_{3/2}, F = 3\rangle$ transition by 35 MHz for a duration of 145 ms, while the repumping intensity I_{repump} is ramped down by a factor of 200. After the dark MOT, the MOT quadrupole field is switched off and molasses cooling is applied for 5 ms, resulting in a peak atomic density of 3×10^{10} cm^{-3} and a temperature of about 20 μK. Subsequently, a magnetic bias field at ~ 3.23 G is switched on along the longitudinal direction of the atomic cloud. The atoms are then optically pumped to the $|g\rangle = |5S_{1/2}, F = 1\rangle$ hyperfine state by shuttering off the repumping light 3 ms before the cooling light is extinguished. The time sequence of our experiment is summarized in Fig. 7.6 (a).

The optical trap is formed by a tightly focused laser beam at $\lambda = 1030$ nm with a $1/e^2$ radius of 36 μm. The beam is left on during the experimental cycles at 7 W, leading to radial and axial trapping frequencies of $\omega_r = 2\pi \times 2$ kHz and $\omega_z = 2\pi \times 10$ Hz, respectively, and a trap depth of $k_B \times 500$ μK, with k_B denoting the Boltzmann's constant. For typical operating conditions, 2×10^5 atoms are transferred into the optical trap (untrapped atoms are allowed to free fall for 30 ms). The temperature of the atoms after the transfer increases to 45 μK, possibly due to the heating associated with the optical pumping. Together with the measured radial and axial rms radius of 5.5 μm and 0.85 mm, respectively, we derive a peak atomic density of 10^{12} cm^{-3}
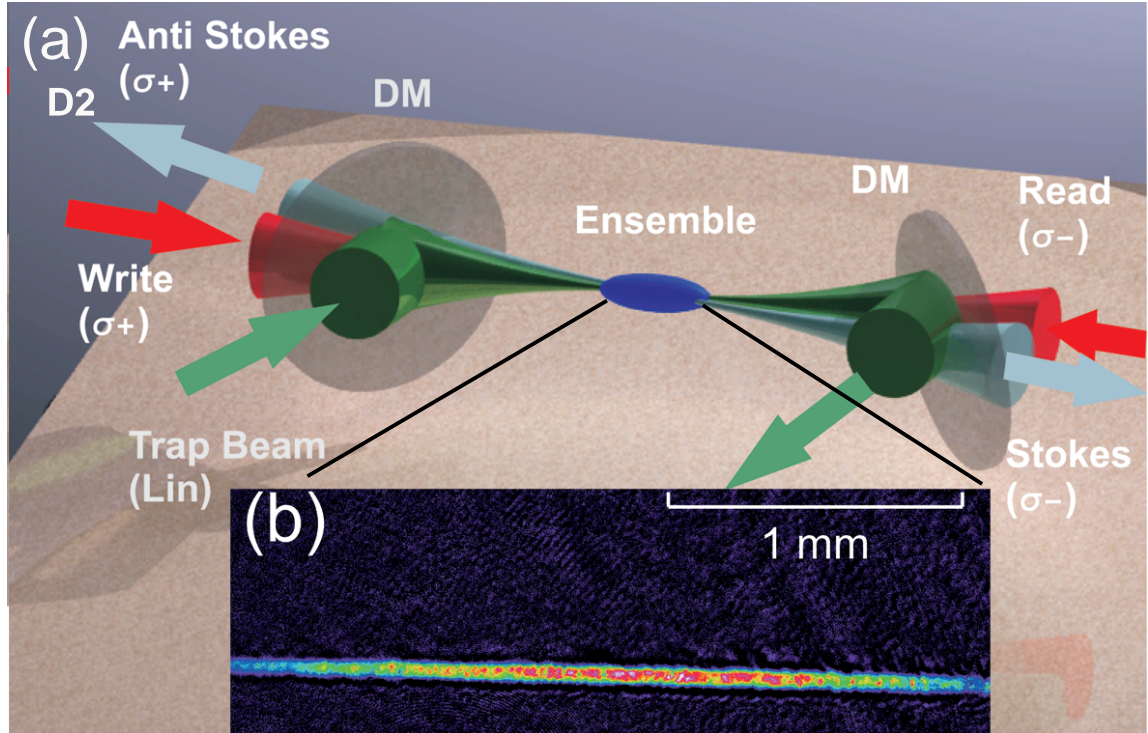
Figure 7.5: A schematic of the experiment. (a) The atoms are confined in an optical trap formed by a red-detuned, single beam ((FORT). The optical-trapping beam is overlapped with *write* and *read* beams, in counterpropagating direction, on the dichroic mirror (DM) and is blocked by a beam dump (BD) on the other side of the atoms. Single-photon detectors, D1 and D2, are placed at an angle of 2° with respect to the optical trap to detect the Stokes and anti-Stokes fields, respectively. (b) An absorption image of optically trapped atoms along the radial direction after a time-of-flight of 0.3 ms.

in the optical trap. Fig. 7.5 (b) shows an absorption image of the optically trapped atoms after a time-of-flight of 0.3 ms.

With all atoms prepared in the ground state $|g\rangle$, a weak *write* pulse illuminates the atomic ensemble for a duration of 100 ns. Fig. 7.6 (b) illustrates the relevant atomic transitions in the experiment. The right-circularly (σ^+) polarized *write* beam, co-propagating with the optical-trapping beam, is blue-detuned $\Delta_w = 100$ MHz from the $|g\rangle \rightarrow |e\rangle = |5P_{1/2}, F = 2\rangle$ transition with a $1/e^2$ radius of 250 μm. Each *write* pulse contains approximately 10^5 photons in the region of the atoms. As a result, there is an extremely small probability ($p_S \ll 1$) of inducing spontaneous Raman transition to the metastable state $|s\rangle = |5S_{1/2}, F = 2\rangle$ and detecting a Stokes photon with left-circularly (σ^-) polarization by a single-photon detector D1. The collection mode of detector D1, with a $1/e^2$ radius of 75 μm, is tilted at an angle of $\sim 2°$ with respect to the *write* beam for frequency filtering.

Prior to the detection of a Stokes photon, the joint state of the atomic collective mode and the Stokes mode is described by $|\phi\rangle \propto |0_a\rangle|0_S\rangle + e^{i\beta}\sqrt{p_S}|1_a\rangle|1_S\rangle + O(p_S)$ [42], where $|i_a\rangle$ and $|i_S\rangle$ denote i quanta of excitations in the atomic collective and Stokes modes, respectively, β is a phase related to the propagation of the Stokes photon [66], and $O(p_S)$ represents terms with higher excitations. Conditional upon a click at detector D1, the Stokes field is projected to $|1_S\rangle$ and a collective atomic superposition state,

$$|1_a\rangle = \frac{1}{\sqrt{N}} \sum_{j=1}^{N} e^{-i(\mathbf{k}_s - \mathbf{k}_w)\cdot\mathbf{r}_j}|g\rangle_1 \cdots |s\rangle_j \cdots |g\rangle_N, \tag{7.3}$$

is created and stored in the ensemble. Here, N is the atom number, $\mathbf{k}_S$ and $\mathbf{k}_w$ are the wave vectors of the Stokes and *write* photons, respectively, and $\mathbf{r}_j$ is the position of the jth atom when it scatters a Stokes photon.

After a controllable time delay (storage time) t, the collective excitation in the atomic ensemble is converted into a photon in the anti-Stokes mode, $|1_{AS}\rangle$. In the experiment, only photons with σ^+ polarization are detected by detector D2, for which the collection mode is matched to detector D1 with a coupling efficiency of 80%. The coherent conversion is accomplished by illuminating the atoms with a strong, σ^- polarized *read* beam that is resonant with the $|s\rangle \rightarrow |e\rangle$ transition and mode-matched to the *write* beam in a counter-propagating configuration. This results in a non-classical pair of Stokes and anti-Stokes photons. The number correlation of the photon pair is thus a useful probe for the storage in the quantum memory, as various sources of decoherence could cause degradation.

We explore the number correlation of the Stokes and anti-Stokes photons by measuring the normalized cross-correlation function, or the quantum mechanical degree of second-order coherence, of the two fields [54], $g_{S,AS} = p_{S,AS}/p_S p_{AS}$, where $p_{S,AS}$ is the joint probability of detecting one photon by both detectors within the same experimental trail, and p_S (or p_{AS}) is the probability of detecting a Stokes (or anti-Stokes) photon individually. For a non-classical photon pair, $g_{S,AS}$ violates the classical constraint set by the Cauchy-Schwarz inequality [172], $g_{S,AS}^2 \leq g_{S,S}g_{AS,AS}$, where $g_{S,S}$
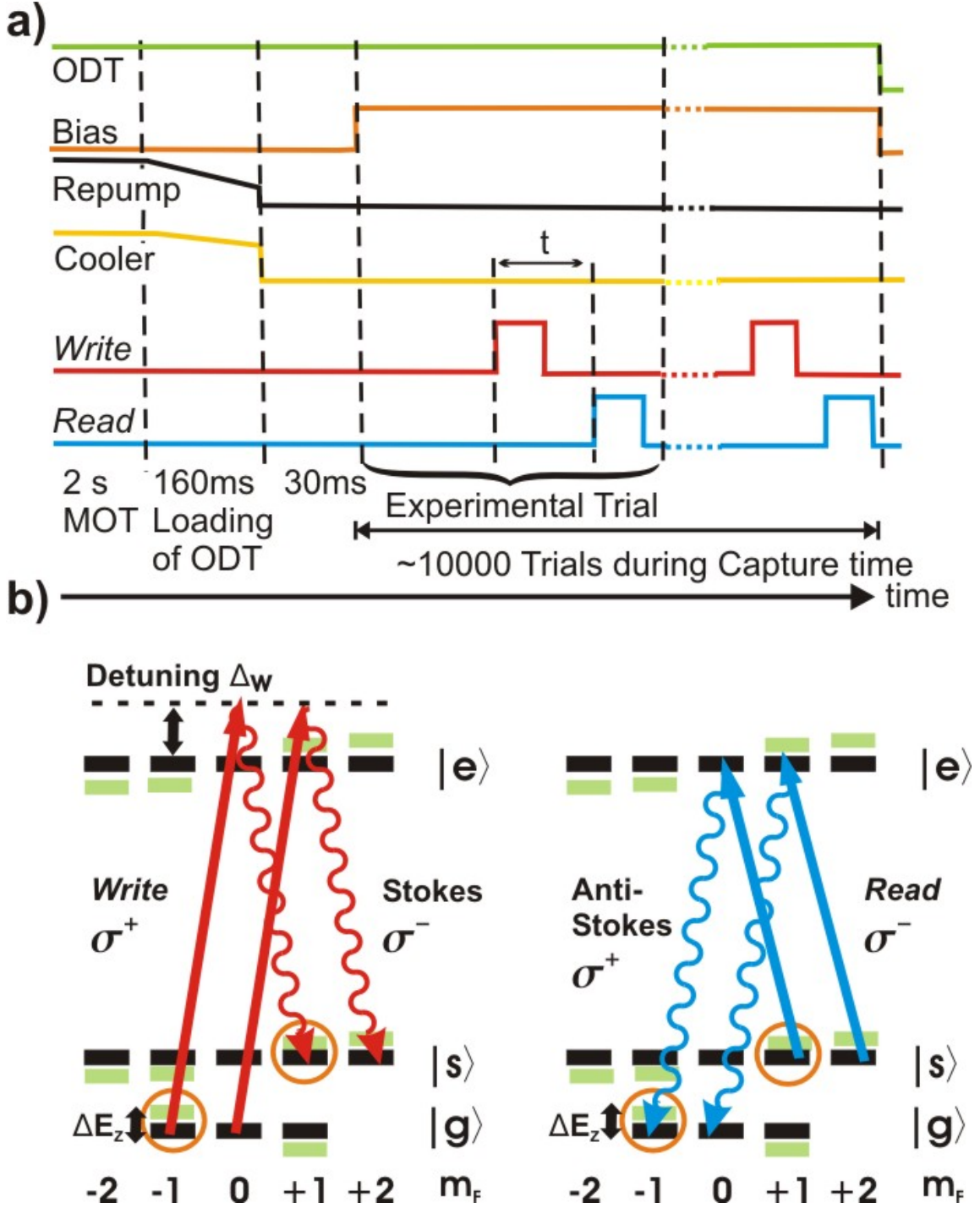
Figure 7.6: Time sequence of one experimental cycle and the relevant atomic transitions in the experiment. (a) After the MOT is switched off, the atoms are loaded into an optical trap with a transfer efficiency of $\sim 5\%$. Typically, 10000 alternating *write* and *read* pulses with lengths of 100 ns and 500 ns respectively and and a controllable time delay of t, illuminate the atomic ensemble. A clean pulse, which erases any excitation not retrieved in the previous trial, consists of a 1 μs pulse of *read* light. (b) The left and right diagrams illustrate the atomic levels involved in the *write* and *read* processes, where $|g\rangle = |5S_{1/2}, F = 1\rangle$, $|s\rangle = |5S_{1/2}, F = 1\rangle$, and $|e\rangle = |5P_{3/2}, F = 2\rangle$. The relevant Zeeman states are the $|F, m_F\rangle = |1, -1\rangle, |2, 1\rangle$ (clock states) and $|F, m_F\rangle = |1, 0\rangle, |2, 2\rangle$ (non-clock states).

and $g_{AS,AS}$ are the normalized auto-correlation functions [173]. In our experiment, the anti-Stokes and Stokes fields are both in thermal states, $g_{S,S} = g_{AS,AS} = 2$ [79], and therefore measuring $g_{S,AS} > 2$ is an indication of non-classical correlation.

Fig. 7.7 illustrates our main result where the normalized cross-correlation function is measured for various time delays between the *write* and *read* pulses. Violations of the Cauchy-Schwarz inequality are observed for delays up to 60 μs. The observed violations correspond to the temporal storage of the non-classical correlation between the Stokes and anti-Stokes photons as well as the atomic collective state in the quantum memory. The measured $g_{S,AS}$ function follows a Gaussian decay with two time constants. The Gaussian dependence is a consequence of the inhomogeneous phase broadening of the collective state due to the residual magnetic field [66] and the Maxwell velocity distribution of the atoms [174] (see section (7.1)). The two time scales result from different Zeeman components of the atomic ensemble. During the *write* process, both the $|c_1\rangle \rightarrow |e\rangle \rightarrow |c_2\rangle$ (clock) and $|F = 1, m_F = 0\rangle \rightarrow |e\rangle \rightarrow |F = 2, m_F = 2\rangle$ (non-clock) transitions contribute to the detection of Stokes photons with σ^- polarization. Likewise, the reversed transitions are involved in the detection of anti-Stokes photons with σ^+ polarization during the *read* process.

The time dependence of the normalized cross-correlation function thus can be described by $g_{S,AS}(t) = 1 + A_{nc}e^{-(t/\tau_{nc})^2} + A_c e^{-(t/\tau_c)^2}$ [74], where τ_c and τ_{nc} are the coherence times, or lifetimes, of the quantum memory, and the coefficients A_c and A_{nc} depend on the relative strengths of the clock and non-clock transitions as well as the initial atomic population in the Zeeman sublevels of the $F = 1$ manifold. Two lifetimes obtained from the fit to the measurement are $\tau_{nc}^{\text{exp}} = 16(3)$ μs and $\tau_c^{\text{exp}} = 45(5)$ μs. The fast decay in the short time scale is mainly due to the decoherence induced by the residual magnetic field for the atoms in the non-clock state. From τ_{nc}^{exp}, the inhomogeneity of the magnetic field is estimated to be approximately 10 mG, which is comparable to what has been observed in previous experiments [74, 77, 66]. The slow decay in the long time scale, on the the hand, is associated with the atoms in the clock state. The corresponding decay time τ_c^{exp} is well beyond the limit τ_{nc}^{exp} imposed by the residual magnetic field, which indicates the robustness of the clock state.

The thermal motion of the atoms after the *write* process accounts for the remaining decoherence in our experiment [112]. The atomic motion induces dephasing in the collective state through the position-dependent phase factors in Eq. 7.3. During the quantum storage, an atom travelling with a velocity of $\boldsymbol{v}$ leads to an additional phase of $(\mathbf{k}_s - \mathbf{k}_w) \cdot \delta\mathbf{r}$ with $\delta\mathbf{r} = \boldsymbol{v}t$. The consequent dephasing results in a decay in the normalized cross-correlation function with a time scale of $\tau_c^{\text{th}} \sim 1/(v|\Delta\mathbf{k}|)$, where v is the velocity of the atom along the direction of $\Delta\mathbf{k} = \mathbf{k}_s - \mathbf{k}_w$. In our experiment, v and $|\Delta\mathbf{k}|$ are estimated to be 66 mm/s and 290 mm^{-1}, respectively, and a lifetime of $\tau_c^{\text{th}} \cong 53$ μs is inferred. The agreement between τ_c^{th} and τ_c^{exp} thus implies the preservation of coherence in the optical trap during the quantum storage. The discrepancy is likely due to the misalignment of the magnetic bias field.
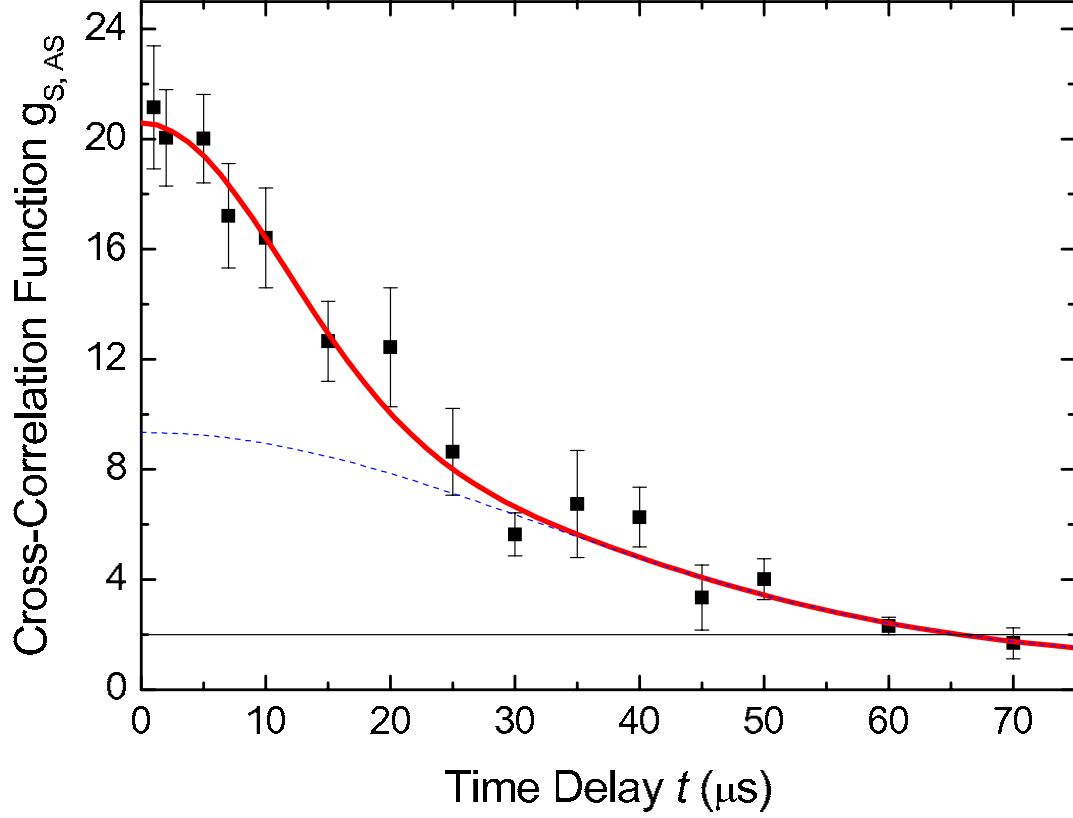
Figure 7.7: Normalized cross-correlation of the Stokes and anti-Stokes fields as a function of the time delays between the *write* and *read* pulses. Non-classical correlation is observed for storage times up to 60 μs. The curve is a Gaussian fit with two time constants, $\tau_{nc} = 16(3)$ μs and $\tau_c = 45(5)$ μs, and its asymptotic value of 1 as time delay $t \gg \tau_c$ corresponds to the probabilistic coincidence events, $p_{S,AS} = p_S p_{AS}$. The dotted line is a decay curve with only one time constant τ_c, assuming the absence of atoms in the non-clock state. The horizontal line at $g_{S,AS} = 2$ indicates the onset of quantum correlation. The error bars indicate the statistical errors.

7.2.3 Discussion

In conclusion, we have realized a quantum memory with optically trapped atoms for collective atomic states. Non-classical correlations of the photon pair, arising from the spontaneous Raman scattering and the retrieval of the collective atomic state, are observed for storage times up to 60 μs. The measured lifetime of the quantum memory associated with the atoms in the clock state is beyond the limit imposed by the residual magnetic field, which shows the robustness of the clock state. Together with the non-dissipative confinement provided by the optical trap, the quantum memory has a potential storage time of seconds. The observed storage time is currently limited by the thermal motion of the atoms. With an atomic ensemble at a lower temperature, a longer storage time could be achieved. For example, a temperature of submicro-Kelvin could be obtained by employing evaporative cooling in a crossed optical trap [175], which will greatly reduce the atomic motion and thus extend the storage time beyond milliseconds. Alternatively, one could confine the atoms in an optical lattice and expect a storage time of seconds. We also note that the inhomogeneous light shift in the red-detuned optical trap could be improved by confining the atoms in a blue-detuned "box" trap [176]. Lastly, our experiment utilizes the atoms in the clock state as well as the non-clock state. One could also realize a quantum memory composed of atoms purely in the clock state, for instance, by optically pumping all atoms into the state $|c_1\rangle$ before each experimental trial.

Chapter 8

Conclusions and Outlook

Quantum memory is a key element for long distance quantum communication with atomic ensembles and linear optics. This implementation needs relatively simple ingredients which makes it very attractive. In this thesis, we have reported on our work on a DLCZ-type quantum memory implemented with ultra-cold ^{87} Rubidium atoms. We conclude by summarizing the main results and give an outlook.

Atoms released from a MOT serve as atomic ensemble. Non-classical light was generated with them which violated the Cauchy-Schwarz inequality by a factor of 50. The lifetime was measured as $\tau_c = 12.5 \pm 2.6$ μs. It was limited due to the dephasing of the Zeeman components due to residual magnetic fields. By adding an electronic feedback circuit we employed the quantum memory to build a deterministic single photon source. We could increase the excitation probability by a factor of twelve while preserving the single photon quality.

Subsequently we generated pairs of entangled photons by synchronization of two of this sourcetype. The measurement of the Hong-Ou Mandel dip in time and frequency domain shows the narrow bandwidth, i.e. an estimated coherence time of 25 ± 1 ns FWHM. By overlapping the single photon on a BS photonic entanglement was achieved. The pairs violated Bell's inequality by 5 standard deviations. The narrow bandwidth of the single photons and the high efficiency for entanglement generation makes such a source an ideal candidate for large scale quantum communication.

In the single photon source a higher probability for single photon generation can be achieved if the storage time is longer. Storage times of 30 μs are far from requirements of practical implementation as well. Thus the isolation of an overlooked dephasing mechanism is an important step to realize these goals. By optical pumping into first-order magnetic field insensitive states the dephasing process due to stray fields present in previous experiments was reduced and the motion of the atoms was identified as limiting factor. The diffusion of atoms due to their thermal motion can be suppressed by the generation of long wavelength spin wave. In this way storage times of one millisecond could be achieved. The limitation due to the loss of the untrapped atoms under gravity from the detection modes needs to be addressed. In order to provide confinement of the atoms for longer storage times an atomic ensemble in an optical dipole trap was used as quantum memory. Addressing first-

order magnetic field insensitive states increased the storage time compared to the first MOT experiments, but was still limited to the dephasing due to diffusion of the atoms. The possibility to generate nonclassical light from confined atoms with a high optical depth could be demonstrated. A life time of the trap of $\tau_{LFT} = 19 \pm 2$ s clearly shows the suitability of optical trapping of atomic ensembles for implementing quantum memories with lifetimes of seconds.

Based on these achievements and conclusions important improvements and long-term developments for an advanced quantum memory based on atomic ensembles and single photons can be made. As we have seen two important limitations still have to be tackled. The improved reduction of the thermal motion of the atoms is necessary for the suppression of the diffusion. A possible solution to this is the application of an optical lattice in order to restrict the volume in which the atoms can move. But this one comes at the price of a another dephasing mechanism. We have seen that the differential light shift in a far-red detuned optical dipole trap limits the storage time to some milliseconds. Thus a blue-detuned trap where the atoms are trapped in the intensity minimum is more favorable. The disadvantage of having a differential light shift can greatly reduced by a hollow-beam or optical box configuration. In order to provide the necessary additional reduction of the motion of atoms a blue-detuned optical lattice has a reduced effect, since the atoms can experience in average a non-negligible differential light shift. The set-up of on optimal trap geometry is a long-term development since memory times of hundred of seconds are necessary for practical continental communication applications.

A more short term improvement is the lowering of the ensembles' temperature by application of sub-Doppler cooling or evaporative cooling [120] in the optical dipole trap. A one-dimensional optical lattice can also reduce the thermal motion. The application of a compensation laser to the red-detuned dipole trap can compensate the differential light shift and overcome the limit set by it. By changing the trap geometry of the optical dipole trap the Fresnel number can be changed to $F \sim 1$ in order to collect more photons. The installation of a detection which is able to resolve the waist of the atomic cloud could increase the signal "strength" even more.

In order to further increase the retrieve efficiency it is possible to install a cavity with a low finesse around the atomic ensemble. By the enhanced memory time and an increased retrieve efficiency it possible to achieve a generation probability of single photons by the deterministic source in the order of 90%. Thus it can enable a significant progress for linear optical quantum information processing (LOQIP).

The results presented in this thesis provide an important step for an implementation of long distance quantum communication. Despite the immense progresses made in this field of research, there are still many open questions to answer and many technical problems to solve. But for sure, it will stay a very exciting area of research in the near future.

Appendix A

List of Publications

Within the framework of the thesis the following publications have been finalized:

- **Thorsten Strassel**, Shuai Chen, Yu-Ao Chen, Zhen-Sheng Yuan, Bo Zhao, Jörg Schmiedmayer, and Jian-Wei Pan. Deterministic and Storable Single-Photon Source Based on a Quantum Memory. Phys. Rev. Lett. **97**, 173004 (2006)
  see also http://arxiv.org/abs/quant-ph/0607036.

- Zhen-Sheng Yuan, Yu-Ao Chen, Shuai Chen, Bo Zhao, Markus Koch, **Thorsten Strassel**, Yong Zhao, Gan-Jun Zhu, Jörg Schmiedmayer, and Jian-Wei Pan. Synchronized Independent Narrow-Band Single Photons and Efficient Generation of Photonic Entanglement. Phys. Rev. Lett. **98**, 180503 (2007).

- **Thorsten Strassel,** Chih-Sung Chuu, Bo Zhao, Markus Koch, Yu-Ao Chen, Shuai Chen, Zhen-Sheng Yuan, Jörg Schmiedmayer, and Jian-Wei Pan. Demonstration of a Quantum Memory with Optically Trapped Atoms. Accepted for Publication by Phys. Rev. Lett. (2008)
  see also http://arxiv.org/abs/0808.2687.

- Bo Zhao, Yu-Ao Chen, Xiao-Hui Bao, **Thorsten Strassel**, Chih-Sung Chuu, Xian-Min Jin, Jörg Schmiedmayer, Zhen-Sheng Yuan, Shuai Chen, and Jian-Wei Pan. A Millisecond Quantum Memory for Scalable Quantum Networks. Submitted to Nature Physics (2008).

Appendix B

Excited State Polarizability

In order to evaluate the strength of the optical transitions it is necessary to evaluate the dipole matrix elements $\langle f|\hat{\mathbf{d}}|i\rangle$. Due to the fine and hyperfine coupling the quantum numbers n, L are not 'good' quantum numbers anymore. Therefore the overlap of the wavefunctions must be described in terms of the complete set of quantum number n, L, J, I, F, S, m for the ground state and $n', L', J', I', F', S', m'$ for the excited state.

We recall that the energy shift in the dressed state picture is

$$\Delta E_i = -\frac{\mathcal{E}^2}{4\hbar} \sum_{f \neq i} |\langle i| \mathbf{d} |f\rangle|^2 \frac{1}{\Delta_{eff}}, \tag{B.1}$$

where Δ_{eff} describes the effective detuning from the transition $f \to i$. With the Wigner-Eckart theorem the transition matrix elements $\langle i|\mathbf{d}|f\rangle$ is expressed by a reduced matrix $\langle F||e\mathbf{r}||F'\rangle$ and the Clebsch-Gordan coefficients $\langle F, m_F|F', 1, m'_F, q\rangle$, where q denotes the polarization [114]:

$$\langle i|\mathbf{d}|f\rangle = \langle F, m_F|F', 1, m'_F, q\rangle\langle F||e\mathbf{r}||F'\rangle \tag{B.2}$$

The Wigner $6j$ symbol is employed when further simplifying the reduced matrix element into a fully reduced matrix element $\langle J||e\mathbf{r}||J'\rangle$:

$$\langle F||e\mathbf{r}||F'\rangle = \langle J||e\mathbf{r}||J'\rangle(-1)^{F'+J+I+1}\sqrt{(2F'+1)(2J+1)} \begin{pmatrix} J & F & 1 \\ F' & J' & I \end{pmatrix}_{6j} \tag{B.3}$$

The energy shift accounting for the complete set of quantum numbers is

$$\Delta E_i = -\frac{1}{4} \sum_{n',J',F',m'} \frac{1}{\hbar\Delta'_{if}} \left|\langle n, J, I, F, m|\hat{\mathbf{d}}\cdot\mathcal{E}|n', J', I, F', m'\rangle\right|^2 \tag{B.4}$$

The sum is evaluated over all $|f\rangle$ with quantum number n', J', F', m' and energies $E_f \neq E_i$. evaluation of the dipole moment matrix elements by computing the wave functions overlap is difficult. As shown in [92] the dipole matrix element is related

to the lifetime of the transition, where experimental data can be used. The life time $\frac{1}{\tau_{JJ'}}$ is given by

$$\frac{1}{\tau_{JJ'}} = \frac{\omega_{if}^3}{3\pi\epsilon_0\hbar c^3}\frac{2J+1}{2J'+1}|\langle J|e\mathbf{r}|J'\rangle|^2. \tag{B.5}$$

Then the light shift reads as

$$\Delta E(J, F, m_F) = \frac{3\pi c^2 I}{2}\sum_{J',F',m_F'}\frac{(2J'+1)(2F'+1)}{\tau_{JJ'}\Delta_{FF'}'\omega_{FF'}^3}\begin{Bmatrix} J & J' & 1 \\ F' & F & I \end{Bmatrix}_{6j}^2 |\langle F, m_F|F', 1, m_F', q\rangle|^2, \tag{B.6}$$

which includes the effective detuning

$$\frac{1}{\Delta_{FF'}'} = \frac{1}{\omega_{FF'} - \omega} + \frac{1}{\omega_{FF'} + \omega} \tag{B.7}$$

An alternative way is to use the oscillator strength of the $i = nJ \longrightarrow f = n'J'$ transition instead of the lifetime. The oscillator strength of the transition $f \to i$ is defined as

$$f_{if} = \frac{2m_e\omega_{if}}{3\hbar e^2(2J+1)}|\langle nJ|d|n'J'\rangle|^2. \tag{B.8}$$

It is related to the life time τ_{if} by

$$A_{fi} = \frac{1}{\tau_{fi}} = \frac{e^2\omega_{if}^2}{m_e c^3\epsilon_0 2\pi}f_{fi}. \tag{B.9}$$

Comparison between equation (B.6) and equation (5.2) leads to

$$\alpha(\omega) = \frac{3e^2}{2m_e}(2J+1)(2F+1)\sum_{f=n',J',F',m'}(2F'+1)\frac{f_{if}}{\omega_{if}\Delta_{if}}\begin{pmatrix} F & 1 & F' \\ -m & q & m' \end{pmatrix}^2\begin{Bmatrix} J & F & I \\ F' & J' & 1 \end{Bmatrix}^2. \tag{B.10}$$

The oscillator strengths and the transition frequencies can be found in databases. For our optical dipole trap potential the polarizability of the $5^2P_{1/2}, F = 2$ level is valuable in order to compute the light shift of the *write* and *read* transitions from their vacuum value.

Table B.1 summarized the most relevant oscillator strengths. Using these values in equation 5.9 we obtain a polarizability of $\alpha = -2.89 \cdot 10^{-38}\frac{C^2s^2}{kg}$ at a wavelength of 1030 nm. The minus sign indicates that the energy of the level is shifted upwards. For states with angular momentum $J > 1/2$ one can derive from equation (B.4) that there is independent of the incident polarization of the laser field a quadratic m_F-sublevel dependence given by [178] [179] and the light shift can be decomposed into

$$\Delta E(J > 1/2) = \alpha_{sc} + \alpha_{vec}m_F + \alpha_{ten} \cdot F(m_F^2), \tag{B.11}$$

where α_{sc} denotes the scalar, α_{vec} the vectorial and α_{ten} the tensorial part of the light shift. For linear (π) light the vectorial part is zero (α_{vec}) but the quadratic

Table B.1: Oscillator strengths for selected transitions from the $5^2P_{1/2}$ level of ^{87}Rubidium [177].

State	n_f	L_f	J_f	λ [nm]	f_{if}
$5^2S_{1/2}$	5	0	$\frac{1}{2}$	795	0.340
$6^2S_{1/2}$	6	0	$\frac{1}{2}$	1324	-0.1946
$7^2S_{1/2}$	7	0	$\frac{1}{2}$	728	-0.018
$4^2D_{3/2}$	4	2	$\frac{3}{2}$	1475	-0.634
$5^2D_{3/2}$	5	2	$\frac{3}{2}$	762	-0.052

term is non vanishing. The function F for a linear light field with the quantization axis chosen parallel to the polarization axis is

$$F = \frac{3m_F^2 - F(F+1)}{F(2F-1)}.$$ (B.12)

A careful derivation yields for all contributions for state v [146] (neglecting the hyperfine interaction):

$$\Delta E_v = -\frac{1}{2}\alpha_0(\omega)\mathcal{E}^2 - \frac{1}{2}\alpha_2(\omega)\frac{3m^2 - j_v(j_v+1)}{j_v(2j_v-1)}\mathcal{E}^2$$ (B.13)

$$\alpha_0^v(\omega) = \frac{2}{3(2j_v+1)}\sum_k \frac{\langle k||d||v\rangle^2(E_k - E_v)}{(E_k - E_v)^2 - \omega^2}$$ (B.14)

$$\alpha_2(\omega) = -4C\sum_k(-1)^{(j_v+j_k+1)}\left\{\begin{pmatrix} j_v & 1 & j_k \\ 1 & j_v & 2 \end{pmatrix}\right\} \times \frac{\langle k||d||v\rangle^2(E_k - E_v)}{(E_k - E_v)^2 - \omega}$$ (B.15)

$$C = \left(\frac{5j_v(2j_v-1)}{6(j_v+1)(2j_v+1)(2j_v+3)}\right)^{1/2}$$ (B.16)

Care has to be taken with respect to the units when using values from databases. The formula (B.15) uses atomic units: for E and ω the atomic energy is $E_h = 4.3597 \cdot 10^{-18}$J, the polarizability is converted into SI-units by multiplication of a factor $1.648 \cdot 10^{-41}$. Using the electric-dipole elements computed in [146] the tensor polarizability for the $5p_{3/2}$ level for a linear light field with 1030 nm is $\alpha_2 \sim 572$ [a.u.]. The scalar part is $\alpha_0 \sim -1589$ [a.u.]. The 7 transitions listed in table (B) have been included in this computation.

Another approach can be chosen by evaluation of the Schrödinger equation with a one electron model (alkali atom) and a decomposition of the atom-light interaction. The light-shift of a magnetic hyperfine state with quantum numbers F and m_F for

Table B.2: Oscillator strengths for selected transitions from the $5^2P_{3/2}$ level of ^{87}Rubidium [146].

Transition	λ [nm]
$5p_{3/2} - 5s_{1/2}$	780
$5p_{3/2} - 6s_{1/2}$	1367
$5p_{3/2} - 7s_{1/2}$	741
$5p_{3/2} - 8s_{1/2}$	616
$5p_{3/2} - 9s_{1/2}$	566
$5p_{3/2} - 4d_{5/2}$	1529
$5p_{3/2} - 5d_{5/2}$	776

multiple linear light fields $1..i..N$ is given by the eigenvalues of the matrix [145]:

$$E = E_{hfs} - \frac{1}{2\epsilon_0 c} \sum_{a=1}^{N} (\alpha_0^I + \alpha_2^i T^i) I_i, \qquad (B.17)$$

Q_i is a matrix with components $\langle F, m_F | Q_\mu | F', m_F' \rangle$ with $Q_\mu = [3\hat{J}_\mu^2 - J(J+1)]/J(2J-1)$. I_i is the intensity of laser field i and J_μ is electronic angular momentum operator in direction of the respective laser field. The scalar polarizability is the same for all m-components and defined as average of x-,y- and z- components: $\alpha_0 = (\alpha_{xx} + \alpha_{yy} + \alpha_{zz})/3$. The tensor polarizability $\alpha_2^i = (a_{xx} - \alpha_{zz})/3$. For a trapping light of 1064 nm [180] they are $\alpha_0[5S_{1/2}] = 733$ (a_0^3), $\alpha_0[5P_{3/2}] = -1166$ (a_0^3) and $\alpha_2[5P_{3/2}] = 567$ (a_0^3), which is comparable to our results for 1030 nm.

Hyperfine Interaction   The hyperfine splitting needs to be added by the interaction Hamiltonian:

$$V_{hfs} = \hbar \mathcal{A} \mathbf{I} \cdot \mathbf{J} + \hbar \mathcal{B} \frac{6(\mathbf{I} \cdot \mathbf{J})^2 + 3\mathbf{I} \cdot \mathbf{J} - 2I(I+1)J(J+1)}{2I(2I-1)2J(2J-1)}, \qquad (B.18)$$

where $\mathcal{A} = h \cdot 84.7185$ MHz and $\mathcal{B} = h \cdot 12.4965$ MHz are the hyperfine structure constants of ^{87}Rubidium $5P_{3/2}$ [114]. The elements of equation (B.18) which are non-zero are:

$$\langle Fm_F | V_{hfs} | Fm_F \rangle = -\frac{1}{2} \mathcal{A} K + \hbar \mathcal{B} \frac{\frac{3}{2} K(K+1) - 2I(I+1)J(J+1)}{2I(2I-1)2J(2J-1)}, \qquad (B.19)$$

where $K = F(F+1) - I(I+1) - J(J+1)$.

Appendix C

^{87}Rubidium reference

Spectroscopy[114]				
D-1 line	λ_0	$5s^2S_{1/2} \to 5p^2P_{1/2}$	795.0	nm
natural life time	τ	$\equiv 1/\Gamma$	27.70(4)	ns
natural linewidth	$\Gamma/2\pi$		5.75	MHz
saturation intensity	I_0	$\equiv \pi h c\Gamma/3\lambda_0^3$	1.49	mW/cm^2
D-2 line	λ_0	$5s^2S_{1/2} \to 5p^2P_{3/2}$	780.2	nm
natural life time	τ	$\equiv 1/\Gamma$	26.24(4)	ns
natural linewidth	$\Gamma/2\pi$		6.07	MHz
saturation intensity	I_0	$\equiv \pi h c\Gamma/3\lambda_0^3$	1.67	mW/cm^2
Laser cooling (D-2 line):				
Doppler-temperature	T_D	$\equiv \hbar\Gamma/2k_B$	146	μk
typical Doppler-velocity	v_D	$\equiv \sqrt{2k_BT_D/M}$	16.7	cm/s
recoil temperature	T_R	$\equiv (\hbar k_L)^2/mk_B$		
		$= 2E_R/k_B$	361	nK
recoil veloctiy	v_R	$\equiv \hbar k_L/m$	5.88	mm/s
recoil frequency	ω_R	$\equiv E_R/\hbar = \hbar k_L^2/2m$	$2\pi\times$ 3.77	kHz
thermal deBroglie	Λ	$\equiv h/\sqrt{2\pi m k_B T}$	15.5	nm (T$_D$)
wavelength			312	nm (T$_R$)
Gravitation:	mg/k_B		1.03	mK/cm
	mg/h		21.4	MHz/cm
	mg/μ_B		15.3	G/cm
mass number	A		87	
mass	m		$1.443 \cdot 10^{-24}$	kg
Scattering Parameter :[122]	$a_{2,2}$		109(10)	a_0
(s-wave scattering-length a_{F,m_F})	$a_{1,-1}$		106(6)	a_0

Appendix D

AOM Driver

During the course of the project an electronic driver circuit for acousto optical modulators (AOM) has been developed in cooperation with the electronic workshop of the "Physikalisches Institut". It was partially motivated by cost reduction. There is an excessive need for AOMs in order to conduct the experiments for the DLCZ scheme. Another reason is the fact, that there is a variety of driver circuits available on the market, but they all come with advantages and disadvantages. So the main design consideration was a cost-effective home-built device fulfilling the requirements on switching speed (< 100 ns), amplification bandwidth ($60 - 260$ MHz), rf-power ($0.5 - 3$Watt), extinction ratio (> 90 dB), external intensity adjustment, external frequency control ($60 - 260$ MHz), display and protection against back reflection of power due to imperfect impedance matching.

The result are the devices with type numbers A395, A389 and A402. Their amplification bandwidth is still limited such that different amplifier chips must be used for 80 MHz, 110 MHz and 260 MHz AOMs. This limitation is overcome by a new prototype which provides a bandwidth from 40 MHz to 500 MHz with a maximum output power of 33 dBm. The device provides the frequency and power on a display as well and is currently under test.

The remaining drawback is the availability of wide-ranged tunable voltage controlled oscillators (VCOs). There is no commercially VCO with can provide a tuning range matching the bandwidth of the broadband amplifier. Therefore the VCOs have to be matched to the desired frequency range. Additionally the frequency dependent Output-Amplitude of the VCO adds another obstacle to the aim of constant power output of the AOM driver for that frequency range. A DDS provides an alternative which is in principle capable of overcoming these problems. The bottleneck of this approach is the communication of the computer to the DDS in order to provide the correct frequency tuning words. An approach by using a USB connection questions the real time capability of the AOM driver and adds additional programming complexity to the experimental control program. The use of an analog-to-digital converter (ADC) which converts the analog control voltage of the experimental control to a 32-bit frequency tuning word for the DDS is difficult since 14 bit ADC components are the state of art. A concept to connect this components is currently

investigated and looks very promising.

An AOM driver unit consists of two circuit boards which are mounted inside a HF-tube. The rf-signal is transmitted with a shielded coaxial cable from the control board (figure (D.1))to the amplifier board (figure (D.2)). The SMA connectors for the inputs and the output are located on the frontpanel of the unit. The rf output is connected to the AOM. The inputs are for the TTL switch signal, the analog frequency control and the analog output level control. Further on there are the switches for amplifier on/off, cw-mode on/off, external/internal frequency adjustment and external/internal level adjustment. There are holes for the potentiometers necessary to adjust the working point of the amplifier and the internal frequency and level control.

Four driver units can be mounted in a single rack which provides clean supply voltages and allows the data connection of the two circuits boars of a unit via the backplane.
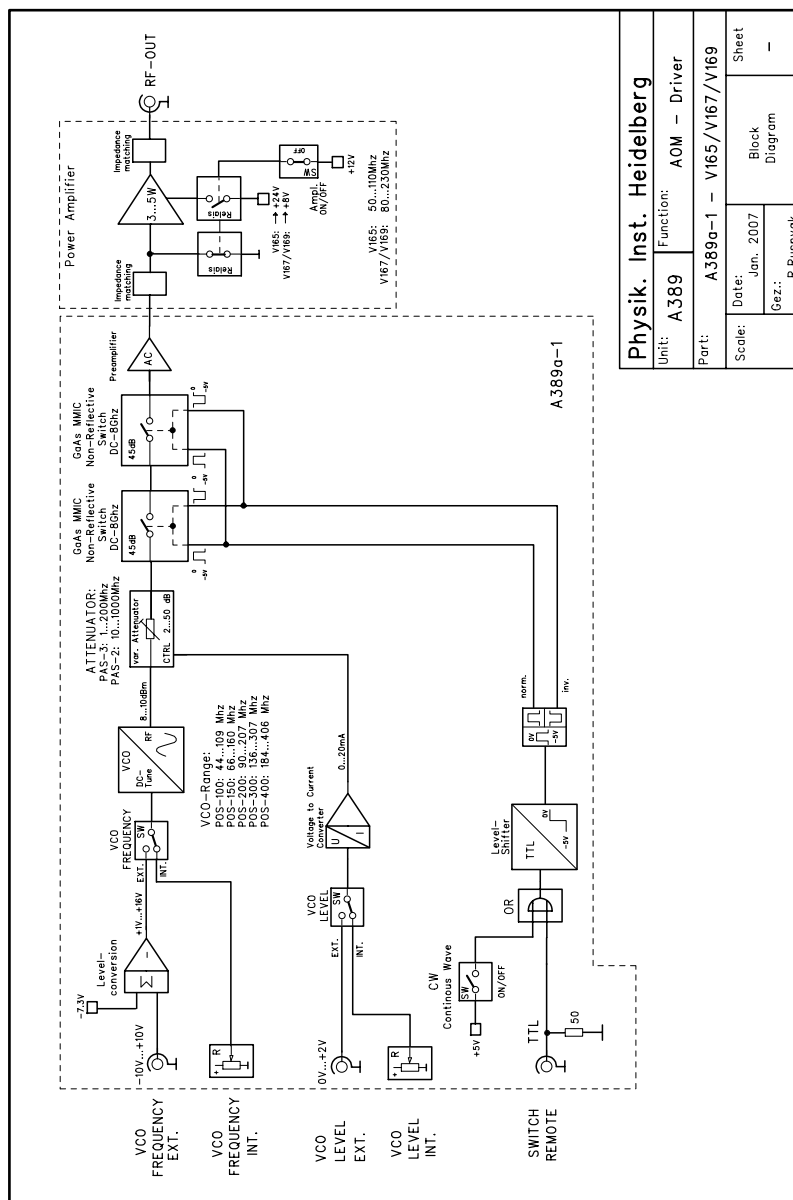
Figure D.1: Circuit board with radio-frequency source, attenuator and switches.
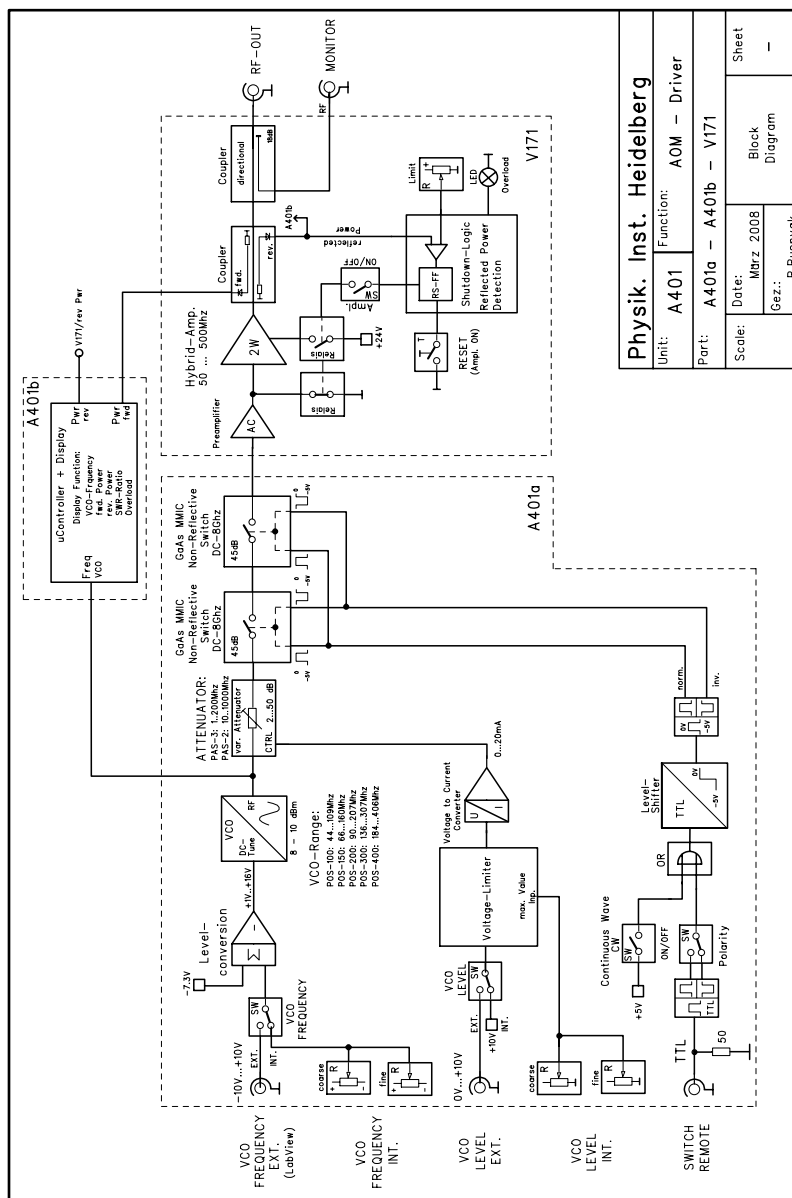
Figure D.2: Circuit board with amplifier.

Appendix E

Phase-Lock Card

The frequency stabilization of the lasers with the frequency modulation (FM) locking circuit enables locking to resonance lines from Doppler-free saturation spectroscopy on atomics or from cavities. A frequency offset (FO) locking circuit can stabilize the frequency of laser relative to an already stabilized laser with a frequency offset range from MHz to GHz depending of the bandwidth of the photodiode used for the detection of their beating signal. The linewidth of the beating signal can be as small as 1.2 MHz. For applications of Raman spectroscopy or stored light experiments where two-photon transitions a smaller relative linewidth is necessary to obtain the two-photon resonance [120]. For that purpose the frequency stabilization in a Littrow setup with a piezo [135] is not sufficient. Let us consider two optical light fields with fixed frequency ω_i (i=1,2) and fluctuating phase ϕ_i. Their electrical fields are given by

$$E_1(t) = E_{01} \cos(\omega_1 + \phi_1(t)) \tag{E.1}$$
$$E_2(t) = E_{02} \cos(\omega_2 + \phi_2(t)). \tag{E.2}$$

The frequency difference is then

$$\Delta\omega = \frac{d}{dt}\left[\omega_1 t - \phi_1(t) - \omega_2 t - \phi_2(t)\right]. \tag{E.3}$$

Only if the relative phase between the lasers is constant $\phi_1 - \phi_2 = $ const the frequency difference $\Delta\Omega = \omega_1 - \omega_2$ is fixed. Thus phase locking between the lasers in required in order to achieve a small linewidth [181]. Thus an optical phase lock-loop (OPLL) needs to be implemented. Figure (E.1) shows a schematic of the set-up. The master laser is frequency stabilized by an FM-lock (see chapter (5)). A part of the laser light is overlapped with light from the so-called slave laser which has to be stabilized to the master laser. The beating signal of the two light fields is detected by a fast photodiode. An electronic phase detector compares the phase of the beating signal with a local oscillator. The feedback in order to control the phase of the laser light cannot be achieved by the piezo feedback loop with a bandwidth of ~ 10 kHz. A fast feedback signal on the laser current with a bandwidth of approximately 1.3 MHz

can in addition to the frequency stabilization control the phase [1]. The feedback loop drives (within its capture range) the frequency of the beating signal (if VCO1 is not used) to the frequency of VCO2. Then it controls the phase of the beating signal with respect to this local oscillator. The resulting linewidth (3dB) of the beating signal of the two lasers is measured with ≈ 10 Hz. The power in this carrier signal is $\sim 80\%$.

---

[1]The modulation of the laser current modulates the phase of the laser frequency. A constant modulation frequency adds sidebands to the laser frequency [135].
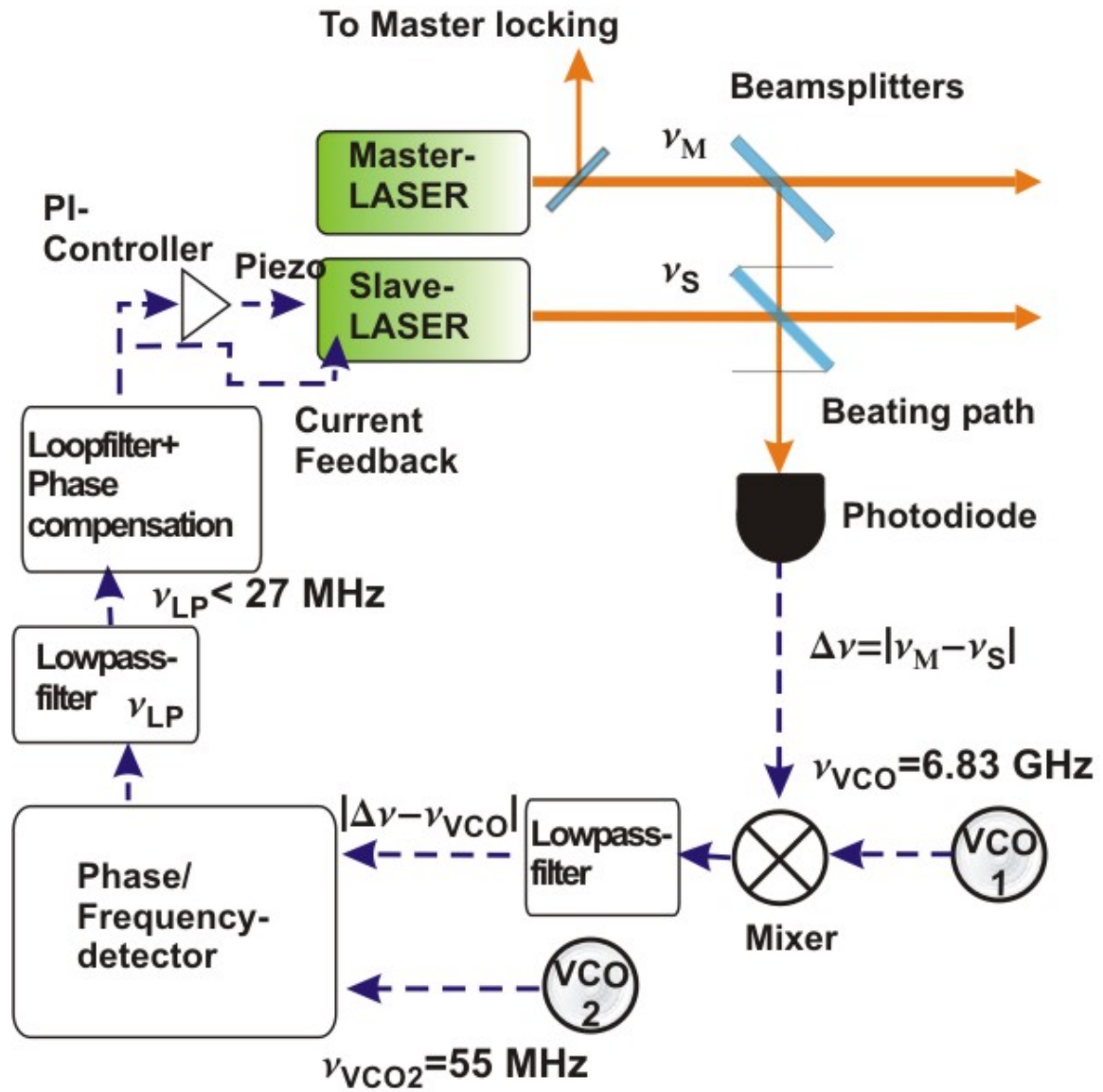
Figure E.1: Schematic set-up for the relative phase-stabilization of two lasers. The master laser is locked to an atomic resonance or cavity. On the beating path parts of the master and the slave laser are overlapped. A sufficiently fast photodiode detects the beating signal of the two light fields.
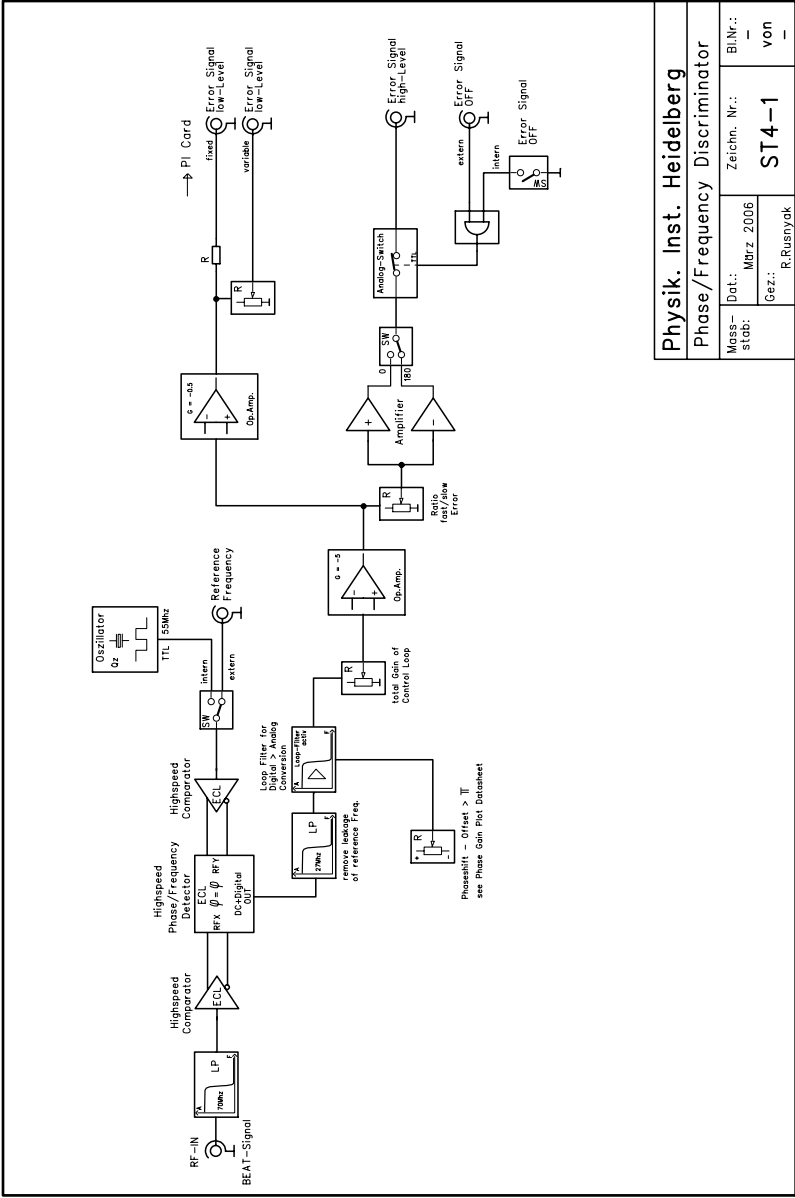
Figure E.2: Circuit board of the phase-lock card for a frequency/phase stabilization of a laser.
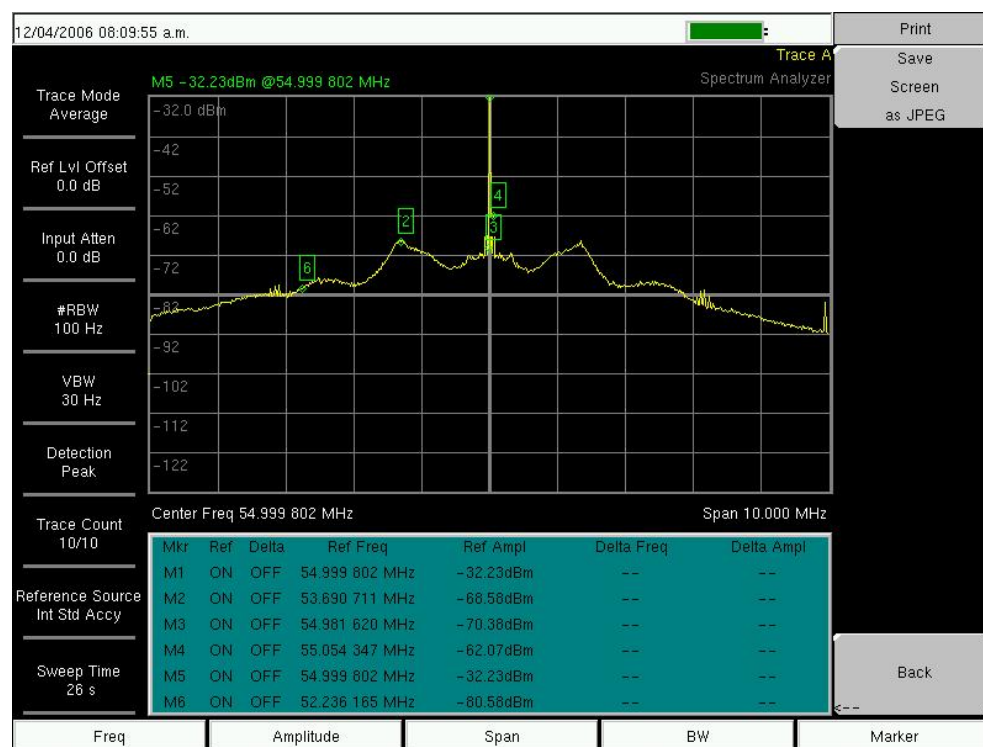
Figure E.3: Spectrum analysis of the beating signal: The bandwidth of the feedback loop can be estimated by the two servo pumps on the left and right side of the signal peak, i.e. beating signal. The measurement is done in the closed-loop mode with a 10 percent power splitter coupling out the signal from the photodiode for the spectrum analyzer.
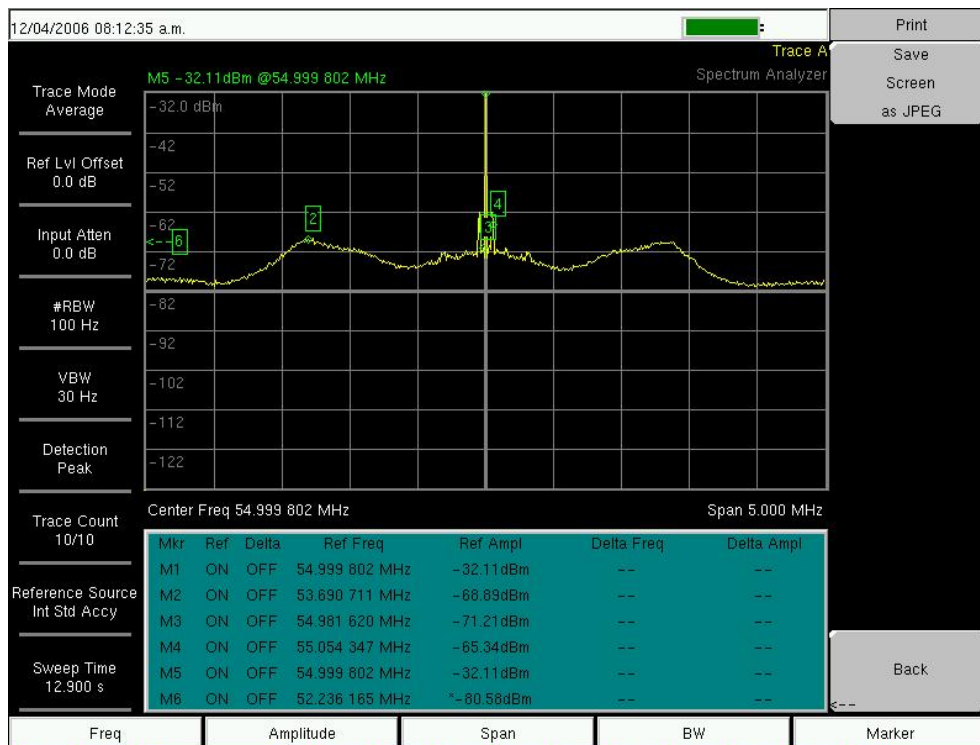
Figure E.4: Zoom of Spectrum analysis:[2] indicates one of the servo bumps
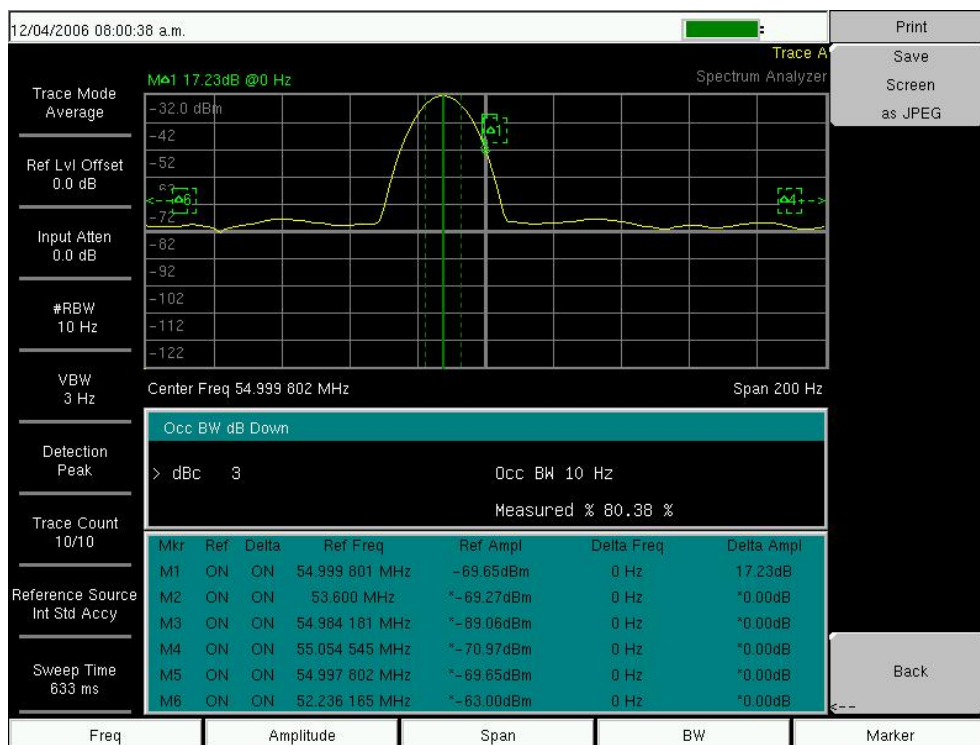
Figure E.5: Zoom of Spectrum analysis: The measurements of the beating signal's linewidth (3dB) of about 10 Hz (!) is limited by the resolution bandwidth of the spectrum analyzer. The capture range of the circuit is about 10 MHz.

Appendix F

Microwave Antenna

For the microwave spectroscopy a microwave antenna for a frequency of ~ 6.8 GHz has been designed and built. Due to the need for linear and circular polarization and the relativ simple mechanical design a helix antenna has been selected. It provides a clean (depending of the rotational direction) right or left handed circular polarized beam. Therefore the antenna must operate in the axial mode, i.e. the main lobe of the antenna is directed along the symmetry axis. The gain or directivity of an antenna is the increase of a directionality compared to an isotropic radiator. Between a pitch angle of $12° < \alpha < 15°$ and an circumference between $\frac{3}{4} < C_\lambda < \frac{4}{3}$ when $n > 3$ the gain is approximately given by the empirical expression [182]

$$D_{dB} = 11.8 + 10 \cdot \log(nC_\lambda^2 S_\lambda), \tag{F.1}$$

where n is the number of turns, S_λ is the slope (in units of wavelength) and the circumference is denoted by C_λ (in wavelength units). The half-power beamwidth is $HPBW = \frac{52}{C_\lambda\sqrt{nS_\lambda}}$[degrees]. These parameters have to be optimized and balanced. An increased gain and a small beamwidth "focus" the available microwave energy which is provided by an amplifier into a specific area. In the experiment the antenna is directed onto the atoms through a CF-40 viewport of the the stainless steel vacuum chamber. The diameter of the metal tube is similar to the wavelength of the microwave of 44.1 mm. The tube of the chamber serves therefore as a waveguide for the microwave field which has been tested.

A plexiglass rod of 11 mm diameter serves as carrier for the helix wire. A spiral groove is milled into the rod in order to carry the copper wire ($\varnothing = 1$ mm). Due to the electric permittivity of the material the wavelength $\lambda_{medium} = \frac{\lambda}{\sqrt{\epsilon_r}}$is reduced. The values of the dielectric constant at 7 GHz given in the literature are varying from $\epsilon_r = 2.474$ to $\epsilon_r = 3.5$ (at constant temperature of 22°). In order to completely enclose the helix wire with plexiglass a tube of that material is fit onto the rod. A brass plate with a diameter of 2 cm $> \lambda/2$ serves as reflector an thus increases the gain. The gain of the antenna is very sensitive to the slope of the turns (pitch angle) and the circumference and the uncertainty in the correct dielectric constant

causes that the numerical simulations [1] give only a rough value of ~ 16.24 dBi. Measurements of the gain with the so-called three antenna method yield a gain for the antenna of $\approx 19.4 \pm 1.2$ dBi.

The impedance of the antenna arises mainly at the central feeding point where the copper wire passes a hole in the reflector plate. There a SMA connector is attached. The impedance is typically ~ 120 Ω. But by tapering the wire end and proper calculation of a dielectric spacer between the wire end and the reflector plate the antenna can be matched to 50 Ω. This is reflected by the small standing wave ratio (SWR) which has been measured with a Vector Network analyzer (see figure (F.5)).

---

[1]SuperNEC (Commercial program) or NEC4Free (freeware)
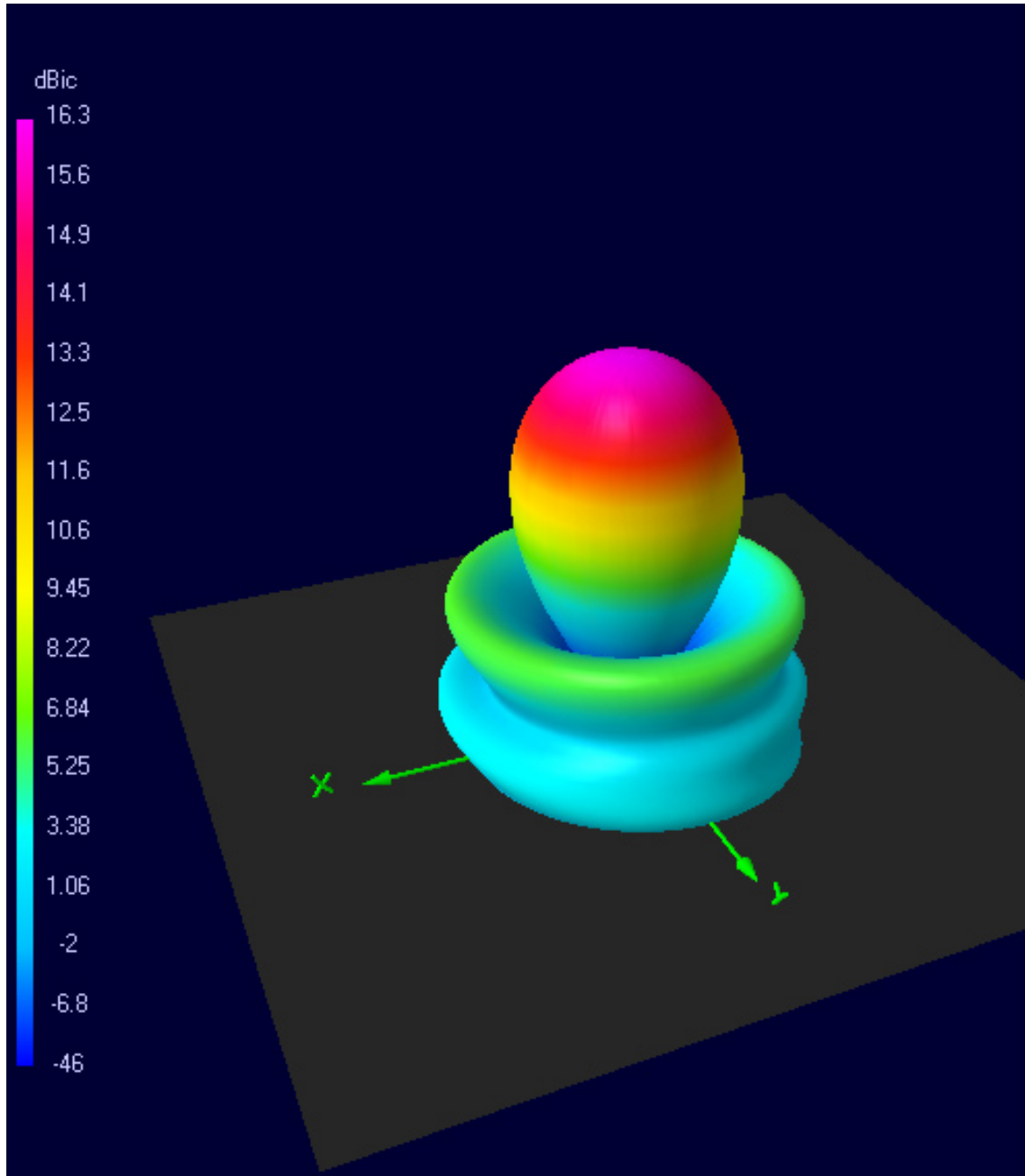
Figure F.1: Simulation of emission pattern of a helical microwave antenna for 6.83 GHz. The right hand circular polarization gain of the antenna is plotted for all spatial directions. The metal plate in the x-y plane serves as reflector, thus there no emission into the negative z-direction. 8 turns with central feed are simulated. The first side-lobe is suppressed by $\sim$ 10 dB.
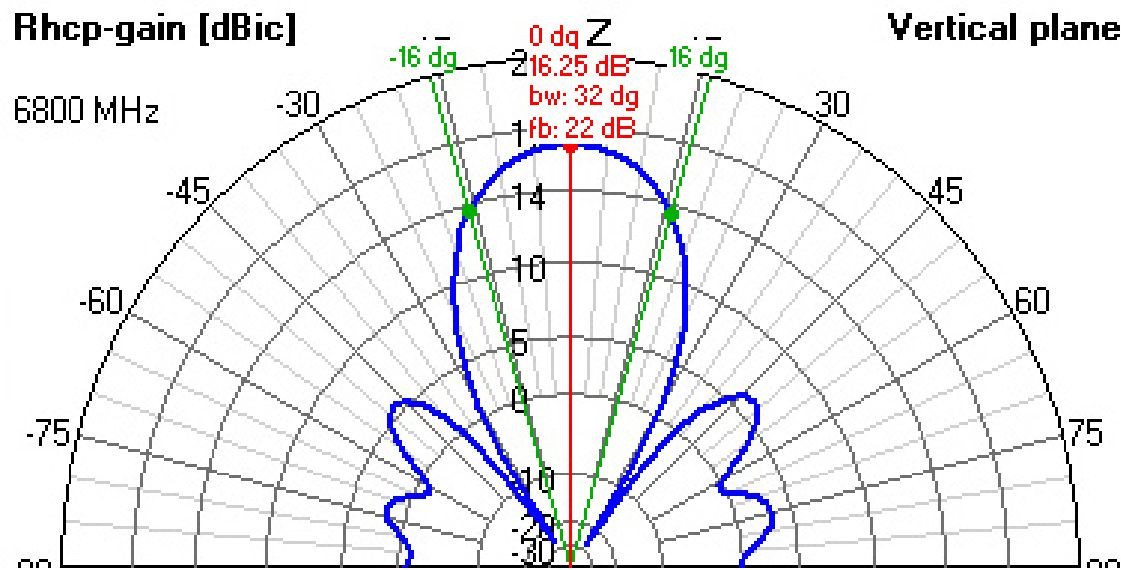
Figure F.2: Simulation of emission pattern of a helical microwave antenna for 6.8 GHz: The right hand circular polarization gain as function of the angle from antenna axis in the x-z plane. There is a high directionality and the opening angle of the main lobe is about 34°
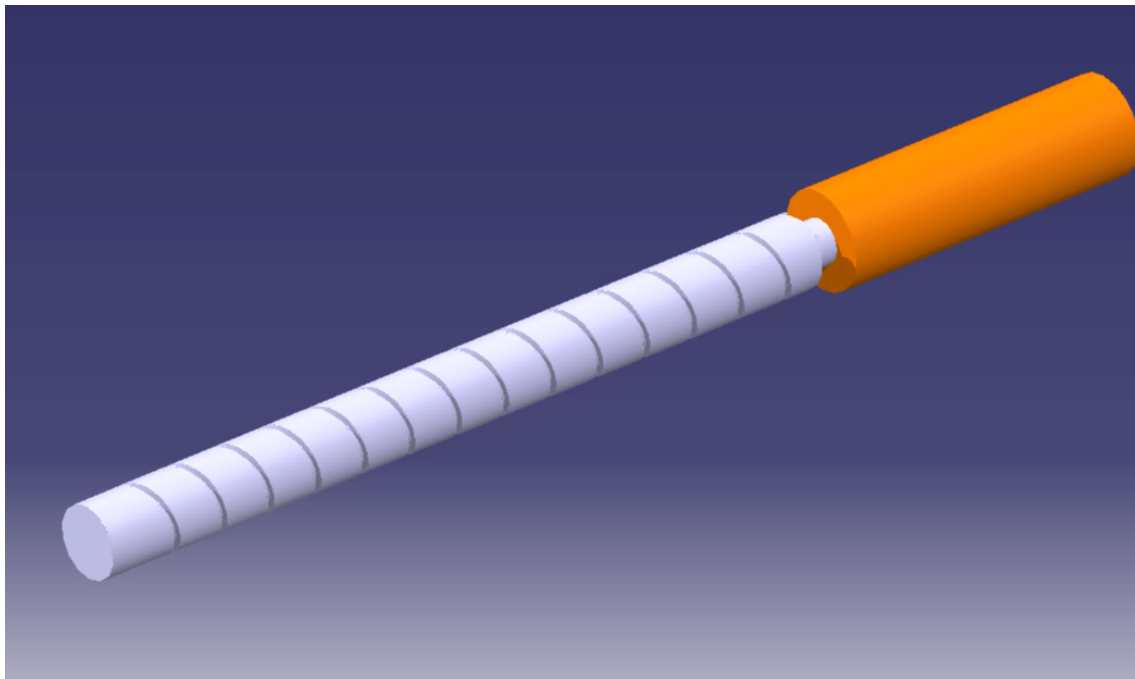
Figure F.3: CATIA (Dassault Systems: Version V5) design of a helical microwave antenna for 6.8 GHz: In order to reduce the dimensions of the antenna plexiglass (PMMA) is used. Due to the dielectric effect of the material which covers the windings of copper wire the wavelength of the microwaves in the plastic is reduced and such the size and spacing of the wire turns are smaller. An antenna with 15 turns is displayed. The realized antenna has 8.25 turns.
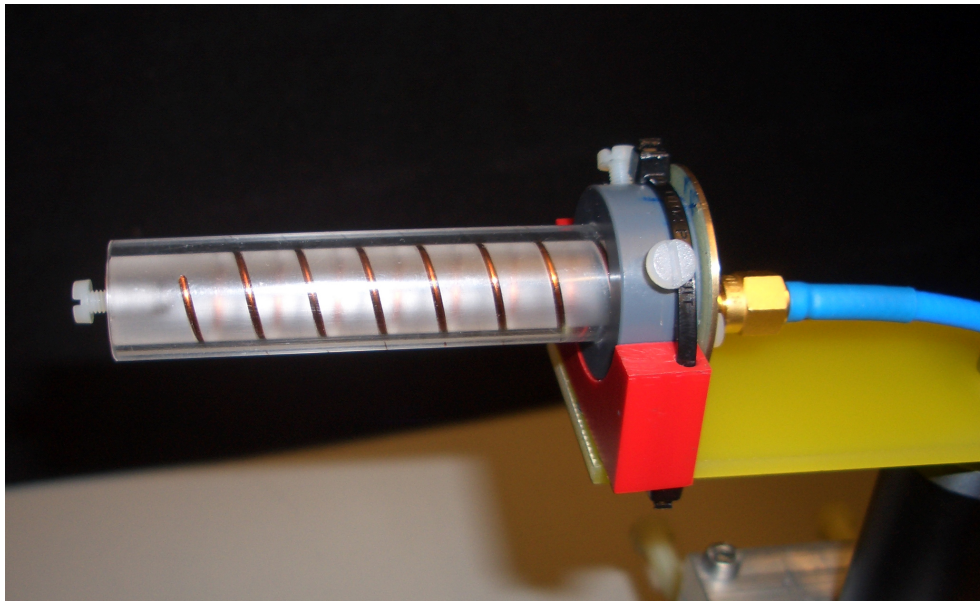
Figure F.4: Picture of the antenna on a rail system during the gain measurements. The rail system allows the variation of the antennas' separation without changing their relative angle.
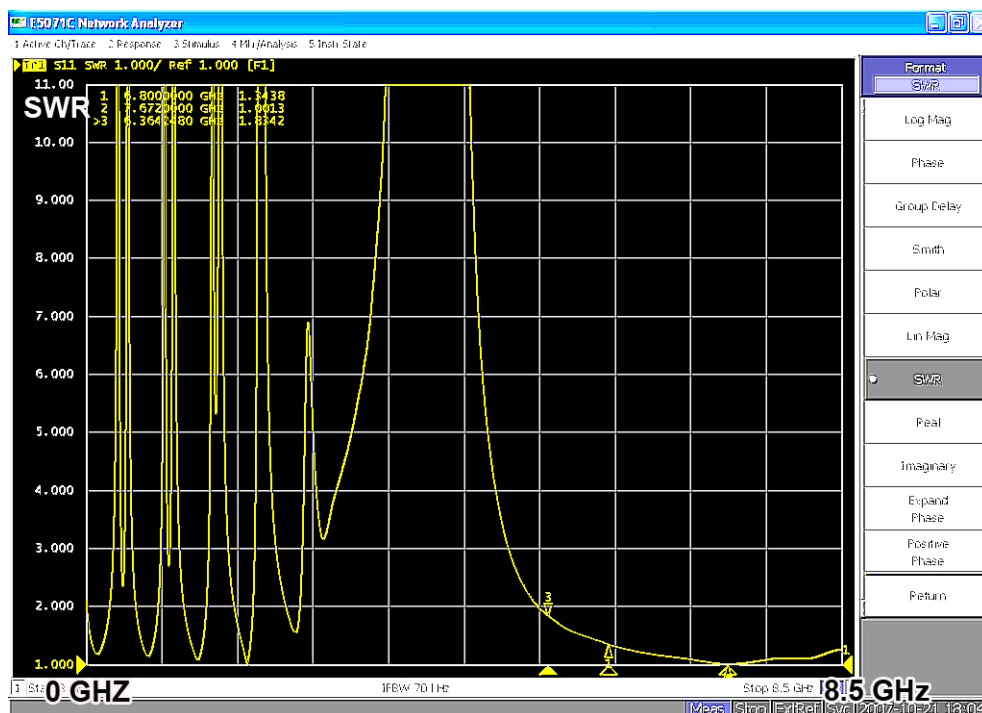

Figure F.5: SWR analysis with a Network Analyzer: At 6.83 GHz a SWR of ~ 1.34 is measured which means that the impedance matching is excellent. The large bandwidth of the antenna can be estimated from the data as well. The standing wave ratio between 6 GHz and 8.5 GHz is below 2.

Appendix G

Microwave Amplifier

In the current experiment a commercial microwave amplifier and switch has been used. For future measurements a amplifier has been developed. A GaAs MMIC amplifier provides $\sim$ 4 Watts of microwave power. The gain of the chip is only 20 dB. In order to obtain the maximum output of 33 dBm the input signal must have a power level of 13 dBm.
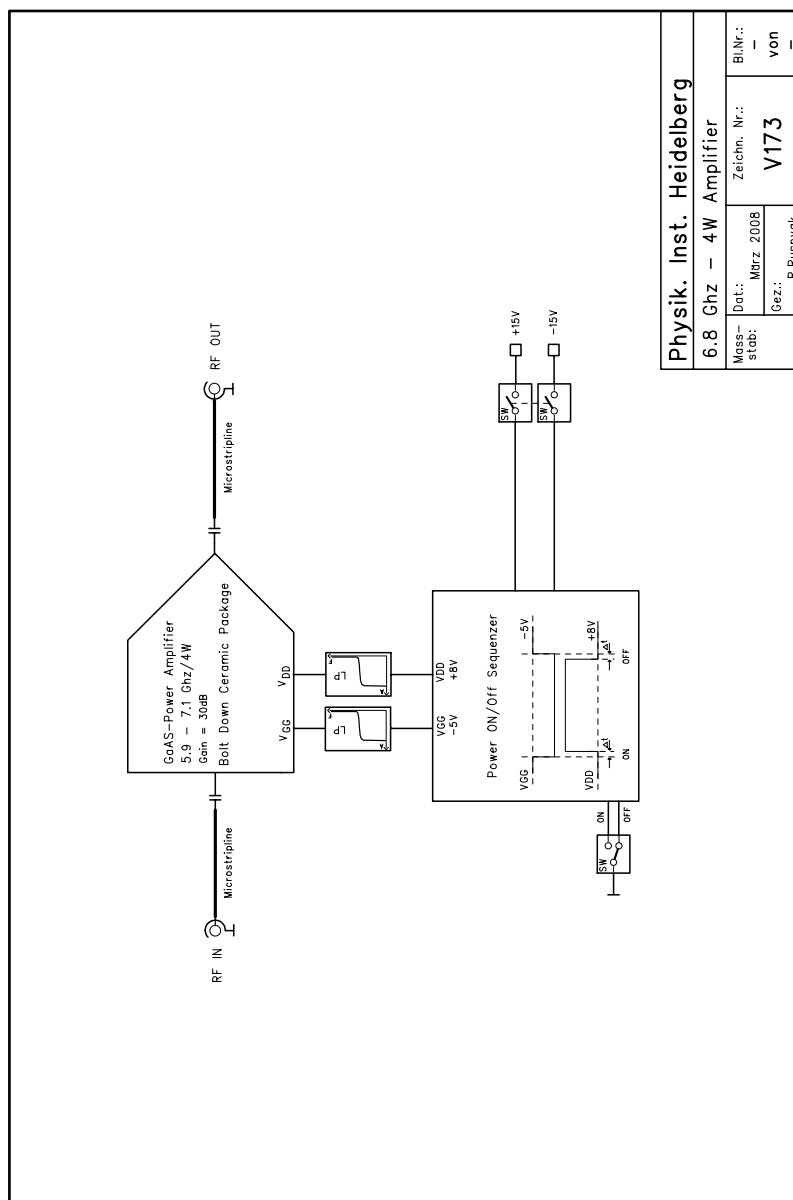
Figure G.1: Microwave switch: Two fast microwave switches are connected with microstrip connections to the input and output SMA connectors. Logic components translate an incoming TTL signal for switching into the proper switching voltages of the chips. A metal housing provides rf shielding. Two switches are necessary in order to achieve an extinction ratio > 70 dB.

Figure G.2: Microwave Amplifier for to 7 GHz: The GaAs MMic amplifier chip is mounted on circuit board with microstrip lines which have 50 Ohm impedance. The chip with the strip lines and SMA connectors has a metal housing as shielding and heat sink. In order to switch on/off the source and drain voltages in the correct sequence a sequencer circuit is attached to the amplifier's supply connections.

Appendix H

LevelConverter

Some of the employed commercial AOM drivers [1] have only a 50 Ω analog input for switching and controlling the intensity of the rf power. Its input voltage range is from 0 V to 1 V. For our experiment only fast switching ($\sim$ 50 ns) between ON and OFF is necessary. The logic box which generates the fast digital signals for the experiments provides a 50 Ω compatible TTL [2] signal where low level is between 0 V and 0.8 V and high level is defined between 2.2 V and 5 V. Especially the low level is critical since in the off-state there should be as low "leakage" light as possible.
In order to achieve an excellent match from TTL H/L levels to the analog AOM input levels 1V/0V at 50 Ω a level converter was developed. Besides the level conversion and the analog "0" it provides the necessary switching times in the nanosecond regime. The logic state of the output signal is reversed with respect of the input signal. The analog high level "H" at the output can be adjusted from 0.9 V to 5 V. There are two options for this adjustments: an internal potentiometer or an external analog voltage signal set this level. In order to achieve a H-level as low as 0.9 V a diode can added by a switch which causes a voltage drop of a few hundred mV.

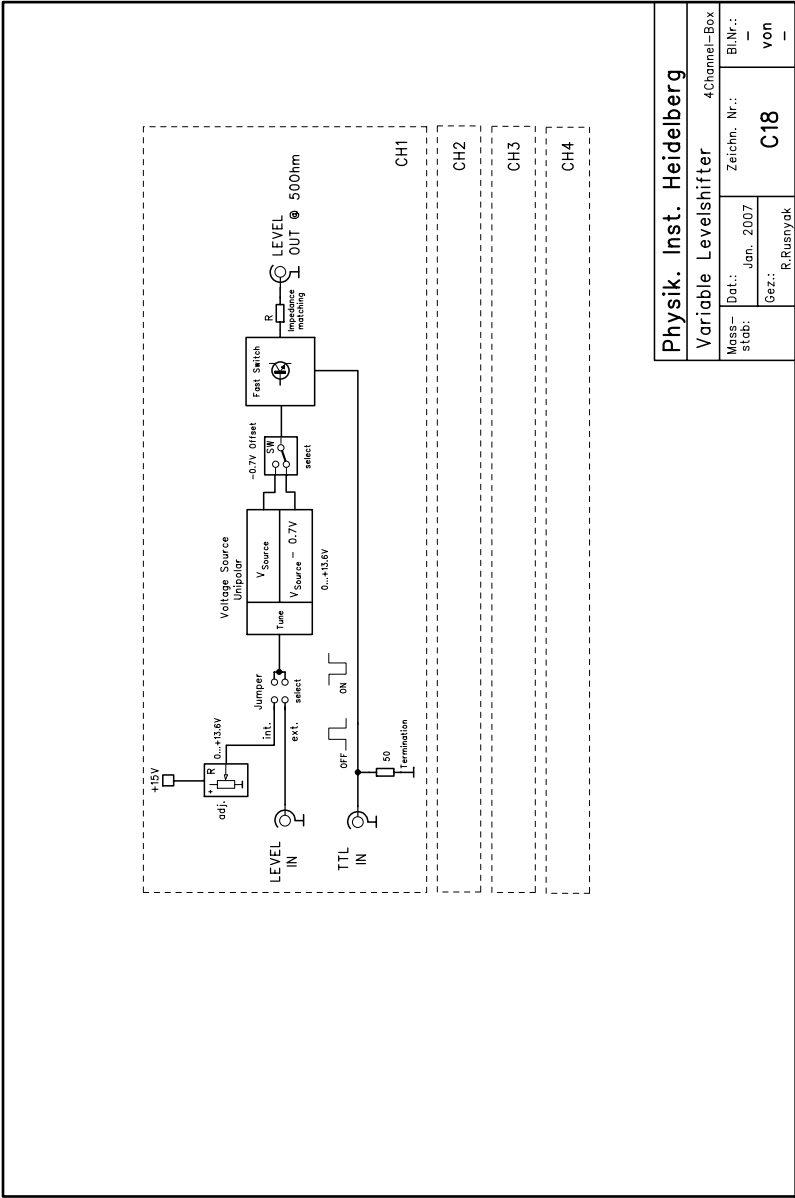---

[1]NEOS
[2]Transistor-Transistor Logic

Figure H.1: Schematics of one channel of the level converter. Four channels are arranged parallel on a single circuit board. The $\pm 15V$ supply voltage is provided by an external power supply.

Acknowledgement

With these final words I want to thank all the people for contributing to the success of this thesis:

Prof Jian-Wei Pan for supervising this thesis and providing me many freedoms and excellent possibilities during the course of the experiments.

Prof. Michael Fleischhauer for his kindness to referee this thesis.

Prof. Jörg Schmiedmayer for many exciting and stimulating ideas and for the nice Versadisk-Laser as well as for the coffee machine.

Prof. Andreas Mielke and Priv.Doz. Maarten DeKieviet as examiners in the oral examination.

Dr. Yu-Ao Chen for the excellent team work, his invaluable help always at the right time and of course all the fun.

Markus Koch for his hard and excellent work as well as for the cool lunch conversations. Good Luck for your Ph.D. project!

Dr. Bo Zhao for sharing his theoretical insights and being a great office mate.

Dr. Shuai Chen and Dr. Zheng-Shen Yuan for the great work and good team spirit.

Dr. Yu-Ao Chen, Dr. Bo Zhao, Dr. Alexander Goebel and Alexander Dück for proofreading this thesis.

Dr. Dennis Heine and Dr. Marco Wilzbach for sharing their experience in setting up stable laser systems and sharing lab equipment. Special thanks to D. H. for sharing the funny and not funny times of office life and in teaching.

Dr. Alexander Goebel for lending lab equipment and giving us a hand always at the right time.

Stephanie Manz for building Fabry Perots and sharing the experiences of running the thermal cell set-up.

Bibliography

[1] G. Vernam, "Cipher printing telegraph systems for sectret wire and radio telegraphic communications," *J. Am. Inst. Electr. Eng.*, vol. 45, pp. 109–115, 1926.

[2] R. L. Rivest, A. Shamir, and L. M. Adleman, "A method of obtaining digital signatures and public-key cryptosystems," *Commun. ACM*, vol. 21, pp. 120–126, 1978.

[3] M. A. Nielsen and I. L. Chuang, *Quantum Computation and Quantum Information.* 2001.

[4] P. W. Shor, "Polynomial-time algorithms for prime factorization and discrete logarithms on a quantum computer," in *Proceedings of the 35th Annual Symposium on Foundations of Computer Science*, 1994.

[5] W. Wootters and W. Zurek, "A single quantum cannot be cloned," *Nature*, vol. 299, p. 802, September 1982.

[6] D. Dieks, "Communication by EPR devices," *Phys. Lett*, vol. 92A, p. 271, August 1982.

[7] C. H. Bennett and G. Brassard, "BB84," in *Proceedings of the IEEE International Conference on Computers, Systems and Signal Processing*, p. 175, IEEE, IEEE, New York, 1984.

[8] C. H. Bennett, G. Brassard, and N. D. Mermin, "Quantum cryptography without Bell's theorem," *Phys. Rev. Lett.*, vol. 68, pp. 557–559, Feb 1992.

[9] N. Gisin, G. Ribordy, W. Tittel, and H. Zbinden, "Quantum cryptography," *Rev. Mod. Phys.*, vol. 74, pp. 145–195, Mar 2002.

[10] A. K. Ekert, "Quantum cryptography based on Bell's theorem," *Phys. Rev. Lett.*, vol. 67, pp. 661–663, 1991.

[11] H. Weier, T. Schmitt-Manderbach, N. Regner, C. Kurtsiefer, and H. Weinfurter, "Free space quantum key distribution: Towards a real life application," *Fortschritte der Physik*, vol. 54, no. 8-10, pp. 840–845, 2006.

[12] T. Schmitt-Manderbach, H. Weier, M. Fürst, R. Ursin, F. Tiefenbacher, T. Scheidl, J. Perdigues, Z. Sodnik, C. Kurtsiefer, J. G. Rarity, A. Zeilinger, and H. Weinfurter, "Experimental demonstration of free-space decoy-state quantum key distribution over 144 km," *Phys. Rev. Lett.*, vol. 98, p. 010504, 2007.

[13] K. Mattle, H. Weinfurter, P. G. Kwiat, and A. Zeilinger1, "Dense coding in experimental quantum communication," *Phys. Rev. Lett.*, vol. 76, pp. 4656–4659, 1996.

[14] A. Einstein, B. Podolsky, and N. Rosen, "Can quantum-mechanical description of physical reality be considered complete?," *Phys. Rev.*, vol. 47, pp. 777–780, May 1935.

[15] P. G. Kwiat, E. Waks, A. G. White, I. Appelbaum, and P. H. Eberhard, "Ultrabright source of polarization-entangled photons," *Phys. Rev. A*, vol. 60, pp. R773–R776, Aug 1999.

[16] D. Bouwmeester, J.-W. Pan, K. Mattle, M. Eibl, H. Weinfurter, and A. Zeilinger, "Experimental quantum teleportation," *Nature*, vol. 390, p. 575, Dec 1997.

[17] D. Bouwmeester, J.-W. Pan, M. Daniell, H. Weinfurter, and A. Zeilinger, "Observation of three-photon Greenberger-Horne-Zeilinger entanglement," *Phys. Rev. Lett.*, vol. 82, p. 1345, 1999.

[18] J.-W. Pan, D. Bouwmeester, M. Daniell, H. Weinfurter, and A. Zeilinger, "Experimental test of quantum nonlocality in three-photon Greenberger-Horne-Zeilinger entanglement," *Nature*, vol. 403, pp. 515–519, 2000.

[19] J.-W. Pan, M. Daniell, S. Gasparoni, G. Weihs, and A. Zeilinger, "Experimental demonstration of four-photon entanglement and high-fidelity teleportation," *Phys. Rev. Lett.*, vol. 86, pp. 4435–4438, May 2001.

[20] J.-W. Pan, C. Simon, C. Brukner, and A. Zeilinger, "Entanglement purification for quantum communication," *Nature*, vol. 410, pp. 1067–1070, 2001.

[21] J.-W. Pan, S. Gasparoni, R.Ursin, G. Weihs, and A. Zeilinger, "Experimental entanglement purification of arbitrary unknown states," *Nature*, vol. 423, p. 417, May 2003.

[22] J.-W. Pan, D. Bouwmeester, H. Weinfurter, and A. Zeilinger, "Experimental entanglement swapping: Entangling photons that never interacted," *Phys. Rev. Lett.*, vol. 80, p. 3891, 1998.

[23] J.-W. Pan, S. G. M. Aspelmeyer, T. Jennewein, and A. Zeilinger, "Experimental realization of freely propagating teleported qubits," *Nature*, vol. 421, pp. 721–725, 2003.

[24] T. Jennewein, C. Simon, G. Weihs, H. Weinfurter, and A. Zeilinger, "Quantum Cryptography with Entangled Photons," *Phys. Rev. Lett.*, vol. 84, p. 4729, 2000.

[25] Q. Zhang, A. Goebel, C. Wagenknecht, Y.-A. Chen, B. Zhao, T. Yang, A. Mair, J. Schmiedmayer, and J.-W. Pan, "Experimental quantum teleportation of a two-qubit composite system," *Nature Physics*, vol. 2, pp. 678–682, 2006.

[26] R. Ursin, F. Tiefenbacher, T. Schmitt-Manderbach, H. Weier, T. Scheidl, M. Lindenthal, B. Blauensteiner, T. Jennewein, J. Perdigues, P. Trojek, B. Oemer, M. Fuerst, M. Meyenburg, J. Rarity, Z. Sodnik, C. Barbieri, H. Weinfurter, and A. Zeilinger, "Free-space distribution of entanglement and single photons over 144 km," *Nature Physics*, vol. 3, p. 481, June 2007.

[27] W. Tittel, J. Brendel, H. Zbinden, and N. Gisin, "Quantum Cryptography using entangled photons in energy-time Bell states," *Phys. Rev. Lett*, vol. 84, no. 20, p. 4737, 2000.

[28] M. Aspelmeyer, H. R. Böhm, T. Gyatso, T. Jennewein, R. Kaltenbaek, M. Lindenthal, G. Molina-Terriza, A. Poppe, K. Resch, M. Taraba, R. Ursin, P. Walther, and A. Zeilinger, "Long-distance free-space distribution of quantum entanglement," *Science*, vol. 301, pp. 621–623, 2003.

[29] C.-Z. Peng, T. Yang, X.-H. Bao, J. Zhang, X.-M. Jin, F.-Y. Feng, B. Yang, J. Yang, J. Yin, Q. Zhang, N. Li, B.-L. Tian, and J.-W. Pan, "Experimental free-space distribution of entangled photon pairs over 13 km: towards satellite-based global quantum communication," *Phys. Rev. lett.*, vol. 94, p. 150501, 2005.

[30] R. Ursin, T. Jennewein, J. Kofler, J. M. Perdigues, L. Cacciapuoti, C. J. de Matos, M. Aspelmeyer, A. Valencia, T. Scheidl, A. Fedrizzi, A. Acin, C. Barbieri, G. Bianco, C. Brukner, J. Capmany, S. Cova, D. Giggenbach, W. Leeb, R. H. Hadfield, R. Laflamme, N. Lutkenhaus, G. Milburn, M. Peev, T. Ralph, J. Rarity, R. Renner, E. Samain, N. Solomos, W. Tittel, J. P. Torres, M. Toyoshima, A. Ortigosa-Blanch, V. Pruneri, P. Villoresi, I. Walmsley, G. Weihs, H. Weinfurter, M. Zukowski, and A. Zeilinger *(available at http://arxiv.org/abs/0806.0945)*.

[31] C. H. Bennett, G. Brassard, C. Crépeau, R. Jozsa, A. Peres, and W. K. Wootters, "Teleporting an unknown quantum state via dual classical and Einstein-Podolsky-Rosen channels," *Phys. Rev. Lett.*, vol. 70, pp. 1895–1899, Mar 1993.

[32] S. J. van Enk, J. I. Cirac, and P. Zoller, "Photonic channels for quantum communication," *Science*, vol. 279, p. 205, January 1998.

[33] E. Biham, B. Huttner, and T. Mor, "Quantum cryptographic network based on quantum memories," *Phys. Rev. A*, vol. 54, pp. 2651–2658, Oct 1996.

[34] J. I. Cirac, P. Zoller, H. J. Kimble, and H. Mabuchi, "Quantum state transfer and entanglement distribution among distant nodes in a quantum network," *Phys. Rev. Lett.*, vol. 78, p. 3221, 1997.

[35] T. Wilk, S. C. Webster, A. Kuhn, and G. Rempe, "Single-atom single-photon quantum interface," *Science*, vol. 317, pp. 488–490, 2007.

[36] A. D. Boozer, A. Boca, R. Miller, T. E. Northup, and H. J. Kimble, "Reversible state transfer between light and a single trapped atom," *Phys. Rev. Lett.*, vol. 98, p. 193601, 2007.

[37] D. F. Phillips, A. Fleischhauer, A. Mair, R. L. Walsworth, and M. D. Lukin, "Storage of light in atomic vapor," *Phys. Rev. Lett*, vol. 86, p. 783, 2001.

[38] M. Fleischhauer, A. Imamoḡlu, and J. P. Marangos, "Electromagnetically induced transparency: Optics in coherent media," *Rev. Mod. Phys.*, vol. 77, pp. 633–673, 2005.

[39] L. V. Hau, S. E. Harris, Z. Dutton, and C. H. Behroozi, "Light speed reduction to 17 metres per second in an ultracold atomic gas," *Nature*, vol. 397, p. 594, December 1999.

[40] C. Liu, Z. Dutton, C. Behroozi, and L. Hau, "Observation of coherent optical information storage in an atomic medium using halted light pulses," *Nature*, vol. 409, p. 490, Jan 2001.

[41] H.-J. Briegel, W. Dür, J. I. Cirac, and P. Zoller, "Quantum repeaters: The role of imperfect local operations in quantum communication," *Phys. Rev. Lett.*, vol. 81, pp. 5932–5935, Dec 1998.

[42] L.-M. Duan, M. D. Lukin, J. Cirac, and P. Zoller, "Long-distance quantum communication with atomic ensembles and linear optics," *Nature*, vol. 414, p. 413, Nov 2001.

[43] Z.-B. Chen, B. Zhao, Y.-A. Chen, J. Schmiedmayer, and J.-W. Pan, "Fault-tolerant quantum repeater with atomic ensembles and linear optics," *Physical Review A (Atomic, Molecular, and Optical Physics)*, vol. 76, no. 2, p. 022329, 2007.

[44] B. Zhao, Z.-B. Chen, Y.-A. Chen, J. Schmiedmayer, and J.-W. Pan, "Robust creation of entanglement between remote memory qubits," *Physical Review Letters*, vol. 98, no. 24, p. 240502, 2007.

[45] N. Sangouard, C. Simon, B. Zhao, Y.-A. Chen, H. de Riedmatten, J.-W. Pan, and N. Gisin, "Robust and efficient quantum repeaters with atomic ensembles and linear optics," *Physical Review A (Atomic, Molecular, and Optical Physics)*, vol. 77, no. 6, p. 062301, 2008.

[46] L. Jiang, J. M. Taylor, and M. D. Lukin, "A fast and robust approach to long-distance quantum communication with atomic ensembles," *Phys. Rev. A*, vol. 76, p. 012301, 2007.

[47] C. Simon, H. de Riedmatten, M. Afzelius, N. Sangouard, H. Zbinden, and N. Gisin, "Quantum repeaters with photon pair sources and multimode memories," *Phys. Rev. Lett.*, vol. 98, p. 190503, 2007.

[48] E. Knill, R. Laflamme, and G. J. Milburn, "Quantum computation with linear optics," *Nature*, vol. 409, p. 46, 2001.

[49] M. A. Nielsen, "Optical quantum computation using cluster states," *Phys. Rev. Lett.*, vol. 93, p. 040503, Jul 2004.

[50] M. A. Nielsen, "Quantum computation by measurement and quantum memory," *Physics Letters A*, vol. 308, no. 2-3, pp. 96–100, 2003.

[51] C. H. van der Wal, M. D. Eisaman, A. André, R. L. Walsworth, D. F. Phillips, A. S. Zibrov, , and M. D. Lukin, "Atomic memory for correlated photon states," *Science*, vol. 301, pp. 196–200, 2003.

[52] M. Eisaman, L. Childress, A. André, F. Massou, A. Zibrov, and M. Lukin, "Shaping quantum pulses of light via coherent atomic memory," *Phys.Rev.Lett*, no. 93, p. 233602, 2004.

[53] S. Manz, T. Fernholz, J. Schmiedmayer, and J.-W. Pan, "Collisional decoherence during writing and reading quantum states," *Physical Review A (Atomic, Molecular, and Optical Physics)*, vol. 75, no. 4, p. 040101, 2007.

[54] A. Kuzmich, W. Bowen, A. Boozer, A. Boca, C. Chou, L.-M. Duan, and H. Kimble, "Generation of nonclassical photon pairs for scalable quantum communication with atomic ensembles," *Nature*, vol. 423, p. 731, Jun 2003.

[55] D. N. Matsukevich and A. Kuzmich, "Quantum State Transfer Between Matter and Light," *Science*, vol. 306, p. 663, 2004.

[56] D. N. Matsukevich, T. Chanelière, M. Bhattacharya, S.-Y. Lan, S. D. Jenkins, T. A. B. Kennedy, and A. Kuzmich, "Entanglement of a photon and a collective atomic excitation," *Phys. Rev. Lett.*, vol. 95, p. 040405, 2005.

[57] D. N. Matsukevich, T. Chaneliere, S. Jenkins, S.-Y. Lan, T. A. B. Kennedy, and A. Kuzmich, "Deterministic Single Photons via Conditional Quantum Evolution," *Phys. Rev. Lett.*, vol. 97, p. 013601, 2006.

[58] T. Chanelière, D. N. Matsukevich, S. D. Jenkins, S.-Y. Lan, T. A. B. Kennedy, and A. Kuzmich, "Storage and retrieval of single photons transmitted between remote quantum memories," *Nature*, vol. 438, p. 833, December 2005.

[59] T. Chaneliere, D. N. Matsukevich, S. D. Jenkins, T. A. B. Kennedy, M. S. Chapman, and A. Kuzmich, "Quantum telecommunication based on atomic cascade transitions," *Physical Review Letters*, vol. 96, no. 9, p. 093604, 2006.

[60] T. Chanelière, D. N. Matsukevich, S. D. Jenkins, S.-Y. Lan, R. Zhao, T. A. B. Kennedy, and A. Kuzmich, "Quantum interference of electromagnetic fields from remote quantum memories," *Physical Review Letters*, vol. 98, no. 11, p. 113602, 2007.

[61] S.-Y. Lan, S. D. Jenkins, T. Chaneliere, D. N. Matsukevich, C. J. Campbell, R. Zhao, T. A. B. Kennedy, and A. Kuzmich, "Dual species matter qubit entangled with light," *Phys. Rev. Lett.*, vol. 98, p. 123602, 2007.

[62] S. D. Jenkins, D. N. Matsukevich, T. Chaneliere, A. Kuzmich, and T. A. B. Kennedy, "Theory of dark-state polariton collapses and revivals," *Physical Review A (Atomic, Molecular, and Optical Physics)*, vol. 73, no. 2, p. 021803, 2006.

[63] C. W. Chou, S. V. Polyakov, A. Kuzmich, and H. J. Kimble, "Single-photon generation from stored excitation in an atomic ensemble," *Phys. Rev. Lett.*, vol. 92, p. 213601, May 2004.

[64] C. W. Chou, H. de Riedmatten, D. Felinto, S. V. Polyakov, S. J. van Enk, and H. J. Kimble, "Measurement-induced entanglement for excitation stored in remote atomic ensembles," *Nature*, vol. 438, p. 828, October 2005.

[65] C.-W. Chou, J. Laurat, H. Deng, K. S. Choi, H. de Riedmatten, D. Felinto, and H. J. Kimble, "Functional quantum nodes for entanglement distribution over scalable quantum networks," *Science*, vol. 316, p. 1316, 2007.

[66] D. Felinto, C. W. Chou, H. de Riedmatten, S. V. Polyakov, and H. J. Kimble, "Control of decoherence in the generation of photon pairs from atomic ensembles," *Phys. Rev. A*, no. 72, p. 053809, 2005.

[67] D. Felinto, C. W. Chou, J. Laurat, E. W. Schomburg, H. de Riedmatten, and H. J. Kimble, "Conditional control of the quantum states of remote atomic memories for quantum networking," *Nature Physics*, vol. 2, p. 844, 2006.

[68] H. de Riedmatten, J. Laurat, C. W. Chou, E. W. Schomburg, D. Felinto, and H. J. Kimble, "Direct measurement of decoherence for entanglement between a photon and stored atomic excitation," *Physical Review Letters*, vol. 97, no. 11, p. 113603, 2006.

[69] J. Laurat, H. de Riedmatten, D. Felinto, C.-W. Chou, E. Schomburg, and H. J. Kimble, "Efficient retrieval of a single excitation stored in an atomic ensemble," *Optics Express*, vol. 14, p. 6912, 2006.

[70] J. Laurat, C. wen Chou, H. Deng, K. S. Choi, D. Felinto, H. de Riedmatten, and H. J. Kimble, "Towards experimental entanglement connection with atomic ensembles in the single excitation regime," *New Journal of Physics*, vol. 9, no. 6, p. 207, 2007.

[71] K. S. Choi, H. Deng, J. Laurat, and H. J. Kimble, "Mapping photonic entanglement into and out of a quantum memory," *Nature (London)*, vol. 452, p. 67, 2008.

[72] D. A. Braje, V. Balić, S. Goda, G. Y. Yin, and S. E. Harris, "Frequency mixing using electromagnetically induced transparency in cold atoms," *Phys. Rev. Lett.*, vol. 93, p. 183601, 2004.

[73] V. Balic, D. A. Braje, P. Kolchin, G. Y. Yin, and S. E. Harris, "Generation of paired photons with controllable waveforms," *Physical Review Letters*, vol. 94, no. 18, p. 183601, 2005.

[74] S. Chen, Y.-A. Chen, T. Strassel, Z.-S. Yuan, B. Zhao, J. Schmiedmayer, and J.-W. Pan, "Deterministic and storable single-photon source based on a quantum memory," *Physical Review Letters*, vol. 97, no. 17, p. 173004, 2006.

[75] Z.-S. Yuan, Y.-A. Chen, S. Chen, B. Zhao, M. Koch, T. Strassel, Y. Zhao, G.-J. Zhu, J. Schmiedmayer, and J.-W. Pan, "Synchronized independent narrow-band single photons and efficient generation of photonic entanglement," *Phys. Rev. Lett.*, vol. 98, p. 180503, 2007.

[76] S. Chen, Y.-A. Chen, B. Zhao, Z.-S. Yuan, J. Schmiedmayer, and J.-W. Pan, "Demonstration of a stable atom-photon entanglement source for quantum repeaters," *Phys. Rev. Lett.*, vol. 99, p. 180505, 2007.

[77] Y.-A. Chen, S. Chen, Z.-S. Yuan, B. Zhao, C.-S. Chuu, J. Schmiedmayer, and J.-W. Pan, "Memory-built-in quantum teleportation with photonic and atomic qubits," *Nature Physics*, vol. 4, p. 103, 2008.

[78] Z.-S. Yuan, Y.-A. Chen, B. Zhao, S. Chen, J. Schmiedmayer, and J.-W. Pan, "Entanglement swapping with storage and retrieval of light: A building block of quantum repeaters," *in press (available at http://lanl.arxiv.org/abs/0803.1810)*, 2008.

[79] M. O. Scully and M. S. Zubairy, *Quantum Optics*. Cambridge University Press, 1 ed., 1997.

[80] P. Hiskett, D. Rosenberg, C. Peterson, R. Hughes, S. Nam, A. Lita, A. Miller, and J. Nordholt, "Long-distance quantum key distribution in optical fibre," *New J.Phys.*, vol. 8, p. 193, 2006.

[81] R. Ursin, T. Jennewein, M. Aspelmeyer, R. Kaltenbaek, M. Lindenthal, P. Walther, and A. Zeilinger, "Quantum teleportation across the Danube," *Nature*, vol. 430, p. 849, August 2004.

[82] J. D. Jackson, *Classical Electrodynamics*. John Wiley and Sons, 3rd ed., 1998.

[83] A. Bayat, V. Karimipour, and I. Marvian, "Threshold distances for transmission of EPR pairs through Pauli channels," *Phys.Lett.A*, vol. 355, p. 81, June 2006.

[84] C. H. Bennett, G.Brassard, S. Popescu, B. Schumacher, J. A. Smolin, and W. K. Wootters, "Purification of noisy entanglement and faithful teleportation via noisy channels," *Phys. Rev. Lett.*, vol. 76, p. 722, 1996.

[85] W. Dür, H.-J. Briegel, J. I. Cirac, and P. Zoller, "Quantum repeaters based on entanglement purification," *Phys. Rev. A*, vol. 59, pp. 169–181, Jan 1999.

[86] D. Deutsch, A. Ekert, R. Jozsa, C. Macchiavello, S. Popescu, and A. Sanpera, "Quantum privacy amplification and the security of quantum cryptography over noisy channels," *Phys. Rev. Lett.*, vol. 77, pp. 2818–2821, Sep 1996.

[87] S. J. van Enk, J. I. Cirac, and P. Zoller, "Ideal quantum communication over noisy channels: A quantum optical implementation," *Phys. Rev. Lett.*, vol. 78, pp. 4293–4296, Jun 1997.

[88] M. Fleischhauer and M. D. Lukin, "Dark-state polaritons in electromagnetically induced transparency," *Phys. Rev. Lett.*, vol. 84, pp. 5094–5097, 2000.

[89] M. D. Lukin, S. F. Yelin, and M. Fleischhauer, "Entanglement of atomic ensembles by trapping correlated photon states," *Phys. Rev. Lett.*, vol. 84, pp. 4232–4235, 2000.

[90] M. Raymer and J. Mostowski, "Stimulated Raman scattering: Unified treatment of spontaneous initiation and spatial propagation," *Phys. Rev. A*, vol. 24, p. 1980, Oct 1981.

[91] M. Raymer, I. Walmsley, J. Mostowski, and B. Sobolewska, "Quantum theory of spatial and temporal coherence properties of stimulated Raman scattering," *Phys. Rev. A*, vol. 32, pp. 332–344, Jul 1985.

[92] R. Loudon, *The Quantum Theory of Light*. Oxford University Press, 1st ed., 1973.

[93] L. M. Duan, J. I. Cirac, and P. Zoller, "Three-dimensional theory for interaction between atomic ensembles and free-space light," *Phys. Rev. A*, vol. 66, p. 023818, 2002.

[94] B. Zhao, *Robust and efficient quantum repeater with atomic ensembles and linear optics*. PhD thesis, Universität Heidelberg, 2008.

[95] C. Mewes and M. Fleischhauer, "Two-photon linewidth of light ıstoppingȷ via electromagnetically induced transparency," *Phys. Rev. A*, vol. 66, p. 033820, Sep 2002.

[96] R. H. Dicke, "Coherence in spontaneous radiation processes," *Phys. Rev.*, vol. 93, p. 99, Jan 1954.

[97] L. Mandel and E. Wolf, *Optical Coherence and Quantum Optics*. Cambridge, UK: Cambridge University Press., 1995.

[98] A. Kuzmich, W. P. Bowen, A. D. Boozer, A. Boca, C. W. Chou, L.-M. Duan, and H. J. Kimble, "Generation of nonclassical photon pairs for scalable quantum communication with atomic ensembles," *Nature (London)*, vol. 423, p. 731, 2003.

[99] A. Kuhn, M. Hennrich, and G. Rempe, "Deterministic single-photon source for distributed quantum networking," *Phys. Rev. Lett.*, vol. 89, p. 067901, Jul 2002.

[100] J. J. Longdell, E. Fraval, M. J. Sellars, and N. B. Manson, "Stopped light with storage times greater than one second using electromagnetically induced transparency in a solid," *Phys. Rev. Lett.*, vol. 95, p. 063601, 2005.

[101] B. Kraus, W. Tittel, N. Gisin, M. Nilsson, S. Kröll, and J. I. Cirac, "Quantum memory for nonstationary light fields based on controlled reversible inhomogeneous broadening," *Phys. Rev. A*, vol. 73, p. 020302(R), 2006.

[102] M. U. Staudt, S. R. Hastings-Simon, M. Nilsson, M. Afzelius, V. Scarani, R. Ricken, H. Suche, W. Sohler, W. Tittel, and N. Gisin, "Fidelity of an optical memory based on stimulated photon echoes," *Phys. Rev. Lett.*, vol. 98, p. 113601, 2007.

[103] M. U. Staudt, M. Afzelius, H. de Riedmatten, S. R. Hastings-Simon, C. Simon, R. Ricken, H. Suche, W. Sohler, , and N. Gisin, "Interference of multimode photon echoes generated in spatially separated solid-state atomic ensembles," *Phys. Rev. Lett.*, vol. 99, p. 173602, 2007.

[104] M. D. Eisaman, A. André, F. Massou, M. Fleischhauer, A. S. Zibrov, and M. D. Lukin, "Electromagnetically induced transparency with tunable single-photon pulses," *Nature*, vol. 438, p. 837, December 2005.

[105] D. N. Matsukevich, T. Chaneliere, S. D. Jenkins, S.-Y. Lan, T. A. B. Kennedy, and A. Kuzmich, "Observation of dark state polariton collapses and revivals," *Physical Review Letters*, vol. 96, no. 3, p. 033601, 2006.

[106] A. V. Gorshkov, A. André, M. Fleischhauer, A. S. Sørensen, and M. D. Lukin, "Universal approach to optimal photon storage in atomic media," *Phys. Rev. Lett.*, vol. 98, p. 123601, 2007.

[107] B. Julsgaard, A. Kozhekin, and E. S. Polzik, "Experimental long-lived entanglement of two macroscopic objects," *Nature*, vol. 413, p. 400, 2001.

[108] J. F. Sherson, H. Krauter, R. K. Olsson, B. Julsgaard, K. Hammerer, I. Cirac, and E. S. Polzik, "Quantum teleportation between light and matter," *Nature*, vol. 443, pp. 557–560, 2006.

[109] J. Sherson, A. S. Sorensen, J. Fiurasek, K. Molmer, and E. S. Polzik, "Light qubit storage and retrieval using macroscopic atomic ensembles," *Physical Review A (Atomic, Molecular, and Optical Physics)*, vol. 74, no. 1, p. 011802, 2006.

[110] L. Hartmann, B. Kraus, H.-J. Briegel, and W. Dur, "Role of memory errors in quantum repeaters," *Physical Review A (Atomic, Molecular, and Optical Physics)*, vol. 75, no. 3, p. 032310, 2007.

[111] A. V. Gorshkov, A. André, M. Lukin, and A. S. Sørensen, "Photon storage in Λ-type optically dense atomic media. ii. free-space model," *Phys. Rev. A*, vol. 76, p. 033805, 2007.

[112] C. Mewes and M. Fleischhauer, "Decoherence in collective quantum memories for photons," *Phys. Rev. A*, vol. 72, p. 022327, 2005.

[113] J. B. Brask and A. S. Sorensen, "Memory imperfections in atomic-ensemble-based quantum repeaters," *Physical Review A (Atomic, Molecular, and Optical Physics)*, vol. 78, no. 1, p. 012350, 2008.

[114] D. A. Steck, *Rubidium 87 D line data: Version 2.0.1.* http://george.ph.utexas.edu/~dsteck/alkalidata, 2003.

[115] M. Eisaman, *Generation, Storage and Retrieval of Nonclassical States of Light Using Atomic Ensembles.* PhD thesis, Harvard University, 2006.

[116] S. Manz, "Privat communication.".

[117] A. V. Gorshkov, A. Andre, M. D. Lukin, and A. S. Sorensen, "Photon storage in lambda-type optically dense atomic media. i. cavity model," *Physical Review A (Atomic, Molecular, and Optical Physics)*, vol. 76, no. 3, p. 033804, 2007.

[118] D. Felinto. Private Communication.

[119] H. J. Lewandowski, D. M. Harber, D. L. Whitaker, and E. A. Cornell, "Observation of anomalous spin-state segregation in a trapped ultracold vapor," *Phys. Rev. Lett.*, vol. 88, p. 070403, 2002.

[120] H. J. Metcalf and P. van der Straten, *Laser Cooling and Trapping.* Springer, 1999.

[121] M. Khudaverdyan, W. Alt, I. Dotsenko, L. Forster, S. Kuhr, D. Meschede, Y. Miroshnychenko, D. Schrader, and A. Rauschenbeutel, "Adiabatic quantum state manipulation of single trapped atoms," *Physical Review A (Atomic, Molecular, and Optical Physics)*, vol. 71, no. 3, p. 031404, 2005.

[122] C. Pethick and H. Smith, *Bose-Einstein Condensation in Dilute Gases.* Cambridge University Press, 2002.

[123] S. Bali, K. M. O'Hara, M. E. Gehm, S. R. Granade, and J. E. Thomas, "Quantum-diffractive background gas collisions in atom-trap heating and loss," *Phys. Rev. A*, vol. 60, pp. R29–R32, Jul 1999.

[124] S. Schneider, *Bose-Einstein Kondensation in einer magnetischen Z-Falle.* PhD thesis.

[125] S. J. J. M. F. Kokkelmans, H. M. J. M. Boesten, and B. J. Verhaar, "Role of collisions in creation of overlapping bose condensates," *Phys. Rev. A*, vol. 55, pp. R1589–R1592, Mar 1997.

[126] P. S. Julienne, F. H. Mies, E. Tiesinga, and C. J. Williams, "Collisional stability of double Bose condensates," *Phys. Rev. Lett.*, vol. 78, pp. 1880–1883, Mar 1997.

[127] J. Weiner, V. S. Bagnato, S. Zilio, and P. S. Julienne, "Experiments and theory in cold and ultracold collisions," *Rev. Mod. Phys.*, vol. 71, pp. 1–85, Jan 1999.

[128] S. Dürr, K. W. Miller, and C. E. Wieman, "Improved loading of an optical dipole trap by suppression of radiative escape," *Phys. Rev. A*, vol. 63, p. 011401, Dec 2000.

[129] M. V. Romalis and E. N. Fortson, "Zeeman frequency shifts in an optical dipole trap used to search for an electric-dipole moment," *Phys. Rev. A*, vol. 59, pp. 4547–4558, Jun 1999.

[130] T. Takekoshi, J. R. Yeh, and R. J. Knize, "Quasi-electrostatic trap for neutral atoms," *Optics Communications*, vol. 114, p. 421, February 1995.

[131] A. Kaplan, M. F. Andersen, T. Grunzweig, and N. Davidson, "Hyperfine spectroscopy of optically trapped atoms," *Journal of Optics B: Quantum and Semiclassical Optics*, vol. 7, no. 8, pp. R103–R125, 2005.

[132] R. Ozeri, L. Khaykovich, and N. Davidson, "Long spin relaxation times in a single-beam blue-detuned optical trap," *Phys. Rev. A*, vol. 59, pp. R1750–R1753, Mar 1999.

[133] T. Huga, Y. Torii, N. Shiokawa, T. Hirano, Y. Shimizu, and H. Sasada *Phys. Rev. Lett.*, vol. 78, p. 4713, 1997.

[134] N. Davidson, H. Jin Lee, C. S. Adams, M. Kasevich, and S. Chu, "Long atomic coherence times in an optical dipole trap," *Phys. Rev. Lett.*, vol. 74, pp. 1311–1314, Feb 1995.

[135] M. Wilzbach, "Aufbau eines Experiments zur miniaturisierten und integrierten Detektion neutraler Atome," Master's thesis, Universität Heidelberg, 2002.

[136] W. Demtröder, *Laser Spectroscopy.* Springer Verlag, 1993.

[137] Y.-A. Chen, *Quantum Manipulation of Photons and Atoms: The Application in Quantum Information Processing.* PhD thesis.

[138] G. A. Askaryan, "Effects of the gradient of a strong electromagnetic beam on electrons and atoms," *Sov. Phys. JETP,*, vol. 15, p. 1088, 1962.

[139] I. I. Sobelman, *Atomic Spectra and Radiative Transitions.* Springer Series on Atoms and Plasmas, Springer-Verlag, 2nd ed., 1992.

[140] R. Grimm, M. Weidemüller, and Y. B. Ovchinnikov, "Optical dipole traps for neutral atoms," *Adv. Atom. Mol. Opt. Phy*, vol. 42, p. 95, 2000.

[141] C. Cohen-Tannoudji, J. Dupont-Roc, and G. Grynberg, *Atom-Photon Interactions.* Wily-Interscience, 1992.

[142] G. Morigi and J. Eschner, "Doppler cooling of a coulomb crystal," *Phys. Rev. A*, vol. 64, p. 063407, Nov 2001.

[143] M. Koch, "Atomic ensembles in an optical dipole trap: Towards a quantum memory with long storage time," Master's thesis, Universität Heidelberg.

[144] J. Y. Kim, J. S. Lee, H. H. Han, and D. Cho, "Optical dipole trap without inhomogeneous AC Stark broadening," *Journal of the Korean Physical Society*, vol. 42, no. 4, p. 483, 2003.

[145] P. Griffin, K. Weatherill, S. MacLeod, R. Potvliege, and C. Adams, "Spatially selective loading of an optical lattice by light-shift engineering using an auxiliary laser field," *New J. Phys.*, vol. 8, p. 11, January 2006.

[146] B. Arora, M. S. Safronova, and C. W. Clark, "Magic wavelengths for the np-ns transitions in alkali-metal atoms," *Physical Review A (Atomic, Molecular, and Optical Physics)*, vol. 76, no. 5, p. 052509, 2007.

[147] W. Ketterle, D. Durfee, and D. Stamper-Kurn, "Making, probing and understanding Bose-Einstein condensates," *Proceedings of the 1998 Enrico Fermi summer school on Bose-Einstein condensation in Varenna*, vol. arXiv:cond-mat/9904034v2, 1999.

[148] W. Ketterle, K. B. Davis, M. A. Joffe, A. Martin, and D. E. Pritchard, "High densities of cold atoms in a dark spontaneous-force optical trap," *Phys. Rev. Lett.*, vol. 70, pp. 2253–2256, Apr 1993.

[149] K. W. Miller, *Trapping and Cooling Rubidium in Far-off-resonant Optical Dipole Traps*. PhD thesis, University of Colorado, 2004.

[150] G. Cennini, G. Ritt, C. Geckeler, and M. Weitz, "Bose-Einstein condensation in a C02-laser optical dipole trap," *Appl. Phys. B*, vol. 77, no. 8, pp. 773–779, 2003.

[151] B. Lounis and M. Orrit *Rep. Prog. Phys.*, vol. 68, p. 1129, 2005.

[152] P. Michler, A. Kiraz, C. Becher, W. V. Schoenfeld, P. M. Petroff, L. Zhang, E. Hu, and A. Imamoglu, "A Quantum Dot Single-Photon Turnstile Device," *Science*, vol. 290, no. 5500, pp. 2282–2285, 2000.

[153] C. Santori, M. Pelton, G. Solomon, Y. Dale, and Y. Yamamoto, "Triggered single photons from a quantum dot," *Phys. Rev. Lett.*, vol. 86, pp. 1502–1505, Feb 2001.

[154] M. Keller, B. Lange, K. Hayasaka, W. Lange, and H. Walther, "Continuous generation of single photons with controlled waveform in an ion-trap cavity system," *Nature*, vol. 431, p. 1075, 2004.

[155] C. Kurtsiefer, S. Mayer, P. Zarda, and H. Weinfurter, "Stable solid-state source of single photons," *Phys. Rev. Lett.*, vol. 85, pp. 290–293, Jul 2000.

[156] C. Santori, D. Fattal, J. Vuckovic, G. S. Solomon, and Y. Yamamoto, "Single-photon generation with InAs quantum dots," *New J. Phys.*, vol. 6, p. 89, 2004.

[157] C. W. Chou, H. de Riedmatten, D. Felinto, S. V. Polyakov, S. J. van Enk, and H. J. Kimble, "Measurement-induced entanglement for excitation stored in remote atomic ensembles," *Nature*, vol. 438, pp. 828–832, 2005.

[158] M. D. Lukin, "Colloquium: Trapping and manipulating photon states in atomic ensembles," *Rev. Mod. Phys.*, vol. 75, pp. 457–472, Apr 2003.

[159] G. R. P. Grangier and A. Aspect *Europhys. Lett.*, vol. 1, p. 173, 1986.

[160] R. Raussendorf and H. J. Briegel, "A one-way quantum computer," *Phys. Rev. Lett.*, vol. 86, pp. 5188–5191, May 2001.

[161] D. E. Browne and T. Rudolph, "Resource-efficient linear optical quantum computation," *Physical Review Letters*, vol. 95, no. 1, p. 010501, 2005.

[162] R. Kaltenbaek, B. Blauensteiner, M. Zukowski, M. Aspelmeyer, and A. Zeilinger, "Experimental interference of independent photons," *Physical Review Letters*, vol. 96, no. 24, p. 240502, 2006.

[163] T. Yang, Q. Zhang, T.-Y. Chen, S. Lu, J. Yin, J.-W. Pan, Z.-Y. Wei, J.-R. Tian, and J. Zhang, "Experimental synchronization of independent entangled photon sources," *Physical Review Letters*, vol. 96, no. 11, p. 110501, 2006.

[164] C. K. Hong, Z. Y. Ou, and L. Mandel, "Measurement of subpicosecond time intervals between two photons by interference," *Phys. Rev. Lett.*, vol. 59, pp. 2044–2046, Nov 1987.

[165] J. F. Clauser, M. A. Horne, A. Shimony, and R. A. Holt, "Proposed experiment to test local hidden-variable theories," *Phys. Rev. Lett.*, vol. 23, pp. 880–884, Oct 1969.

[166] J. Simon, H. Tanji, J. K. Thompson, and V. Vuletić, "Interfacing collective atomic excitations and single photons," *Phys. Rev. Lett.*, vol. 98, p. 183601, 2007.

[167] D. M. Harber, H. J. Lewandowski, J. M. McGuirk, and E. A. Cornell, "Effect of cold collisions on spin coherence and resonance shifts in a magnetically trapped ultracold gas," *Phys. Rev. A*, vol. 66, p. 053616, 2002.

[168] M. Greiner, O. Mandel, T. Esslinger, T. W. Hänsch, and I. Bloch, "Quantum phase transition from a superfluid to a Mott insulator in a gas of ultracold atoms," *Nature (London)*, vol. 415, p. 39, 2002.

[169] P. Zoller, Th. Beth, D. Binosi, R. Blatt, H. Briegel, D. Bruss, T. Calarco, J.I. Cirac, D. Deutsch, J. Eisert, A. Ekert, C. Fabre, N. Gisin, P. Grangiere, M. Grassl, S. Haroche, A. Imamoglu, A. Karlson, J. Kempe, L. Kouwenhoven, S. Krö, G. Leuchs, M. Lewenstein, D. Loss, N. Lütkenhaus, S. Massar, J.E. Mooij, M.B. Plenio, E. Polzik, S. Popescu, G. Rempe, A. Sergienko, D. Suter, J. Twamley, G. Wendin, R. Werner, A. Winter, J. Wrachtrup, and A. Zeilinger, "Quantum information processing and communication," *The European Physical Journal D*, vol. 36, pp. 203–228, nov 2005.

[170] M. Żukowski, A. Zeilinger, M. A. Horne, and A. K. Ekert, ""event-ready-detectors" Bell experiment via entanglement swapping," *Phys. Rev. Lett.*, vol. 71, pp. 4287–4290, 1993.

[171] P. Treutlein, P. Hommelhoff, T. Steinmetz, T. W. Hänsch, and J. Reichel, "Coherence in microchip traps," *Phys. Rev. Lett.*, vol. 92, p. 203005, May 2004.

[172] J. F. Clauser and M. A. Horne, "Experimental consequences of objective local theories," *Phys. Rev. D*, vol. 10, pp. 526–535, 1974.

[173] To measure $g_{S,S}$ (or $g_{AS,AS}$), one would direct the Stokes (or anti-Stokes) field onto a 50/50 beamsplitter with a single-photon detector placed behind each output port, then $g_{S,S}$ (or $g_{AS,AS}) = p_{1,2}/p_1 p_2$, where $p_{1,2}$ and $\{p_1, p_2\}$ are the joint and individual probability of detecting one photon by the two detectors, respectively.

[174] B. Zhao, Y.-A. Chen, X.-H. Bao, T. Strassel, C.-S. Chuu, Z.-S. Yuan, S. Chen, and J.-W. Pan, "A millisecond quantum memory for scalable quantum networks," *submitted to Nature Physics*, 2008.

[175] M. D. Barrett, J. A. Sauer, and M. S. Chapman, "All-optical formation of an atomic Bose-Einstein condensate," *Phys. Rev. Lett.*, vol. 87, p. 010404, 2001.

[176] T. P. Meyrath, F. Schreck, J. L. Hanssen, C.-S. Chuu, and M. G. Raizen, "Bose-Einstein condensate in a box," *Physical Review A (Atomic, Molecular, and Optical Physics)*, vol. 71, no. 4, p. 041604, 2005.

[177] M. S. Safronova, C. J. Williams, and C. W. Clark, "Relativistic many-body calculations of electric-dipole matrix elements, lifetimes, and polarizabilities in rubidium," *Phys. Rev. A*, vol. 69, no. 2, p. 022509, 2004.

[178] R. Schmieder, "Matrix elements of the quadratic Stark effect on atoms with hyperfine structure," *Am. J. Phys.*, vol. 40, no. 297, 1972.

[179] J. Angel and P. Sanders, "The hyperfine structure stark effect; i. theory," *Proc. Roy. Soc. A*, vol. 305, p. 125, 1968.

[180] P. F. Griffing, *Laser Cooling and Loading of Rb into A Large Period, Quasi-Electrostatic, Optical Lattice.* Phd thesis, Durham University, 2005.

[181] M. Prevedelli, T. Freegarde, and T. W. Hänsch, "Phase locking of grating-tuned diode lasers," *Appl. Phys. B*, vol. 60, pp. 241–248, 1995.

[182] J. Kraus, *Antennas.* McGraw Hill:NewYork, 2nd ed. ed., 1988.